Tuning Ultrafast Chemical Reaction Dynamics in Photoactive Proteins

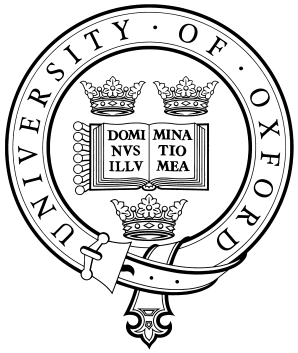

Giovanni Bassolino

Department of Chemistry

University of Oxford

This thesis is submitted for the degree of

Doctor of Philosophy in Physical and Theoretical Chemistry

Balliol College April 2015

To my family

oh fishing vessels
please take this message back
to those I love over
the vast blue ocean's expanse
I've rowed toward endless isles

Ono no Takamura
Kokinshū, IX, 407, translated by L. L. Rodd

hauntingly they cry
the northbound geese of the night-
one from their number
who flew this way in autumn
accompanies them not home

Anonymous
Kokinshū, IX, 412, translated by L. L. Rodd

[...] Ithaka gave you the marvelous journey
Without her you would not have set out
She has nothing left to give you now. [...]

K. P. Kavafis
excerpt from *Ithaka*, translated by E. Keeley and P. Sherrard

Declaration

I hereby declare that except where specific reference is made to the work of others, the contents of this dissertation are original and have not been submitted in whole or in part for consideration for any other degree or qualification in this, or any other university. This dissertation is my own work and contains nothing which is the outcome of work done in collaboration with others, except as specified in the text.

Giovanni Bassolino

April 2015

Abstract

This dissertation investigates the origins of tunable and efficient photochemistry in three different photoactive proteins, bacteriorhodopsin (BR), rhodopsin (RHO) and green fluorescent protein (GFP). In all cases, significant differences exist between the photoreactivity of model chromophores in solution and in the protein environment, in terms of excited state lifetime and efficiency of the primary photochemical process (opsin proteins) or the type of reaction (excited state proton transfer versus C=C double bond photoisomerisation for GFP).

The work presented here investigates for each case to what extent the protein environment is necessary to alter the photochemistry of model chromophores in solution. For GFP and BR steric and electrostatic interactions between the protein pocket and the chromophore are shown to be likely responsible for shaping the excited state surface along which the photoreactions take place. For RHO it is suggested, contrary to current belief, that selection of a reactive ground state conformer might be the main effect generating the observed differences between solution and protein environment.

The solution photochemistry of structurally modified retinal protonated Schiff bases, taken as model chromophores for the opsin proteins, is studied with continuous wave irradiation experiments and ultrafast transient spectroscopies. Surprisingly large differences are observed for the isomerisation reaction depending on the starting configuration (*trans* or *cis*) of the photoactive double bond. The current model for BR based on the tuning of the excited state barrier encountered along the isomerisation coordinate is expanded to include the changes in selectivity, speed and efficiency observed for a series of all-*trans* derivatives.

For 11-*cis*, the photoisomerisation in solution is proposed to take place along a barrierless isomerisation coordinate, in contrast with the models currently available in literature. It is suggested that the protein might be discriminating between ground state conformers rather than significantly changing the topography of the reaction coordinate.

For GFP, excited state Raman spectra are recorded for the wild-type protein, two mutants and a model chromophore in solution. It is suggested that the high frequency vibrational modes observed in the excited state spectra of the proteins but not of the model chromophore in DMSO are a sign of a tighter chromophore environment that inhibits the photoisomerisation reaction occurring in solution.

Table of contents

List of figures

List of tables

List of Abbreviations and Acronyms

BBO	β-barium borate
BR	bacteriorhodopsin
CI	conical intersection
CW	continuous wave
DADS	decay associated differential spectrum
ESA	excited state absorption
ESL	excited state lifetime
FC	Franck Condon
FROG	frequency resolved optical gating
GFP	green fluorescent protein
IRF	instrument response function
nBu	*n*-butylamine
NMR	nuclear magnetic resonance
NOE	Nuclear Overhauser Effect
NOPA	non-collinear optical parametric amplifier
PES	potential energy surface
PSB	protonated Schiff base
QY	quantum yield
RHO	rhodopsin
RPSB	retinal protonated Schiff base
SAS	species associated spectrum
SE	stimulated emission

SFG	sum frequency generation
SHG	second harmonic generation
SP	stationary point
TA	transient absorption
TFA	trifluoroacetic acid
VC	vibrational coherences

Chapter 1

Introduction

According to the International Union of Pure and Applied Chemistry, photochemistry is the "[b]ranch of chemistry concerned with the chemical effects of ultraviolet, visible, or infrared radiation".[1] The way photochemical reactions are studied has significantly changed since the introduction of flash photolysis by Norrish and Porter.[2] Furthermore, with the introduction of solid state pulsed lasers, the time scales of the "immeasurably fast reactions" giving the title to Eigen's Nobel lecture[3] has been pushed all the way down to the femtosecond regime, the timescale of molecular vibrations,[4] and the emerging field of attosecond science is pushing it towards the domain of electronic motion.[5] These technological developments have enabled us to directly observe the microscopic kinetic rates, the field of chemical reaction dynamics.[6] A deeper level of understanding of the fundamental photochemical processes has been enabled by the observation of molecular structures "in real time" whilst reactions are taking place.[4] From reactions of small molecules,[4] femtochemistry has since long moved into the domain of biologically relevant macromolecules, whose ultrafast photochemistry is the object of femtobiology.[7]

Light triggered reactions enter everyday life in a variety of ways. Amongst others, the neural stimulus that allows us to read this text or see the world around us is triggered by the absorption and consequent conformational change of photoreceptors in the eye;[8] the

oxygen we breath and the sugars we eat are produced by plants as a result of a multi-step water oxidation and carbon dioxide reduction initiated by absorption of photons in the photosynthetic reaction centres;[9] the circadian timing, the twenty-four hour "biological clock", seems to be regulated by light detection from photoactive proteins different than the receptors present in the cones or rods cells of the eye.[10]

Biological photoreceptors are proteins that upon absorption of a photon undergo structural rearrangements resulting in a *response* from the organisms expressing them.[7,11,12] Present in all three biological domains, from archaea to animals, they are involved in a wide variety of life-sustaining functions, spanning bacterial photosynthesis, phototaxis, vision, regulation of circadian clock, germination, etc.[11,12] Whereas the aminoacids that constitute proteins absorb in the ultraviolet range of the light spectrum (well below 400 nm), most of the sun-light that reaches the Earth surface and can be used for the processes mentioned above has longer wavelengths, peaking around 500 nm.[13] Because of this mismatch between the absorption spectra of the polypeptide backbone and the solar spectrum, photoactive proteins require a co-factor to perform their function,[12] usually a small, polyunsaturated organic molecule, like retinal for the opsins, coumaric acid for the xanthopsins or flavin for chryptochromes, phototropins or BLUF (blue-light using FAD) proteins.[11] The organic co-factor, beyond being responsible for the initial absorption of the incident photons, is involved in an ultrafast photoreaction that triggers the cascade of structural rearrangements generating the response.[12] The primary photochemical steps are reactions like *cis-trans* isomerisation, or electron, proton or energy transfer.[7,11] In the section that follows, I will focus my attention on the opsin family of photoreceptors, whose ultrafast primary photochemical process, *cis-trans* isomerisation of the retinal co-factor, is the object of the major part of this dissertation.

Retinylidene proteins are membrane photoreceptors sharing a common topology of seven transmembrane helices.[14,15] They are classified in two broad families, type I, microbial, and type II, animal rhodopsins.[15] The disposition of the helices differs between the two types,

whilst the retinal chromophore is present in all cases as a protonated Schiff base (PSB) formed with the ε-amino group of a lysine residue of the seventh helix.[15] Microbial rhodopsins usually bind the all-*trans* isomer of retinal, that selectively isomerises to 13-*cis* upon photoexcitation.[14,15] This photoreaction is the trigger for a wide variety of processes depending on the protein involved, such as ion pumping (bacteriorhodopsin, BR, and halorhodopsin), phototaxis (sensory rhodopsins), or ion channeling (channelrhodopsins).[14,15] Type II rhodopsins, on the other hand, bind the 11-*cis* isomer that photoisomerises to all-*trans*.[14,15] They are the primary photoreceptors in the visual process, but their discovery in cells outside the eye supports their involvement in other light-sensing process, like production of melatonin or circadian clock regulation.[8,10,15]

For the present work, the interest towards this class of proteins stems not only from the multitude of biological processes they are involved with but also, and mostly, from the striking differences observed when comparing the solution photoreactivity of the retinal chromophore with the corresponding opsin photochemistry in terms of absorption maximum, excited state lifetime (ESL), isomerisation quantum yield (QY) and photoproducts distribution. In the discussion that follows and within the dissertation I will take as an example BR for type I, and bovine rod rhodopsin (RHO) for type II, as they are the most studied and better understood members of the respective families,[14–17] and, even more importantly, extensive experimental work has been performed with pigment analogues prepared with structurally modified retinals. As a model for the solution photochemistry the *n*-butylamine (nBu) PSB is adopted, for its structural similarity with the chromophore in the protein (Figure 1.1).

BR is one of the four retinylidene proteins found in the archaeon *Halobacterium salinarium*. The biological function of BR is to vectorially pump protons from the cytoplasm to the extracellular medium, generating a chemical gradient that is then exploited for ATP production.[15] The vectorial proton pumping action is performed through a series of conformational changes induced by the photoisomerisation of the chromophore.[18] When all-*trans* retinal

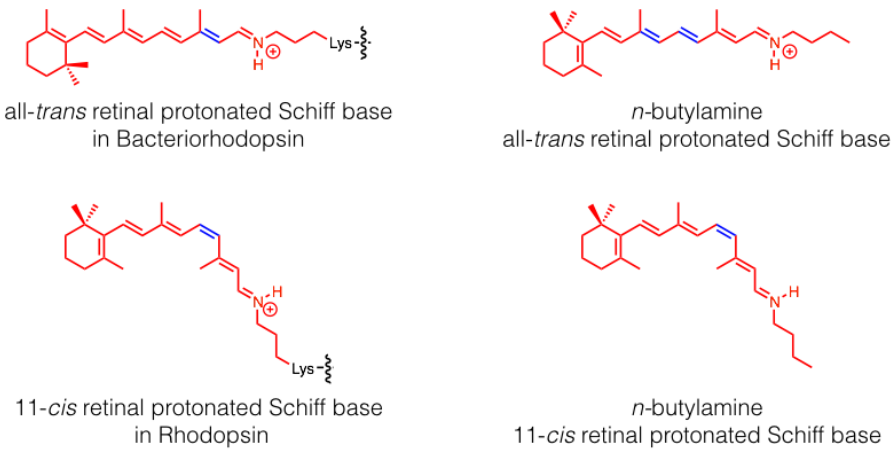

Figure 1.1 All-*trans* and 11-*cis* RPSB within microbial and animal opsins and respective model chromophores in solution. The part in red of the molecule is in common between the co-factor in the protein and the model chromophores. In blue are indicated the photoactive double bonds.

isomerises to the 13-*cis* isomer, a steric clash with the protein pocket produces the energy to support the structural changes that follow. In the case of BR, the protein undergoes a complete photocycle, with retinal never leaving the apoprotein and being ultimately regenerated in the all-*trans* configuration.[14] The other three microbial rhodopsin found in *Halobacterium Salinarium* perform different functions. Halorhodopsin (HR) is an inward-directed chloride pump, whilst the two sensory rhodopsins (SRI and SRII) are involved in negative and positive phototaxis.[14] Following the initial discovery in *Halobacterium salinarium*, other type I opsin proteins have been found in an increasing variety of organisms, like *Eubacteria*, *Eukaryota*, or *Green Algae*.[14,19] Amongst the new members of the microbial opsins family, channelrhodopsins, that work as light-triggered ion channels, have been under the spotlight of the scientific community due to their application in the expanding field of optogenetics.[20]

When bound to BR, all-*trans* RPSB absorbs at 568 nm,[21] photoisomerises selectively to the 13-*cis* isomer with a QY of 0.64,[22] and completes the photoreaction with a time constant between 200 and 500 fs.[23,24] In methanol solution, on the other hand, all-*trans* RPSB absorbs at 445 nm,[25] photoisomerises to a mixture of 11-*cis* and 9-*cis* isomers with QY of $\sim$0.16 and

$\sim$0.05,[25–27] and shows multi-exponential excited state decay kinetics with time constants on the order of 2 and 7 ps.[28–32]

RHO is the photoreceptor of rod outer segment cells, and is responsible for dim light vision.[33] RHO is a sensory G protein-coupled receptor: upon photoexcitation it undergoes conformational changes that enable it to activate transducin, an heterotrimeric protein that amplifies the initial light stimulus and propagates the response along the signalling cascade.[8] The RHO chromophore is 11-*cis* RPSB. The differences in photoreactivity between the protein and methanol solution are as striking as for BR: in RHO, the absorption maximum is red-shifted from 442 to 498 nm,[14,25] the QY is increased from 0.19[25,26] to 0.65[34] and the primary photoreaction is complete in 200 fs,[35,36] whilst the ESL in solution is $\sim$2-3 ps.[37]

A huge amount of experimental work has been devoted towards understanding the origins of the observed differences.[14,16,38] The general conclusion reached is that within the opsin protein steric and electrostatic interactions play a major role in tuning the photochemical properties of the chromophore, red-shifting its absorption, accelerating the reaction speed and significantly increasing its isomerisation efficiency. This idea has been strengthened by the notion that even though between members of the same family not so many residues are conserved, the rate of similarity or identity increases sensibly (from $\sim$30% to $\sim$80-90%) when considering only the aminoacids forming the retinal binding pocket.[15] The work on the solution photochemistry of RPSBs here presented questions exactly this notion: is the protein pocket with its evolution-optimised interactions really necessary for efficient photochemistry to take place? Is it possible, through the introduction of small structural changes on the chromophore, to tune the solution photochemistry to resemble the one observed in the proteins? And, at a more fundamental level, can the solution photochemistry of the model compounds studied still reserve surprises for an investigator after so many years of research on them?

After seeking at least a partial answer to these questions, the latter part of this dissertation examines the case of another photoactive protein for which the environment is known to remarkably affect the photochemical evolution of the chromophore: the green fluorescent protein (GFP).[39] GFP is the ultimate light emitter in the jellyfish Aequorea Victoria.[40] Whilst its biological function is still unclear, it has been suggested it could work as a proton pump,[41] even though not being a transmembrane protein leaves the open question of the usefulness of pumping protons within the cytoplasm in the first place. For the last twenty years GFP has been under the spotlight of the scientific community due to its unique properties of being an easily expressed photoactive protein that does not require any external co-factor to fluoresce.[42] It has been shown that its fluorophore is formed by spontaneous condensation of three residuals during the folding process,[43] rendering it an ideal fluorescent label to study biological systems.[42] The relevance of GFP within this investigation of tuneable photochemistry of biological chromophores stems from the dramatically different photoreactivity observed for its model chromophore (**HBDI**, Figure 1.2) in solution.

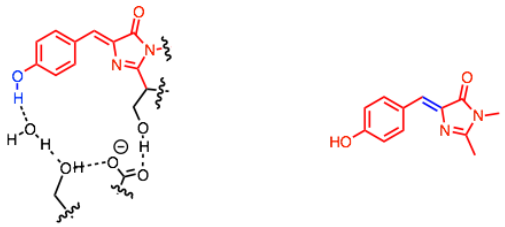

Figure 1.2 Structures of GFP fluorophore and model chromophore used in this work, **HBDI**. The structure in red is identical in the two cases, whilst in blue is highlighted the reactive part of the molecule in each environment.

When enclosed in the protein, the GFP chromophore upon absorption of a photon undergoes an excited state proton transfer generating a deprotonated species responsible for the observed fluorescence.[44] If the protein is denatured[45] or model chromophores are irradiated in solution, no fluorescence is observed.[46] The excited state is instead deactivated via an extremely efficient photoisomerisation around the exocyclic C=C double bond, with

a QY of $\sim$0.5.[46] Yet, the reported ground state Raman spectra for the model chromophore and GFP are remarkably similar, suggesting an identical initial evolution immediately after photoexcitation.[47] Differently than for RPSBs, researchers have already tried to modulate the model chromophore solution photochemistry via introduction of small structural changes and were partially successful in enhancing the fluorescence, even though photoisomerisation still remained the primary deactivation process.[48] Here, rather than following the same approach as for the RPSB, the great structural insight offered by ultrafast time-domain impulsive Raman spectroscopy[49,50] has been exploited on wild-type GFP, two mutants and the model chromophore, to study the initial excited state evolution of these systems. Whilst most of the compounds presented have already been studied by transient IR,[51] it is hoped that the enhanced exclusive sensitivity to the chromophore and its immediate environment of time-domain Raman spectroscopy sheds some new insight into the tuning mechanisms of the photochemistry.

The dissertation is structured as follows:

Chapter 2 presents the spectroscopic methods adopted for the study of the photochemistry of all systems, namely nuclear magnetic resonance (NMR), ultrafast transient absorption (TA) and excited state time-domain impulsive Raman. A brief description of the principles and of the experiments together with details on data analysis methodology is given.

Chapter 3 presents the results obtained from the investigation of the solution photochemistry of backbone-modified analogues of all-*trans* nBu RPSBs. NMR is used to quantify and identify the photoproducts, whilst transient absorption spectroscopy is used to define an average ESL for each derivative. A correlation is observed between QY, ESL and photoproduct selectivity depending on the nature and position of the introduced structural modification. The results are discussed in terms of a possible model for the solution photochemistry, and a comparison is made with the protein case.

Chapter 4 describes the attempt to extend the model discussed for the all-*trans* photoisomerisation to the analogous reaction of the 11-*cis* isomer. The lack of correlation between ESL and QY points towards substantial differences in the mechanisms of the two photoreactions. In order to investigate these differences, the reaction dynamics are selectively followed via a multipulse population control approach. The finding that the photoisomerisation for the 11-*cis* isomer proceeds with the same speed in methanol and in RHO prompts a reconsideration not only of the currently adopted model for the solution photochemistry of the compound, but also of the role of the protein in tuning its photoreactivity.

Chapter 5 presents the photochemistry of a series of all-*trans* RPSBs prepared with different amines, to red-shift the absorption maximum and reproduce in solution the opsin shift observed in the proteins. For a first series of compounds formed with aromatic amines, no C=C photoisomerisation is observed, and the causes are investigated via excited state impulsive Raman. The preparation of two other derivatives presenting a non-conjugated positive charge on the amine moiety is also described, together with the attempts to measure their photoisomerisation efficiency.

In **Chapter 6** time-domain Raman spectroscopy is first used to follow the excited state proton transfer reaction of wild-type GFP, obtaining for the first time excited state Raman spectra of both the protonated and deprotonated forms of the excited protein. A comparison of these spectra with the excited state Raman spectra for the single point mutant S65T, the heavily mutated "superfolder" GFP, and the model chromophore in solution follows. Finally, wavelength dispersed detection of the probe pulse used in time-domain Raman is used to disentangle the ground state spectra of the two forms of wild-type GFP.

Chapter 2

Spectroscopic methods

Overview

This chapter describes the two main spectroscopic techniques used for the characterisation of the photochemistry of all the derivatives studied. The first section briefly presents nuclear magnetic resonance (NMR) and the types of experiments performed with the information gained from each. The second section introduces the principles of ultrafast transient spectroscopies used to follow reaction dynamics and multi-pulse schemes adopted to generate and probe ground and excited state vibrational coherences (VC).

2.1 Nuclear magnetic resonance

NMR spectroscopy was used for the characterisation of the products of chemical synthesis (retinal protonated Schiff bases, RPSBs, of interest and synthetic intermediates), and to identify and quantify products in photoisomerised mixtures. The following section provides a description of the NMR experiments, together with outlines of the general procedures. The discussion of NMR principles and experiments follows Claridge's 2009[52] and Sunders and Hunter's 1993[53] textbooks.

2.1.1 Basic principles of NMR

The phenomenon exploited by NMR spectroscopy is the polarisation of the microscopic magnetic moments associated with nuclei of non-null spin quantum number induced by a static external magnetic field $\mathbf{B}_0$. Treating the problem classically, a torque operating on the magnetic moments will generate a rotatory motion around the axis of the static magnetic field. The frequency of this motion, the *Larmor frequency*, ω_0, will depend on the intensity of the field and the nature of the nuclei of interest through their gyromagnetic ratio. For nuclei of spin ½, such as ^{1}H and ^{13}C, immersed in a magnetic field B_0 two quantised states are possible, traditionally depicted as parallel (α) or antiparallel (β) with respect to the $\mathbf{B}_0$ axis. As the two states are not isoenergetic, with α being more stable than β, the equilibrated population will be defined according to the Boltzmann distribution. The different populations of α and β states lead to a non-vanishing net component of the total magnetic moment parallel to the external field, the *bulk magnetisation* $\mathbf{M}_0$. The phase for precession along the cones of the two states is not correlated for individual magnetic moments, so that in an equilibrated situation $\mathbf{M}_0$ does not have any amplitude in the plane perpendicular to $\mathbf{B}_0$ (Figure 2.1.1)

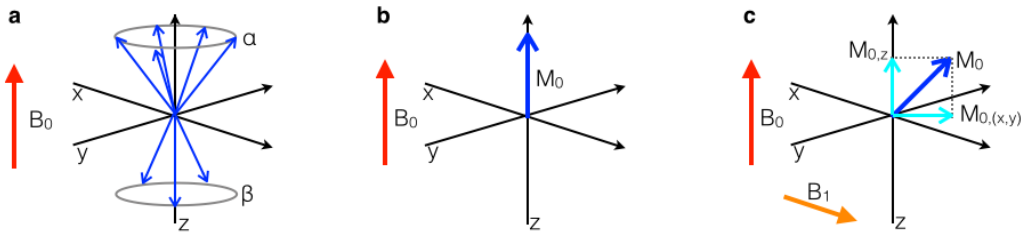

Figure 2.1.1 Origin of bulk magnetisation vector $\mathbf{M}_0$ and NMR signal. (a) The applied static magnetic field B_0 (red arrow) along z generates two possible processional cones (grey circles) along which the magnetic moments of the nuclei (blue arrows) can lie. As the α state with z component parallel to $\mathbf{B}_0$ axis is lower in energy, it will be more populated, with the excess being determined by the magnitude of $\mathbf{B}_0$. (b) Random phase in the (x,y) plane annihilates any transversal component of the bulk magnetisation, leaving $\mathbf{M}_0$ (blue arrow) lying along the z axis. (c) Application of a second magnetic field along x or y ($\mathbf{B}_1$, orange arrow) tilts the bulk magnetisation $\mathbf{M}_0$. The transversal component ($\mathbf{M}_0$(x,y), light blue arrow) in the (x,y) plane generates the signal detected during an NMR experiment.

The NMR signal is generated by interaction of the sample with a radio frequency pulse oscillating at ω_0, which generates a magnetic field $\mathbf{B}_1$ in the (x,y) plane perpendicular to B_0. In a system of reference rotating at a frequency ω_0, $\mathbf{B}_1$ exerts a torque on the bulk magnetisation $\mathbf{M}_0$, generating a magnetisation component in the direction perpendicular to $\mathbf{B}_0$ and $\mathbf{B}_1$. The time duration of the radio frequency pulse determines the angle by which the bulk magnetisation turns towards the (x,y) plane. Thus, the $\mathbf{B}_1$ field induces coherent spin rotation in the (x,y) plane, which induces an oscillating current in the reception coils of conventional NMR spectrometers. The Larmor frequency ω_0 of a certain type of nucleus like ^{1}H is affected by the specific molecular environment: bonding electrons, adjacent atoms and diamagnetic electronic currents all alter the $\mathbf{B}_1$ field experienced by the nucleus, so that the spin rotates at an effective frequency ω_{eff}, which is shifted from the Larmor frequency. The effect of the chemical environment on the frequency of the individual nuclei is referred to as *shielding*. NMR spectra are reported in relative units, the *chemical shift*, defined as the normalised difference in parts per million between the observed frequency ω_{eff} and the Larmor frequency of a reference compound, ω_{ref}.

$$\delta = \frac{\omega_{\text{eff}} - \omega_{\text{ref}}}{\omega_{\text{ref}}}. \tag{2.1.1}$$

When analysing spectra, the terms *high* and *low* field refer to zones of the spectrum of lower and higher chemical shift, respectively.

NMR active nuclei can couple via spin-spin interactions mediated by bonding electrons, an effect called *scalar coupling*. If two nuclei are coupled, in the rotating frame system of reference, their resonances will be split into components rotating at frequencies separated by the scalar coupling constant J. Figure 2.1.2 shows a comparison of the energy level schemes of two uncoupled nuclei with resonance frequencies H_A and H_X and the same two nuclei coupled with coupling constant J, illustrating the splitting of the energy levels with coupling.

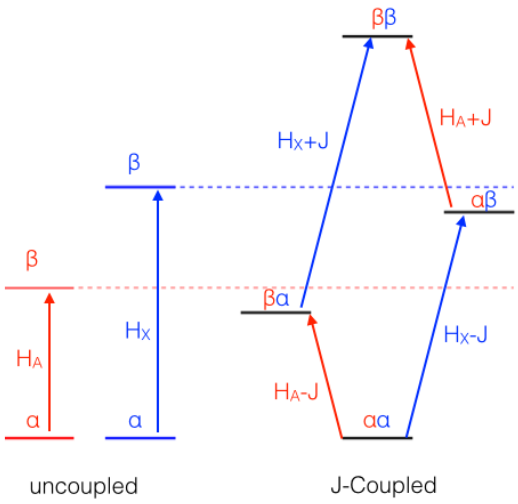

Figure 2.1.2 Comparison of energy level schemes for two spin ½ nuclei A and X in absence (left) and presence (right) of scalar coupling with coupling constant J. The uncoupled transition frequencies are indicated as H_A and H_X. The coupled level scheme shows the origin of the splitting of the resonances into doublets.

Scalar coupling provides information on the connectivity between nuclei, and arises between nuclei of the same type (i.e., two protons, homonuclear coupling) as well as of different types (i.e., ^{1}H and ^{13}C, heteronuclear coupling). The appearance of split resonances (multiplets) arising from scalar coupling depends on the number of coupling nuclei and on their type and spin quantum numbers. In the above example both nuclei have the same spin quantum number ½, like protons, and each nucleus experiences only one other coupling partner.

A different type of coupling, *dipolar coupling*, is exploited to retrieve information about spatial proximity of nuclei. Dipole coupling through space affects the local magnetic fields experienced by the nuclei. Tumbling of the molecule or molecular groups in solution can alter the relative orientation of the coupling nuclei, inducing time dependent fluctuations in the effective field. If the frequency content of the effective field matches the frequency gap between spin states, a mutual spin flip can occur, following the same principle enabling the radio frequency pulse to induce a spin flip for a nucleus. Due to their strong dependence on

internuclear distance, experiments probing dipolar coupling are a powerful tool to determine spatial proximity of nuclei within a molecule. The mutual dipole interaction is the basis for the Nuclear Overhauser Effect (or Enhancement) NOE. The NOE is defined as the intensity change experienced by the resonance frequency of a nucleus when the nuclear spin equilibrium population of another nucleus in its vicinity is perturbed.[52,53] The perturbations usually involve saturation or inversion of the equilibrium population for a resonance via an appropriate pulse scheme, and are schematically shown in Figure 2.1.3. As the NMR signal is generated when a difference in population between the two spin states occurs, saturating a resonance would make it disappear from the acquired spectrum, whilst population inversion would make it appear with the same intensity but negative amplitude.

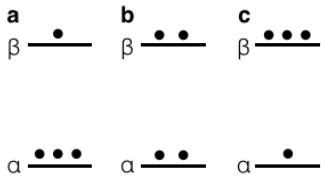

Figure 2.1.3 Effect on the equilibrium population of a spin transition (a) of saturation (b) and inversion (c) for an ensemble of nuclei. Dots represent equal amounts of the nuclei generating the transition considered.

As the experiments (2D and 1D NOESY) performed in this work involve (un)selective population inversion of resonances, only this case will be further discussed, but the same principles apply when saturating a transition rather than inverting it. The perturbation to the population distribution is considered instantaneous (transient NOE), and the experiment monitors the resulting relaxation.

To understand the origin of the NOE, it is useful to compare the population scheme of two isolated nuclei of spin ½, dipolarly coupled before and after the perturbation is applied, as well as their response to it. In Figure 2.1.4 and the discussion that follows, S indicates the *source* nucleus, whose population is perturbed and I the nucleus of *interest*, for which the NOE is observed. The perturbation is shown as orange arrows. The possible relaxation

processes are shown as solid lines and marked W_{nX} with n = 0, 1, 2 referring to the zero, single and double quantum transitions possible within the system, and X specifying the nucleus I or S for the single quantum transitions. Transitions in the figures are colour coded, using blue, red and green lines for single, double and zero quantum transitions, respectively. As in Figure 2.1.3, population of a spin state for the molecular ensemble is represented by dots. Below each energy and population diagram are shown the corresponding signals intensities for the two resonances. The purple bar is a reference for the magnitude of the unperturbed signals.

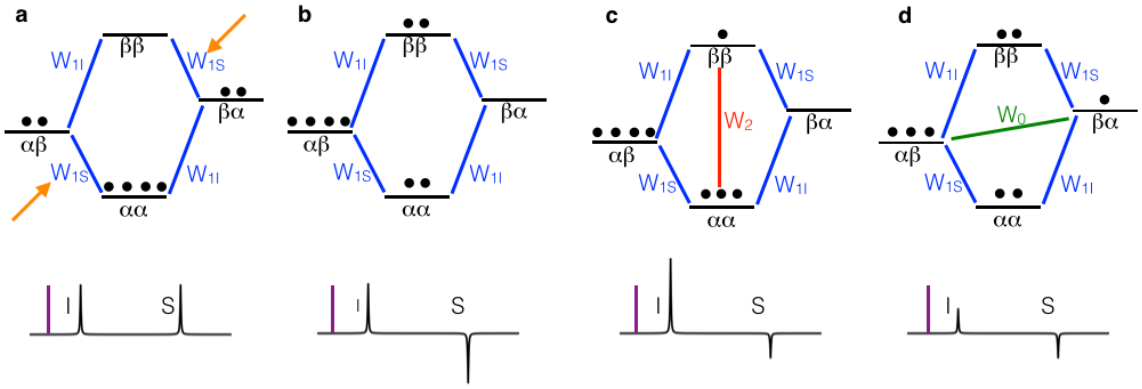

Figure 2.1.4 Effect of population inversion and cross-relaxation pathways on the signal intensities of two dipolar coupled resonances. Below each population diagram are shown the corresponding signal intensities for the two resonances. The purple line is a reference for the unperturbed signal intensity. a) Equilibrium population of the coupled system, perturbed by inversion of the population of spin S (orange arrows). b) Population following inversion, before any relaxation occurs. c) Relaxation of the inverted population by a double quantum transition pathway, increasing the intensity of the I resonance. d) Relaxation of the inverted population by a zero quantum transition pathway, decreasing the intensity of the I resonance.

The equilibrium population of the four states arising by dipolar coupling is shown in Figure 2.1.4a. The energy difference between the $\alpha\beta$ and $\beta\alpha$ states is negligible compared to the Larmor frequencies of the nuclei, so that at a first approximation, following the Boltzmann distribution, the respective populations can be considered equal. Upon selective population inversion of the S resonance transitions, before any relaxation occurs, the situation depicted in Figure 2.1.4b arises. No change in the amplitude of the signals can yet be observed,

but the S resonance is 180 degrees out of phase compared to I. The two possible pathways for relaxation from this situation are the double-quantum (W_2, red line, Figure 2.1.4c) or zero-quantum (W_0, green line, Figure 2.1.4d) transitions. The W_2 path transfers population from the $\beta\beta$ to the $\alpha\alpha$ state, resulting in increased population differences for the transition giving rise to the I resonance and hence an increase in its signal amplitude as compared to the unperturbed case. In contrast, the W_0 path reduces the population differences for the I transition and hence its signal amplitude. The amplitude of the measured signal, or, in other words, the magnitude of the NOE observed will be determined by the kinetic competition between the available pathways. In the case of transient NOE experiments, another important parameter determining the magnitude of the observed NOE is the mixing time t_{mix} between the perturbing and reading pulses. For very "short" [a] mixing times, the relaxation of the nucleus of interest I is dominated by the dipolar interaction with the irradiated nucleus S, and the amplitude of the NOE signal {S-I} is proportional to the concentration of the sample [X], the inverse of the sixth power of the inter-nuclear distance r_{SI} and the mixing time t_{mix}, according to Equation 2.1.2.

$$\{S{-}I\} = k \cdot [X] \cdot {r_{\mathrm{SI}}}^{-6} \cdot t_{\mathrm{mix}}. \tag{2.1.2}$$

If Equation 2.1.2 holds, the experiment operates in the linear regime.

2.1.2 NMR experiments used in this work

With the exception of proton NMR spectra, that were used to determine the concentration and photoisomerisation quantum yield (QY) of irradiated samples as described in Section 2.1.3 below, all other NMR experiments were used for characterisation or structural assignment

[a] The definition of short depends on the size of the molecule observed, hence the quotation marks.

purposes. The following section briefly describes the information retrieved from each type of experiment.

^{1}H - Proton spectra were used to determine the chemical shifts of the protons, and the signal integrals were used to determining concentration and photoisomerisation QY of irradiated samples (see Section 2.1.3 for further details).

^{13}C decoupled - Proton-decoupled carbon spectra were used to determine the chemical shifts of the carbons.

COSY - COSY spectra reveal up to three bonds distance scalar coupling between protons.

HSQC - HSQC spectra reveal heteronuclear scalar coupling between carbon atoms and directly attached protons.

HMBC - HMBC spectra reveal heteronuclear scalar coupling between carbon atoms and protons distant two to three bonds.

TOCSY (1D or 2D) - TOCSY spectra reveal proton correlations within the same spin system, and, in contrast to COSY, also reveal couplings between nuclei that are more than three chemical bonds apart. In the 1D version, a single resonance is selected, and signals are observed for the other protons belonging to the same spin system.

NOESY (1D or 2D) - NOESY spectra reveal dipolar coupling between protons. Presence of a NOESY cross peak between two resonance indicates spatial proximity. In Chapter 4, 1D transient NOE experiments were used to determine the conformer distribution of 11-*cis* RPSB in solution.

2.1.3 Measurement of photoisomerisation yields

For all the molecules studied in solution in the present work, *cis-trans* photoisomerisation of a double bond was the only process generating photoproducts. The QY of such a process is defined as the number of molecules of product formed, M_{photo}, per amount of photons

absorbed, $N_{\text{Ph,abs}}$ (Equation 2.1.4), and can be thought of as the probability for a certain product to be formed after photoexcitation by a single photon:

$$\text{QY} = \frac{M_{\text{photo}}}{N_{\text{Ph,abs}}}. \tag{2.1.3}$$

Irradiation experiments were performed on 1 mL of a concentrated ($\sim$3 mM) solution of the compound of interest in deuterated solvent. Two light sources with different irradiation wavelengths, λ_{irr}, were used depending on the system under study: a 370 nm emitting LED for **HBDI**, and a 532 nm continuous wave (CW) laser for RPSBs. In the former case, only a relative efficiency in d_6-DMSO vs. d_8-THF was determined, whilst for RPSBs absolute QYs were measured. Irradiation times, t_{irr}, were adjusted not to exceed 10-15% photoproduct formation. Due to the elevated concentration (and hence optical density) of the working solution, the number of absorbed photons can be considered equal to the number of incident photons:

$$N_{\text{Ph,abs}} = N_{\text{Ph,inc}} = \frac{P_{\text{inc}} \cdot t_{\text{irr}} \cdot \lambda_{\text{irr}}}{hc}. \tag{2.1.4}$$

where h and c are Planck's constant and the speed of light. For CW laser irradiation, the incident power on the sample, P_{inc}, was measured with a photodiode. For the 370 nm LED used in the **HBDI** experiments, only a rough estimate of the incident power ($\sim$0.4 mW) could be obtained with the photodiode, due to the poor accuracy in the UV of the available detector. To overcome this limitation, the photoisomerisation QY in DMSO was measured relatively to the reported value for the same reaction in THF.[46] Further details on the experimental conditions adopted in the two cases will be given in the relevant chapters and Appendices. The number of photoproduct molecules formed, M_{photo} was calculated as

$$M_{\text{photo}} = [\text{Sample}] \cdot V_{\text{irr}} \cdot F_{\text{photo}} \cdot N_{\text{A}}, \tag{2.1.5}$$

with [Sample] being the sample molar concentration, V_{irr} the volume of irradiated solution, F_{photo} the fraction of the photoproduct in the irradiated mixture and N_{A} Avogadro's number.

Photoisomerization products were identified by the growth of new NMR peaks with irradiation. A non-irradiated aliquot of solution was kept wrapped with aluminium foil as a dark control sample, and its ^{1}H NMR spectrum was measured at the beginning and after the irradiation to discriminate between new resonances from products formed by photoinduced or thermal processes. As an example, in Figure 2.1.5 the spectrum of an irradiated mixture (blue) of native (**NAT**) all-*trans* RPSB compared with the dark control spectra recorded at the beginning (black) and at the end (red) of the measurement reveals characteristic photoproduct(s) resonances marked with black stars, which are present or increase in intensity only in the irradiated spectrum (blue). For all other small peaks a thermal contribution is also (red stars) or exclusively (orange stars) present. In these cases, an increase in the peak intensity is observed in both the irradiated and non-irradiated spectra (blue and red, respectively).

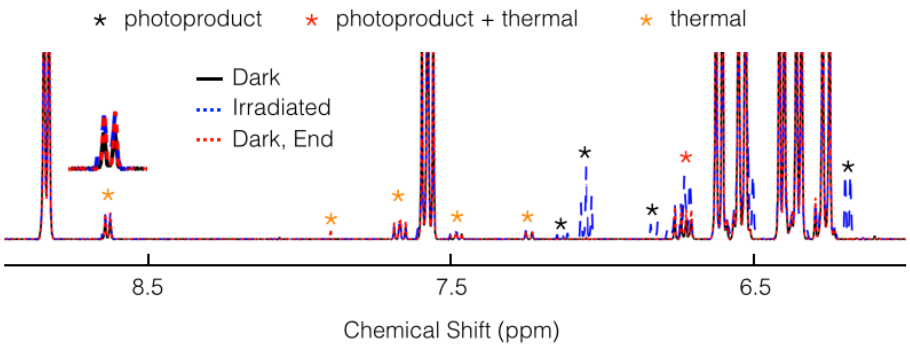

Figure 2.1.5 Identification of photoproducts signatures by comparison of ^{1}H NMR spectra of an irradiated solution (blue) with those from a non-irradiated solution at the beginning (black) and at the end (red) of the irradiation time.

The composition of the starting material and photoproduct(s) mixture generated after irradiation was obtained by integration over the corresponding resonance peaks in the ^{1}H NMR spectrum. As shown in Figure 2.1.6, a region of ∼0.15 ppm before and after each peak central frequency was isolated (black) and a suitable range was selected (red) and averaged to perform a background subtraction before integrating over the peak area (green). The error on the area of each signal was considered to be 10%.[52]

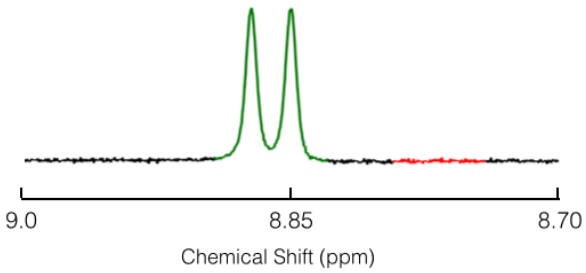

Figure 2.1.6 Integration of a resonance. The range marked in red was averaged and subtracted before integrating the range marked in green.

Whenever possible, multiple resonance peaks were averaged to obtain compositional information. From propagation of errors on the integrated areas and other sources (measured power, time, volumes), a total error between 10 and 15 % of the final QY value was obtained, unless otherwise stated.

The molar concentration of the sample, [Sample], had to be evaluated by an independent measurement. For most compounds studied in this work the molar extinction coefficients are not available, so that spectrophotometric methods were not a practicable option. The sample concentration was obtained from the ^{1}H NMR spectrum of a non-irradiated solution of the compound of interest with added a known amount of solvent used as internal standard. The standard was selected to have the least spectral overlap with sample peaks. A solution of internal standard with a known concentration was prepared by diluting 10 μL of standard in 1 mL of deuterated solvent, and adding 10 μL of this solution to a known volume (usually between 500 and 700 μL) of sample solution. From the integrals over the standard and

sample peaks, A_{sample} and A_{standard}, and the standard concentration [Standard], the sample concentration is obtained as

$$[\text{Sample}] = [\text{Standard}] \cdot \frac{A_{\text{sample}}}{A_{\text{standard}}} \cdot \frac{N_{\text{standard}}}{N_{\text{sample}}}, \tag{2.1.6}$$

where N_{standard} and N_{sample} are the number of protons contributing to the respective NMR resonance signals (e.g. N_{standard} = 6 for for the ring signals of benzene at 7.37 ppm).

2.1.4 Photoproduct determination

With the protocol described above, the QY of photoproduct(s) formation could be determined, but without independent knowledge of the ^{1}H NMR spectra of the other isomers no conclusion could be drawn on the identity of the product(s). This problem was particularly severe for the retinal work, as no proton spectra in MeOD of the several isomers of the RPSBs for the compounds studied was available in the literature. To overcome this problem, two approaches were followed, depending on whether during the synthesis of the studied derivative the aldehydes of the other isomers were isolated in sufficient purity and amount to allow for complete NMR characterisation of the corresponding PSBs. In this case, the identity of the photoproduct was established by comparison of the ^{1}H NMR spectra of the isolated PSB isomer with the photoproduct signals observed during the QY measurements. When this approach was not practicable, identification of the photoproduct was attempted in the irradiation mixture through a series of ^{1}H NMR experiments, investigating scalar or dipolar coupling (COSY, 1D or 2D TOCSY and NOESY). When following the latter approach, longer irradiation times were adopted to obtain a higher percentage composition of the product of interest. As examples of both approaches, the identification of the photoproducts for all-*trans*-**14-Me** RPSB will be now discussed.

all-*trans*-14-Me RPSB photoproducts

During continuous wave irradiations two sets of new signals with QYs of 0.11 and 0.03 appeared in the spectrum (Figure 2.1.7). The resonance peaks at 6.95 and 8.97 ppm marked with orange stars were used to evaluate the main product formed, whilst for the secondary one the peaks at 7.33, 7.45 and 9.13 ppm (marked with green stars) were used.

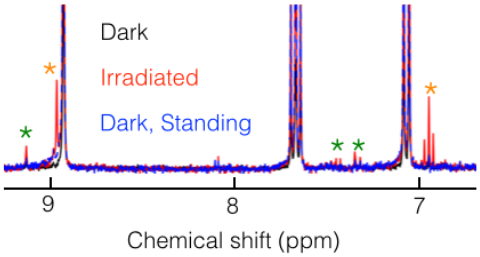

Figure 2.1.7 ^{1}H NMR spectra for the QY measurements of all-*trans*-**14-Me** RPSB, before (black) and after (red) irradiation, and of a control sample (blue, dashed). Orange and green stars mark the resonances used to quantify the main and secondary photoproducts, respectively.

In order to assign the stereochemistry of the main photoproduct a series of 1D NOESY (t_{mix} = 600 ms) measurements was performed on an irradiated sample (Figure 2.1.8).

The signal at 6.95 ppm is a doublet of a doublet with equal coupling constants, suggesting assignment to the H11 proton (possibly of an 11-*cis* isomer): only H11 has two vicinal protons, whereas all the other polyenic protons have only one vicinal proton and appear as simple doublets, except for H15, which appears as a singlet. To test this hypothesis, a selective 1D NOESY spectrum was recorded irradiating the peak at 6.95 ppm. Correlations with a methyl group at 2.06 ppm and a doublet at ppm 6.33 ppm were observed (Figure 2.1.8b). The fact that correlation with only one methyl group (and not two) was observed supports the hypothesis of the isomerisation occurring at the C11=C12 double bond. In this case, the methyl group showing dipolar coupling with H11 would be Me9. Upon selective irradiation of this methyl group, the doublet of doublets at 6.95 ppm (H11) and another doublet at 6.46 ppm were observed as expected. The latter was assigned to H7, as H15 should have appeared as a singlet for the reasons discussed above (not to mention at a very different

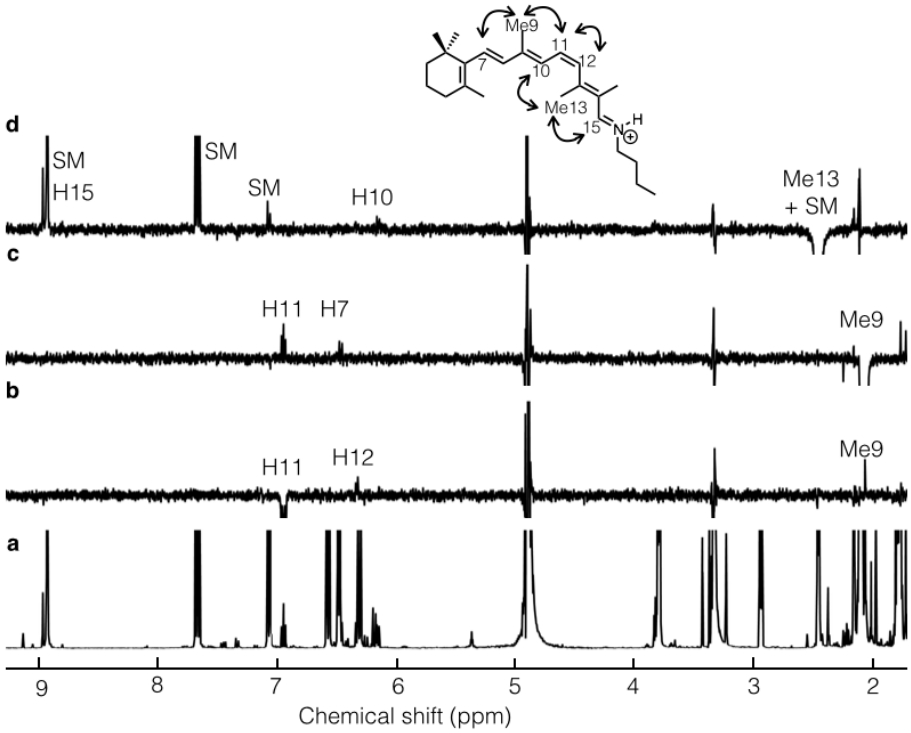

Figure 2.1.8 Determination of the main photoproduct for all-*trans*-**14-Me** RPSB. The structure of the photoproduct with the supporting NOESY correlation observed is reported on the top of the ^{1}H NMR spectrum of (a) the irradiated mixture, together with the NOESY spectra recorded upon irradiation of (b) H11, (c) Me9 and (d) Me13. SM indicates signal from the starting material generated by non perfect selective irradiation.

chemical shift). This confirmed the assignment of the resonance at 2.06 ppm as Me9 and of the main photoproduct as 11-*cis*. To gain further support, another irradiation of a singlet at 2.44 ppm was performed (Figure 2.1.8d), and a singlet at 8.96 ppm and a doublet at 7.07 ppm were observed. The singlet was immediately identifiable as H15 due to its multiplicity and peculiarly low field resonance, whilst the doublet was assigned as H10, and the irradiated methyl recognised as Me13. The suggested structure for the photoproduct, together with the NOESY correlations supporting it are shown on top of Figure 2.1.8.

The secondary photoproduct was identified as the 13-*cis* isomer by comparison of the resonances observed upon irradiation with the ^{1}H spectrum of the pure 13-*cis*-**14-Me** RPSB (Figure 2.1.9), whose NMR spectra could be recorded and characterised as the corresponding aldehyde was isolated in sufficient quantity during the preparation of the all-*trans* isomer.

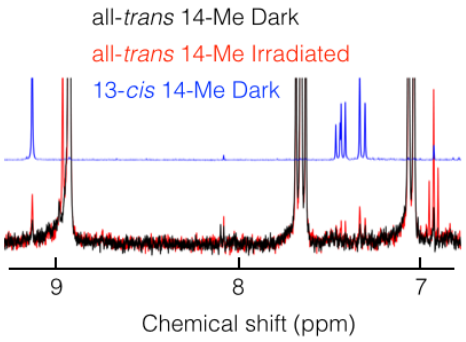

Figure 2.1.9 Comparison of ^{1}H NMR spectra for a non-irradiated (black) and irradiated (red) solution of all-*trans*-**14-Me** RPSB and a non-irradiated solution of 13-*cis*-**14-Me** RPSB (green). The correspondence of the frequencies used to quantify the secondary photoproduct QY identifies it as the 13-*cis* isomer.

2.2 Ultrafast laser measurements

Ultrafast laser spectroscopy provides insight into the earliest dynamics directly after photoexcitation. Femtosecond transient absorption (TA) spectroscopy was used as a tool to study electronic relaxation processes and in some cases also to gain information about ground

and excited state vibrational activity. A multi-pulse version of the TA technique enabled isolation of vibrational spectra from the individual electronic states. This section gives a brief description of the principles of the techniques and the experimental conditions.

2.2.1 Transient absorption

Theory

TA spectroscopy is a tool widely used to investigate reaction dynamics. The principle of this technique is to measure the changes in absorbance of a *probe* pulse by the system in the presence and absence of an excitation (*pump*) pulse (Figure 2.2.1).[54,55]

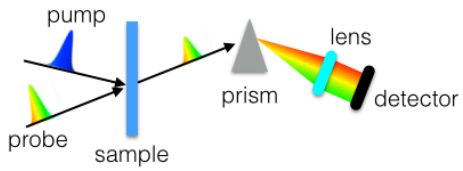

Figure 2.2.1 Scheme of a pump-probe experiment. The effect on the sample excited by the pump pulse is investigated by the probe pulse, which is imaged on a detector after being dispersed to achieve wavelength resolution.

The signal discussed in TA is the difference between the absorbance of the probe recorded in the presence (OD_{ON}) and absence (OD_{OFF}) of the pump pulse and relates to the transmittance T measured by the camera as

$$\Delta OD = (OD_{\mathrm{ON}} - OD_{\mathrm{OFF}}) = -\log_{10}(1 + \frac{\Delta T}{T_{\mathrm{OFF}}}) = -\log_{10}(1 + \frac{T_{\mathrm{ON}} - T_{\mathrm{OFF}}}{T_{\mathrm{OFF}}}). \quad (2.2.1)$$

According to the current understanding, pump-probe spectroscopy can be described by the third-order nonlinear polarisation response of the sample. The following section draws on the works from the groups of Mukamel,[56,57] Ernsting[58–61] and Mathies[62] to present a qualitative picture of TA measurements.

Energy ladder diagrams allow us to visualise and discuss the contributions to the TA signal. In these diagrams, successive electronic states of a molecule are shown as stacked thick horizontal lines. Thinner lines are usually adopted to represent higher vibrational energy levels within an electronic state. Time moves from left to right. Interactions with electric fields are shown by straight arrows to represent individual interactions of the system with the electric fields that generate the third order polarisation response whose interaction with the probe electric field produces the observed signal (wavy lines). Solid or dashed arrows indicate interaction of the field with the *bra* or *ket* side of the molecular wave-function within the *density matrix* formalism.[63] In the density matrix formalism, a system is described in a chosen basis set by a density matrix with the same number of rows and columns as the states forming the basis set considered. The diagonal elements represent the probability of finding the system in a certain state of the basis set. If the off-diagonal elements of the density matrix are non-zero, the system is said to be in a coherent superposition of the corresponding states.[63] *Kets* and *bras* denote individual "dimensions" of the basis set and their conjugate complex, respectively.

Considering for the moment only electronic energy levels, two electric field interactions are required to generate a population in the first excited state, changing both the real and imaginary part of the wave-function, as represented in Figure 2.2.2a. For sequential pathways, the system interacts first twice with the pump (blue) and then with the probe (orange). Within this scenario, three types of signals can arise in a TA measurement: stimulated emission (SE), excited state absorption (ESA) and ground state bleach. SE arises when the system populates an excited state and upon interaction with the probe returns to the ground state with emission of a photon. SA occurs when the system upon interaction with the probe is excited into an upper energy level by absorption of a probe photon. These two processes can be visualised with the energy ladder diagrams shown in Figure 2.2.2b and c, respectively. Ground state bleach is a negative feature in the differential optical density spectrum due to

a reduced absorption of the probe by the ground state population of the system, which has been depleted by excitation following interaction with the pump pulse (Figure 2.2.2d).

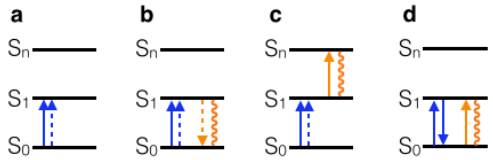

Figure 2.2.2 Energy ladder diagrams for dominant processes in TA spectroscopy. (a) Absorption of a photon as a double interaction with the real (*ket*, solid line) and imaginary (*bra*, dashed line) part of the system wave-function (b) stimulated emission, (c) excited state absorption and (d) ground state bleach. Blue and orange colours are used to indicate interaction with the pump and probe electric fields, respectively. The wavy line indicates the interaction of the generated third order polarisability.

If the interacting pulse has sufficient bandwidth in the frequency domain to cover more than one vibrational state, or equivalently, is short enough in the time domain, it forms a time-dependent coherent superposition of two vibrational states (Figure 2.2.3a and b). The *bra* and *ket* parts of the wave-function then occupy different vibrational energy levels. After the first interaction with the electric field, before the generation of the population or VC, the system is in an electronic coherent state, with the wave-function a superposition of both S_1 and S_0 electronic states.

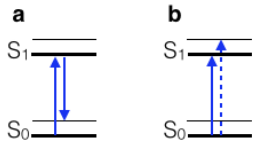

Figure 2.2.3 Resonant generation of vibrational coherence in the (a) ground and (b) excited electronic state.

TA experiments are generally described as four wave mixing experiments, involving two interactions with the pump pulse and two with the probe pulse. If the two interactions with the pump precede the two interactions with the probe, i.e. if the two pulses are well separated in time, only sequential contributions as the ones just discussed are present in the detected signal. On the contrary, if they are simultaneously present on the sample, pathways with

mixed pump and probe order can also contribute, and form a coherent spike or coherent artefact around zero delay time.[60]

An intuitive way of thinking about TA is the *doorway-window* description proposed by Mukamel.[56] In this picture, the pump pulse is considered as a *doorway* that prepares the system in a non-stationary state, whose time evolution is investigated by the probe pulse, which constitutes an observation *window*. Mukamel further discusses three general conditions that should hold in order for this picture to be accurate, and for the measured spectrum not to be a convolution of a "real" spectrum and the pulse intensity profiles.[56] The first is for the pump and probe pulses to be well separated in time: in this case, the mixed order interaction term is prevented from contributing to the signal; secondly, for the pulses to be short compared to the nuclear dynamics under investigation, otherwise the experimental time resolution would not be sufficient to observe the process; and, finally, for the pulses to be long compared to the electronic dephasing time of the coherence between ground and excited states formed by the first pump electric field interaction.

Experimental Setup

For the work on RPSBs, TA experiments were used to determine the excited state lifetime (ESL) of each compound. The compressed pump pulses were centred at 500 nm to be resonant with the red edge of the S_0-S_1 transition and had a duration between 20 and 30 fs, yielding an overall time resolution of the experiment on the order of 35 fs. In this scenario, the pump pulse duration is longer than the typical electronic dephasing time, but it can only resolve some of the nuclear dynamics. The pump and probe pulses can be considered separate for delays longer than 100 fs. As the excited state lifetime was always greater than 100 fs for all compounds discussed in this thesis, the time resolution was adequate for resolving the electronic relaxation.

Laser pulses of 180 fs duration were delivered by a LightConversion PHAROS-6W amplifier, with a fundamental frequency of 1030 nm and an output power of 5.5 W at 10 kHz repetition rate. The broadband white light used as a probe (500-850 nm) was generated by self-focusing and self-modulation in sapphire from 15 mW of the fundamental beam. To generate the pump pulse centred at 500 nm (30-100 nJ) a two-stage non-collinear optical parametric amplifier (NOPA)[64,65] was used. The NOPA was seeded by white light and pumped by the third harmonic of the fundamental beam (343 nm, 500 mW), generated by a sequence of second harmonic generation (SHG)[64] and sum frequency generation (SFG)[64] in β-barium borate (BBO). The pump pulse was compressed with chirped mirrors (Layertec) and characterised by SHG frequency resolved optical gating (FROG)[66] in a 10 μm BBO crystal. Probe pulses were detected with a single shot prism spectrograph[67] equipped with a LW-ELIS-1024A-1394 detector. The pulse conversion processes mentioned above are all non-linear optical phenomena, depending on the higher order polarisability properties of the crystals used. SHG and SFG can be described as processes where two photons of frequency ω_1 and ω_2 and wavevector $\mathbf{k_1}$ and $\mathbf{k_2}$ combine to generate a third photon of frequency ω_3 and wave vector $\mathbf{k_3}$ according to the relationships given in Equations 2.2.2-3

$$\omega_3 = \omega_1 + \omega_2, \tag{2.2.2}$$

$$\mathbf{k}_3 = \mathbf{k}_1 + \mathbf{k}_2. \tag{2.2.3}$$

with $\omega_1 = \omega_2$ and $\omega_3 = 2\omega_1$ in the case of SHG.[64] A different kind of non-linear optical process governed by similar principles is exploited in optical parametric amplifiers (OPAs).[64,65] In these devices, photons from a high power beam, the pump, split into two photons of lower energy. Seed pulses stimulate the transition over a certain frequency band and are amplified during the process, forming the signal pulses. The complementary frequency components form the so-called idler pulses. Energy conservation holds, i.e.,

$$\omega_{pump} = \omega_{seed} + \omega_{idler}. \tag{2.2.4}$$

For the process to be efficient, the phase matching condition between the wave vectors of the pulses must be respected as well.[64,65] The non-collinear arrangement of pump and seed beams in a NOPA allows to phase-match over a broader spectral bandwidth, so that shorter pulses can be generated. Schemes of the processes involved in SHG/SFG and in NOPAs are shown in Figure 2.2.4.

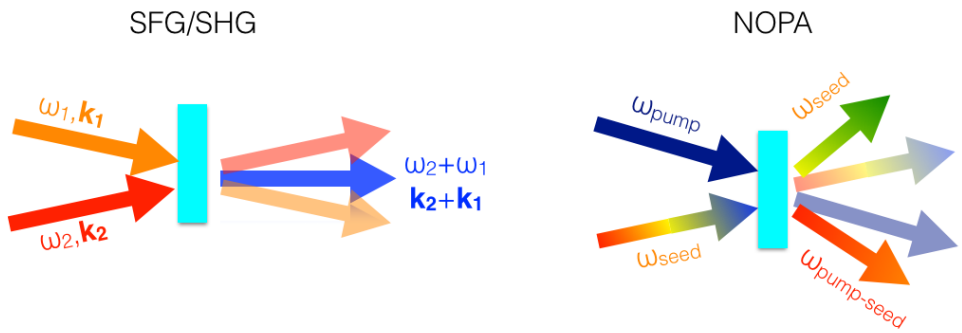

Figure 2.2.4 Non-linear optical processes exploited to convert femtosecond pulses to different frequencies. Left: sum frequency (SFG) and second harmonic generation (SHG). Right: Non-collinear optical parametric amplifier (NOPA). Power is transferred from the pump beam to colours of the seed beam for which the phase matching condition is met.

SHG-FROG[66] is a spectrally dispersed autocorrelation technique for ultrafast pulse characterisation. The pulse to be characterised is split into two beams, which are focused onto a thin nonlinear BBO crystal. By varying the delay between the two beams, spectrograms of the pulse are measured in time-frequency domain. From the spectrograms, the time dependent intensity and phase of the pulse can be retrieved. The latter provides information on the instantaneous frequency of the pulse, or, in other words, how well compressed it is.

Flow cells with path lengths of 500 and 200 μm and windows thickness of 120 μm were used for the experiments. The flow rate was fast enough to ensure replenishment of the sample between consecutive measurements.

Data Analysis

The discussion of the global lifetime analysis approach adopted in this work follows the description of the method found in Shrager and Hendler,[68] van Stokkum et al.[69] and Ruckebusch et al.[70]publications.

As the probe pulse was not compressed, the data had to be corrected for the group velocity dispersion of the probe before proceeding with further analysis. A correction curve was obtained from the coherent spike formed during temporal overlap of pump and probe pulses in a solvent-only measurement, as suggested by work from the Ernsting group.[59] The origin of this signal is due to mixed order interactions between pump and probe (i.e., pump-probe-pump) and, for this reason, gives contribution to the signal only for the time interval when the two pulses overlap around t_0. The temporal envelope of this signal is related to the correlation of the pump and probe pulses, and its full width at half maximum (σ) is usually taken as an indication of the time resolution of the experiment.[70]

To obtain the correction curve, the central part of the coherent signal was isolated by application of a square filter and modelled as a three parameter Gaussian (Equation 2.2.4) for each individual wavelength (Figure 2.2.5).

$$\mathrm{G(t)} = A \cdot e^{-\frac{2.35^2 \cdot (t-t_0)^2}{2\sigma^2}}, \tag{2.2.5}$$

where A, t_0 and σ are the fitting parameters representing the amplitude, the position and the full width half maximum of the Gaussian.

The wavelength-dependent Gaussian peak position t_0 was then used to correct the TA data for group velocity dispersion (Figure 2.2.6c, red). The estimated position of t_0 obtained by examining the appearance of the coherent signal was further evaluated during the global fit routine. The fitting routine evidenced on average a discrepancy of about 10 fs between

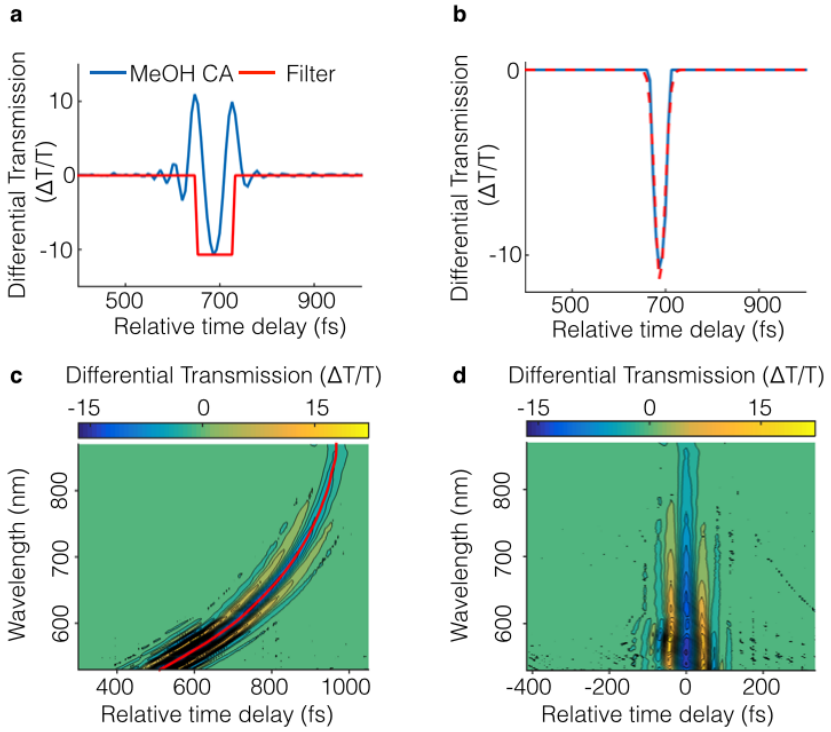

Figure 2.2.5 Time correction procedure for a solvent only trace. (a) Time cuts at 600 nm (light blue) with square filter applied (red) to generate data to fit. (b) Filtered data (light blue) and Gaussian fit (red, dashed) at 600 nm. MeOH only trace (c) before and (d) after chirp correction. The correction curve for chirp correction is shown as a red line on top of the chirped trace in (c).

the estimated and retrieved position of t_0. During preprocessing of the data the spectra were corrected for the group velocity dispersion but no subtraction of the solvent coherent response was performed. As a coherent response from the system under investigation is expected around t_0 as well, a term accounting for the solvent and system contribution to the measured signal had to be included in the fitting routine. The coherent artefact was thus modelled as a combination of Gaussian derivatives from 0^{th} up to 8^{th} order.[58]

A typical differential optical density map for native *n*-butylamine (nBu) all-*trans* RPSB obtained from the experimental setup described above is shown in Figure 2.2.6. The data in the Figure have been acquired in MeOH with 60 fs delay steps. The total acquisition time was about 15 minutes.

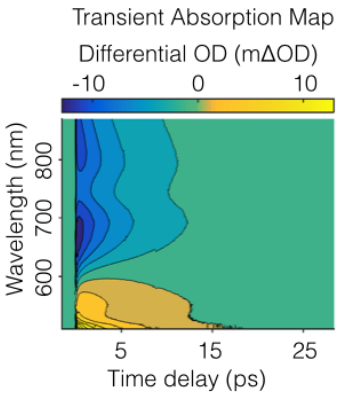

Figure 2.2.6 TA map of nBu all-*trans* RPSB in MeOH, excited with a 30 fs pulse centred at 500 nm (20 nJ). The probe pulse power was adjusted to 2 nJ.

To extract temporal and spectral information, the TA data can be represented as a 2D matrix S(λ, t), where each row contains information about the time behaviour of the signal at a particular wavelength λ and each column contains spectral information at a particular pump-probe time delay t.

$$S(\lambda, t) = \sum_i DADS_i(\lambda) \cdot f_i(t). \tag{2.2.6}$$

The temporal evolution of each component f(t) is described as an exponential decay term convoluted with an instrument response function (IRF) modelled as a Gaussian, according to Equation 2.2.7.

$$f_i(t) = \mathrm{IRF} \otimes e^{-\frac{t}{\tau_i}} = e^{-\frac{t-t_0}{\tau_i}} \cdot \mathrm{erfc}\left(-\frac{t-t_0}{\sigma} + \frac{\sigma}{2\tau_i}\right), \tag{2.2.7}$$

where σ is the effective time resolution of the experiment, estimated as the cross correlation between the pump and the transform limit of the probe[58,71] and erfc is the complementary error function. Kovalenko et al. have theoretically proved the equivalence of using a chirped or transform-limited broadband probe as long as the investigated response is relatively "slow" compared to the duration of the probe.[58]

In a global lifetime analysis, all wavelengths are simultaneously modelled with a series of such exponential decays, retrieving common time constants τ_i. For each exponential decay the wavelength-dependent amplitudes yield a spectrum, the decay associated differential spectrum (DADS(λ)). The DADS do not have an immediate physical meaning: they would correspond to spectra of real species only if dealing with a mixture of independent decaying species.[68] The information retrieved from global lifetime analysis is the minimum number of characteristic times present in the analysed data, i.e., the minimum number of physical processes observed.[70] As discussed in greater detail in the following chapter, relating the excited state dynamics retrieved for RPSBs to actual physical processes is far from trivial.[32] For all the RPSBs studied, three or four time constants at most were sufficient to describe the individual data sets, but evidence from CW irradiations suggested that a greater number of processes is likely to contribute as discussed in Chapter 3. For this reason and with the need of comparing a discrete amount of compounds displaying different photochemical behaviours, an average ESL was defined as an estimate of the time spent by the system in the excited state. This quantity allowed an intuitive comparison of the average time spent by

each compound in the excited state, even though at risk of oversimplifying the complexity of the real situation. When application of a kinetic model is instead viable, it is possible to transform the retrieved time constants with associated DADS in the j time-dependent concentrations c(t) and species associated spectra A(λ).

$$\mathrm{S}(\lambda, \mathrm{t}) = \sum_j \mathrm{A}_j(\lambda) \cdot \mathrm{c}_j(\mathrm{t}). \tag{2.2.8}$$

The procedure involves first generation of a square *kinetic matrix*, **K**, for the chosen model, whose off-diagonal elements K_{ij} are the rate of transformation of the species i into the species j, and the diagonal elements K_{ii} describe the total decay of the species i.[72] The elements of **K** are obtained from the time constants τ_i retrieved from the global optimization routine. **K** is then diagonalised with a unitary transformation, and the retrieved eigenvalues are the rates of the processes described by the kinetic model applied. Expressing the DADS(λ) in the same basis set used to diagonalise **K** yields the species associated spectra A(λ). While this approach has not been followed for RPSBs, it has been applied in the case of the excited state vibrational activity map for **wtGFP** in Chapter 6.

2.2.2 Excited state vibrational spectra

In this section, isolation of excited-state vibrational spectra is discussed following a recent publication by Wende et al.[50] As considered in Section 2.2.1, the interaction of a system with a pulse of short duration in the time domain can generate VC that can be probed by a subsequent pulse. There are two possible scenarios for generating VC in the excited state and two possible scenarios for isolating it from ground state and solvent contributions. All of those have been used in different parts of the work presented in this dissertation, and will thus be described here briefly.

The first option to generate VC in an electronic excited state is to excite the system with a short pulse (purple arrows in Figure 2.2.7a, the same as in Figure 2.2.3b). This will generate nuclear wavepackets on both the excited and the ground electronic states. Furthermore, there will be an additional non-resonant impulsive Raman contribution from the solvent. Since VC is generated by impulsive stimulated Raman scattering, the active modes are determined by the same selection rules as for resonant or pre-resonant Raman scattering.

In this scenario, the short pulse has the function of transferring population from the ground to the excited state and generating VC in the two states. These two roles can also be performed by two different pulses, as illustrated in Figure 2.2.7b: a "long" *actinic* pulse (blue arrow) populates the excited state and a short *Raman pump* (red arrow) generates VC in both populated states.

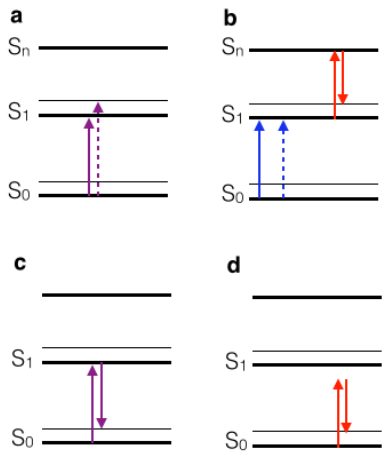

Figure 2.2.7 Comparison of the two ways to generate vibrational coherence (VC) in an excited electronic state. (a) VC generation by excitation with a short pulse (purple arrow). (b) VC generation with a short pulse (red arrow) after excitation with a longer pulse (blue arrow). (c,d) In both cases VC is generated in the ground electronic state as well.

Decoupling the excitation pulse from the Raman pump has a significant consequence: VC can be initiated at any point in time, not only simultaneously with the excitation of the system, and by doing so, the modes in which the VC is generated in the excited state do no longer necessarily match the active ones in the Franck Condon (FC) region accessible from the ground state. The difference becomes more pronounced, if during the time delay between

the actinic and the Raman pump pulses the system evolves along its excited state potential energy surface (PES), reaching a geometry (i.e., symmetry) different from the equilibrated ground state. All the Raman selection principles and rules still hold for the interaction with the Raman pump, but the starting geometry and the gradients of the two PESs involved in the generation of the VC might be different than the ones observed when the system is in the equilibrated ground state geometry, resulting in different spectra.

The spectrally dispersed signal from a probe interacting with the system after the generation of the VC, will have superimposed on an electronic signal an oscillatory component containing contributions from all the vibrationally excited modes of the sample: from the solvent and from the ground and excited state populations of the investigated chromophore. In order to isolate the excited state vibrational contribution, two approaches are possible, one involving more post-processing of the data, and the other being a population control scheme requiring an additional measurement with a fourth pulse.

In the first approach traces are recorded in the presence and absence of the actinic pulses, denoted here by ON and OFF, with the Raman pump always present. The ON trace has contributions from solvent, ground state and excited state, whilst in the OFF trace the latter contribution will not be present as no excited state population is generated before the interaction with the Raman pump takes place.

$$\mathrm{ON} = a \cdot \chi_{\mathrm{solv}} + b \cdot \chi_{\mathrm{S}_0} + c \cdot \chi_{\mathrm{S}_1}, \tag{2.2.9}$$

$$\mathrm{OFF} = a' \chi_{\mathrm{solv}} + b' \cdot \chi_{\mathrm{S}_0}, \tag{2.2.10}$$

with χ being the VC contribution from the system specified in the subscript. If the solvent contribution is small or negligible, for example in the case of weak Raman scatterers such

as water, isolation of the χ_{S_1} term can be achieved by subtracting an appropriately scaled version of the OFF trace. The scaling factor can be determined by fitting regions of the spectrum with peaks that can be attributed to S_0. Ideally, the selected peaks should belong to S_0 only, but multiple overlapping peaks may be used as well under the assumption that the relative amplitudes of the peaks in the S_0 spectrum are not affected by the presence of the actinic pulse. This approach is likely to fail if the solvent gives a non-negligible contribution to the detected VC. The main reason for the failure can be intuitively grasped from Equations 2.2.9-10: if χ_{solv} is not zero, there is no scaled subtraction of the two traces that will isolate χ_{S_1}. This problem can be circumvented if the subtraction is performed between traces where the same coherences are originally generated and in one of the two the coherences of interest are somehow depleted. To achieve this, a long (∼200 fs) *dump* pulse resonant with an excited state transition is added to the experiment after the Raman pump, as shown in Figure 2.2.8. The long duration of the dump pulse (green arrows) ensures that no additional VC is generated with the population transfer.

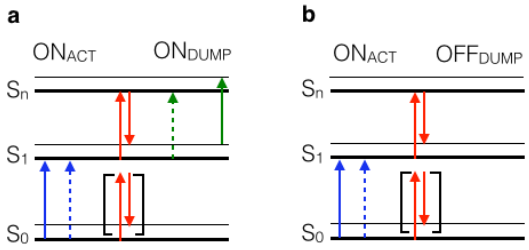

Figure 2.2.8 Addition of a dump pulse (green arrows) to isolate excited state coherences. The dump pulse is too long in time to generate any detectable coherence in the upper excited state. The square brackets indicates that for non-excited molecules coherences are generated in the ground state as well.

The VC contributions to the two traces can then be expressed as follows:

$$\mathrm{ON_{ACT}OFF_{DUMP}} = a \cdot \chi_{solv} + b \cdot \chi_{S_0} + c \cdot \chi_{S_1}, \tag{2.2.11}$$

$$\mathrm{ON_{ACT}ON_{DUMP}} = a \cdot \chi_{\mathrm{solv}} + b \cdot \chi_{\mathrm{S_0}} + c(1-\gamma) \cdot \chi_{\mathrm{S_1}}. \tag{2.2.12}$$

A direct subtraction of the two traces will isolate the $\chi_{\mathrm{S_1}}$ component. To make sure that there are no spurious signals introduced by the dump pulse, a comparison between the coherence activity map of the isolated $\chi_{\mathrm{S_1}}$ and the map obtained in a similar manner from traces without the actinic pulse ($\mathrm{OFF_{ACT}ON_{DUMP}}$-$\mathrm{OFF_{ACT}OFF_{DUMP}}$) is made, and eventually a scaled subtraction is performed. An example is shown in Figure 2.2.9 for the excited state of the GFP model chromophore, **HBDI**, in DMSO solution.

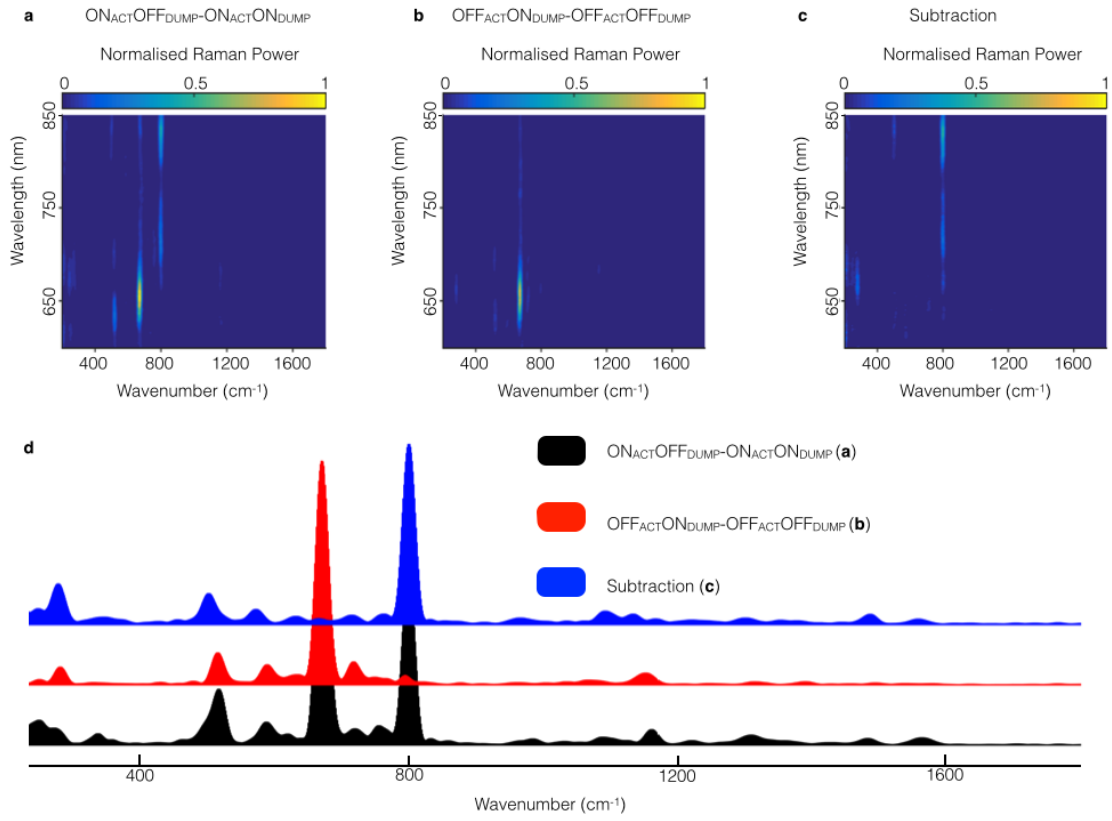

Figure 2.2.9 Subtraction of dump-induced signals from isolated excited state vibrational spectra. (a) Map of isolated excited state Raman spectra. (b) Map of dump-induced vibrations. (c) Map of excited state Raman spectra with subtracted dump-induced signals. (d) Comparison of the spectra obtained by averaging the maps (a,b,c) over the entire wavelength range shown.

The final TA difference map, is an N x M matrix containing the vibrations sampled at M points in the time domain for the N detected wavelengths. Apodisation with an appropriate

window, followed by zero-padding to L points and Fourier transform yields an N x L map containing a spectrum of L points for each wavelength. As the coherent activity is probed in the time domain, it is retrieved as a convolution of the VC spectrum of interest and an instrument response function due to the limited time-resolution of the experiment.[73] To correct for this, the Fourier transform spectrum has to be scaled by a frequency-dependent factor, obtained from an estimate of the effective time resolution within the probed wavelength range.[74] In order to perform these experiments, up to four pulses were needed: an excitation pulse, a Raman pump, a dumping pulse and the probe. The broadband (500-850 nm) probe pulse was generated as described in Section 2.2.1. All the other pulses were generated by white light-seeded NOPAs. As actinic pump, 200 fs long pulses were used at 400 and 480 nm for the GFP work, whilst a 9 fs pulse centred at 500 was used for the retinal work described in Chapter 5. As Raman pumps, sub-10 fs pulses centred at 800 nm or 520 nm were used, whilst 200 fs pulses centred at 760, 800 or 890 nm were used as dump pulses. Stepsize calibration was performed by measuring a solvent only trace and matching the frequencies of the retrieved Raman spectrum with the ones reported in the AIST spectral database for organic compounds.[75]

Chapter 3

RPSB I: Tuning *trans* to *cis* photoisomerisation in solution

Overview

The objective of the present chapter is to understand whether it is possible to shift all-*trans* retinal protonated Schiff base (RPSB) solution photochemistry towards the speed, efficiency and selectivity observed for the opsin proteins in an environment where evolution-optimised electrostatic and steric interactions are not present. By doing this, it is hoped to shed new light on the factors regulating the outcome of the *trans* to *cis* photoisomerisation reaction. To this purpose, the solution photochemistry of a series of structural analogues of all-*trans* RPSBs is investigated in terms of excited state lifetime (ESL), photoisomerisation quantum yield (QY) and selectivity. A correlation is found between ESL, QY - the longer the former, the higher the latter - and the presence and position of polarisable substituents along the backbone. It is also shown how the presence of substituents is a powerful tool to alter the selectivity of the reaction. A simplified model is proposed at the end of the chapter to explain the observed behaviour, and is put into context and compared with the existing literature for the solution and protein photochemistry. Most of the results presented have been already

published.[74,76,77] Transient absorption (TA) measurements have been performed by Matz Liebel and Christoph Schnedermann. Syntheses of the derivatives has been done by Tina Sovdat. NMR experiments other than ^{1}H have been performed by Tim Claridge and Barbara Odell. QY measurements, photoproducts identification and data analysis and interpretation have been performed by the author.

3.1 all-*trans* RPSB photochemistry in bacteriorhodopsin and in solution

The first reaction chosen to explore tuneable photochemistry in photoactive protein is the *trans* to *cis* photoisomerisation of all-*trans* RPSB whose structure and (non-IUPAC) numbering system used throughout this work are shown in Figure 3.1.1.

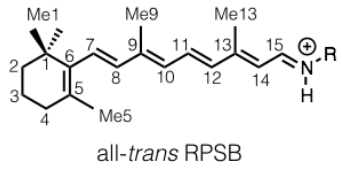

Figure 3.1.1 Structure and numbering system adopted for the all-*trans* RPSBs discussed in this work

Within this chapter, the RPSB formed with *n*-butylamine (nBu) and trifluoroacetic acid (TFA) in methanol (MeOH) (R= *n*-butyl in Figure 3.1.1) is used as a benchmark system for the solution photoreactivity, whilst for the protein environment, bacteriorhodopsin (BR, R= Lys in Figure 3.1.1) is taken as model for the type I archaeal opsins, as is the longest known and most extensively studied and understood member of its family.[18]

When dissolved in MeOH, nBu all-*trans* RPSB has its absorption maximum at 440 nm, (ε = 51800 L mol^{-1} cm^{-1})[25] considerably blue shifted if compared with the absorption of BR at 568 nm.[21] Upon photoexcitation, a multi-exponential decay has been reported, with a sub-ps component attributed to relaxation out of the Franck Condon (FC) region,

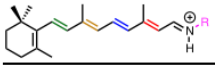

	BR	*n*Bu (MeOH)
R	Lys	*n*Bu
abs λ_{max} (nm)	568	440
Excited State Lifetime (ps)	0.5	4.3
Product (QY)	13-*cis*(0.64)	11-*cis*(0.16) 9-*cis* (0.05)

Table 3.1.1 Comparison of all-*trans* RPSB photochemistry in opsins and solution. Reproduced in part from Bassolino et al., *J. Am. Chem. Soc.*, 2014, **136**, 2650. Copyright 2014 American Chemical Society.

plus two other time constants in the 2 to 8 ps range, the first being usually around 2 ps and the second between 6 and 7 ps. These kinetics have been followed by TA,[28–30,32], or fluorescence up-conversion,[31,78] and differ remarkably from the time-scale observed in BR, for which a photoisomerisation time constant between 200 and 500 fs[23,24] has been reported. According to published works, the main photoproduct in solution is the 11-*cis* isomer, formed with a QY between 0.13 and 0.20 depending on irradiation conditions; as secondary photoproducts both 9-*cis* and 13-*cis* have been reported, with QYs in the range 0.01-0.02.[25,26] QYs have been measured by monitoring the change in the UV-Vis absorption (both stationary[27] and transient[25]), by HPLC (preceded[25] or not[26] by a hydrolysis step) and by NMR[79] (in CD_2Cl_2). Once again, this behaviour differs from the protein case, where the reaction is highly selective, yielding exclusively the 13-*cis* isomer with a three-fold higher QY (0.64).[22] A comparison between the photochemistry of BR and nBu all-*trans* RPSB in MeOH is shown in Table 3.1.1.

The significant differences between the two environments prompted extensive experimental efforts in an attempt to formulate a model for the reaction that could explain not only the observed features but also the degree of tunability.

3.1.1 all-*trans* RPSB photoisomerisation: experiments and models.

The ultrafast photoisomerisation rate observed for BR[23,80–82] led to the proposal that the 13-*cis* configuration in the J_{620} product was formed following a barrierless relaxation from the FC region along a torsional coordinate completed by a decay on the isomerised ground state potential energy surface (PES) through a conical intersection (CI) with a time constant of $\sim$ 500 fs, as shown in Figure 3.1.2.

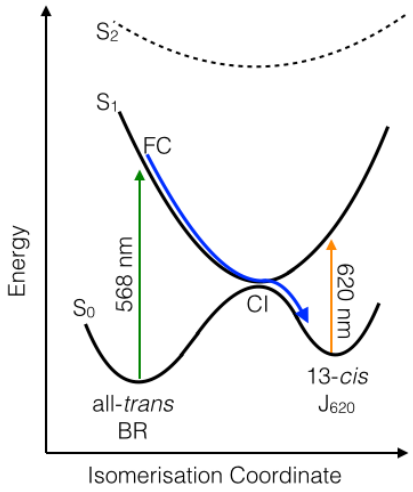

Figure 3.1.2 Two-state model proposed for RPSB photoisomerisation in BR, including the first photoproduct (J_{620}).

Other evidence accumulated over the years pointed towards a more complex isomerisation model than the one originally suggested.[83] It was noted that the stimulated emission (SE) is considerably Stokes shifted compared to the ground state absorption, has a very short rise time but does not spectrally evolve in time between 200 fs and 1 ps. The sub 200 fs evolution was possibly attributed to an overlapping excited state absorption (ESA) between states with varying energy gap.[83,84] Even more in contrast with the suggested model was the observation that the fluorescence lifetime of BR increased significantly with reduction in temperature up to 60±15 ps,[85] but the QY for the formation of the K_{590} intermediate was found to be unaffected all the way down to 77 K.[86,87] Furthermore, a variety of BR mutants showed

significantly different kinetics without comparable change in the photoisomerisation QY.[88,89] As a result, refinements to the model for retinal photoisomerisation in BR were proposed to take into account the discrepancies listed above between the experimental data and the original *two-state*, barrierless model, and also from the insight gained by investigating the solution photoreactivity.

Measurements of the change in dipole moment upon excitation for all-*trans* RPSB in solution showed that a significant electronic redistribution takes place following population of S_1, and could determine the direction of migration of the positive charge to be towards the β-ionone ring.[90] This trend was later confirmed by a computational investigation,[91] that suggested the initial relaxation in the excited state to proceed along skeletal stretching coordinates and found a further increase upon torsion of the electron density migration towards the Schiff base end of the molecule, giving the CI region a twisted intramolecular charge transfer (TICT) character. The primary process following excitation would have then been an adaptation of the single and double C-C skeletal bonds to the different electronic distribution of the new state, resulting in a reduction of the bond length alternation between the two types of bond.[92] This picture of the reaction coordinate initially characterised by high frequency stretching modes was in better agreement with the evolution suggested by resonance Raman spectra.[93] The torsional modes needed to couple the S_1 and S_0 states bringing the system towards the CI would then be excited by intramolecular vibrational energy redistribution. This idea was later supported by FSRS experiments on BR.[94]

From the observed multi-exponential decay of the RPSB excited state dynamics in solution measured by TA or fluorescence up-conversion spectroscopy,[29,78] the existence of a small barrier in S_1 was inferred, and by monitoring the variation of fluorescence lifetime and QY with temperature, an activation barrier for isomerisation of 600 cm^{-1} was estimated in MeOH.[28] The emissive state, both in BR and in solution, was identified as the region before the barrier, the stationary point (SP). As the origin of the barrier is supposed to be an avoided

crossing between the first two singlet excited states S_1 and S_2, this new model came to be known as *three-state model* (Figure 3.1.3).[83]

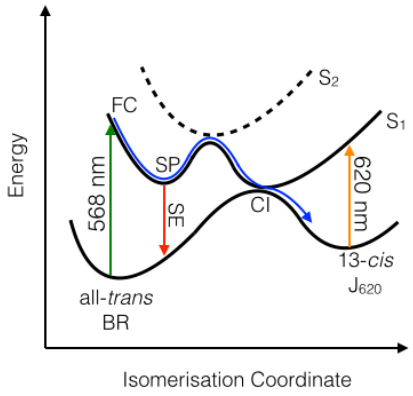

Figure 3.1.3 Three-state model for RPSB photoisomerisation in BR.

Even though a barrier along the isomerisation coordinate had already been found by other computational investigations[92] and was never completely excluded by the researchers supporting the two-state model,[95] its presence was eventually ascertained only when dynamic electron correlation started being taken into proper account by using more sophisticated functionals.[96] The electron dynamic correlation can be thought of as the contribution of the σ-π polarisation into the description of the ionic state S_1, ultimately being another way of involving the third state S_2 into the model.[97] A very recent investigation of the TA on the femtosecond time-scale in the NIR region (>900 nm) for all-*trans* RPSB in EtOH revealed an ESA that was assigned to the S_1-S_2 transition. The same feature was not observed in BR, but the authors suggested the possibility of such a band to be shifted even further to the red in the protein.[98]

The two newly introduced features of the reaction model, i.e., the excited state evolution along two different coordinates and the presence of a small barrier along the path to the CI, could explain several of the observations discussed above, such as the temperature dependence of the BR fluorescence lifetime, the constancy of the BR SE spectrum in the 200 fs - 1 ps time range, the multi-exponential decay observed in the protein and in

solution and the non-isomerised structure of the SP. The independence of isomerisation speed and efficiency observed for BR mutants could be rationalised by considering the rate determining step of the reaction to be the passage over the barrier along the isomerisation coordinate, with the evolution towards the CI and its crossing being so fast to become spectrally undetectable(Figure 3.1.3).[24,83,84] The photochemical selectivity of the protein was rationalised in terms of kinetic competition between existing isomerisation pathways for all the double bonds of the polyenic chain, differing and being discriminated by the heights of the encountered barriers.[24]

Even though the general features of the model could explain the protein and solution photochemistry individually, what remains largely unclear is how the change of environment from protein to solution modifies the excited state PES to produce the differences illustrated in Table 3.1.1. To gain a better understanding of the factors involved, two main roads have been taken: on the one hand, the conditions of solution irradiation experiments such as solvent,[31] wavelength of irradiation,[27,32] amine for the formation of the Schiff base,[99] were varied in an effort to find and rationalise changes in reaction dynamics and QY; on the other hand, structurally modified retinals where used to generate BR analogues whose functionality was then investigated.[100–104] Broadly speaking, by following the former strategy, only relatively small variations of reaction dynamics and efficiency have been observed, keeping the solution photochemistry well distinct from the one observed in the proteins.

The second approach mentioned above encompassed preparation of retinal analogues with modified backbones to investigate the effect of specific steric interactions within the chromophore itself and between the chromophore and the protein pocket. Structurally modified retinals, a few examples of which are shown in Figure 3.1.4, were initially used in pigment preparation studies,[105,106] to determine the degree of adaptability of the retinal binding pocket to the increased steric hindrance of the new co-factors.

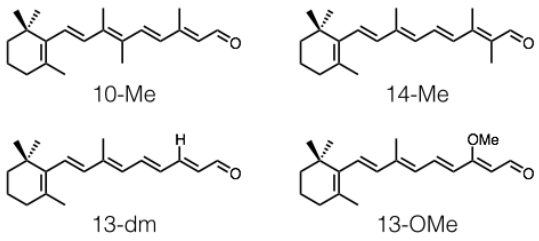

Figure 3.1.4 Examples of structurally modified retinals frequently used in pigment preparation studies.

On the resulting pigments, spectroscopic measurements (mainly vibrational spectroscopy, Raman or FTIR,[104,107,108] but also TA in the ps to ms regime[109–113]) were performed to investigate changes in the BR photocycle or the proton pumping functionality via photocurrent measurements.[111,114] These studies focused and brought great understanding on the "minimum requirements" retinal-like co-factors should possess for pigment formation and functionality.

To the best of my knowledge, no measurements with sufficient temporal resolution to investigate the photoisomerisation dynamics nor the quantum efficiency were performed for the BR analogues. As will be discussed in Chapter 4, the situation is slightly different for studies on rhodopsin (RHO) analogues, for some of which QY and isomerisation dynamics have been reported.[115–122] In any case, for the retinal derivatives used with both proteins, very little information exists on their solution photochemistry. Some results in terms of isomerisation QY and dynamics are available for the aldehydes,[123–128] and to a lower extent, for the PSBs,[37,126,129,130] with the latter being the biologically relevant form of the chromophore for the isomerisation reaction. In other words, scarce information is available on the effects that backbone modifications might have on the "intrinsic" reactivity of the RPSBs. If for the "locked" derivatives the isomerisation reaction on the blocked double bond was clearly prevented by structural constraints, subtler changes such as the addition or removal of methyl groups along the polyenic chain have tacitly been considered not to affect other aspects than intra- or inter-molecular steric interactions.

The work in the present and the following chapter questions the validity of this assumption for the all-*trans* and 11-*cis* RPSB isomers and investigates whether "small" structural modifications can indeed affect the photochemistry in terms of excited state lifetime, photoisomerisation QY and selectivity in solution, an environment without the evolution-optimised steric and electronic interactions between chromophore and protein often invoked to explain the observed differences in reactivity. This is interesting not only for the possible new insight or refinement brought to the current photoisomerisation model, but also as an exploration of the tools available to chemists to "custom-tailor" the photoreactivity of molecular systems.

3.2 Photochemical characterisation of model compounds

3.2.1 Choice of the model compounds

To explore the effect of backbone substitution on the photochemistry of all-*trans* RPSB a first series of derivatives with methyl groups added or removed along the polyenic chain is chosen to test whether the substitution position (Table 3.2.1) could be used as a handle to tune the reactivity. The idea underlying this series stems from consideration of the charge transfer character of the excited state found by dipole solution measurements[90] and computational calculations:[91] the migration of the positive charge towards the β-ionone ring might be affected by the presence (absence) of methyl groups in appropriate positions along the backbone.

A second series of derivatives (Table 3.2.2) is then prepared by adding substituents of different nature at the same backbone position. To this end, C10 is chosen for being the position that yields the greatest effect upon addition of a new substituent along the backbone (see Sections 3.2.2 and 3.2.3 for the results). The substituents are chosen to span a range of steric and electronic features.

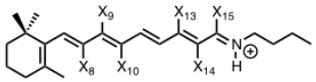

Compound	X_8	X_9	X_{10}	X_{13}	X_{14}	X_{15}
NAT	**H**	**Me**	**H**	**Me**	**H**	**H**
8Me	**Me**	Me	H	Me	H	H
9-dm	H	**H**	H	Me	H	H
9,13-dm	H	**H**	H	**H**	H	H
10-Me	H	Me	**Me**	Me	H	H
10,14-Me	H	Me	**Me**	Me	**Me**	H
13-dm	H	Me	H	**H**	H	H
14Me	H	Me	H	Me	**Me**	H
15Me	H	Me	H	Me	H	**Me**

Table 3.2.1 Chain substituents for the RPSBs with number and position of methyl groups modified. Reproduced in part from Bassolino et al., *J. Am. Chem. Soc.*, 2014, **136**, 2650. Copyright 2014 American Chemical Society.

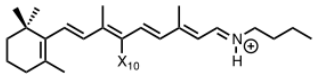

Compound	Nat	10-Me	10-iPr	10-Si	10-F	10-Cl	10-Br
X_{10}	-H	$-CH_3$	$-CH(CH_3)_2$	$-CH_2Si(CH_3)_3$	-F	-Cl	-Br

Table 3.2.2 C10 substituted RPSBs

The nomenclature of the compounds used in the tables does not follow IUPAC guidelines and is designed to make the modification of the naturally occurring retinal backbone easily identifiable. To the best of my knowledge all of these derivatives except for **10-Si** and **10-iPr** have been used for pigment preparation studies with BR or RHO as described at the end of the previous section. The preparation of the retinal derivatives presented here and in Chapter 4 - with the exception of native 11-*cis* retinal obtained as a generous donation from Dr. Crouch of the National Eye Institute, National Institutes of Health - has been the subject of Tina Sovdat's DPhil work.[131] As the preparation of the compounds discussed in the present chapter is not the object of this dissertation, in Appendix A characterisation data (NMR and high resolution mass spectra) are reported only for the PSBs, as relevant for the photochemical studies. Characterisation data for the synthetic intermediates can be found in the SI of the relevant publications.[76,77,131]

The photochemistry of the model compounds was characterised with the techniques discussed in Chapter 2. Two types of measurements were performed: continuous wave (CW) irradiation in deuterated methanol (CD_3OD, MeOD) followed by NMR to determine the amount and nature of photoproducts formed, and ultrafast time-resolved TA measurements in MeOH to determine the reaction kinetics or, as discussed below, the ESL.

3.2.2 Quantum yields and photoproducts distribution

The QYs were measured following the procedure described in Chapter 2.1.2. Briefly, a MeOD solution of the RPSB of interest ($\sim$3 mM) was irradiated under magnetic stirring in a 4 mL pyrex tube with a 532 nm CW laser whose beam was expanded to a diameter of $\sim$0.7 cm, to be completely contained within the pyrex tube. The incident power was adjusted with absorbing filters to $\sim$0.2 mW, and due to the high working concentration resulting in samples of elevated optical density, absorption of all the incident photons could be assumed. Control experiments on **NAT** were performed with a 5-fold higher power (1 mW) to ensure operation within the linear regime, and no differences were observed in the retrieved QYs between the two powers.

The QYs were evaluated with Equation 2.1.3

$$\mathrm{QY} = \frac{M_{\mathrm{photo}}}{N_{\mathrm{Ph,abs}}}, \tag{2.1.3}$$

with M_{photo} being the number of photoproduct molecules formed, and $N_{\mathrm{Ph,abs}}$ the number of absorbed photons. The latter was calculated from the incident power (P_{inc}), the irradiation time (t_{irr}) and wavelength (λ_{irr}), according to Equation 2.1.4

$$N_{\mathrm{Ph,abs}} = N_{\mathrm{Ph,inc}} = \frac{P_{\mathrm{inc}} \cdot t_{\mathrm{irr}} \cdot \lambda_{\mathrm{irr}}}{hc}. \tag{2.1.4}$$

M_{photo} was evaluated as Equation in 2.1.5

$$M_{\mathrm{photo}} = [\mathrm{Sample}] \cdot V_{\mathrm{irr}} \cdot F_{\mathrm{photo}} \cdot N_{\mathrm{A}}, \tag{2.1.5}$$

The stereoisomers formed by photoexcitation were determined with one of the two methods specified in Chapter 2.1.3: by comparison of the ^{1}H NMR spectrum of the new resonances observed in the irradiated mixture with the ^{1}H NMR spectrum of a suspected candidate, or via a series of 1D and 2D NMR experiments on the irradiation mixture. The relevant NMR data are reported in Appendix A. The results of the CW irradiation experiments are summarised in Table 3.2.3, where the absorption maximum for the RPSBs in MeOH, the internal standard used to determine the sample concentration, the photoproducts identities and QYs are reported.

Close inspection of the data presented in Table 3.2.3 is helpful in understanding the way TA data have been analysed. Upon irradiation of **NAT** RPSB formation of only 11-*cis* and 9-*cis* isomers was observed, in contrast to previous reports,[25,26] where a small but non-negligible QY for the formation of the 13-*cis* isomer was found. It was already shown by Childs and Shaw[79] that the method in which the irradiation mixture is analysed can affect the results. Comparison of the compositions retrieved analysing irradiated mixtures of all-*trans* RPSB by directly measuring ^{1}H NMR in CD_2Cl_2 or by HPLC preceded by a hydrolysis step resulted in a larger apparent yield of the 13-*cis* isomer in the second case.[79] Due to discrepancy with previous reports, the need was felt of monitoring the photo-conversion of all-*trans* **NAT** RPSB for longer irradiation times than the ones used in the QY or photoproduct

Compound	Abs Max (nm)	Internal Standard	PP1 (QY)	PP2 (QY)	TOT QY
NAT	446	Benzene	11-*cis* (0.16)	9-*cis* (0.05)	0.21
8-Me	434	Pyridinium ion	11-*cis* (0.08)	7-*cis* (0.05)	0.13
9-dm	438	Benzene	11-*cis* (0.25)	N.I. (0.01)	0.26
9,13-dm	438	Pyridinium ion	11-*cis* (0.22)	9-*cis* (0.09)	0.31
10-Me	450	Benzene	11-*cis* (0.09)	-	0.09
10,14-Me	456	Benzene	11-*cis* (0.08)	9-*cis* (0.01)	0.09
13-dm	440	Benzene	11-*cis* (0.33)	9-*cis* (0.19)	0.52
14-Me	444	Ethyl Acetate	11-*cis* (0.11)	13-*cis* (0.03)	0.14
15-Me	432	Pyridinium ion	11-*cis* (0.09)	13-*cis* (0.03)	0.15[a]
10-iPr	445	Benzene	11-*cis* (0.07)	N.I. (0.05)[b]	0.12
10-F	440	Dichloromethane	N.I. (0.12)	-	0.12
10-Cl	438	Pyridinium ion	N.I. (0.01)	-	0.01
10-Br	438	Dichloromethane	N.I. (0.02)	-	0.02
10-Si	470	Benzene	N.I. (0.13)	-	0.13

N.I.: Not Identified.
[a] A third, not identified photoproduct was observed with QY 0.03.
[b] Excluded to be 9-*cis* by ^{1}H NMR spectra comparison

Table 3.2.3 CW irradiation experiments results

determination experiments. The composition (in percentage) of the irradiation mixture is shown in Figure 3.2.1 as a function of the converted amount of the starting all-*trans* isomer. The composition has not been reported as a function of the irradiation time as conspicuous volumes of solution were taken out to measure the ^{1}H NMR spectra. Due to the reduction of the amount of irradiated material the conversion rate varied during the experiment if measured in percentage term.[a] Whereas there is a clear increase in 11-*cis* (red line) and 9-*cis* (magenta line) products, the amount of 13-*cis*, present in the starting mixture as a $\sim$1% impurity, remains unchanged for the duration of the experiment.

There is a parallel between the trend of QY formation for the 11-*cis* isomer, the main photoproduct formed for all the derivatives studied, and the total isomerisation yield. Whenever a methyl group is added at any position along the backbone (red entries in Table 3.2.3), be it closer to the β-ionone ring or towards the Schiff base moiety, both values drop. On

[a] If the composition of a mixture is stated in percentage as in the present case, the conversion rate varies with the concentration and/or the volume of solution irradiated. With the same illumination intensity and quantum efficiency (i.e., the same number of molecules photoisomerising per time unit), converting 20% of the starting material of a more concentrated solution or higher volumes takes longer than reaching the same percentage conversion for less concentrated solutions or smaller volumes.

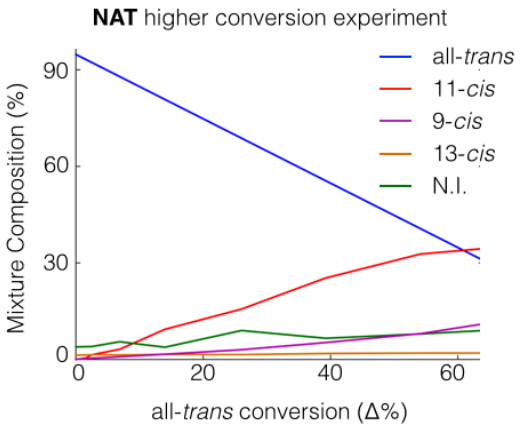

Figure 3.2.1 Higher conversion experiment for **NAT**. The signal for the product marked as N.I. is very likely due to a mixture of 15-*sin* isomers. Reproduced in part from the supporting material of Bassolino et al., *J. Am. Chem. Soc.*, 2014, **136**, 2650. Copyright 2014 American Chemical Society.

the contrary, removal of an existing methyl from the backbone (blue entries) always results in their increase. In three (**8-Me**, **10-Me**, **14-Me**) or possibly four cases (including **15-Me**, for which a third unidentified photoproduct was detected), formation of the 9-*cis* isomer is suppressed as well. The structural changes for all the derivatives with altered number of methyls, i.e., addition or removal of methyl groups, with respect to the **NAT** backbone are reported in magenta in Figure 3.2.2. The coloured double bonds are the ones for which photoisomerisation has been proven to occur and "+" and "-" signs indicate whether the measured photoisomerisation QY for the underlying double bond is higher or lower, respectively, than the one observed for the corresponding double bond for the **NAT** backbone.

The identities and QYs for the secondary photoproducts support the existence of independent isomerisation pathways for each possible photoproduct. For the **9-dm** derivative the 11-*cis* QY is increased whilst no secondary photoproduct has been detected. On the other hand, photoproducts different than 11-*cis* and 9-*cis* were observed for **8-Me**, **14-Me** and **15-Me**. Upon irradiation of **8-Me** the 7-*cis* isomer was formed, whilst the 13-*cis* isomer was found for the other two compounds. In all these cases, the newly isomerising double bonds were close to the methylation site. In other words, if addition of a methyl group inhibited the

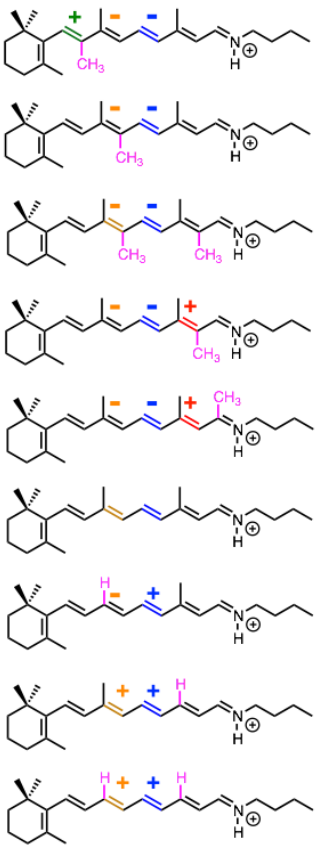

Figure 3.2.2 Photoproduct distributions for the backbone-modified derivatives. The structural changes compared to **NAT** are marked in magenta. Isomerising double bonds are colour-coded (green, orange, blue and red for 7-*cis*, 9-*cis*, 11-*cis* and 13-*cis*, respectively). The "+" or "-" signs indicate increased or decreased photoreactivity of the corresponding double bond compared to **NAT**. Reproduced in part from Bassolino et al., *J. Am. Chem. Soc.*, 2014, **136**, 2650. Copyright 2014 American Chemical Society.

production of the naturally occurring 9-*cis* isomer, so did the removal for the **9-dm** derivative, whilst new photoproducts were observed for the extra-methylated backbones. The fact that for the same derivative the production of some isomers is inhibited whilst others are activated points towards a scenario where separate reactive pathways exists for each possible isomer (Scheme 3.2.1), as suggested by Gai et al.[24] Further insight on such a model is offered by considering the reaction dynamics in the next section.

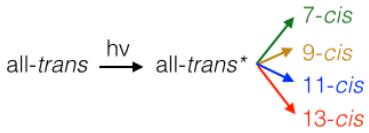

Scheme 3.2.1. Photoreaction scheme for all-*trans* isomers. The results suggest the existence of different pathways for each possible isomer.

3.2.3 Transient absorption measurements and excited state lifetimes

TA data were recorded for every compound under similar conditions. Solutions of RPSB in MeOH of final optical densities 0.7-1 at the absorption maximum in a 200 μm flow cell were excited by ∼20-30 fs pulses centred at 500 nm. The transient spectra were probed with a chirped white light in the 530-900 nm region from negative (∼500 fs before excitation) to positive time delays for long enough to follow the excited state decay of the SE band in the >600 nm region.

A typical TA contour map for nBu **NAT** RPSB alongside with spectra at selected time points and kinetics at representative wavelengths in the SE region are shown in Figure 3.2.3. Experimental data are coloured, with the fit (*vide infra*) plotted on top as a dashed black line. In the probed spectral range, three bands are clearly visible: an ESA in the blue edge of the spectrum, (λ<600 nm) and a broad SE band above 600 nm. The latter overlaps with another ESA band centred at 750 nm, resulting in a double peaked appearance.[32] On the blue edge of the spectrum, ground state bleach is expected to be present, but is likely overcompensated

by ESA. Similar features have been observed for all the derivatives discussed in this chapter, as can be seen by the images in Appendix A.

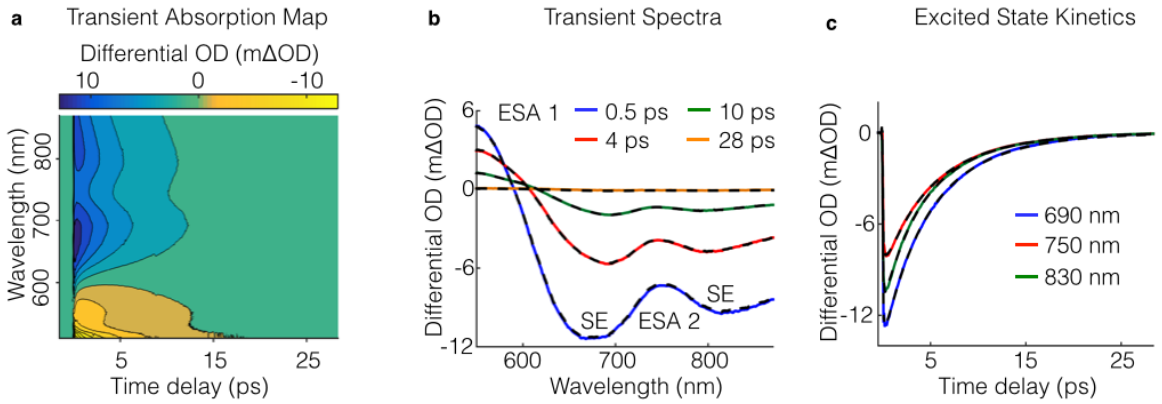

Figure 3.2.3 TA data for nBu **NAT** RPSB. (a) TA map; (b) Transient spectra at the indicated times after photoexcitation. The dominant features in the probed region include two excited state absorption (ESA) bands and a broad stimulated emission band (SE); (c) Kinetic cuts at selected wavelengths showing the excited state kinetics. In (b) and (c) the experimental data are plotted in colour with the corresponding fit shown as a black dashed line on top. Reproduced in part from Bassolino et al., *J. Am. Chem. Soc.*, 2014, **136**, 2650. Copyright 2014 American Chemical Society.

The most common and straightforward approach to analyse TA data involves fitting it to a minimum number of amplitude-weighted exponential decays, generally referred to as global analysis or global optimisation routine.[68–70] The data set (S(λ,t)) was described in the terms of Equation 3.2.1, obtained by combining Equations 2.2.6 and 2.2.7, as a sum of independently decaying components, each with an associated characteristic time constant (τ_i) and decay associated differential spectrum (DADS(λ)$_i$).

$$S(\lambda, t) = \sum_i DADS_i(\lambda)(IRF \otimes e^{-\frac{t}{\tau_i}}). \tag{3.2.1}$$

IRF is a model for the instrument response function and $\otimes$ indicates a convolution. The expression adopted in the fitting routine for the term in square brackets for each time point t, i.e., the convolution of the exponential term with the instrument response, was given in Equation 2.2.7 as

Compound	τ_1 (ps)	τ_2 (ps)	τ_3 (ps)
NAT	0.30	2.1	6.3
8-Me	0.11	1.0	3.3
9-dm	0.18	1.1	4.7
9,13-dm	0.19	2.1	10.3
10-Me	0.15	0.73	2.3
10,14-Me	0.25	0.50	2.2
13-dm	0.30	2.0	7.7
14-Me	0.22	1.3	4.5
15-Me	0.26	1.2	4.6
10-iPr	0.11	0.54	1.9
10-F	0.24	1.7	5.1
10-Cl	0.20	1.1	2.5
10-Br	0.25	1.2	4.8
10-Si	0.44	1.9	4.4

Table 3.2.4 Time constants retrieved from global fit of TA data

$$\mathrm{IRF} \otimes e^{-\frac{t}{\tau_i}} = e^{-\frac{t-t_0}{tau_i}} \cdot \mathrm{erfc}\left(-\frac{t-t_0}{\sigma} + \frac{\sigma}{2\tau_i}\right), \qquad \text{(2.2.7 rev.)}$$

where t_0 is the time point when pump and probe pulses overlap, τ_i is the i-th characteristic time constant, σ is a parameter related to the time resolution of the experiment and erfc indicates the complementary error function.

In agreement with previous reports[28–30,32] multi-exponential decay of the excited state features was observed, and all data sets were fitted with three time constants, reported in Table 3.2.4 for all the derivatives studied. The shortest retrieved time constant could be attributed to a combination of the system leaving the FC region along the stretching coordinate discussed in the introduction[92,93] and a dielectric response of the solvent to the new electronic distribution of the solute. The range of values retrieved (0.1-0.4 ps) is in good agreement with the expectation for the solvent response.[132] In other words, the first time constant can be regarded as representative of the system leaving the FC region and moving towards the SP (Figure 3.1.3).

Compound	k_2 (ps^{-1})[a]	k_3 (ps^{-1})[a]	PP1 calc	PP2 calc	PP1/PP2 calc	PP1/PP2 expt
NAT	0.48	0.16	0.75	0.25	3.0	3.2
8Me	1.00	0.30	0.77	0.23	3.3	1.6
9-dm	0.91	0.21	0.81	0.19	4.3	25
9,13-dm	0.48	0.10	0.83	0.17	4.9	2.4
10-Me	1.43	0.43	0.77	0.23	3.3	[b]
10,14-Me	2.00	0.45	0.81	0.19	4.4	8
13-dm	0.50	0.13	0.79	0.21	3.9	1.7
14Me	0.77	0.22	0.78	0.22	3.5	3.7
15Me	0.83	0.22	0.79	0.21	3.8	3[c]
10-iPr	2.00	0.53	0.79	0.21	3.8	1.4
10-F	0.59	0.20	0.75	0.25	3.0	[b]
10-Cl	0.91	0.29	0.76	0.24	3.2	[b]
10-Br	0.83	0.21	0.80	0.20	4.0	[b]
10-Si	0.53	0.23	0.70	0.30	2.3	[b]

[a] rate constant evaluated as $1/\tau$
[b] No secondary photoproduct detected
[c] Third photoproduct detected not considered

Table 3.2.5 Calculated and experimental photoproducts distribution

To attribute a physical meaning to the other two time constants is more complex. If multiple channels exist as suggested by the variation in QYs and selectivities, a straightforward connection between the retrieved time constants and reactive pathways cannot be made. For example, attributing the intermediate and the longest time constants to the major and secondary photoproduct, respectively, would yield an isomer distribution in reasonable agreement with that measured for **NAT**,**14-Me** and **15-Me** assuming the crossing efficiency of the CI to be the same for all channels, but would fail when applied to the other derivatives, as shown in Table 3.2.5. Another problem of this explanation is that also derivatives such as **10-Me**, **10-F**, or **10-Si**, for which a single photoproduct was detected, showed a tri-exponential decay.

Usually, a kinetic model is applied after the global optimisation in order to determine the number of species present and their associated spectra (SAS).[68] The difference between the approaches can be subtle but crucial for a correct interpretation and use of the fit results. If a global analysis with three exponential terms of the types here used is conducted on a data set,

the system is treated as being formed by three independently decaying species (A*, B* and C*), a model that, in kinetic terms, could be called "parallel". A*, B* and C* would all be present at time zero defined immediately after the sample interaction with the excitation pulse, and would decay, with their respective time constants, to the corresponding primed species (A', B' and C'). These can be the reactants (A, B, C) or products or long lived intermediates whose evolution is not complete within the probed time delay. In photochemistry this is not a very common scenario, and, more specifically, it is highly unlikely to be the correct one for RPSBs in solution, so that the failure of the approach tempted above is not truly surprising. To apply a kinetic model, the first step is to choose amongst the several possible ones, i.e. sequential or branching, with reversible or irreversible steps, such as shown in Scheme 3.2.2.

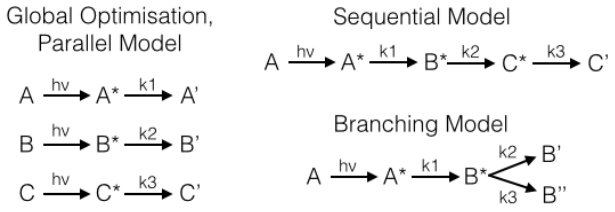

Scheme 3.2.2. Comparison of different kinetics models.

Elaborated kinetics analyses have been applied[27,31,133,134] in an attempt to propose a unifying model for RPSB photochemistry, but scarce agreement has been reached apart from some general features like the multi-exponentiality of the decay and the presence of a barrier along the isomerisation coordinate - with the latter being debated at length within the computational community.[92,95,96,135] One of the RPSBs features rendering the analysis difficult is the lack of characteristic signals for each individual isomer, as they all exhibit a broad absorption spectrum peaked near 440 nm differing only in the extinction coefficient.[25] This means that whereas within the proteins, photoproducts are easily identified by their shifted absorption maximum and their kinetics can be conveniently followed by monitoring the correct spectral region, this is not the case for RPSBs in solution. Multipulse experiments have been performed on all-*trans* RPSB to identify the reactive channel,[134] and a single

photoisomerisation time constant was retrieved of about 3-4 ps that varies with the nature of the solvent. This model suggests that there is a single reactive channel for **NAT** in solution, and that multiple isomers would be formed after reaching the CI. This is in contrast both with the model proposed by Gai et al. for BR,[24] and with what would be expected on the basis of the CW irradiation experiments described above: the independent variation of the amount and nature of isomers formed suggests that they are produced through different reaction pathways (Scheme 3.2.1). Due to the lack of isomer-specific features within the recorded data that would allow to follow the individual formation kinetics, and the necessity for comparing a series of derivatives showing highly varied QYs and selectivities, no attempt was made to apply a kinetic model. The main reason behind this choice is that the actual number of channels is likely to be higher than the two (or three, including the initial relaxation) values retrieved. Inspection of the decay associated spectra retrieved for **NAT** shown in Figure 3.2.4 might strengthen this point: the DADS for the shortest time constant (0.3 ps) could represent a rise of the ESA and SE bands in the probed region; the DADS of the intermediate time constant (2.1 ps) presents dispersive features typical of spectral shifts, with the one associated with the longest time constant (6.3 ps) showing the spectral signatures of excited state decay (to be confronted with the transient spectra in Figure 3.2.3).

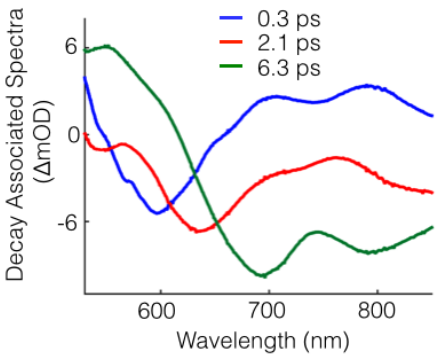

Figure 3.2.4 Decay associated spectra (DAS) retrieved from global fitting of **NAT** TA data, with the respective time constants indicated in the legend.

Error estimate for the global analysis

The first step to perform the global analysis consisted in choosing the number of exponential terms to include. In order to do so, the optimisation algorithm was run with an increasing number of exponential terms until a satisfactory fit could be obtained, as judged by the appearance of the residuals. In Figure 3.2.5 is shown the comparison of a biexponenital and triexponential fit and the residuals at selected wavelengths for the **NAT** dataset previously discussed. The biexponential fit was judged unsatisfactory because of the inadequate description provided particularly of the first picosecond dynamics, on the contrary of the good agreement between reconstructed and experimental data shown by the triexponential fit.

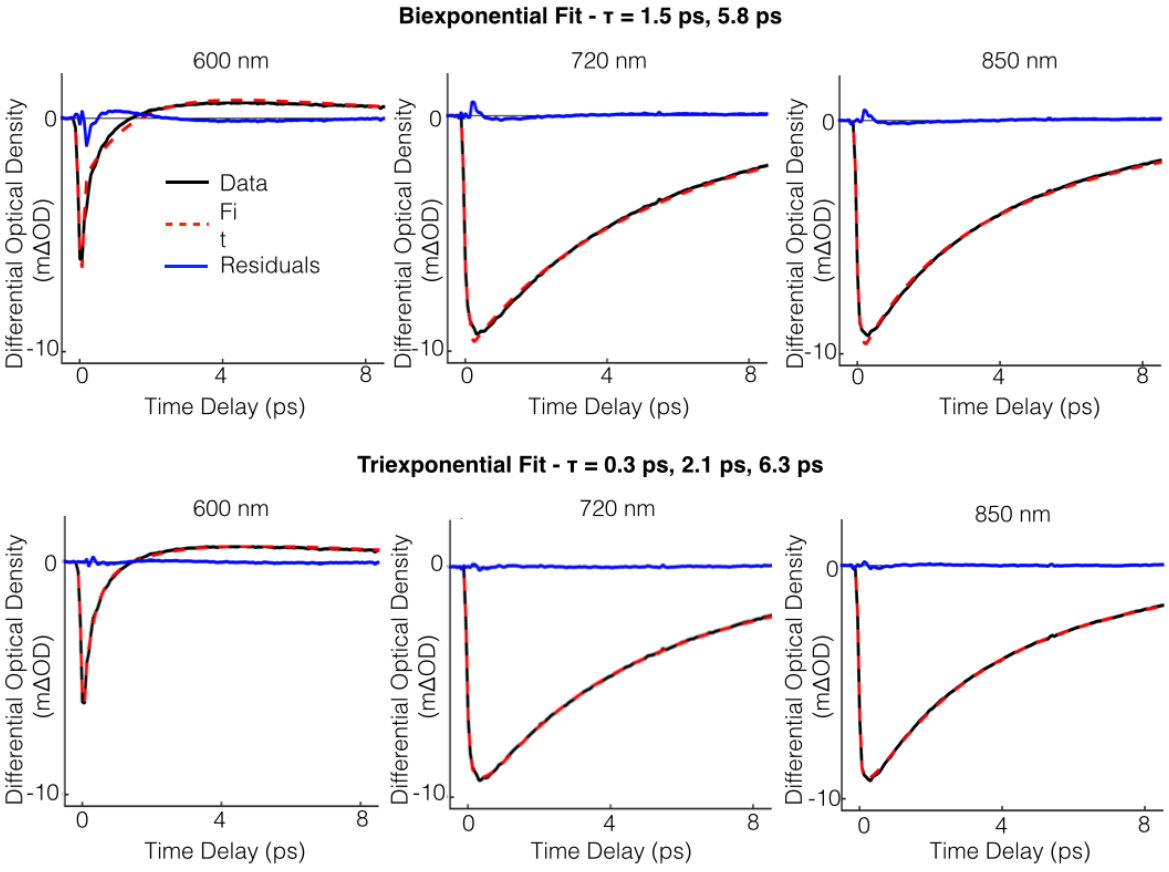

Figure 3.2.5 Biexponential vs. triexponential global fitting of **NAT** TA data at selected wavelength.

The decay time constants τ_i obtained within the chosen triexponential scheme were optimised in a non-linear least-square sense exploiting the *lsqnonlin* MATLAB [136] function.

Starting Guesses			Retrieved time constants		
τ_1 (ps)	τ_2 (ps)	τ_3 (ps)	τ_1 (ps)	τ_2 (ps)	τ_3 (ps)
0.3	2.1	6.3	0.3017	2.1326	6.3028
0.1	1.8	7	0.3017	2.1326	6.3028
0.05	1	15	0.3017	2.1327	6.3029

Table 3.2.6 Dependence of global optimisation outcome on starting guesses

Whilst in principles there is a built-in function, (*nlparci*), to obtain confidence intervals and hence error estimates on fitting parameters for non-linear least-square optimisations, it was not applicable in the present case as not converging during the evaluation of the covariance matrix. The covariance matrix contains information on the partial derivatives of a parameter with respect to the other fitting parameters. A possible explanation is that a fitting was being attempted of data matrices of over 100K points with only three to five parameters (the three decay constants, the IRF temporal width and the t_0 position). The amplitude at the individual wavelengths that constitute the DADS are, in fact, not treated as explicit parameters in the fit but are recovered indirectly from a matrix decomposition following a guess of the time-dependent concentrations. This has computational advantages, but, as just discussed, renders the estimate of the errors of the fitting parameters non-trivial. To have an estimate of such errors, the global optimisation routine was launched multiple times on the same dataset to ascertain the following two aspects: firstly, that the minima found were not an artifact of the starting guess provided; secondly, to what extent two of the time constants were affected by the value assumed by the third one.

To ensure that the retrieved values for the time constants were true solution of the minimisation problem and not an artifact of the starting guesses provided, the global analysis was performed multiple times feeding different initial values. As shown in Table 3.2.6 for **NAT**, the retrieved time constants were not affected by the initial guess provided.

Table 3.2.6 might lead to think that the error on each time constant is indeed small, but that might not be the case. As discussed below, fits of comparable quality could be obtained

Starting Guesses			Retrieved time constants		
τ_1 (ps)	τ_2 (ps)	τ_3 (ps)	τ_1 (ps)	τ_2 (ps)	τ_3 (ps)
0.25	2.1	6.3	**0.25**	2.0	6.2
0.35	2.1	6.3	**0.35**	2.2	6.4
0.3	**1.7**	6.3	0.24	**1.7**	6.1
0.3	**1.9**	6.3	0.27	**1.9**	6.1
0.3	**2**	6.3	0.28	**2**	6.2
0.3	**2.3**	6.3	0.33	**2.3**	6.4
0.3	2.1	**5.9**	0.23	1.8	**5.9**
0.3	2.1	**6.1**	0.26	1.9	**6.1**
0.3	2.1	**6.5**	0.34	2.3	**6.5**
0.3	2.1	**6.7**	0.38	2.5	**6.7**

Table 3.2.7 Interdependence of retrieved time constants from global optimisation routine. Bold entries were kept fixed during the optimisation.

with values of time constants different up to 15-20 % than the ones reported in the above table. To ascertain the interdependence of the retrieved fitting parameters, the global analysis was performed fixing the value of one time constant while optimising the other two. Results for fits of comparable quality as judged by the appearance of the residuals are reported in Table 3.2.7. As can be seen from the table, varying the fixed time constant up to ±15-20 % for the first two time constants and ±8-10 % for the longest one, still yielded reasonably good fit to the data. The observed behaviour can possibly explain the troubles mentioned above in the evaluation of the covariance matrix.

In an analogous way, an error estimate was needed for the DADS associated with the individual time constants. To obtain such a quantity, the DADS retrieved for the unconstrained fit were compared with the DADS obtained from the constrained optimisations (i.e., like the ones reported in Table 3.2.7 for **NAT**) with the smallest and highest value of the relevant time constant (Figure 3.2.6). In this way, a relative error of ±10% on the amplitude of the individual DADS was estimated in the region where the stimulated emission signal has the maximum amplitude (660-875 nm in the present case).

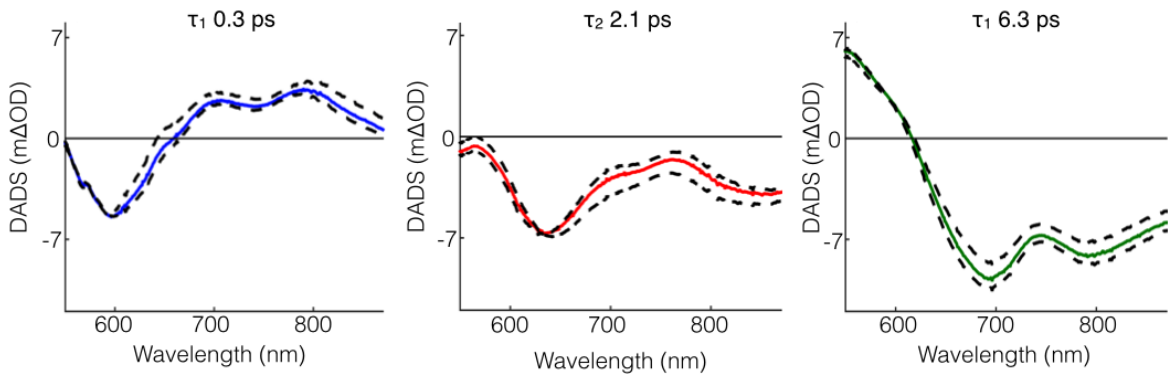

Figure 3.2.6 Error estimate on DADS.Coloured lines are the DADS retrieved from the global routine with all three time constants optimised, whilst black dashed lines correspond to the DADS retrieved by the smallest/biggest value assumed by the corresponding time constant reported in Table 3.2.7.

Excited state lifetimes

Considering the issues associated with the kinetic analysis and the scarcity of the starting material available for most of the compounds, a different approach was adopted to compare the dynamics in a simple and intuitive manner. An ESL was defined for each derivative, and was intended as an indicator of the average time spent by the system in the excited state following absorption of a photon. The first approach adopted consisted in averaging the retrieved time constants weighted by the amplitude of the respective DADS. A lifetime value was determined for each wavelength according to Equation 3.2.2, and the ESL of the compound was calculated by averaging the values retrieved in the spectral region of the SE band.

$$\mathrm{ESL}(\lambda) = \frac{\sum_i \tau_i |\mathrm{DADS}_{i\lambda}|}{\sum_i |\mathrm{DADS}_{i\lambda}|}. \tag{3.2.2}$$

The retrieved ESL for **NAT** is shown in Figure 3.2.7. The red line superimposed on the TA map shows the individual lifetime values for the corresponding wavelengths, and a comparison is made with another way of defining the lifetime, as the time taken for the signal

Retrieved time constants			
τ_1 (ps)	τ_2 (ps)	τ_3 (ps)	ESL (ps)
0.25	2.0	6.2	4.2
0.35	2.2	6.4	4.4
0.24	**1.7**	6.1	4.1
0.27	**1.9**	6.1	4.2
0.28	**2**	6.2	4.3
0.33	**2.3**	6.4	4.4
0.23	1.8	**5.9**	4.2
0.26	1.9	**6.1**	4.3
0.34	2.3	**6.5**	4.4
0.38	2.5	**6.7**	4.5

Table 3.2.8 Error estimate on the ESL evaluated via Equation 3.2.2. Numbers in bold are time constants kept fixed during the fitting routine

to decay by a factor 1/e from its maximum amplitude (black line). Analogous maps for all the derivatives are shown in Appendix A. The error stated for the 1/e method is the standard deviation of the mean[137] of the values retrieved in the spectral range used to evaluate the ESL. A similar method could not be straightforwardly applied to the DADS weighted ESL, as the error on the individual time constants and associated spectra should be taken into account. A reasonable estimate for such error seem to be within in the 10-15% range, considering that whilst error propagation due to the multiplication of the time constant for the amplitude is expected to accumulate the effect of the two relative uncertainties, still an average over a few hundreds value of the selected spectral region is made. An indirect confirmation of this estimate can be obtained by examining the lifetime values in Table 3.2.8, obtained applying Equation 3.2.2 to each of the fits results (time constants and associated DADSs) reported in Table 3.2.7.

The underlying idea behind Equation 3.2.2 is that no model is applied and each time constant is treated as a decay of the excited state, rather than a possible rise or spectral shift of the band. Whilst this may sound drastic, it is an attempt to avoid imposing models on the data. Stating, as done in the previous section, that the shortest time constant represents the system leaving the FC region and reaching the SP, means already choosing between a

branching model in the FC region or one in the SP. Whilst the data presented in this work cannot discriminate between the two models, due to the impossibility of selectively follow each of the suggested channels, both have been proposed in literature.[24,91–93,134]

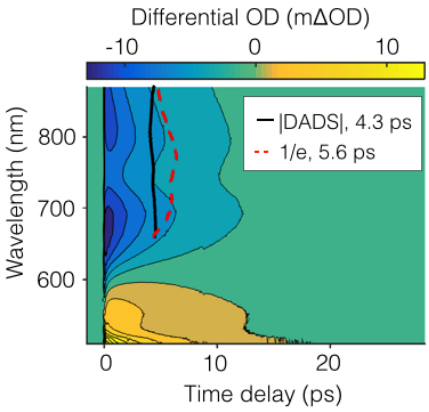

Figure 3.2.7 Determining the excited state lifetime (ESL) for **NAT**. The ESL retrieved for each wavelength using the DADS-weighted average (black) and 1/e (red) methods is superimposed on the TA map.

As an alternative method, the band integral[138] over the Vis-NIR spectral region was evaluated according to Equation 3.2.3, and subsequently estimated by fitting with a least-square optimisation method of the retrieved curve with a biexponential decay function. The ESL was then evaluated as the weighted average of the two retrieved time constants. Uncertainties on the individual coefficients of the least square optimisation were obtained through the dedicated MATLAB built-in function, *nlparci*. Uncertainties on the ESL have been obtained through propagation of the errors estimated for the coefficients.

$$\mathrm{BI}(\lambda) = \int_{\lambda_1}^{\lambda^2} \frac{\Delta\lambda}{\lambda} d\lambda. \tag{3.2.3}$$

The advantage of the band integral approach is that it should be an exclusive measurement of the decay kinetics without 'contamination' from spectral shifts internal to the evaluated band. As shown in Figure 3.2.8, a monoexponential function does not adequately describe the

Range Eval (nm)	Retrieved ESL (ps)	
	Monoexp	Biexp
550-875	4.55±0.04	4.5±0.1
600-875	4.97±0.04	4.9±0.2
660-875	5.42±0.04	5.4±0.2

Table 3.2.9 Variation of ESL retrieved from the band integral method with the spectral range considered

observed decay kinetics, and even a biexponential function is somewhat insatisfactory in the very early time points. The multiexponentiality of the decay should be expected based on the existence of multiple and independent reactive channels inferred from the QY measurements (Scheme 3.2.1). The presence of a rise in the first few hundreds of femtoseconds can possibly be explained by the choice of the spectral window used for evaluating the band integral. As Table 3.2.9 and Figure 3.2.8 show for **NAT**, extending the spectral region for the evaluation of the band integral further reduces the retrieved ESL, possibly because a greater contribution from the 300 fs decay component is included.

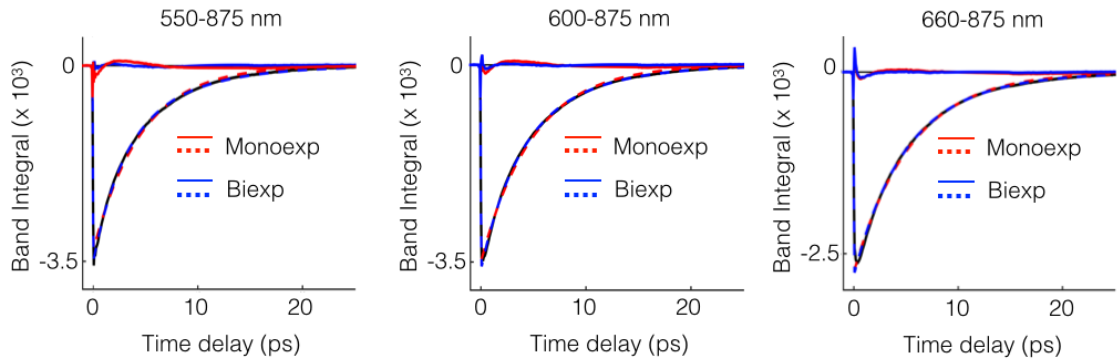

Figure 3.2.8 Band integral dependence from spectral range considered. The band integrals are plotted as black lines. The fit and the residuals are plotted as dashed and solid coloured lines, respectively.

The ESLs for all the compounds evaluated with the three methods discussed are reported in Table 3.2.10. Whilst the values reported in the table vary even significantly in absolute terms depending on the method chosen and the spectral window considered within each method, the trend observed is the same independently of the approximations and choices

Compound	Range eval. (nm)	IDASI (ps)	1/e (ps)	BI (ps)
NAT	660-875	4.3	5.63±0.03	5.4±0.2
8-Me	610-850	1.7	2.79±0.03	2.7±0.1
9-dm	640-935	3.5	4.36±0.04	4.4±0.2
9,13-dm	640-915	7.1	11.55±0.05	10.7±0.8
10-Me	625-875	0.54	0.68±0.01	0.55±0.02
10,14-Me	690-925	0.40	0.39±0.01	0.33±0.04
13-dm	660-880	5.7	7.42±0.04	7.0±0.2
14-Me	685-855	1.7	1.83±0.01	1.9±0.1
15-Me	645-920	2.8	2.94±0.04	3.0±0.2
10-iPr	630-885	0.19	0.254±0.005	0.17±0.02
10-F	675-850	3.0	4.45±0.05	4.3±0.3
10-Cl	700-900	1.5	1.91±0.02	1.85±0.03
10-Br	650-850	1.1	1.26±0.02	1.3±0.2
10-Si	650-880	2.1	2.48±0.02	2.3±0.1

Table 3.2.10 Retrieved excited state lifetimes

made. This strongly suggests that whatever errors are introduced by the choices made applying any of the three models presented for the evaluation of the ESL, they affect in the same way the values retrieved for the whole series of derivatives. It should be remarked that only relative trends will be discussed in the context of this dissertation, and that at no point any special meaning will be attributed to the individual values retrieved for the ESL. The only considerations that are going to be made are in a relative sense (i.e., is the value retrieved for derivative X greater/smaller than the value for derivative Y), and this trend is unaltered within each of the methods presented. In the figures that follow, the lifetimes obtained from the band integral are plotted to ease the visualisation of the discussed trends, but it is worth remarking that all the arguments would equally hold if any of the other two methods was used.

These results reveal clear trends: replacing hydrogens with any group along the backbone always shortens the ESL, whilst removal of methyl groups increases it (with the single exception of **9-dm**). In a simplified picture, which will be discussed in greater detail in the next section, the ESL defined in this way could be thought of as the average time spent by a derivative in the excited state. As multiple reactive and non reactive pathways likely exist, each one with its own excited state barrier,[24] the ESL can be also regarded as the average

of the system's time constants to overcome the barriers encountered along the different de-excitation pathways when leaving the SP and moving towards the CI.

3.3 Tuning the photoisomerisation reaction

In the following section the results from the CW irradiation experiments and the TA experiments are analysed together in an attempt to understand the origin of the differences in photochemical behaviour for the derivatives. The ESLs retrieved from TA measurements and the QYs and selectivities obtained from the CW irradiation experiments are compared as bar graphs in Figure 3.3.1. The colour code indicates different features in the two cases: in Figure 3.3.1a it refers to the type of backbone modification performed, whilst in Figure 3.3.1b it is used to identify the *cis* isomer produced by the photoreaction. Horizontal lines are a reference for the **NAT** compound.

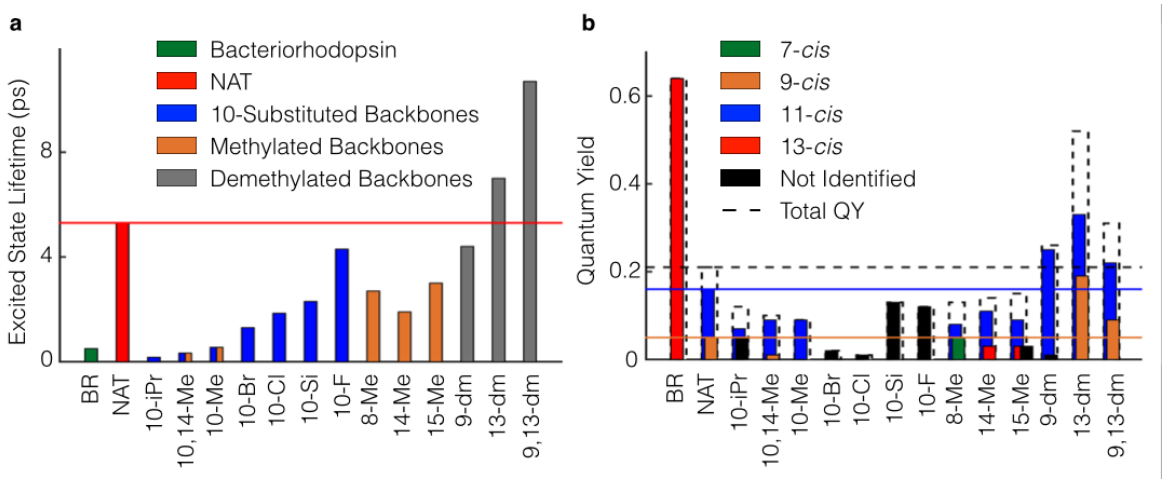

Figure 3.3.1 Comparison of (a) ESLs and (b) QY for RPSB derivatives. Colouring indicates the type of backbone modification in (a) and the identity of photoproduct in (b). Horizontal lines serve as reference for the values found for **NAT**. Reproduced in part from Bassolino et al., *J. Am. Chem. Soc.*, 2014, **136**, 2650. Copyright 2014 American Chemical Society.

Inspection of these two figures reveals a correlation between the ESL and the isomerisation QY for the solution photochemistry: longer ESLs tend to correspond to higher QYs, and *vice versa*. This observation is in striking contrast with the trend for BR, for which efficiency

and lifetime were found to be independent,[24,88,89] and suggests that for each pathway the height of the excited state barrier might affect the crossing efficiency at the CI. A way of representing this correlation is shown in Figure 3.3.2 for a single de-excitation pathway.

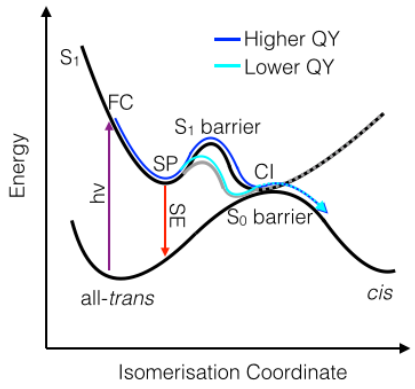

Figure 3.3.2 Schematic for a typical *trans-cis* isomerisation pathway. Indicated are the Franck Condon (FC) region, the stationary point (SP), the conical intersection (CI) together with the two barriers (in S_1 and S_0) encountered along the isomerization coordinate. Two S_1 barriers of different height are shown in different colours, and labeled according to their photoisomerisation efficiency.

The FC region of the all-*trans* configuration in the S_1 PES is initially populated by an excitation pulse (purple arrow). From there, a rapid relaxation follows likely along backbone stretching coordinates[92,93] towards a SP where it encounters an excited state barrier. Ruhman's[139] and Zgrablic's[134] population control experiments on BR and **NAT** have shown that at the SP the photochemically active double bonds have not yet isomerised. In the representation of Figure 3.3.2, the height of the S_1 barrier determines the crossing point between the PESs of S_1 and S_0 states, generating a second, "spectroscopically silent", barrier in the proximity of the CI, that the system has to overcome in order to complete the photoisomerisation. The higher this second barrier is, the lower will be the probability of crossing it, thus generating a qualitative correlation between the height of the SP barrier, the crossing point between the two PESs and the photoisomerisation efficiency. The PESs drawn in the Figure 3.3.2 do not arise from computational work. Even though the way the CI is

depicted in Figure 3.3.2 is unusual it offers an intuitive and qualitative way of explaining the observed relationship between ESL and QY.

The data in Figure 3.3.1 help to further clarify this model, more specifically concerning the origin of the observed effects of substitution on photoreactivity. The ESLs for the 10-substituted derivatives steadily decrease when adding larger and more polarisable groups, moving down along the halogen group (**10-F**, **10-Cl**, **10-Br**) as well as with alkyl substituents, when exchanging hydrogen with methyl and *iso*-propyl groups (**NAT**, **10-Me**, **10-iPr**). Considering the charge transfer character of the first singlet excited state[90,91] it is not unreasonable to imagine that substituents interact with a moving electronic density or, equivalently, developing partial positive or negative charges, not only towards the β-ionone ring moiety but also at the Schiff base end of the polyenic chain. The more polarisable the substituent, the stronger this interaction would be. In other words, the more reactive case in Figure 3.3.2 would apply for backbones where polarisable substituent(s) have been removed (i.e., de-methylated products), whilst the less reactive case would corresponds to derivatives with added substituents.

A computational work on model RPSBs has been reported proposing that addition of methyl groups along the backbone significantly reduces the ESL in water when compared to non-methylated derivatives, and attributed this effect to a more efficient deactivation of the methylated derivatives upon reaching the crossing seam.[140] Even though no mention was made about the photoreaction efficiency, another point is made in the same work recalling papers by other researchers[141,142] about the effect of the solvent on the CI topography, with water shifting it towards a more *peaked* rather than *sloped* character (Figure 3.3.3). This aspect is highly relevant for the reaction efficiency as well as the ESL, as a previous computational study[143] linked the CI topography with reaction yield and selectivity, recognising a peaked CI as leading to more photoproduct and potentially faster excited state deactivation. The picture emerging from these studies agrees only partially with the ESLs and QYs results

reported above: if it is true that methylation accelerates the excited state decay, it does so at the expense of the reaction efficiency.

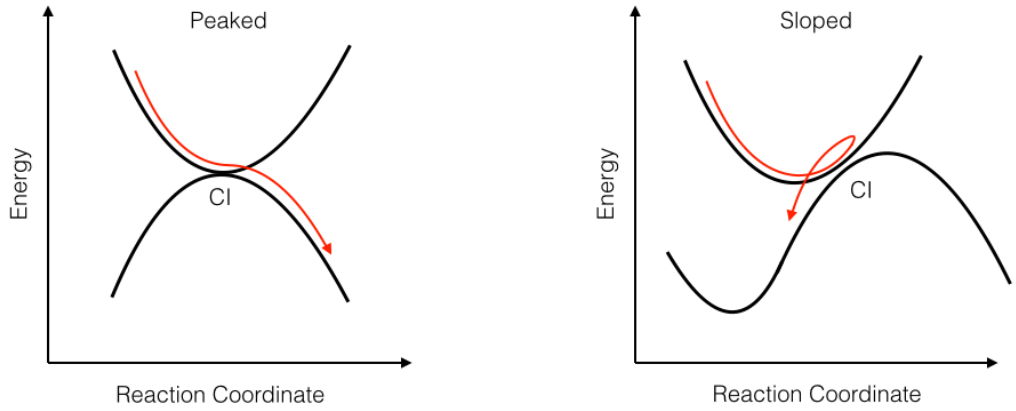

Figure 3.3.3 Effect of CI topography on the photoisomerisation outcome. The peaked case is more likely to lead to a successful photoreaction than the sloped one. Figure modelled on Figure 1 of reference 137.

It was already discussed in Section 3.2.2 how the position of substituents along the backbone is a powerful handle to tune the reaction selectivity, activating or deactivating isomerisation pathways with a greater effect closer to the modification site. The barrier-tuning mechanism just described can qualitatively explain the changes in selectivity, as shown in Figure 3.3.4-6 and discussed below.

A possible scenario for **NAT** is shown in Figure 3.3.4a and b. Once the system has reached the SP region, at least four pathways are available leading to each of the possible *cis* isomers, indicated in the Figure 3.3.4a as coloured arrows. The branching at the SP region agrees with the model proposed by Gai et al.[24] and with the backbone still being in an overall "all-*trans*-like" configuration.[134,139] The selection between the "active" channels would be kinetic in origin, based on the relative heights of the excited state barriers,[24] represented as black circles along the pathways. The efficiency of photoproduct formation would depend, instead, on the height of the barrier (amaranth circles) encountered in the CI region (red dots) on the ground state surface. This is an important difference with the model proposed for BR,

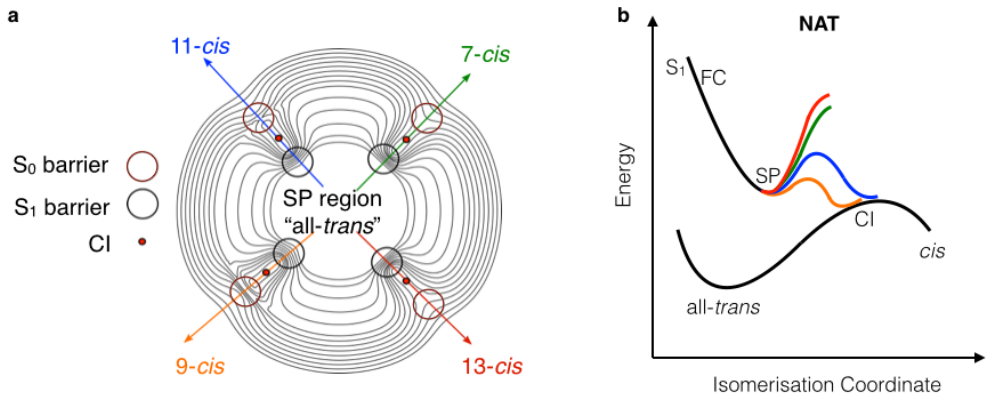

Figure 3.3.4 Multidimensional picture of **NAT** photoisomerisation pathways. Within the Figure, the colours of the arrows are isomer specific: green for 7-*cis*, orange for 9-*cis*, blue for 11-*cis* and red for 13-*cis*. (a) Multidimentional representation of the SP region in the excited state potential energy surface for **NAT**. The S_1 and S_0barriers are shown as black and amaranth circles, respectively, with the CI region being marked as a red dot. (b) 2D representation for **NAT** of the pathways shown in (a). Reproduced in part from Bassolino et al., *J. Am. Chem. Soc.*, **2014**, 136, 2650. Copyright 2014 American Chemical Society.

but is required to take into account the correlation between ESL and QYs found in solution but not in the protein.

Figure 3.3.4b is a different representation of the same scenario shown in Figure 3.3.4a. From the SP at least four pathways indicated by solid lines lead to the several possible *cis* isomers colour coded in the same way as in Figure 3.3.4a. The S_1 barrier encountered along two of them (7-*cis* and 13-*cis*, green and red, respectively) is too high for those channels to be competitive over the 11-*cis* (blue) and 9-*cis* (orange) pathways. The latter might be slightly favoured in the kinetic competition at the SP, but is likely to encounter a higher barrier to complete the photoisomerisation, leading to a relatively poor QY for 9-*cis* (5%, vs. 16% for 11-*cis*).

Figure 3.3.5 shows what could happen to the energy barriers upon methylation at C14 or C15. By addition of a more polarisable substituent, the barriers would be lowered as discussed in Figure 3.3.2, with a strongest effect expected for the pathway leading to the 13-*cis* isomer, closer to the modification site. In the figure, both pathways for the **NAT** backbone (solid lines) and methylated backbones (dashed lines) are shown for comparison.

Compound	ESL (ps)	PP1 (QY)	PP2 (QY)
NAT	5.4	11-*cis* (0.16)	9-*cis* (0.05)
14-Me	1.9	11-*cis* (0.11)	13-*cis* (0.03)
15-Me	3.0	11-*cis* (0.09)	13-*cis* (0.03)
8-Me	2.7	11-*cis* (0.08)	7-*cis* (0.05)

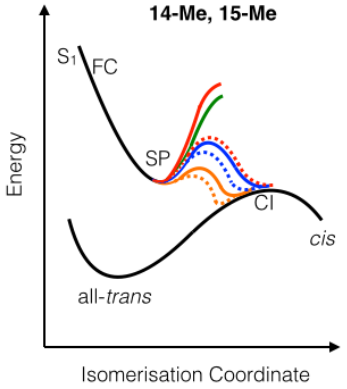

Figure 3.3.5 Effect of methylation on the isomerisation pathways for the **14-Me** and **15-Me** derivatives. The table reports the ESLs and QYs for the compounds discussed. The pathways are colour-coded according to the isomer formed as in Figure 3.3.4. Reproduced in part from Bassolino et al., *J. Am. Chem. Soc.*, 2014, **136**, 2650. Copyright 2014 American Chemical Society.

For the methylated compound, 9-*cis* would still be the preferred channel at the SP region, but would exhibit an even lower QY due to the higher second barrier, eventually becoming undetectable. The efficiency of 11-*cis* isomer formation would also be expected to decrease, as indeed is observed (QY of 9-11%). A new pathway must have become competitive, though, as shown by the appearance of 13-*cis* as a secondary photoproduct (QY of 3%). Within the proposed barrier-tuning mechanism, the low yield for 13-*cis* could have two possible origins, differing by the degree of reduction of the corresponding excited state barrier. In one scenario, the barrier could be lowered as shown in the figure, leaving the channel still not favoured at the SP branching but making it sufficiently competitive (in kinetic terms) with the other two while rendering it very successful in completing the isomerisation trajectory due to a very low ground state barrier. On the other hand, the barrier could be lowered somewhere in between the S_1 barriers for 11-*cis* and 9-*cis* pathways, favouring it even more in the kinetic competition, but losing efficiency at the CI crossing stage. Due to the lack of data that would enable us to follow the formation kinetics of the individual isomers, it is not possible to discriminate between these two situations. Time resolved vibrational spectroscopy could potentially help resolving this question, depending on the availability of well-isolated

isomer-specific marker bands. An almost identical reasoning, swapping the role of 13-*cis* pathway with the 7-*cis* one, would explain the product distribution observed for **8-Me**.

Compound	ESL (ps)	PP1 (QY)	PP2 (QY)
NAT	5.4	11-*cis* (0.16)	9-*cis* (0.05)
9-dm	4.4	11-*cis* (0.25)	N.I. (0.01)
9,13-dm	10.7	11-*cis* (0.22)	9-*cis* (0.09)
13-dm	7.0	11-*cis* (0.33)	9-*cis* (0.19)

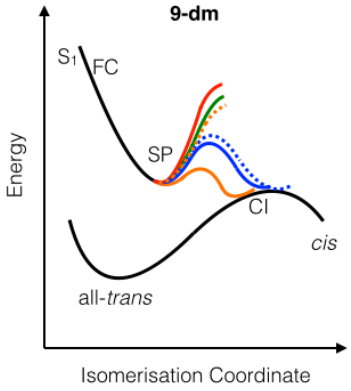

Figure 3.3.6 Effect of demethylation on the isomerisation pathways. The table reports the ESLs and QYs for the compounds discussed. The pathways are colour-coded according to the isomer formed as in Figure 3.3.4.

Thinking along similar lines, with the scheme in Figure 3.3.6 it would be possible to explain the selectivity for **9-dm** or the increase in QY of **13-dm** and **9,13-dm**. Removal of a methyl group from the C9 is expected to make all excited state barriers rise, with the greatest effect for the 9-*cis* pathway, and this probably happens to the extent of inhibiting its formation whilst promoting the 11-*cis* isomer. Comparison of the results for **13-dm** and **9,13-dm** reveals another limitation of the suggested model: even though the latter derivative presents an higher ESL, the total photoisomerisation QY and the QYs for the formation of the individual isomers are lower than the ones measured for the singly demethylated derivative. This could be explained by the presence of a non-reactive channel becoming competitive once the reactive pathways gets excessively slowed down, but, once again, further experimental proofs of this hypothesis would be needed.

The proposed model is not meant to be complete or exhaustive, yet allows a simple rationalisation for most of the results observed for the solution photochemistry of backbone substituted RPSBs. Its extension to the protein photochemistry is not straightforward: while tuning the excited state barriers is a means to changing the photoisomerisation selectivity,[24]

within the presented results a coupling was observed between the ESLs and the reaction efficiencies which has not been observed before for BR mutants. This suggests that the role of the protein might not be limited to tuning the barriers in the SP region, but would affect the CI topography as well. Concerning the mechanism(s) of tuning the photochemistry, the presented results suggest an interaction of the polarisable substituents with a moving electronic density along the polyenic backbone. It has already been noted that in the retinal binding pocket there are several aromatic polarisable residuals[144] and that the pocket sequence is the most conserved region among different opsins.[15]

Considering briefly (a few) other members of the vast microbial opsin family, it should be mentioned that significant variations in photoreaction dynamics and quantum efficiency have been reported, and no immediate or clear correlation can be found between the two values for different proteins. For example, amongst the four opsins found in *Halobacterium Salinarium*, a photoisomerisation quantum yield of 30% has been measured for halorhodopsin[145], whilst for the two sensory rhodopsins (SRI and SRII) values in the range 0.4-0.5 have been reported.[146,147] An equal significant variation in isomerisation dynamics has been found: whilst SRII reacts on a comparable timescale to BR,[148] an excited state decay with time constants on the order of 5 and 33 ps has been observed for SRI,[148] whilst for halorhodopsin from *Halobacterium Salinarium* a 1.5 ps isomerisation time constant has been determined by probing the femtosecond transient absorption in the mid-IR range.[149] The same study proved that in the case of halorhodopsin, a branching in the excited state population takes place, and that the photoproduct is formed only for the initial part of the excited state lifetime.[149] This scenario is similar to the one proposed for **NAT** in solution by Zgrablic et al.,[134] but seems to be more the exception than the rule amongst the microbial opsins. The groups of Kandori and Tahara in their studies of a variant of halorhodopsin from *Natronomonas Pharaonis* suggested a similar branching to take place,[150] but their hypothesis was later disproved by a population control experiment by Ruhman et. al[151]. The study of Kandori'

and Tahara's group is of particular interest within this dissertation because while studying the effect of the halide ion on the *Natromonas pharaonis* halorhodopsin, they found an inverse correlation between excited state lifetime and photoisomerisation yield, with the iodide having the longest lifetime and the highest quantum efficiency.[150] Whilst the population control experiment supports a reaction scheme similar to BR, i.e., a three-state model without branching during the evolution on the excited state (Figure 3.1.3), the correlation between ESL and QY for the halide series might suggest that in the case of halorhodopsin the height of the excited state barrier determines the crossing point with the ground state surface (Figure 3.3.2), in a similar way to what observed for RPSB in solution but not in BR.

Even though the finest details are still unclear, this work suggests that tuning of the photochemical properties of the RPSB is achieved through non-bonded, electrostatic interactions between the chromophore and the surrounding amino-acids.

3.4 Conclusions

The solution photochemistry of a series of analogues of all-*trans* RPSBs has been investigated by means of NMR and TA spectroscopy. The effects of structural modifications on the polyenic chain in terms of ESL, photoisomerisation QY and selectivity have been reported. All three parameters were found to be affected by the presence of polarisable substituents: a correlation was observed between an average excited state decay time constant with photoisomerisation efficiency, while new reactive channels leading to different isomers than the ones occurring for the native backbone were activated. On the basis of these results, it was suggested that the photoproduct distribution is determined by kinetic competition between different reactive pathways in the excited state, with the outcome depending on the height of the barriers encountered along each isomerisation coordinate. To explain the correlation with the reaction efficiency, the height of the barriers on which the ESL depends should also determine the crossing point with the ground state PES, and, consequently, the height of a

second barrier that would need to be overcome to complete the photoisomerisation. The height of the first barrier would be inversely proportional to the second one, thus explaining the relatively low reaction efficiency of the faster decaying derivatives. The presence of polarisable substituents along the polyenic chain seems to be able to alter the excited state barriers, and, consequently, the photoproduct formation efficiency and selectivity. Whereas the presence of polarisable residuals in the BR pocket where the retinal chromophore is bound supports the idea of photochemical tuning via non-bonded electrostatic interactions, the observed independence of reaction speed and efficiency in the opsin environment suggests that the topology of the CI region must be somewhat different from the one encountered in solution.

Chapter 4

RPSB II: The 11-*cis* to all-*trans* photoisomerisation

Overview

This chapter probes whether and to which degree the model found for all-*trans* retinal protonated Schiff base (RPSB) photoisomerisation discussed in Chapter 3 can be extended to the 11-*cis* to all-*trans* photoreaction, in the light of the existing experimental evidence supporting a high degree of similarity between the two processes. The photochemistry of two derivatives with added substituents at the C10 position is investigated and whilst a reduction in the excited state lifetime (ESL) is observed, the isomerisation quantum yield (QY) is found to be unaffected. Prompted by this evidence and the possible existence of an ultrafast channel suggested by transient absorption (TA) data, the photoproduct formation dynamics for the native backbone for all-*trans* and 11-*cis* RPSBs in solution is followed with a population control experiment. The results are compared with analogous measurements for bovine rod rhodopsin (RHO), and support the existence of an intrinsic ultrafast reactive channel for the 11-*cis* to all-*trans* photoisomerisation reaction independently of the environment. This is in striking contrast with the idea currently held that the role of the protein is to speed up the

isomerisation rate significantly affecting the excited state potential energy surface (PES). The work presented in this chapter is being included in a forthcoming publication. Retinals with modified backbones have been prepared by Tina Sovdat. The TA measurements have been performed by Matz Liebel and Christoph Schnedermann, the population control experiments by Alex Duarte and Jong Min Lim. All NMR experiments but ^{1}H spectra have been acquired with the assistance of Barbara Odell or Tim Claridge. Measurements of the reaction yields and all data analysis and interpretation have been done by the author.

4.1 11-*cis* RPSB photochemistry in rhodopsin and in solution

RHO is considered to be the benchmark protein for the type II opsin family. RHO is found in the rod outer segment cells, and is the primary photoreceptor responsible for dim light vision.[33] Due to its central role in the vision process, a huge amount of experimental effort has been directed towards understanding the mechanism of the ultrafast and efficient photochemistry observed.[14,16] Amongst the visual pigments, RHO is the most extensively studied, probably due to its easier purification from the rod outer segment cells as compared to the colour visual pigments from the cones.[16] Similarly to what was done in the previous chapter, the *n*-butylamine (nBu) protonated Schiff base (PSB) of the 11-*cis* isomer in MeOH is taken as a model for the solution photochemistry (Figure 4.1.1).

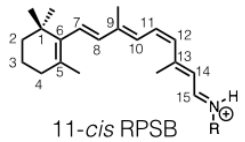

Figure 4.1.1 11-*cis* RPSB. In RHO R= Lys, in MeOH R= butyl

The light-induced dynamics of 11-*cis* RPSB in solution has been reported to be very similar to that for the all-*trans* isomer. They show similar absorption maxima in MeOH (442

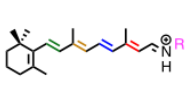

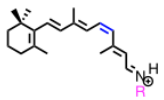

	BR	*n*Bu (MeOH)	RHO	*n*Bu (MeOH)
R	Lys	*n*Bu	Lys	*n*Bu
abs λ_{max} (nm)	568	440	498	440
Excited State Lifetime (ps)	0.5	4.3	~0.05	4.0
Product (QY)	13-*cis*(0.64)	11-*cis*(0.16) 9-*cis* (0.05)	all-*trans* (0.65)	all-*trans* (0.19)

Table 4.1.1 Comparison of RPSBs photochemistry in opsins and solution. Reproduced in part from Bassolino et al., *J. Am. Chem. Soc.*, 2014, **136**, 2650. Copyright 2014 American Chemical Society.

vs. 445 nm for 11-*cis* and all-*trans*, respectively) with the molar extinction coefficient being half in the case of the 11-*cis* isomer (51800 vs 23300 L mol^{-1} cm^{-1}).[25] A change in dipole moment upon excitation suggests a charge transfer character of the optically active excited state,[90] further supported by computational studies.[91] Fluorescence decay, a signature of excited state population, is multi-exponential with a 0.1 – 0.6 ps and a 2 – 7 ps component in the 605-695 nm range.[37,152,153] The complex decay kinetics observed have been attributed to environment inhomogeneity,[37] and are on the same timescale of the one observed for all-*trans* RPSB.[78] The photoisomerisation reaction is highly selective yielding only the all-*trans* isomer. QY values have been reported in 0.19-0.26[25,26] range, without significant variation with excitation wavelength.[126] When bound to opsin, the absorption maximum shifts to lower energy (498 nm),[14] the QY increases three-fold (0.65),[34] and, most significantly, the photoisomerisation has been shown to complete on the 200 fs timescale.[35,36] This process is even faster than the all-*trans* —> 13-*cis* isomerisation in bacteriorhodopsin (BR, 500 fs).[23,24] A comparison of the photochemistry for 11-*cis* RPSB in the protein and in solution is shown in Table 4.1.1, together with the data for all-*trans* RPSB in MeOH and BR already shown in Table 3.1.1.

4.1.1 Current understanding of the 11-*cis* to all-*trans* photoisomerisation

Initial evidence for the isomerisation in the protein environment taking place on an ultrafast timescale originated from trapping of photointermediates at low temperatures and picosecond time-resolved TA studies;[16] specifically, the latter were not able to resolve the formation of bathorhodopsin within the time resolution of the experiment. Further support to the sub-picosecond isomerisation came from measurements of fluorescence QY[154] and resonant Raman intensity analysis.[155] In 1991 Schoenlein et al.[35] published the first TA study of RHO with ∼40 fs time-resolution, finding that formation of the primary intermediate photorhodopsin is complete within the first 200 fs. The presence of low-frequency oscillations assigned to the photoproduct was taken as an evidence of the coherent nature of the isomerisation process, and its speed as an indication of unconstrained motion within the protein pocket.[156] Femtosecond stimulated Raman spectroscopy[157,158] helped proving the central role played in the photoreaction by hydrogen-out-of-plane modes in leading the excited system towards the conical intersection (CI) with the ground state. High time resolution TA in the near IR region down to 1020 nm was able to follow the movement of the photoexcited system towards and after crossing the CI by monitoring the disappearance of the stimulated emission (SE) and the subsequent appearance of the photoproduct absorption.[159]

Analogous to BR, the extremely high reaction rate observed for the isomerisation reaction prompted suggestions that the evolution in the protein environment proceeds on a barrierless excited state PES (*two-state*, two modes model,[35] Figure 4.1.2).

In RHO, in contrast to BR,[83] the emission maximum has been reported to shift with the excitation wavelength, suggesting that the fluorescence originates from a non-stationary state,[160] in agreement with a continuous evolution of the system towards the CI. Computational studies found, similarly to what has been reported for BR, an ultrafast decay of the excited state evolving initially along stretching coordinates of the retinal backbone followed

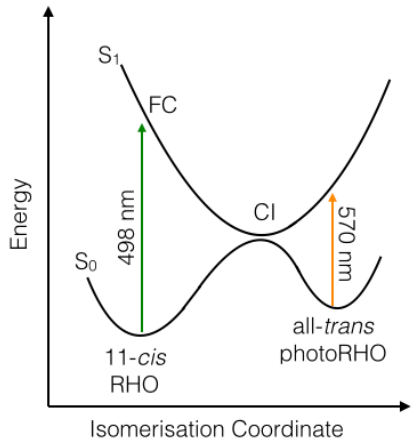

Figure 4.1.2 Two-state model for RPSB photoisomerisation in RHO. The absorption maxima of RHO and the primary photoproduct, photorhodopsin, are indicated as green and orange arrows, respectively. FC: Frank Condon region. CI: Conical Intersection.

by coupling to the torsional modes leading to the formation of the isomerised product.[95] Other aspects determining the isomerisation outcome such as the role of the hydrogen out of plane vibration phase at the moment of crossing the CI,[161,162] the pre-twisting of the backbone[163] or the solvent friction[141,142] have also been investigated computationally.

When comparing all-*trans* RPSB photochemistry in solution and in BR it is possible to envision a general mechanism of tuning the isomerisazion efficiencies and rates for the several possible photoproducts by affecting the heights of the excited state barriers encountered along each reactive path, as proposed by Gai et al.[24] and in Chapter 3 of this dissertation. Doing the same for 11-*cis* RPSB in solution and in RHO is not straightforward without invoking a substantial effect of the protein environment on the excited state PES. Becker's suggestion[126] that the photoisomerisation of 11-*cis* in the two environments follows similar picosecond kinetics, thus excluding the need of special remodelling of the PES by RHO, was advanced three years before direct evidence of the femtosecond time-scale of the isomerisation reaction in opsin. Taking, as was done by both experimentalists and theoreticians, the observed picosecond fluorescence decay as a measure of the photoisomerisation rate[37,91,95,152,164,165] left

the scientific community with the need to reconcile the ultrafast and barrierless photoreaction in the protein with the much slower one in solution.

It was first proposed that the presence of a stationary plateau (and possibly small barriers)[166] corresponding to the region of the excited state PES where energy is transferred between two coordinates (backbone stretching and torsions) leading to the CI might explain the complex and slower decay in solution. Within the protein environment, due to electrostatic and steric interaction, the extension of said plateau would be reduced or disappear to yield the barrierless and ultrafast evolution suggested by time resolved spectroscopy.[135] In the last two years, computational studies on 11-*cis* RPSB models have been published for the gas phase photoisomerisation that found a barrier along the isomerisation coordinate in the excited state,[167] or retrieving remarkably similar minimum energy pathways when starting from the all-*trans* or 11-*cis* isomer.[96]

As already mentioned in Chapter 3, the preparation of pigment analogues with isotopically labeled and/or structurally modified retinals has been pursued to assign the Raman spectra of RHO and its photointermediates to provide structural information,[168–173] and to explore the role of steric interactions between the chromophore and the opsin protein.[101,102,164,174] Within this second type of studies, QYs and sometimes kinetics were reported for RHO analogues prepared with (de)methylated or fluorinated retinals (Table 4.1.2), and conclusions have been drawn about the chromophore-protein interactions on their basis, like the importance of the ring methyl groups for pigment formation[101] or the presence of potential hydrogen donor groups in the closeness of H10.[115]

To the best of my knowledge, amongst the derivatives of Table 4.1.2, only for the **13-dm** derivative the photochemistry of the protonated Schiff base has been investigated separately from the protein environment,[129] yielding results not too dissimilar from the native backbone under similar irradiation conditions. Yet, it was shown in Chapter 3 for the all-*trans* isomer that structural modification of the type reported in Table 4.1.2 can dramatically affect

Chromophore	Quantum Yield	Ref
NAT	0.65	A
8-F	0.6	B
10-F	0.65	B
10-Cl	0.33	B
10-Me	0.32	B
10-Me,13-dm	0.59-0.46	C
11-Me	0.28	D
11-Me,13-dm	0.18	D
12-F	0.47	E
12-Me	0.54	D
13-dm	0.3-0.5	D,F,G,H
13-Et	0.52	I
14-F	0.51	B
14-Me	0.55	I

A. Kim J.E., et al., *Biochemistry*, **2001**, *40*, 13774
B. Liu, R.S.H. et al., *Biochemistry*, **1986**, *25*, 7026
C. Koch, D. and Gärtner, W., *Photochem. Photobio.*, **1997**, *65*, 181
D. Verhoeven M.A., et al., *J. Mol. Biol.*, **2006**, *363*, 98
E Bovee-Geurts P.H.M. et al, *J. Am. Chem. Soc.*, **2009**, *131*, 17933
F. de Grip, W.J. et al., *Pure Appl. Chem.*, **1997**, *69*, 2091
G.Nelson R., et al., *Proc. Natl. Acad. Sci USA.*, **1970**, *66*, 531
H.Gärtner, W. and Ternieden, S., *J. Photochem. Photobio. B*, **1996**, *33*, 83
I. Karnaukhova E., et al., *Bioorg. Chem.*, **1999**, *27*, 372

Table 4.1.2 Quantum yields of RHO analogues with structurally modified retinals.

the photoreactivity of RPSBs in solution. As no QY data are available for the BR pigment analogues, no comment can be made on the effect of these changes in the protein environment. On the other hand, if the photoisomerisation reaction for the 11-*cis* isomer presents features similar to the all-*trans* one as generally accepted, the results in Table 4.1.2 would be due to a combination of chromophore-protein interactions and changes to the chromophore reactivity caused by the structural modification.

Prompted by the considerations exposed above, a photochemical study like the one described in Chapter 3 was conducted for the 11-*cis* isomers of the modified retinal derivatives shown in Figure 4.1.3.

Native (**NAT**) 11-*cis* retinal was obtained as a generous donation from Dr. Crouch of the National Eye Institute, National Institutes of Health. The preparation of the retinal derivatives presented in this and the previous chapter has been the subject of the DPhil dissertation of Tina Sovdat. Characterisation data (NMR and high resolution mass spectra) are reported

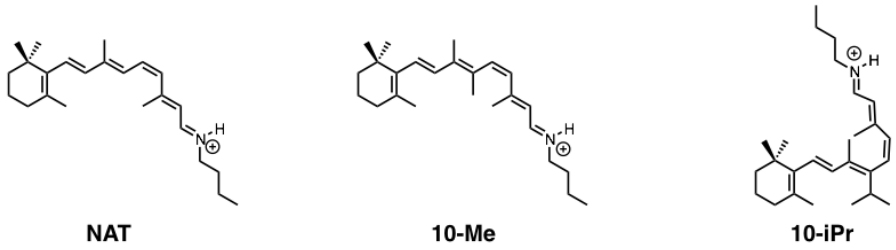

Figure 4.1.3 Structures of the 11-*cis* derivatives with modified backbones.

in Appendix B for the protonated Schiff bases only, as relevant for the photochemical studies. Rhodopsin samples were isolated from bovine retinas following previously published protocols, as described in Appendix B.[175,176]

4.2 Photochemical characterisation

Similar photochemical studies to the ones described in Chapter 3 have been conducted for the 11-*cis* isomers of the **NAT**, **10-Me** and **10-iPr** RPSBs.

4.2.1 Transient absorption and excited state lifetime

TA data for RPSBs were recorded in MeOH solution with optical densities at the absorption maximum of 0.7-1 in a 200 μm thick flow cell. Compressed $\sim$20 fs excitation pulses centred at 500 nm and a chirped broadband white light in the 530-900 nm region were used to perform TA. The pulses were scanned from negative (–500 fs) to positive time delays sufficient to completely describe the decay of the SE band in the spectral region below 650 nm (23 ps for 11-*cis* **NAT**). The probe chirp was corrected for by measuring a trace of pure solvent.[58] Chirp-corrected TA maps for all the derivatives are shown in Figure 4.2.1.

Data were analysed with the same global optimisation routine presented in Chapters 2 and 3, employing three to four exponential decay functions (Equation 2.2.7) together with a

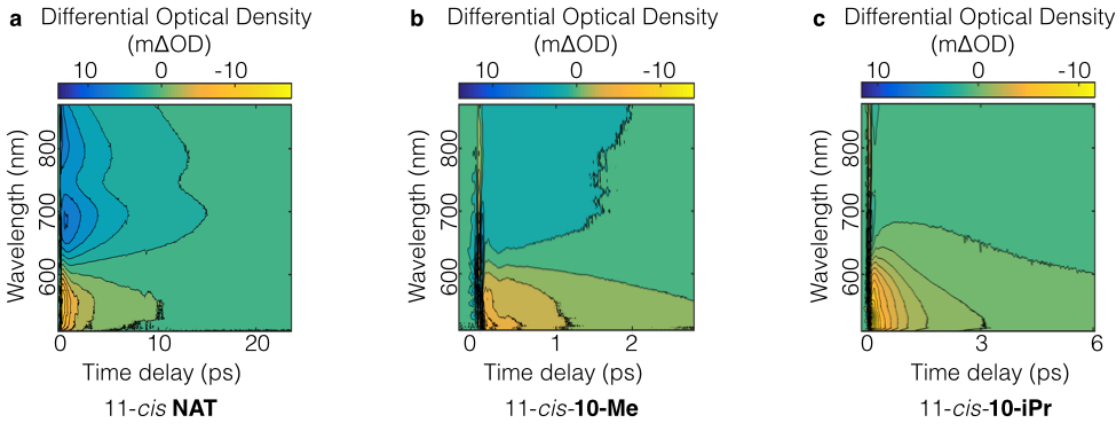

Figure 4.2.1 Transient absorption maps for 11-*cis* (a) **NAT**, (b) **10-Me**, and (c) **10-iPr**.

coherent term modelled as a sum of Gaussian derivatives from 0^{th} to 8^{th} order to describe the response generated by the overlapping of the pump and probe pulses.[58]

$$f_i(t) = IRF \otimes e^{-\frac{t}{\tau_i}} = e^{-\frac{t-t_0}{tau_i}} \cdot \text{erfc}\left(-\frac{t-t_0}{\sigma} + \frac{\sigma}{2\tau_i}\right). \tag{2.2.7}$$

For all the compounds, an ESL for each wavelength was defined according to Equation 3.2.2 as a weighted average of the time constants retrieved from the global optimisation in the spectral region of the stimulated emission band and by fitting the band integral obtained in the same region as described in Chapter 3 .

$$ESL(\lambda) = \frac{\sum_i \tau_i |DADS_{i\lambda}|}{\sum_i |DADS_{i\lambda}|}. \tag{3.2.2}$$

Results of the global optimisation and the ESLs are reported in Table 4.2.1.

The analysis of the TA data and definition of the ESL for the 11-*cis* isomers proved to be more complicated than in the all-*trans* case. The data set for 11-*cis* **NAT** was originally fitted with a coherent term and three exponential decays, yielding an ESL of 3.99 ps. A slightly better fit could be obtained by reducing the orders of Gaussian derivatives included

Compound	Absorption Maximum	τ_1 (ps)	τ_2 (ps)	τ_3 (ps)	τ_4 (ps)	Range eval. (nm)	IDADSI ESL (ps)	BI ESL (ps)
NAT	446	0.30 0.27	2.0 2.2	6.8 6.8	0.062	680-880	4.0[a] 3.1	5.3±0.2
10-Me	430	0.057	0.66	1.9		700-875	0.84[a] 0.27	0.8±0.1[b]
10-iPr	434	0.12	0.49	2.1		730-870	0.49	0.31±0.02[b]

[a] Evaluated without including τ_1
[b] Results of monoexponential fit

Table 4.2.1 Global fit results and ESLs for 11-*cis* RPSBs.

and addition of a fourth, ultrafast (0.062 ps) time constant. The ESL obtained with the four time constants is 3.12 ps. The tri-exponential and tetra-exponential fits are compared at representative wavelengths and time delays in Figure 4.2.2.

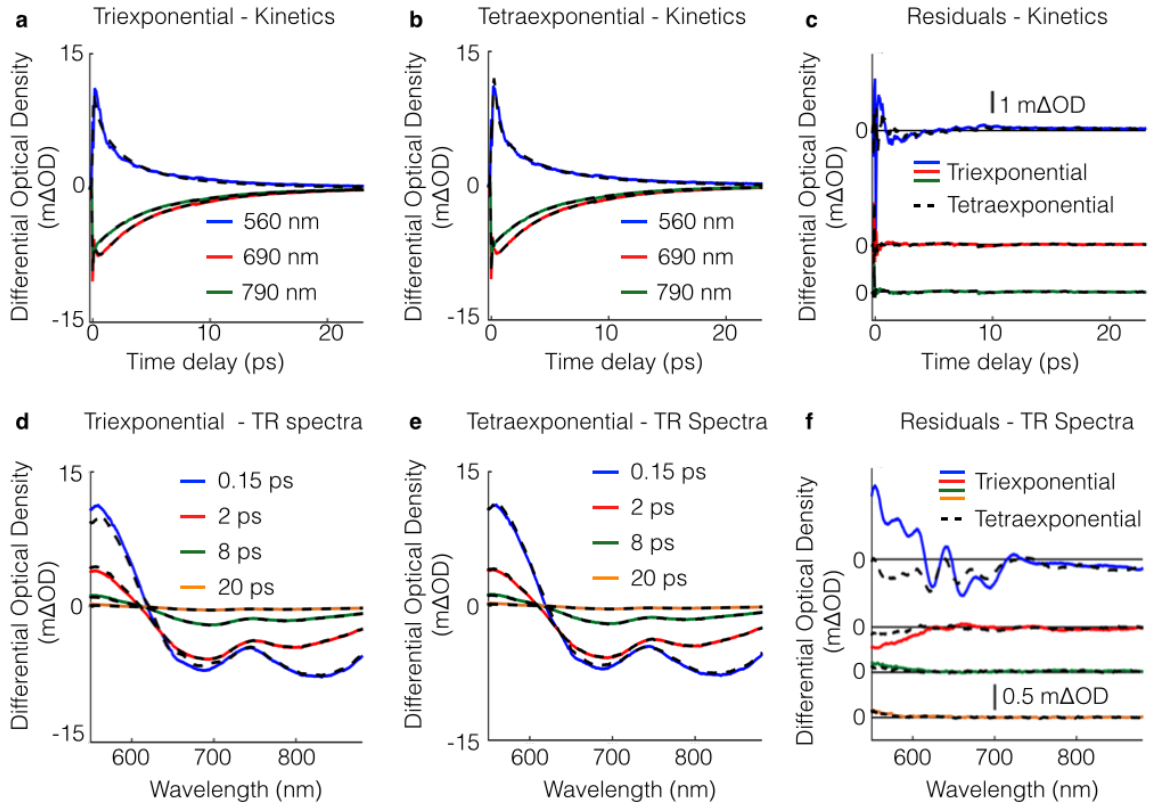

Figure 4.2.2 Comparison of the tri-exponential (a,d) and tetra-exponential (b,e) fit for 11-*cis* **NAT**. Kinetics (a,b) and transient spectra (d,e) at selected wavelengths and time delays. Experimental data are plotted as solid coloured lines, the corresponding fits as black dashed lines. In (c) and (f) are shown the residuals of the kinetics and transient spectra, respectively. The residuals of the tri-exponential fit are plotted as solid coloured lines, with the corresponding residuals of the tetra-exponential fit on top as dashed black lines. The same colour-code as in plots (a-d) is used.

For the other two derivatives, **10-iPr** and **10-Me**, the early time points were significantly affected by the coherent artefact due to the low concentration of the available sample. Cuts at representative wavelengths comparing the solvent only trace (red) with the compound data (light blue) are shown in Figures 4.2.3 and 4.2.4 for **10-Me** and **10-iPr**, respectively.

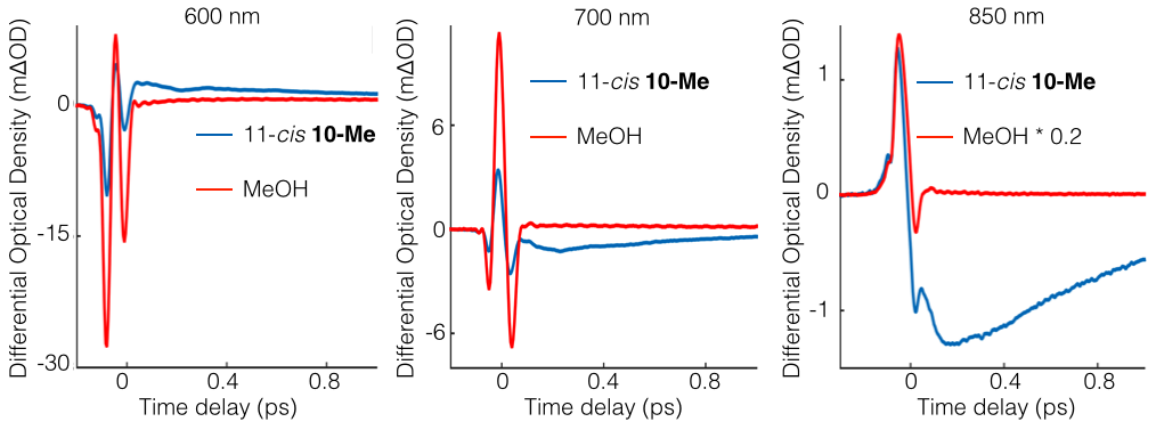

Figure 4.2.3 Comparison of solvent only (red) and 11-*cis*-**10-Me RPSB** transient absorption data (light blue) at selected wavelengths.

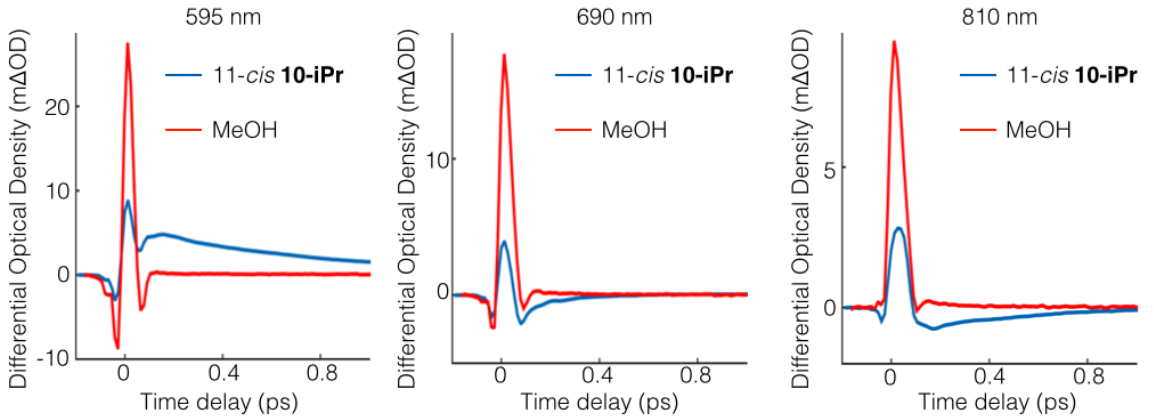

Figure 4.2.4 Comparison of solvent only (red) and 11-*cis*-**10-iPr RPSB** transient absorption data (light blue) at selected wavelengths.

For **10-iPr** the first retrieved time constant (0.12 ps) seemed to be mainly determined by the dynamics of the system, but "contamination" from the coherent response cannot be ruled out. In the **10-Me** case, modelling of the solvent response was not as successful and the extremely small value of the short time constant retrieved (0.06 ps) could be due to a

much higher degree of contamination from the coherent artefact. The |DADS| averaged ESLs evaluated including and excluding the shortest time constant are 0.26 and 0.85 ps, respectively. Even though in absolute terms there is a significant difference between the two, the expected trend of reduction of the ESL upon methylation of the backbone is true irrespective of what values are considered for the **NAT** and **10-Me** derivatives. On the other hand, the question remains whether the very short time constants retrieved have a physical origin different than data analysis artefacts.

4.2.2 Quantum yields and photoproducts identification

Continuous wave (CW) irradiations were performed in a fashion similarly to those previously described. Solutions in MeOD ($\sim$3 mM) were irradiated under magnetic stirring in a 4 mL pyrex tube. Illumination was performed with a 532 nm CW laser (0.2 mW) whose beam was expanded to a maximum diameter of $\sim$0.7 cm, for its section to be still completely contained within the pyrex tube. As for the all-*trans* isomers, the OD of the solutions was high enough to consider complete absorption of incident photons. The photoisomerisation QYs reported in Table 4.2.2 were evaluated as the ratio between the number of photoproduct molecules formed and the number of photons absorbed according to Equations 2.1.3–5

$$\mathrm{QY} = \frac{M_{\mathrm{photo}}}{N_{\mathrm{Ph,abs}}}, \tag{2.1.3}$$

$$N_{\mathrm{Ph,abs}} = N_{\mathrm{Ph,inc}} = \frac{P_{\mathrm{inc}} \cdot t_{\mathrm{irr}} \cdot \lambda_{\mathrm{irr}}}{hc}, \tag{2.1.4}$$

Compound	Photoproduct	QY
NAT	all-*trans*	0.19
10-Me	all-*trans*	0.20
10-iPr	all-*trans*	0.16

Table 4.2.2 Results of QY measurements for 11-*cis* RPSBs.

$$M_{\text{photo}} = [\text{Sample}] \cdot V_{\text{irr}} \cdot F_{\text{photo}} \cdot N_{\text{A}}. \tag{2.1.5}$$

For all derivatives only the all-*trans* photoproduct was observed, as confirmed by comparison of the relevant ^{1}H NMR spectra (see Appendix B).

When evaluating the amount of photoproduct formed, it was necessary to take into account that some all-*trans* was produced spontaneously during the condensation step to obtain the Schiff base. In the case of **NAT** and **10-iPr**, it was sufficient to measure the ^{1}H NMR spectrum of a non-irradiated control sample before and after the ^{1}H NMR of the irradiated mixture. As shown in Figure 4.2.5 for **NAT**, no significant changes were detected in the intensity of the all-*trans* resonances (7.6 ppm, enlarged inset), indicating thermal stability of the derivatives. The small variations found in some of the resonances are likely to be due to formation of the 15-*syn* isomer at the C=N double bond, in analogy to what is observed for the all-*trans* isomer and as suggested by the similarity of the two coupling constants generating the doublet of doublets at 7.15 ppm, clearly visible in the expanded region.

The amount of photochemically generated all-*trans* could be evaluated according to Equation 4.2.1

$$F_{\text{photo}} = F_{\text{trans,irr}} - F_{\text{trans,dark}}, \tag{4.2.1}$$

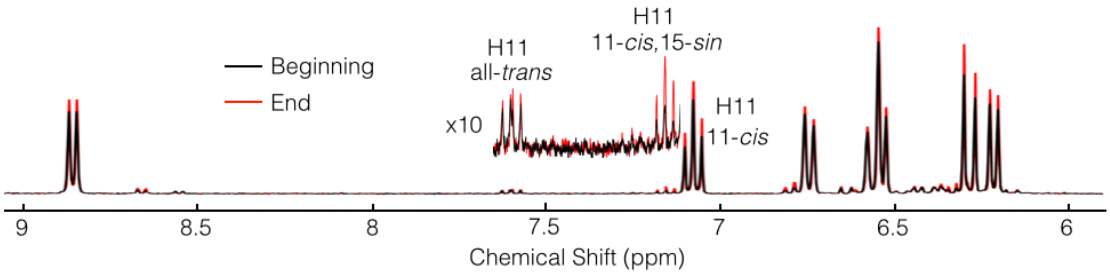

Figure 4.2.5 ^{1}H NMR spectra of a non-irradiated 11-*cis* **NAT** RPSB sample at the beginning (black) and at the end (red) of a typical QY measurement. The differences are mainly due to thermal formation of 11-*cis*-15-*syn* isomer, as suggested by the appearance of the double doublet at 7.15 ppm in the expanded region. The all-*trans* signals do not change significantly, as can be seen by the H11 proton at 7.60 ppm.

where $F_{\text{trans,irr}}$ and $F_{\text{trans,dark}}$ are the composition in fraction of all-*trans* isomer detected in the irradiated sample and in the dark control, respectively.

For **10-Me**, the approach needed to be complemented by another, as thermal isomerisation to the all-*trans* isomer took place during the irradiation and NMR measurements times. In order to properly take into account the thermal contribution, the rate of spontaneous isomerisation was measured by monitoring the increase of the all-*trans* isomer in a non irradiated sample recording ^{1}H NMR spectra at 80 second intervals. The results for the two runs are shown in Figure 4.2.6.

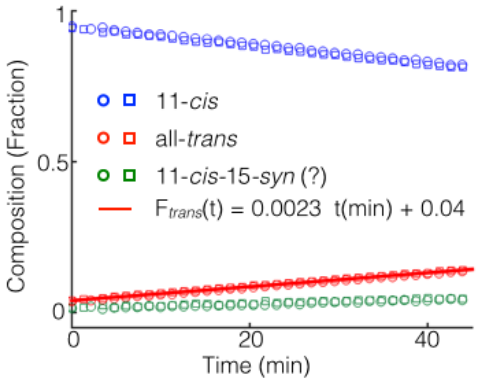

Figure 4.2.6 Thermal isomerization kinetics of 11-*cis*-**10-Me** RPSB

The increase of concentration of the all-*trans* isomer with time followed zeroth order kinetics, and was thus modelled with a first order polynomial (Equation 4.2.2) where the

slope k is the formation rate (in F_{trans} min^{-1}) and the intercept is the fraction of all-*trans* isomer present at the beginning of the measurements, $F_{\text{trans}}(0)$.

$$F_{\text{trans}}(\text{t}) = k \cdot t + F_{\text{trans}}(0) = 0.0023 \cdot t + 0.004. \tag{4.2.2}$$

The time interval between the measurement of the ^{1}H NMR spectra for the non-irradiated and irradiated samples as determined by the NMR spectrometer was considered to determine the amount of all-*trans* formed by thermal decomposition with Equation 4.2.2. The latter quantity was subtracted from the $F_{\text{trans,irr}}$ measured in the irradiated sample to isolate the amount of photoproduct generated.

Due to the error propagation in the subtraction of two quantities, a realistic estimate for the relative error on the QY values presented in Table 4.2.2 is 20-25%, significantly larger than the 10-15% estimated for the all-*trans* isomers in the previous Chapter. Even with this larger uncertainty, comparison of the ESLs and QYs trends for the 11-*cis* isomers clearly shows that the correlation between the two quantities no longer holds on the contrary of the all-*trans* case . For completeness, the values for the relevant all-*trans* derivatives are also reported in Figure 4.2.7.

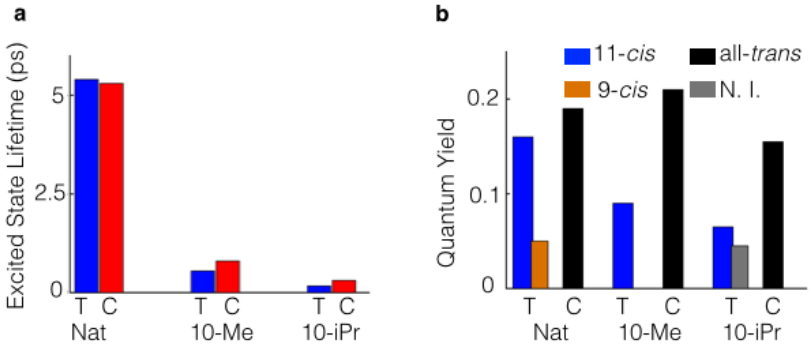

Figure 4.2.7 Comparison of (a) ESLs and (b) QYs for all-*trans* (T) and 11-*cis* (C) isomers for the RPSB derivatives. Colours in (a) indicate the all-*trans* (blue) or 11-*cis* (red) isomer, whilst in (b) indicate the identity of the photoproduct formed.

The reduction of ESL upon addition of polarisable substituents to the backbone applies to both isomers, but no significant reduction of the QY value was detectable for 11-*cis* RPSBs. This lack of correlation clearly prevents extending the model discussed in Chapter 3 for the all-*trans* isomer to the photoisomerisation reaction when starting from the 11-*cis* configuration. A possible explanation could be that after overcoming the excited state barrier, the isomerisation in the 11-*cis* case can happen without encountering a subsequent barrier for all-*trans*. In other words, the crossing point between S_1 and S_0 would be much less sensitive to the height of the excited state barrier when starting from an 11-*cis* configuration than from an all-*trans* one. This would be an analogous situation to what has been suggested to explain the observed independence of QY and isomerisation rate for some BR mutants.[24] Should this be the case, the photoisomerisation rate would still be related to the kinetic behaviour of the SE band appearing below 600 nm for both all-*trans* and 11-*cis* isomers. This could explain why backbone methylation affects only the ESL but not the reaction efficiency. Yet, this data is also consistent with an alternative, much simpler scenario. Recalling the very short time constants (<100 fs) found in the TA data of 11-*cis* **NAT** but not for all-*trans*, it is tempting to imagine the existence of an ultrafast reactive channel for the 11-*cis* to *trans* isomerisation that coexists with (at least) another un-reactive one responsible for the long-lived SE (Figure 4.2.8). This would imply that the ultrafast speed of the 11-*cis* to all-*trans* photoisomerisation is an intrinsic feature of the reaction, rather than the consequence of some unique influence of the protein environment. The following section is dedicated to the attempt to experimentally determine which scenario is relevant.

4.2.3 Following reaction dynamics via population control

In order to discriminate between the two reaction models discussed above a different experimental approach is needed to directly and exclusively follow the photoproduct formation dynamics without interference from non-reactive pathways. In the case of the opsin proteins,

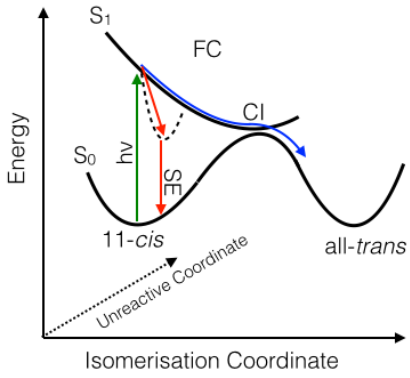

Figure 4.2.8 Hypothetical potential energy surface for 11-*cis* photoisomerisation (blue arrow) displaying another, unreactive coordinate (dashed) responsible for the generation of the stimulated emission (red arrows).

TA is capable of resolving the photoproduct formation[23,35,36] because its absorption maximum is well separated from the one of the starting material with a red shift of 22 and 45 nm in BR and RHO cases, respectively. For RPSBs in solution the difference in absorption maxima between all-*trans* and 11-*cis* isomers is less than 5 nm around 440 nm.[25] In order to follow the photoisomerisation kinetics, an alternative approach based on multipulse population control is required as previously applied to BR[139] and RHO[177,178] (Figure 4.2.9).

In this type of experiment, the system is excited with an actinic pulse (A) while monitoring the absorption of the photoproduct with a probe pulse (Pr) at a fixed time delay after the photoisomerisation dynamics are complete. A third dump pulse (D), that depletes the excited state population, thus photochemically quenching the reaction, is scanned in time. By following the variation of the photoproduct absorption signal as a function of the actinic-dump delay (T) it is possible to directly observe the photoreaction kinetics. For BR this approach successfully determined whether a species detected by transient spectroscopies was an intermediate of the photocycle and how far had the retinal isomerisation progressed at that stage.[139] For RHO, it confirmed the formation kinetics found by TA[177] and proved that it is possible to photochemically revert photorhodopsin to the starting material.[178] More recently, multipulse population control has also been applied to all-*trans* RPSB in solution.[134] In this

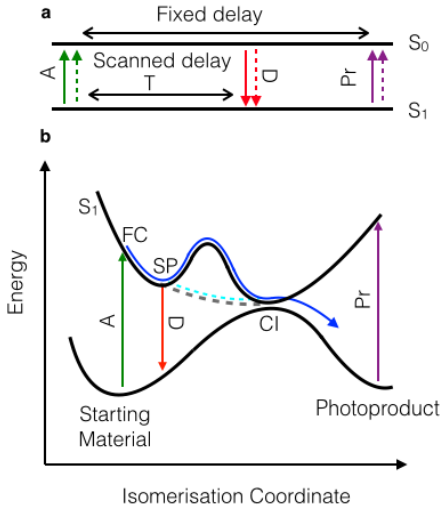

Figure 4.2.9 Multipulse population control scheme to follow photoproduct formation dynamics. (a) Pulse scheme and (b) its effect on a potential energy surface with (black) and without (grey, dashed) barrier along the excited state reaction coordinate. Pulses are represented as colour-coded arrows: actinic (A, green), probe (Pr, purple) and dump (D, red). FC: Franck-Condon region. SP: Stationary point. CI: Conical intersection.

case a long-lived residual signal was followed in the spectral region where ground state bleach appears due to the difference in molar extinction coefficient between the all-*trans* and 11-*cis* isomers (51800 and 23300 L mol^{-1} cm^{-1}, respectively).[25] When all-*trans* is photoexcited with an actinic pulse (20 fs, 500 nm, 100 nJ), ∼20% of the excited molecules isomerise to the less absorbing 11-*cis* isomer. This generates a negative (in ΔOD scale) non-decaying signal in the TA spectrum around 440 nm, present even after all the excited state dynamics are over. If the reaction is "photochemically quenched" by depleting the excited state population with a dump pulse (800 nm, 10 fs, 50 nJ) resonant with the SE band, formation of the 11-*cis* isomer is inhibited and the residual signal consequently reduced. Variation in this residual signal as a function of the delay between the actinic and dump pulses can be probed by monitoring the spectral region of the absorption maximum, at long actinic-probe delays (i.e., >50 ps). The long time delay is needed to ensure that no contributions from excited state features are present.

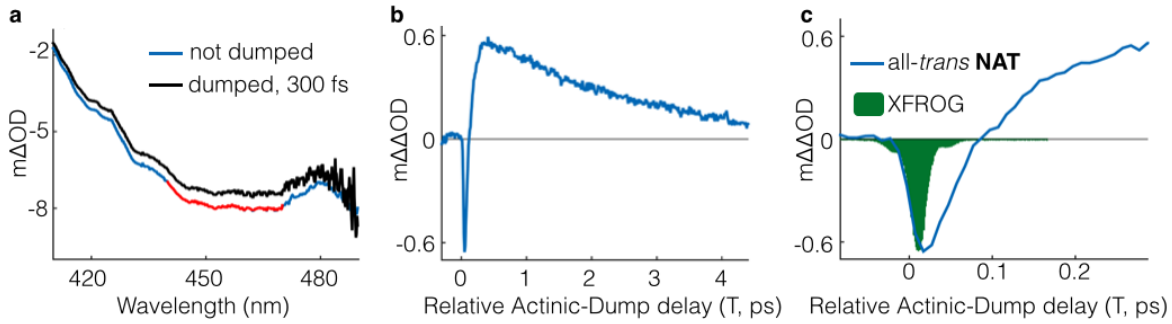

Figure 4.2.10 Results of population control experiments for all-*trans* **NAT** RPSB. (a) Unperturbed (light blue) and dumped (black, actinic-dump delay 300 fs) residual signal at 60 ps actinic-probe delay. The spectral region plotted in red is used to generate the action traces. (b) Double differential optical density (ΔΔOD) action trace as a function of the actinic-dump delay (T). (c) Zoom of the first 300 fs of (b). The green shadowed area is the measured cross-correlation between actinic and dump, scaled to the minimum amplitude of the negative feature of the action trace. Traces have been aligned to yield the same rise.

The residual signal of the unperturbed reaction can be obtained in the absence of the dump pulse or, as done for the data presented here, at negative time delays, when the dump pulse interacts with the sample before the actinic pulse (Figure 4.2.10a, light blue). Subtraction of this negative time delay signal from the action trace obtained by scanning the delay with respect to the dump pulse generates doubly differential optical density (ΔΔOD) maps. A positive sign of the ΔΔOD signal is expected every time upon interaction of the dump with the excited system when production of a less absorbing species is inhibited or a more absorbing species is produced. Conversely, a negative ΔΔOD signal indicates less production of a more absorbing species or more production of a less absorbing species. This will be briefly illustrated taking as an example all-*trans* RPSB, that upon photoexcitation it isomerises mainly to the 11-*cis* isomer. As the molar extinction coefficient of the 11-*cis* isomer is half than the all-*trans* one (23300 vs 51800 L mol^{-1} cm^{-1})[25] a negative differential optical signal (ΔOD) is observed at long time delays in the spectral region of the absorption maxima (around 450 nm, Figure 4.3.10a, light blue). Inhibition of the formation of the 11-*cis* isomer results in a smaller residual negative signal (Figure 4.2.10a, black) and, thus, in a positive double differential optical signal (ΔΔOD). In the case of RPSBs in solution,

the ΔΔOD signal was averaged between 440 and 470 nm (red region in Figure 4.2.10a), yielding kinetic traces like the one reported in Figure 4.2.10b for the all-*trans* isomer after subtraction of the unperturbed ΔOD signal. At actinic-dump time delays greater than 50 fs, a positive signal is observed as expected, peaking to a maximum value at $\sim$ 300 fs and then decaying on the picosecond timescale. This indicates that the photoisomerisation happens within picoseconds, in agreement with expectations from TA measurements and the observed correlation observed between ESL and QY. A negative feature is visible at the very early time delays, indicating that interaction with the dump pulse results in a higher yield of 11-*cis* as compared to the unperturbed photoreaction. Comparison of the width of the negative feature with the cross-correlation trace for the actinic and dump[179] (shown in green in Figure 4.2.10c) reveals that the process is likely to be due to an excited state absorption resonant with the dump. A possible explanation is that the additional energy provided to the system by the second dump photon is used to overcome the barriers encountered along the isomerisation coordinate, but better characterisation of the spectral features at the very early time delays than the one currently available is needed to support this claim. In order to obtain a relevant comparison, the population control experiments on all-*trans***NAT** RPSB and RHO were repeated before applying the same technique to 11-*cis* **NAT**. For the RHO measurements, similar actinic (9.1 fs, centred at 520 nm) and dump (10 fs, centred at 800 nm) pulses were used whilst the bathorhodopsin absorption was probed in the 515-595 nm region at 20 ps delay after excitation. The results for the three compounds are shown in Figure 4.2.11 as normalised double differential optical density (to the maximum for all-*trans* and to the minimum for 11-*cis* and RHO). The scaling has been done according to the sign expected for the double differential optical density signal upon quenching of the relative photoreaction.

Focussing on the first 300 fs reveals that for both RHO and 11-*cis* **NAT** RPSB isomerisation, the photoproduct formation is completed within 250 fs after excitation. Concerning

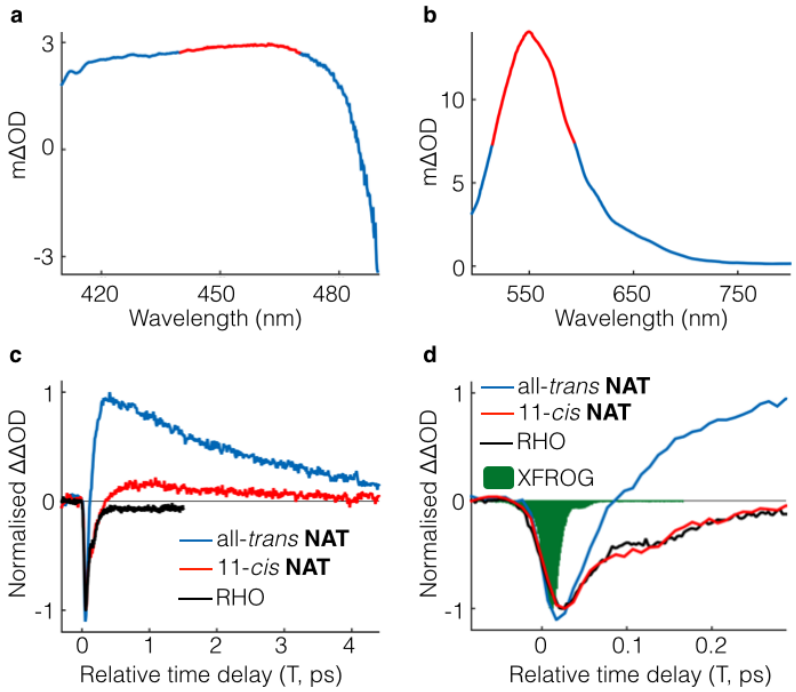

Figure 4.2.11 Population control experiments on all-*trans* and 11-*cis* **NAT** RPSB and RHO. (a) Non-dumped residual signal at 60 ps actinic-probe delay for 11-*cis* **NAT** RPSB. (b) Non-dumped residual signal at 20 ps actinic-probe delay for RHO. The spectral region plotted in red in (a) and (b) was used to generate the action traces. (c) Double differential optical density (ΔΔOD) action trace as a function of the actinic-dump delay (T) for all compounds. (d) Zoom of the first 300 fs of (c). The green shadowed area is the measured cross-correlation between actinic and dump pulses used for the RPSB in solution experiments. Traces were aligned to yield the same rise and normalised to the maximum (all-*trans*) or the minimum (11-*cis* and RHO) according to the expected ΔΔOD sign upon quenching of the photoreaction.

RHO, two features should be noted: a "kink" in the kinetics around 140 fs actinic-dump delay, and a long-lasting negative offset. The offset can be attributed to re-excitation by the dump of photorhodopsin, that back-reverts some of the photoproduct to the 11-*cis* reactant.[178] The "kink" in the kinetics is likely due to a competition between dumping of the naturally occurring 11-*cis* to all-*trans* photoreaction and the dump-induced back-reversion process of photorhodopsin. The latter is the only process still occurring at longer time delays.

The positive ΔΔOD feature at longer time delays observed for 11-*cis* in solution can be explained in (at least) three ways, but no data are currently available to discriminate between them (Figure 4.2.12).

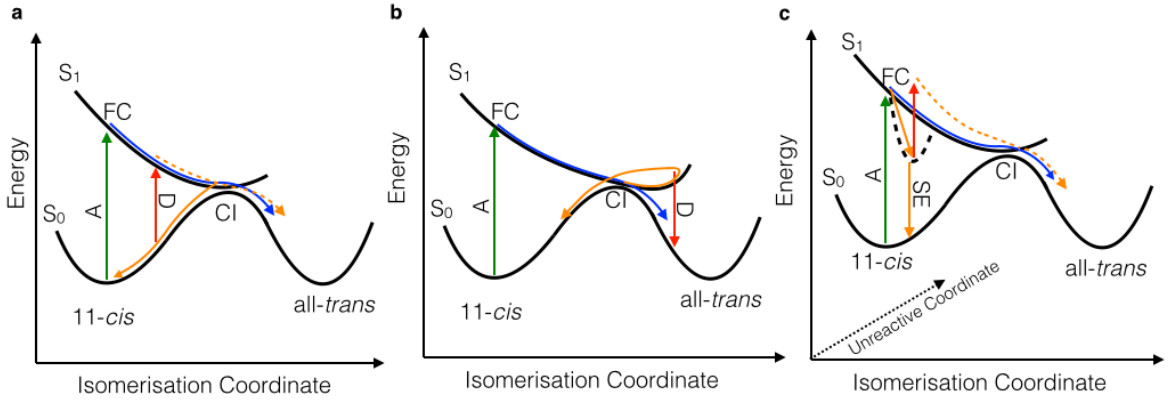

Figure 4.2.12 Possible origins of the positive ΔΔOD signal al long actinic-dump delays in the 11-*cis* **NAT** RPSB action trace. In all three figures, the green and red arrows represent the actinic and dump pulse, respectively; the blue solid arrows represent the ultrafast reactive channel, the solid orange arrows an unreactive portion of the S_1 population and the dotted orange arrows the part of unreactive population that successfully isomerises only after interaction with the dump pulse.

A first possibility (Figure 4.2.12a) is that the dump pulse re-excites a fraction of the molecules that have crossed the CI without successfully completing the photoisomerisation (solid orange arrow) at the first attempt, but manage to do so the second time (dashed orange arrow). The decay of the positive features on the picosecond timescale would be due to vibrational cooling of the un-reacted molecules, that would remove them from the resonance condition with S_1, reducing the excitation efficiency of the dump. This is the contrary of what is observed for RHO, and would require the branching efficiency at the CI to be different in the two

cases - otherwise the same negative feature should have been observed as for the protein. Another possibility (Figure 4.2.12b) is that the crossing point between S_0 and S_1 for the reactive channel is shifted towards a *trans*-like configuration. Most of the reactive molecules might be able to successfully complete the isomerisation within the first 300 fs (blue arrow), but a small fraction might linger in the crossing region and eventually cross the CI with *momentum* towards the *cis* side of the PES (solid orange arrow). If the dump interacts with these molecules before they recross, it would trap them in a *trans*-like configuration, thus increasing the overall yield. A final possibility (Figure 4.2.12c) is that the dump affects the fraction of molecules that have taken the long-lived decay channel in such a way to make them reactive. That the dump interacts with the population generating the long lived SE can be verified by probing the 700-850 nm spectral region 6 ps after excitation (Figure 4.2.13) where a depletion of the SE band is clearly observed (positive ΔΔOD).

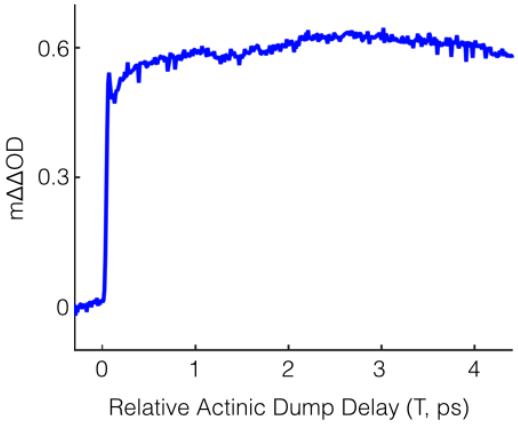

Figure 4.2.13 Action trace for 11-*cis* RPSB in MeOH probed between 700 and 850 nm at a 6 ps delay after excitation.

These measurements indicate that the long-lived decay channel is indeed depopulated by the dump pulse, but bear no information on the chemical evolution of the affected molecules, also considering that an ESA exists on top of the SE band. Different spectroscopic approaches are likely to be required to further investigate these observations. The initial evolution of the 11-*cis* action trace is remarkably similar to that of RHO, and suggests that photoprod-

uct formation is complete for 11-*cis* RPSB in solution on the same timescale as in the protein environment. This is in clear contrast with the assumptions discussed in the introduction that the fluorescence lifetime can be taken as an indication of the photoisomerisation rate[37,91,95,152,164,165] and also explains the lack of correlation between the ESL obtained from the SE band and the QY. Furthermore, it disproves the long held idea that the protein speeds up the isomerisation rate. The scenario supported by the population control experiment is the existence of (at least) one ultrafast reactive path and a long-lived non-reactive channel.

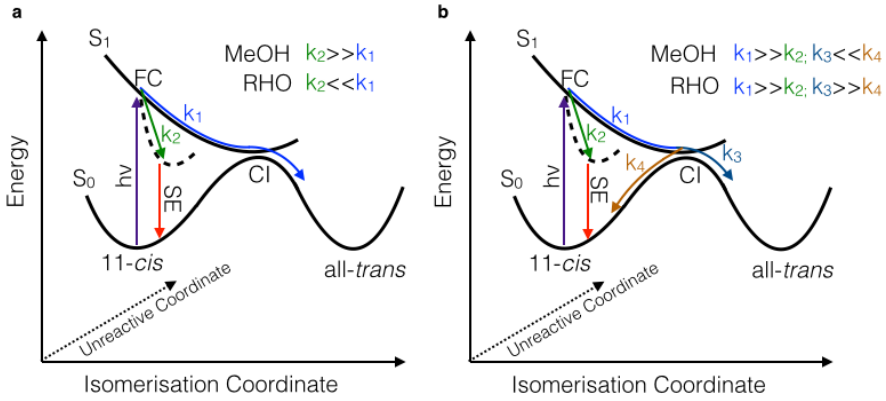

Figure 4.2.14 Branching scenarios for 11-*cis* to all-*trans* photoisomerisation, with the outcome determined by kinetic competition between different pathways. The difference between the protein and solution environment would be in the relative magnitude of the kinetic rates, with the constraint that k_1 is equal in the two cases as supported by the population control experiment.

In the light of the identical time scale found for the reactive channel for 11-*cis* RPSB in solution and in RHO, an explanation must be found for the differences in QY observed between the two environments. If kinetic competition is decisive, it is very likely to happen while leaving the FC region (Figure 4.2.14). Should this be the case, it would indicate that the role of the protein is to suppress (or significantly reduce) the fraction of molecules taking the long-lived channel. How this is achieved would require further investigations, but a few considerations can be made at this point. If the discrimination between the two pathways happens on a kinetics basis, the similarity of the retrieved reaction dynamics in solution and in the protein indicates that RHO must be "slowing down" the initial evolution of the long-lived channel (k_2), that has to be incredibly fast to compete with the reactive path (k_1,

Figure 4.2.14a). Another option would be that the reactive channel is still dominating in the kinetic competition at the branching point (k_1»k_2), but presents a much lower crossing efficiency at the CI for photoproduct formation (k_3«k_4, Figure 4.2.14b). This scenario would require the protein to affect the topography of the CI region and the rate of successful crossing (k_3»k_4) in order to justify the discrepancy in QY between the two environments. Both these lines of reasoning assume that branching takes place during the evolution on the excited state. On the other hand, it is well-known that 11-*cis* retinal in solution exists in (at least) two major conformers 12-*s*-*cis* and 12-*s*-*trans*[180] in solution. Transient NOE data (t_{mix} 800 ms) for 11-*cis* **NAT** RPSB (Figure 4.2.15) show that the same is true in deuterated methanol. A ^{1}H NMR spectrum with the protons of the polyenic chain and the methyl groups assigned is given at the bottom of the Figure. H15 (8.86 ppm) exhibits a characteristic low-field resonance, whilst H11 (7.07 ppm) is identifiable both by its chemical shift and resemblance to a triplet due to the similarity of the coupling constants with H10 and H12 (J= 12.5 and 12 Hz, respectively). H12 (6.21 ppm) can be assigned by its scalar and dipolar coupling with H11, identifying the third proton of that spin system as H10 (6.74 ppm). H14 (6.53 ppm) can be recognised by the scalar coupling with H15 (J= 11 Hz), whilst H7 (6.56 ppm) by the dipolar coupling with Me9 (2.09 ppm). The latter is identified through dipolar coupling with H11. Finally, H8 (6.28 ppm) can be identified via its scalar coupling with H7 (J= 16 Hz) and dipolar coupling with H10. The NOEs shown by H10 with H14 and Me13 and by H12 with H14 and Me13 (highlighted with colours in the Figure) are not compatible with a single solution structure, and reveal the simultaneous presence of two conformers at the C12-C13 single bond, 12-*s*-*trans* and 12-*s*-*cis* (blue and red in Figure 4.2.15, respectively).

Interestingly, the 12-*s*-*trans* conformer resembles the geometry assumed by the chromophore in RHO.[181–183] Computational studies on model systems have recently reported on the dependence of the isomerisation outcome on the starting molecular geometry.[163] The similarity of the isomerisation rate in solution and in the protein revealed by the population

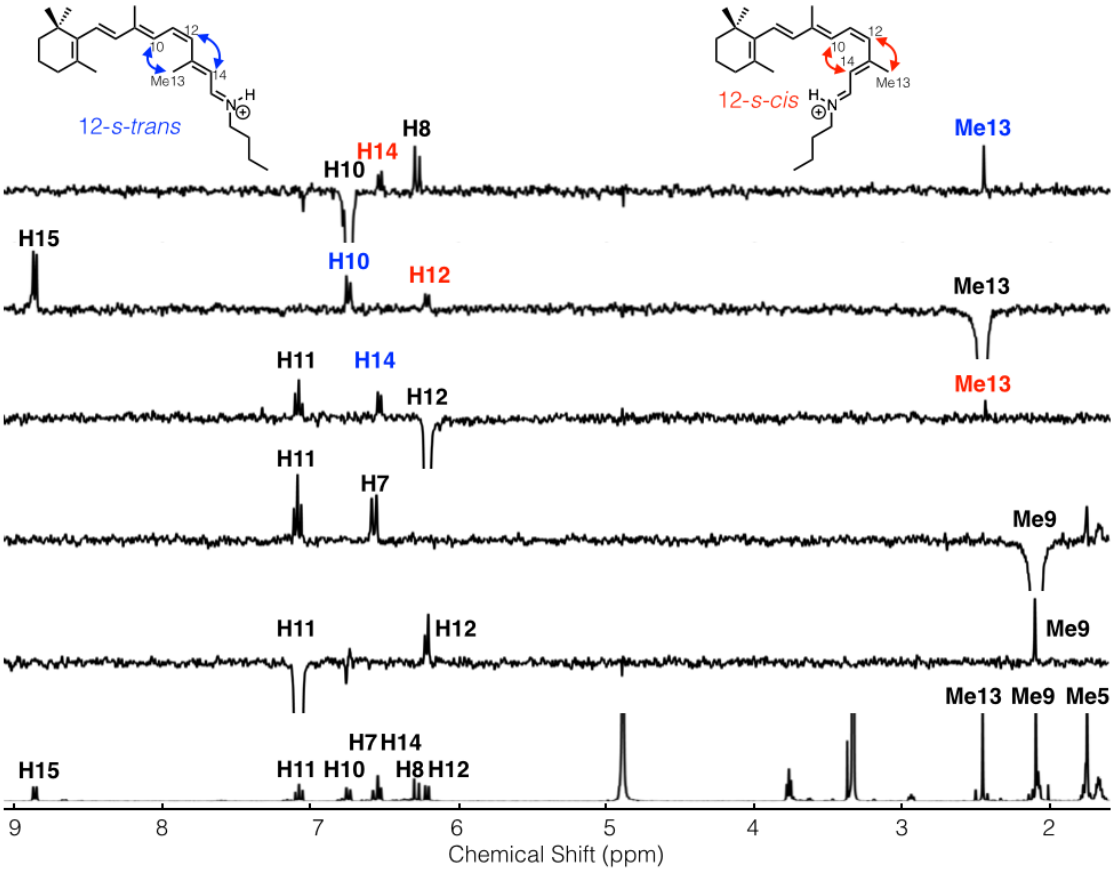

Figure 4.2.15 ^{1}H NMR (bottom) and transient NOE spectra (t_{mix} 800 ms) for 11-*cis* **NAT** RPSB in MeOD. The structures of the two conformations in solution, 12-*s*-*trans* and 12-*s*-*cis*, are shown on top. The double-headed arrows indicate the conformation-specific dipolar couplings (blue for 12-*s*-*trans* and red for 12-*s*-*cis*).

control experiment suggests that the protein might affect the topography of the PES in a much less dramatic way than previously envisioned. The existence of two conformations in solution, only one of which resembles the protein one, could point towards a model where the selection between the ultrafast reactive pathway and the long lived unreactive one is made on the basis of the starting molecular geometry in the ground state.[184] In this scenario, the main role of the protein environment would be to discriminate between conformations, rather than accelerating the reaction dynamics or changing the crossing efficiency at the CI. To gain some insight into this possibility, a new series of transient NOESY measurements were performed on 11-*cis* RPSB in MeOD, with the objective of determining the relative amount of the two conformers and estimate the expected QY in solution assuming that only the RHO-like one is reacting with the same 65% quantum efficiency as in the protein. In order to do so, it is necessary to be able to directly relate the magnitude of the NOE signal with the concentration of the species generating it. A generic transient NOESY signal for proton I (of *interest*) when irradiating proton S (*source*) {S-I} is given by Equation 2.1.2.

$$\{S{-}I\} = k \cdot [\mathrm{X}] \cdot {r_{\mathrm{SI}}}^{-6} \cdot t_{\mathrm{mix}}. \tag{2.1.2}$$

where k is a proportionality constant including physical parameters like the tumbling rate of the molecule in solution and the build-up rate of the NOE signal, [X] is the concentration of the species containing the dipolarly coupled S and I protons, r_{SI} is the distance between the two protons, and t_{mix} is the *mixing time*, an experimental parameter determining for how long after the instantaneous population inversion of the S resonance, the NOE is allowed to develop. Equation 2.1.2 is valid only when operating within the linear regime, i.e., before other relaxation channels affect the magnitude of the NOE signal.[52] Measuring the amplitude of the signals of interest at a series of different t_{mix} ensures that the linear regime approximation holds. The first step in determining the relative amount of the two conformers

consists in finding two conformation-specific signals to monitor. The ground state optimised structures for the two conformers (Figure 4.2.16a) were obtained in Gaussian 09,[185] using ωB97X-D/ cc-pVDZ as potential.[186,187] The signs of the second derivatives of the Hessian matrix were checked to be positive to ascertain the retrieved structures to be true minima.[188]

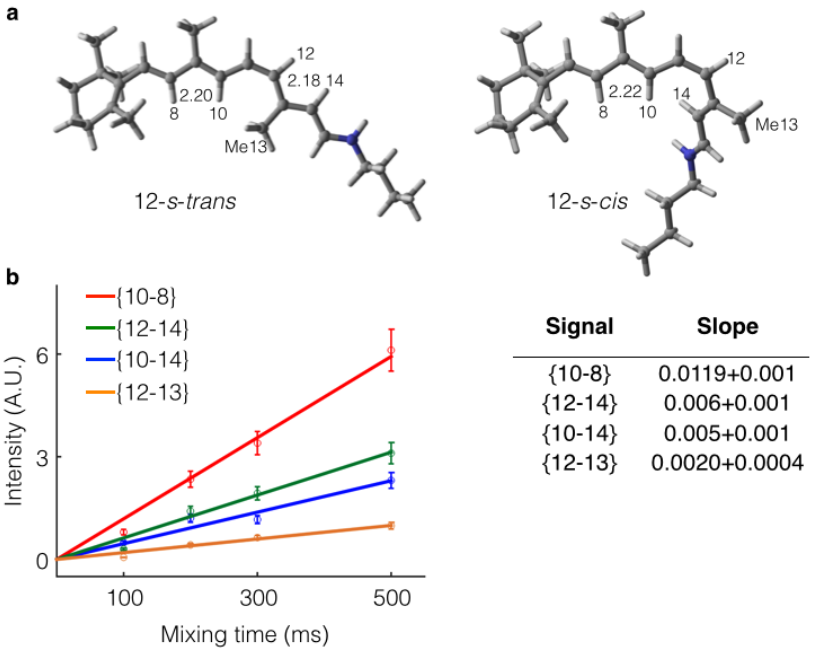

Figure 4.2.16 (a) Ground state optimised structures for the 12-*s-trans* and 12-*s-cis* conformers. The protons whose dipolar coupling has been followed are labelled, and the internuclear distances used to evaluate the conformer abundance are indicated between the corresponding nuclei. (b) Test of linearity for the signal amplitude as a function of the mixing time t_{mix} in the transient NOE experiments. Data are shown as circles with error bars, whilst the least square fits are shown as solid lines. The corresponding slopes are tabulated in the Figure

The H10-H8 distance was found to be the same in both conformers within 1%, and identical within the same error margin to the H12-H14 distance in the 12-*s-trans* conformer. The H12-H14 correlation is expected to be conformer specific, as the 12-*s-cis* is responsible for the H12-Me13 NOE. The equations for the two signals as a function of the mixing time are expected to be

$$\{10-8\} = k \cdot ([12\text{-}s\text{-}cis{+}12\text{-}s\text{-}trans]) \cdot r_{10-8}^{-6} \cdot t_{\text{mix}} = m_{10-8} \cdot t_{\text{mix}} \tag{4.2.3}$$

and

$$\{12-14\} = k \cdot [12\text{-}s\text{-}trans] \cdot r_{12-14}^{-6} \cdot t_{\text{mix}} = m_{12-14} \cdot t_{\text{mix}} \tag{4.2.4}$$

To have comparable values for the magnitude of the observed NOE signals, the {10-8}, {10-14}, {12-14} and {12-13} peaks were integrated separately in each transient NOE spectrum, assigning to the integral of the irradiated resonance the arbitrary value of -100. The signal amplitudes as a function of the mixing time (coloured circles), together with the least square fit (solid lines) to a first degree polynomial with (0,0) intercept are reported in Figure 4.2.16b. The ratio of the slopes of the {12-14} signal over {10-8} yields directly the percentage of the 12-*s*-*trans* conformer, as shown in Equation 4.2.5

$$\frac{m_{12-14}}{m_{10-8}} = \frac{[12\text{-}s\text{-}trans]}{[12\text{-}s\text{-}trans] + [12\text{-}s\text{-}cis]} \tag{4.2.5}$$

Under the assumptions that $r_{12-14} \approx r_{10-8}$ and that r_{10-8} is the same in both conformations as supported by the optimised structures, the percentage of 12-*s*-*trans* is found to be 53±9%, and the estimated QY in solution 0.34±0.06. Considering the assumptions made to estimate this value, its resemblance to the experimental value of 0.19 is remarkable. Although not conclusive, these data support the intriguing possibility that the main role for the protein environment in RHO is the selection of the reactive conformer, with electrostatic interactions possibly fine-tuning an existing ultrafast reactive channel.

4.3 Conclusions

In the present chapter, the photochemical characterisation of three 11-*cis* RPSBs (the native one plus two with modified backbones) has been reported. In contrast to my observations for the all-*trans* isomers, no correlation between the ESL and the photoisomerisation QY was found. Addition of polarisable substituents shortened the decay of the SE band below 650 nm, but the respective QYs remained unaffected. A three-pulses population control scheme was adopted to selectively follow the photoproduct formation dynamics. Comparison of the 11-*cis* results with analogous measurements for all-*trans* and RHO revealed that the 11-*cis* to *trans* photoisomerisation rate is almost identical in solution and in the protein environment, and is much faster than the all-*trans* to 11-*cis* photoreaction in solution. Transient NOE measurements confirmed the existence of the 11-*cis* **NAT** RPSB as two conformers in MeOD solution, one of which resembles the geometry adopted by the retinal chromophore in RHO, and provided information on their relative abundance. Under the assumptions that 11-*cis* RPSB photoisomerises successfully only when excited in the protein-like conformation, and that for said geometry the quantum efficiency is the same than in the protein, an estimate for the solution QY of 0.34±9 similar to the one measured experimentally of 0.19 was obtained. These findings shed new light on the role played by the protein in tuning the photochemistry of the RPSB co-factor. It is suggested that whilst for microbial opsins electrostatic tuning of the excited state barriers encountered along the isomerisation coordinates can be the main effect determining the photoisomerisation rate and efficiency, in the case of visual opsins the primary tuning mechanism might be the selection of a particularly reactive conformation of the chromophore, without significant changes to the photoreaction dynamics. In this regard, it might be of interest to recall a recent study on *Anabaena Sensory Rhodopsin*, where the all-*trans* to 13-*cis* photoisomerisation was found to proceed with a slower and multiexponential decay, whilst the inverse reaction was found to be ballistic as in RHO.[189] Even though further studies and evidence are definitely needed, it is possible that the existence of an excited state

barrier along the isomerisation coordinate is an exclusive features of the reaction in the *trans* to *cis* direction, with the inverse reaction being "naturally" barrierless.

Chapter 5

RPSB III: Mimicking the opsin shift in solution

Overview

With the backbone modification approach discussed in the previous two chapters, tunability of the excited state lifetime (ESL) was achieved and, in the all-*trans* case, of the quantum yield (QY) and product distribution as well. With the exception of the **10-Si** derivative, no appreciable variation of the absorption maximum was observed for any of the derivatives. Within the present chapter, another kind of structural modification, changing the nature of the amine employed for the Schiff base formation, is chosen to shift the absorption maximum and observe effects on reactivity. In a first class of derivatives, aromatic amines are used to red shift the absorption maximum by extension of the conjugation of the polyenic system. A different approach, subtler and more similar to the one acting in the protein, is attempted for another class of derivatives, introducing a second, non-conjugated charge close to the Schiff base end of the molecule. Part of the results presented in this work have already been published.[74,77] The ultrafast spectroscopy experiments were performed by Matz Liebel and Christoph Schnedermann and analysed by myself. The ground and excited state Raman

spectra presented in this chapter have been measured and analysed by Matz Liebel. NOESY NMR spectra have been acquired by Barbara Odell. Every other experiment presented here has been performed and analysed by the author.

5.1 The opsin shift and its origins

Broadly speaking, the *opsin shift* refers to a change in the absorption maximum of the retinal protonated Schiff base (RPSB) chromophore when bound to a protein (498 nm in rhodopsin, RHO, 568 nm in bacteriorhodopsin, BR) compared against a reference solvent, usually MeOH (440 nm).[190–192] With the discovery of more and more members of the opsin family, proteins absorbing from the UV to the red region of the spectrum have been found (Table 5.1.1), and a great amount of experimental work has been dedicated to understand the origins of such tunability. Two main approaches were followed: firstly, the effects on the absorption maximum of the nature of the counterion,[193] or varying hydrogen bonding, polarity and solvation properties of the solvent were investigated;[190] secondly, retinal analogues were designed and their absorption spectrum was measured both in solution and in the reconstructed pigments where possible.[194–196] Even though most of the studies following these approaches focused on the effects on the absorption maximum, attempts to correlate the latter with molecular parameters obtained from other spectroscopic technique such as C=N stretching frequencies from IR[197] or ^{13}C chemical shift from NMR[198] were also made.

One of the most remarkable results obtained with the solution measurements approach was the extrapolation of the absorption maximum of the "naked" (i.e., *in vacuo*) RPSB cation as a true reference to assess the effect of the protein environment. Blatz et al. in 1972 predicted the maximum to be around 590 nm,[199] preceding by more than 30 years and with remarkable accuracy the 610 nm value obtained by the first measurement of the gas phase absorption spectrum.[200] Now that this value is known, its adoption as a new reference for the opsin shift has been proposed.[200,201] While repeating the measurements of the gas

Protein/Solvent	Isomer	Absorption Maximum (nm)	Ref
RPSB	all-*trans*	445	A
RPSB	11-*cis*	442	A
Rhodopsin	11-*cis*	500	B
Bacteriorhodopsin	all-*trans*	560	C
hBVP	11-*cis*	425	B
hGVP	11-*cis*	530	B
hRVP	11-*cis*	560	B
SR I	all-*trans*	580	D
SR II	all-*trans*	487	E

A, Freedman, K.A. and Becker R. S., *J. Am. Chem. Soc.*, **1986**, *108*, 1245
B. Ernst O.P. et al, *Chem. Rev.*, **2014**, *114*, 126
C Oesterhelt D. and Stoeckenius W., *Nature New Biol.*, **1971**, *233*, 149
D Bogomolni R.A. and Spudich, J.L.,, *Proc. Natl. Acad. Sci. USA*, **1982**, *79*, 625
E Spudich E.N. et al., *Proc. Natl. Acad. Sci. USA*, **1997**, *94*, 4960

Table 5.1.1 Absorption maxima of RPSBss in MeOH and several opsin proteins.

phase absorption spectrum, Rajput et al.[201] found a broad plateau in the 530-610 nm region. By comparison with synthetic analogues, they decomposed the retrieved spectrum into two contributions, assigning a first species absorbing at 530 nm to the 6-*s*-*cis* conformation, and another with a maximum at 610 nm to the 6-*s*-*trans* conformer. The blue shifted absorption of the 6-*s*-*cis* conformer is caused by the skewed geometry adopted to reduce the steric repulsion between the geminal methyl groups and the hydrogen on C8, thus reducing the conjugation of the endocyclic double-bond with the polyenic chain. Tuning the absorption maximum by twisting of single bonds is a mechanism active in the proteins, as suggested by the different conformations found in BR and RHO. NMR[202,203] and UV[105] studies on BR and RHO with synthetic or isotopically labelled analogues showed that retinal adopts a 6-*s*-*trans* and a 6-*s*-*cis* conformation in the two cases, respectively (Figure 5.1.1).

It has been long recognised though, that the chromophore structure cannot alone explain the tunability and that a pivotal role must be played by electrostatic interactions. Knowledge of the charge transfer character of the first excited state[90] together with evidence from pigment analogues with partially hydrogenated retinals[194] led to the proposal of an *external*

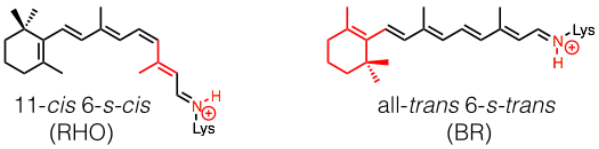

Figure 5.1.1 RPSB configuration in RHO and in BR. The regions of the molecules coloured in red are the ones supposed to interact with the negatively charged groups in the external charge model.

charge model. According to this, the energy gap between the ground and the optically active excited state is determined by the interaction of the positively charged nitrogen with the negative charge of a counterion, and a second negative charge positioned close to C12 (RHO)[204] or the β-ionone ring (BR,[205,206] Figure 5.1.1). While (longer) shorter nitrogen-counterion distances (de)stabilise the ground state, the interaction of the second negative charge with the other end of the molecules stabilises the excited state. Selecting the correct positions for the two negative charges reproduces the experimentally observed shifts.[192]

The limitations of representing the electrostatic interactions of the protein pocket with point charges were clear already in the 1980s, and other possibilities such as exciton interactions or an alternative counterion were also considered.[192] With the availability of higher computing power, more sophisticated quantum mechanical methods have been applied to disentangle the origins and the nature of the chromophore-protein interactions behind the opsin shift. Computational studies that successfully reproduced the absorption maxima for libraries of opsin mutants by taking into account the electrostatic potential of the retinal binding pocket have recently appeared,[207] but the importance of including an adequate treatment of the polarisation response of the pocket has been strongly emphasised.[208,209]

Mutagenesis studies have also helped identifying key residuals, like Glu113 acting as the Schiff base counterion in RHO,[210–212] or identifying the mutations responsible for colour tuning in visual pigments.[213–215] More recently, a remarkable example of protein engineering allowed preparation of a library of mutants of human cellular retinol binding protein (hCRBPII) with absorption maxima ranging from 425 to 644 nm.[216] Very briefly, by careful

selection of the performed mutations, the authors managed to exclude counterion interactions in the form of residues or water mediated bridges with the imine nitrogen and generate a uniform electrostatic field to obtain red shifted pigments. Fine tuning of the absorption maximum wavelength was reached by further addition of positively charged residues close to the Schiff base end of the molecules and complete isolation of the chromophore from the solution medium. Conversely, by introducing negative polarities in the vicinity of the Schiff base, they managed to obtain mutants displaying significant hypsochromic shifts.

Within this chapter the possibility is explored to shift the absorption spectrum in solution by appropriate choice of the amine to form the Schiff base in an environment without optimised chromophore-protein electrostatic interactions. Two approaches are followed. Firstly, the conjugation of the polyenic chain is extended in a "brute-force" way by employing aniline derivatives to form the Schiff base (Figure 5.1.2).

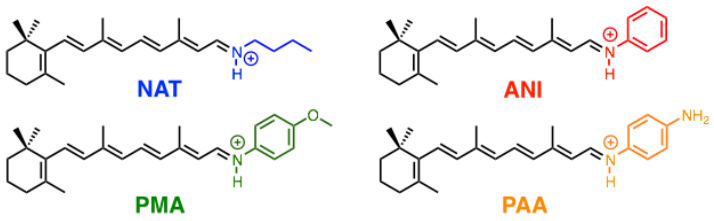

Figure 5.1.2 Structures of **NAT** and RPSBs formed with aromatic amines.

The photochemistry of the three derivatives shown with absorption maxima between 515 and 535 nm is studied in CH_3CN and, for the **ANI** derivative, in MeOH as well. Differing excited state decay kinetics are measured, but in all cases no photoisomerisation is detected. The origins of this lack of photoreactivity are investigated with time-domain Raman spectroscopy. A second approach, inspired by the current understanding of the opsin shift described above, is the introduction of a non-conjugated positive charge close to the Schiff base nitrogen. Derivatives of this kind have since long been used to investigate the origin of the opsin shift in solution and in the protein,[100] but, to the best of my knowledge, no studies of photoreactivity have been performed until recently. In a 2007 work by Bismuth et al.,[217] the

excited state dynamics of a retinal analogue formed with N,N-dimethylethylenediamine (**LIN**, Figure 5.1.3) was measured in trifluoroethanol. The absorption maximum was significantly red shifted down to 520 nm, and the excited state decay was found to be slower than the *n*-butylamine (nBu) in MeOH or EtOH, but the compound isomerisation efficiency was not discussed. Encouraged by the correlation between ESL and photoisomerisation QY found in Chapter 3 for the all-*trans* isomer, the protonated Schiff base with the same amine (**C2**) is prepared for the native backbone, and a study of the photochemistry in MeOH is attempted. The tendency of the compound to hydrolyse prevented me from obtaining any reliable results in that solvent. Lengthening the carbon chain between the two positive charges (**C4**) improves the stability, but significantly reduces the effects on the absorption maximum and, possibly, on the photoreactivity.

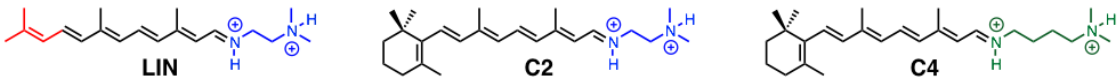

Figure 5.1.3 Structures of the retinal mimic (**LIN**) studied by Bismuth et al.[217] and doubly charged RPSBs studied in this work (**C2** and **C4**).

5.2 Schiff bases formed with aromatic amines

5.2.1 Preparation[218]

Protonated Schiff bases were prepared as shown in Scheme 5.2.1.

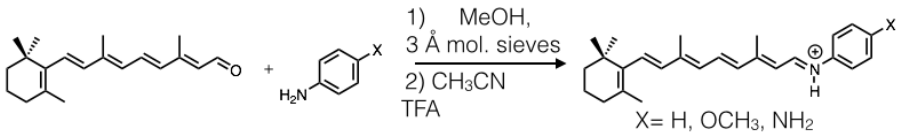

Scheme 5.2.1 Preparation of the RPSBs with aromatic amines.

The reactions were performed in MeOH in the presence of flame dried 3Å molecular sieves, in flasks wrapped with aluminium foil and under magnetic stirring, and left overnight

at room temperature. The reaction mixture was filtered over a celite pad under dim red light, and the solvent removed under vacuum via a rotary evaporator. The Schiff bases obtained in this way were redissolved in deuterated MeOH or CH_3CN and protonation was performed by 50/50 TFA/co-solvent (v/v) to yield a final concentration of acid of 1% (in volume). Both the condensation and the protonation reactions were shown to be quantitative by ^{1}H NMR spectra, where only peaks belonging to the Schiff base and the protonated Schiff base could be detected. Characterisation data for the unprotonated and protonated Schiff bases are given in Appendix C.

The two resonances attributable to H15 in the low field region are due to all-*trans* conformers, as shown for the Schiff base of **ANI** with the NOESY and COSY spectra in Figure 5.2.1. The H15 of major isomer (14-*s*-*trans*-15-*syn*, blue in Figure 5.2.1) shows a strong dipolar coupling with the Me13, a weak coupling with the ortho proton of the aromatic ring and, to an even lower extent, some coupling with the H14, due to the easy rotation around the C14-C15 single bond. The H15 of the minor isomer (14-*s*-*cis*-15-*anti*, red in the figures) exhibits strong coupling with the ortho proton of the aromatic ring and a weaker one with the H14. The latter is identified by a cross-peak in the COSY spectrum. The relevant cross-peaks for both conformers are highlighted in coloured boxes.

As expected, the three new derivatives show a remarkably red shifted absorption spectrum, as can be seen in Figure 5.2.2.

PAA protonation state

For the **PAA** derivative two protonation states are possible, as shown in Figure 5.2.3, strongly differing in the electronic character of the aromatic ring substituent: a neutral amino group behaves as an electron donating group, whilst as an electron withdrawing one if protonated.

In order to determine what protonation state is predominant, a titration with increasing amount of TFA was performed, and the results compared with the one obtained for **ANI**, for

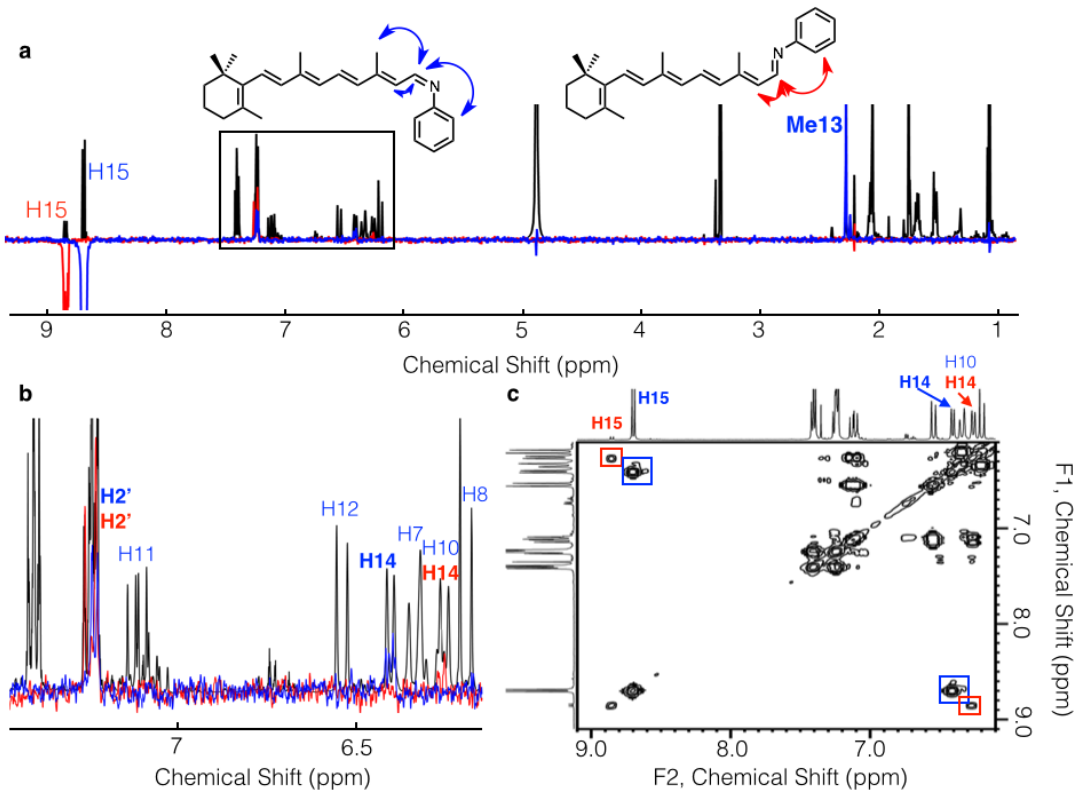

Figure 5.2.1 NMR evidence that the SB of **ANI** exists in two conformers, 14-*s*-*trans*-15-*syn* and 14-*s*-*cis*-15-*anti*, colour-coded in blue and red, respectively. (a) NOESY irradiations of the two H15. (b) Expansions of the boxed region in (a) with protons resonances assigned. (c) COSY spectrum, with cross peaks identifying the two H14 highlighted in coloured boxes.

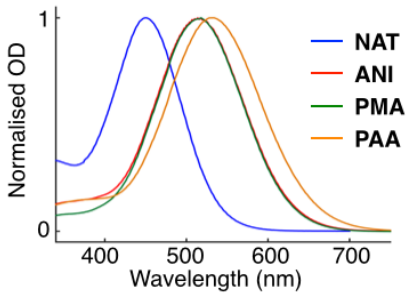

Figure 5.2.2 Absorption spectra of the aromatic RPSBs. Reproduced in part from Bassolino et al., *J. Am. Chem. Soc.*, 2014, **136**, 2650. Copyright 2014 American Chemical Society.

Figure 5.2.3 Two possible protonation states for **PAA**.

which double protonation is not possible. The similar behaviour observed in the two cases, shown in Figure 5.2.4, strongly suggests that only the imine nitrogen is protonated.

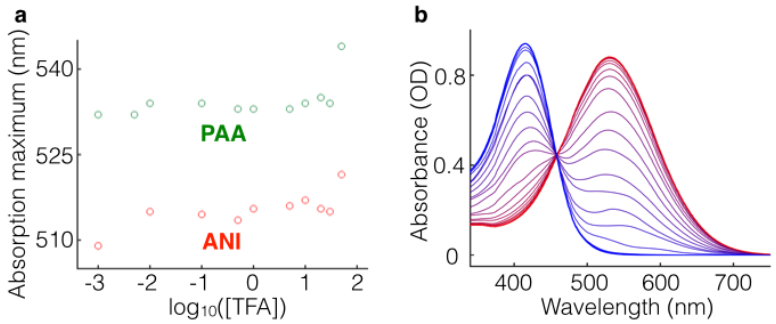

Figure 5.2.4 (a) **ANI** and **PAA** absorption maxima at increasing TFA concentration and (b) **PAA** titration in CH_3CN

5.2.2 Dynamics and quantum yield for aromatic RPSBs

As both **PAA** and **PMA** presented stability issues in MeOH but were found to be stable in CH_3CN with 1% TFA, transient absorption (TA) and continuous wave (CW) irradiation experiments were performed in the latter conditions. Irradiation in deuterated solvent were conducted in pyrex tubes under magnetic stirring with a CW 532 nm laser on ∼3 mM solutions. The beam diameter was expanded to a maximum diameter of ∼0.7 cm, to be completely contained within the test tube. The incident power was adjusted with absorbing filters to 0.2 mW, and, due to the high working concentration resulting in samples of elevated optical density, all incident photons were absorbed. The outcome of the photoreaction was monitored via ^{1}H NMR. As can be seen in Figure 5.2.5 for all the derivatives, no new resonances were observed, the reaction mixtures yielding unchanged spectra after irradiation.

The broad resonance changing position between some of the spectra in the 3-6 ppm region is due to exchangeable protons, most likely water introduced with TFA. These results suggest that the RPSBs formed with aromatic amines all have a QY of 0 for the photoisomerisation reaction, in striking contrast with **NAT**, for which a QY of 0.23 is reported in the same

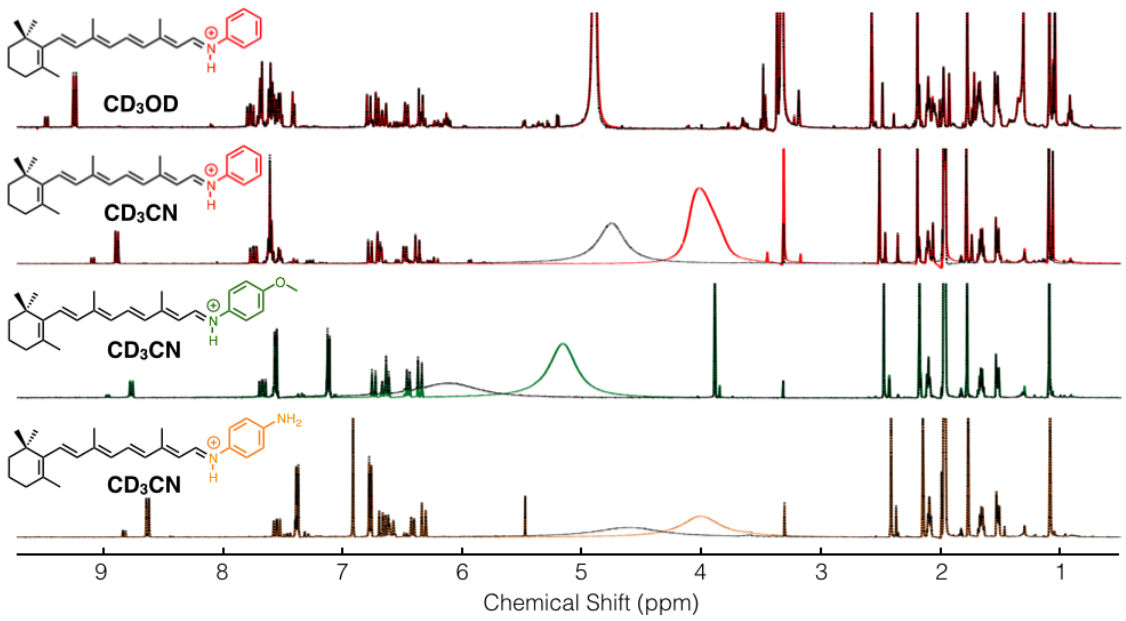

Figure 5.2.5 ^{1}H NMR spectra of the RPSB before (black dashed) and after (coloured) irradiation.

solvent.[26,129] The lack of reactivity observed for **ANI** both in MeOD and CD_3CN suggests it to be an intrinsic features of these derivatives rather than a solvent effect.

TA data were recorded for every compound adopting similar conditions. Solutions of RPSB in CH_3CN of optical density 0.7-1 at the absorption maximum in a 200 μm flow cell were optically excited by ∼20-30 fs pulses centred at 500 nm. The transient spectra were probed with a chirped white light in the 530-850 nm region from negative time delays (∼500 fs before excitation) to positive time delays long enough to describe the excited state decay of the stimulated emission (SE) band in the >600 nm region. In order to have a reference to compare the observed results, **NAT** excited state dynamics were measured in CH_3CN as well. Transient spectra at 1 ps after excitation are shown in Figure 5.2.6 for the three aromatic derivatives and **NAT**. The most striking differences between the aromatic RPSBs and **NAT** are the disappearance of the "double-hump" shape of the SE band in the red, due to a blue shift of the excited state absorption (ESA) band up to ∼650 nm, and the ground state bleach in the blue edge of the probed spectral range.

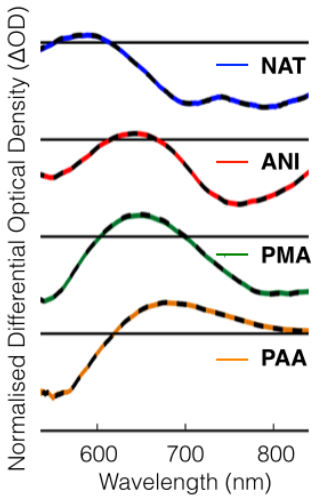

Figure 5.2.6 . Transient spectra at 1 ps after excitation in CH_3CN for **NAT** and the three RPSBs with aromatic amines studied. Reproduced in part from Bassolino et al., *J. Am. Chem. Soc.*, 2014, **136**, 2650. Copyright 2014 American Chemical Society.

Compound	Absorption Maximum (nm)	τ_1 (ps)	τ_2 (ps)	τ_3 (ps)
ANI	516	0.54	7.4	18.0
PMA	516	0.34	2.5	6.3
PAA	532	0.30	1.1	5.0

Table 5.2.1 Global fit results for RPSBs with aromatic amines in CH_3CN

Global fit of the TA data was performed similarly to what is reported in Chapters 2 and 3. Briefly, the data were fitted with a series of exponential decays convoluted with an instrument response function. The results of the fit for the derivatives considered in this chapter are reported in Table 5.2.1, and kinetics at selected wavelengths are compared in Figure 5.2.7. Comparison of **NAT** and **ANI** kinetics in MeOH and CH_3CN (Figure 5.2.7a) shows how the latter solvent tends to slow down the excited state decay. Concerning the kinetics of the aromatic derivatives in CH_3CN, addition of electron-donating groups on the ring significantly accelerates the observed excited state decay.

The excited state dynamics are sufficiently short-lived to exclude radiative processes as main deactivation pathways, but, with the present data, it is not possible to infer anything about the relaxation mechanism following photo-excitation. At a more fundamental level,

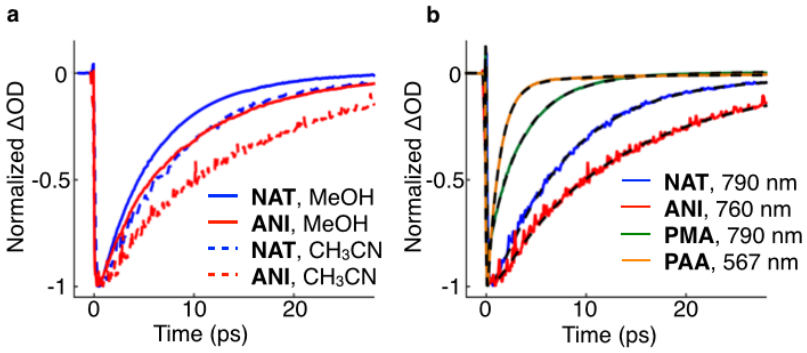

Figure 5.2.7 (a) **NAT** (blue) and **ANI** (red) decay kinetics at 790 and 760 nm, respectively, in MeOH (solid) and CH_3CN (dashed). (b) Decay kinetics of **NAT** and the aromatic RPSBs in CH_3CN at the wavelength stated. Black dashed lines are fits to the data. . Reproduced in part from Bassolino et al., *J. Am. Chem. Soc.*, 2014, **136**, 2650. Copyright 2014 American Chemical Society.

it should be questioned whether the introduction of aromatic rings has affected the Franck Condon (FC) region of the new derivatives beyond bringing the two surfaces involved closer or changing the nature of the excitation transition. In order to address these questions, two routes are followed: on one hand, characterisation of the FC region is attempted via pre-resonant Raman spectroscopy and quantum-mechanical calculations; on the other hand, insight into the deactivation processes is sought via coherent vibrational spectroscopy of the excited state for one of the derivatives (**PMA**).

5.2.3 A change in electronic structure?

Ground state Raman spectra for **NAT** in MeOH and **PMA** in CH_3CN (Figure 5.2.8) were measured with a Perkin Elmer Raman Station 400F, exciting the sample with 10 mW at 785 nm. Neat solvents were measured separately to perform a background subtraction.

The **NAT** Raman spectrum has been fully assigned by Mathies and co-workers[93] partially on the basis of their previous work on the corresponding aldehyde.[219] Briefly, the modes above 1500 cm^{-1} are a combination of C=C stretches, whilst the peaks between 1150 and 1250 cm^{-1} have been assigned to C-C stretches weakly mixed with CCH rocking modes. The bands near 1000 cm^{-1} have been assigned to methyl rock vibrations, whilst the weak bands

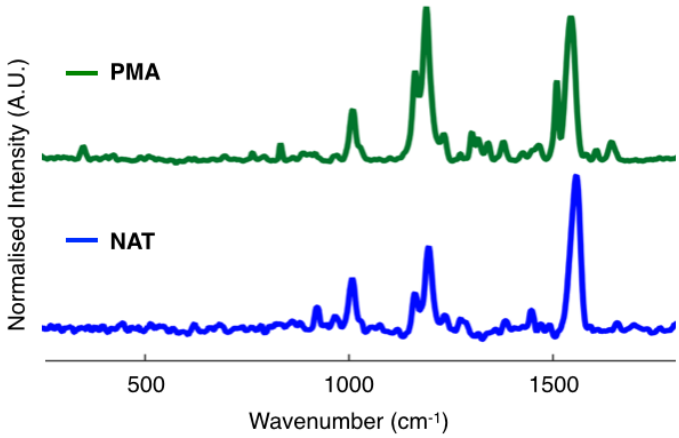

Figure 5.2.8 NAT and **PMA** ground state Raman spectra. Reproduced in part from Liebel et al., *Phys. Rev. Lett.*, 2014, **112**, 238301. Copyright 2014 American Physical Society.

below 1000 cm^{-1} correspond to hydrogen wags.[93] The intensity of a (pre)resonant Raman band in the harmonic approximation reflects the slope of the potential energy surface (PES) along the localised modes contributing to the band and is proportional to the displacement of the equilibrium positions between ground and excited states.[219] This means that the bands and intensities in a Raman spectrum reveal the initial evolution of the system upon photoexcitation, or, equivalently, which vibrational modes are initially activated following the absorption of a photon. The striking similarity between **NAT** and **PMA** Raman spectra strongly suggests that the evolution at the FC region is identical in the two systems. The additional band appearing at 1500 cm^{-1} and the decrease of intensity of the 1560 cm^{-1} band are due to a splitting of the latter caused by coupling with the C=C stretch of the aromatic ring. As additional evidence for the unchanged nature of the FC region independently on the amine, a comparison of the atomic charge distribution at the optimised ground state geometry in S_0 and S_1 was attempted. Calculations were performed in Gaussian 09[185] using a DFT hybrid functional, ωB97X-D[186] for both ground and excited state. Optimised ground state geometries were evaluated using cc-pVDZ[187] as a basis set, and their nature as local minima was verified by checking for the second derivatives of the Hessian matrix to be positive.[188] Merz-Kollman[220,221] (MK) partial atomic charges for the ground and first singlet

excited state were evaluated with the less expensive 6-31+G(d,p)[222,223] basis set. The solvent (MeOH) was treated implicitly at the CPCM level.[224,225] The MK charges of the skeletal atoms (carbons and nitrogen) of the polyenic chain in the ground state and the difference between S_1 and S_0 are shown as bar graphs in Figure 5.2.9a and b, respectively.

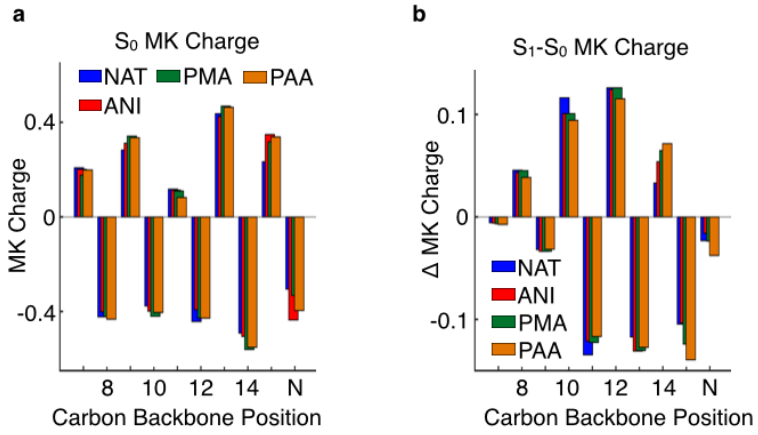

Figure 5.2.9 (a) Merz-Kollman (MK) charges for the atoms of the polyenic chain in the ground state. (b) MK charges difference between S_1 and S_0 for the same atoms. Reproduced from Bassolino et al., *J. Am. Chem. Soc.*, 2014, **136**, 2650. Copyright 2014 American Chemical Society.

A negative (positive) value of the charge indicates higher (lower) electronic density in Figure 5.2.9a or an increase (depletion) of the same upon excitation in Figure 5.2.9b. The resulting patterns are unaffected by the nature of the amine (aromatic or alkyl-substituted) and also by the presence of rings substituents, once again supporting a similar electronic character of the initially populated electronic state for all derivatives.

5.2.4 Excited state vibrational coherences suggest formation of a TICT State

To understand what deactivation process is so efficiently competing with photoisomerisation, the evolution of excited state vibrational coherences (VC) for **PMA** were monitored combining high time resolution transient absorption with an electronic population control approach,[50] as shown in Scheme 5.2.2.

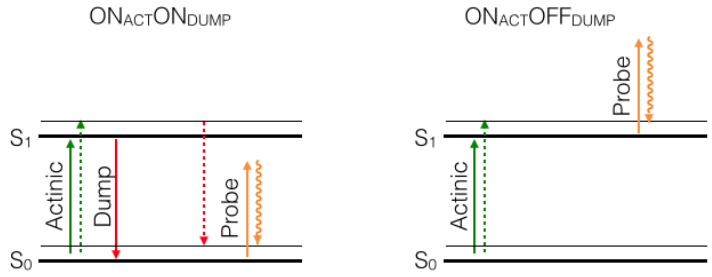

Scheme 5.2.2 Generation of excited state population and vibrational coherence by a short pump pulse (green), followed by depletion of S_1 population by a long dump pulse (red) and probing of the residual coherence by a third pulse (orange). Solid and dashed lines indicates bra and ket interactions.

A solution of **PMA** of final OD 1 at 512 nm in a 200 μm flow cell was excited with an actinic pulse centred at 550 nm of 6.8 fs duration, as measured by SHG-FROG.[66] The system was probed with a broadband white-light spanning from 500 to 900 nm, and population control was achieved with an 800 fs dump pulse centred at 1030 nm. As discussed in Chapter 2, the short actinic pump transfers population from the ground to the excited state and generates VC in all Raman active modes. In the absence of the dump pulse and after subtraction of the electronic decay, an oscillating signal remains corresponding to vibrational wave-packet motion of the solvent and **PMA**, according to Equations 2.2.12.

$$\mathrm{ON_{ACT}OFF_{DUMP}} = a \cdot \chi_{\mathrm{solv}} + b \cdot \chi_{\mathrm{S_0}} + c \cdot \chi_{\mathrm{S_1}}. \tag{2.2.11}$$

In presence of the long dump pulse, a fraction of the excited state population of **PMA** is removed incoherently. The contributions after subtraction of the electronic features are

$$\mathrm{ON_{ACT}ON_{DUMP}} = a \cdot \chi_{\mathrm{solv}} + b \cdot \chi_{\mathrm{S_0}} + c(1-\gamma) \cdot \chi_{\mathrm{S_1}}. \tag{2.2.12}$$

Subtraction of the two traces results in isolation of the S_1 fraction of vibrational motion, γ, depleted by the dump pulse.[50] Windowing and Fourier transform of the oscillating signal yields the spectrum of the VC activity in the excited state for **PMA**, shown in Figure 5.2.10 (green line).

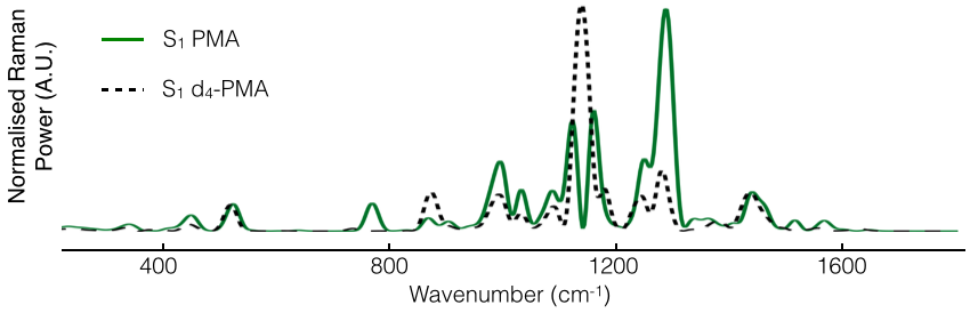

Figure 5.2.10 Excited state coherent vibrational activity for **PMA** (green) and **d_4-PMA** (black, dashed). Reproduced in part from Liebel et al., *Phys. Rev. Lett.*, 2014, **112**, 238301. Copyright 2014 American Physical Society.

There is no significant VC activity below 1000 cm^{-1}, where the torsional modes leading to isomerisation (hydrogen out-of plane vibrations and backbone torsions) would be expected to appear. This is in agreement with the lack of photoisomerisation determined by ^{1}H NMR. On the other hand, most of the vibrational activity remains in the 1100-1300 cm^{-1} region, with the most intense band appearing at 1287 cm^{-1}, a region compatible with aromatic ring vibrational modes. To confirm this assignment, **d_4-PMA**, an isotopically substituted **PMA** with the phenyl hydrogens replaced by deuterium, was prepared using commercially available deuterated *p*-methoxyaniline. The spectrum of the excited state coherences for **d_4-PMA** is shown as a dashed line on top of the hydrogenated one. The intensity of the 1287 cm^{-1} band is significantly reduced, with an intense band appearing at $\sim$1150 cm^{-1}, in agreement with its assignment to Schiff base modes. The similarity of the ground state Raman spectra and ground and excited state charge distribution between **PMA** and **NAT**, leads to the conclusion that the use of an aromatic amine to form the Schiff base does not significantly affect the FC region. The lack of detectable photoisomerisation activity, the absence of torsional signatures

along the polyenic chain and the enhanced vibrational activity of the ring modes in the excited state point towards an active role of the aromatic ring in the deactivation process. In the light of the experimental and computational evidence of a strong charge transfer towards the β-ionone ring as a typical feature of the **NAT** evolution in S_1 and the twisted intramolecular charge transfer (TICT) character of the CI mediating the photoisomerisation reaction, it seems plausible for the aromatic amine to act as a competitive donor of electronic density. This hypothesis is supported by the intense vibrational activity in phenyl modes and with the increase in reaction and deactivation dynamics for derivatives with rings featuring electron donating substituents. It is feasible that the aromatic ring yields a TICT state with the polyenic chain upon twisting of the N-CΦ bond, or generates another CI mediating *syn-anti* isomerisation at the C=N double bond - an easily and quickly reversible reaction which would result in unchanged ^{1}H NMR spectra in the CW measurements performed in this work.

To further test this hypothesis, the preparation was attempted of an aromatic RPSB bearing a strongly electron-withdrawing group, hoping that the character of the new substituent would have disfavoured the donation of electronic density by the aromatic ring, potentially restoring the normally observed photoreactivity. The preparation of a Schiff base with 4-nitroaniline was thus attempted in several solvents (MeOH, $CHCl_3$, CH_3CN, toluene, Et_2O, cyclohexane, *iso*-butanol), with addition of Lewis acids ($Ti(OiPr)_4$) to activate the aldehyde or strong bases (*n*-BuLi) to deprotonate the amine. Unfortunately, it was not possible to observe sufficient conversion of the starting material into the desired imine, the usual conversion being well below 50%. In most cases, evidence suggesting thermal isomerisation of the starting material was found in the ^{1}H NMR of the reaction mixture, as multiple H15 resonances were observed for the aldehyde.

5.3 Doubly charged RPSBs

Doubly charged RPSBs **C2** and **C4** (structures in Figure 5.3.1) were prepared following an analogous procedure to one used for the aromatic derivatives, but stirring the reaction for shorter times.[218]

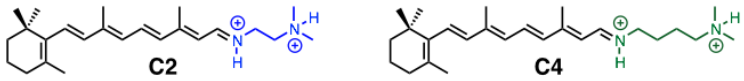

Figure 5.3.1 Doubly charged RPSBs studied

The reactions were performed in MeOH in presence of flame-dried 3 Å molecular sieves, in flasks wrapped with aluminium foil and under magnetic stirring at room temperature. One hour after the addition of the amine, the reaction mixture was filtered over a celite pad under dim red light and the solvent removed under vacuum via a rotary evaporator. The Schiff bases were redissolved in deuterated MeOH and protonation was performed by addition of TFA. Both the condensation and the protonation reaction were shown to be quantitative by ^{1}H NMR spectra, where only peaks belonging to the Schiff base and the RPSB could be detected. Characterisation data for the Schiff bases of **C2** and **C4** and the PSBs of **C4** are given in Appendix C.

5.3.1 Characterising double protonation states and thermal behaviour of C2 and C4

The absorption maximum of the **C2** in EtOH and CH_3CN had been previously reported to be 455[226] and 454[227] nm, respectively, and was found to be 468 nm in MeOH (Figure 5.3.2).

A titration with TFA revealed no clear isosbestic point, suggesting the presence of more than one species, as would be expected if double protonation occurs. Taking as a reference **NAT** absorption maximum at 445 nm, **C2** shows a red shift of 23 nm, in contrast to the

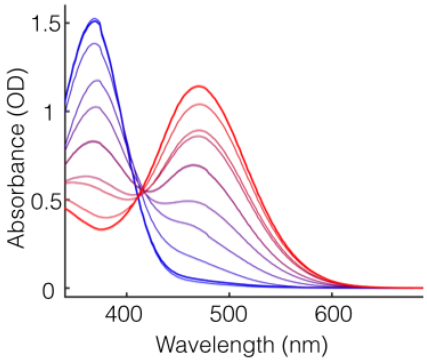

Figure 5.3.2 C2 titration in MeOH

75 nm shift measured by Bismuth et al.[217] for their **LIN** analogue. The differences can be explained comparing the results available in literature for a series of derivatives summarised in Table 5.3.1.

The absorption maximum of **NAT** is red shifted by 22 nm from MeOH to trifluoroethanol (TFE), probably due to different association of the ion pair.[199] Similarly, changing the β-ionone of the native backbone to a linear polyene (nBu-**LIN**) increases the effective length of conjugation resulting in a 23 nm red-shifted PSB, as the steric constraint of the ring imposing a skewed conformation is no longer present.[105] Summing these contribution with the 23 nm shift observed for **C2** yields a 68 nm red shift when passing from **NAT** to **LIN**, in reasonable agreement with the experimental value of 75 nm, suggesting that, to a first approximation, these effects are additive and non-interfering. To gain further evidence of the double protonation, ^{1}H NMR spectra of the amine and of the **C2** Schiff base were measured at increasing acid concentration, as shown in Figures 5.3.3 and 5.3.4.

The signals belonging to the two methyl groups bound to the nitrogen (marked with blue dots in the free amine and red dots in the SB) and to the methylene group closer to the primary nitrogen (green dot) were used as a marker for the protonation state of the dimethylamino and amino group, respectively. Judging by the larger shift of the CH_2 triplet in the free amine upon addition of 1 eq of TFA, the primary amino group is protonated before the tertiary one,

Compound	Solvent	Absorption Maximum (nm)	Ref
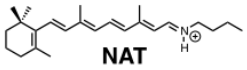 NAT	MeOH TFE(HCl)	445 467	A B
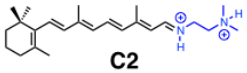 C2	MeOH EtOH CH_3CN	468 455 454	This work C D
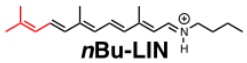 *n*Bu-LIN	MeOH	468	E
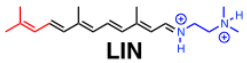 LIN	TFE(TCA)	520	F

A. Freedman, K.A. and Becker R. S., *J. Am. Chem. Soc.*, **1986**, *108*, 1245
B. Sugihara, T. and Kitagawa, T. *Bull. Chem. Soc. Jpn.*, **1986**, *59*, 2929
C. Bassov, T. and Sheves, M. *Biochemistry*, **1986**, *25*, 5249
D. Baasov, T. et al. *Biochemistry*, **1987**, *26*, 3210
E. Sheves, M. et al. *Proc. Natl. Acad. Sci. USA*, **1986**, *83*, 3262
F. Bismuth, O. et al., *J. Phys. Chem. B.*, **2007**, *111*, 2327

Table 5.3.1 Absorption maxima of RPSB analogues

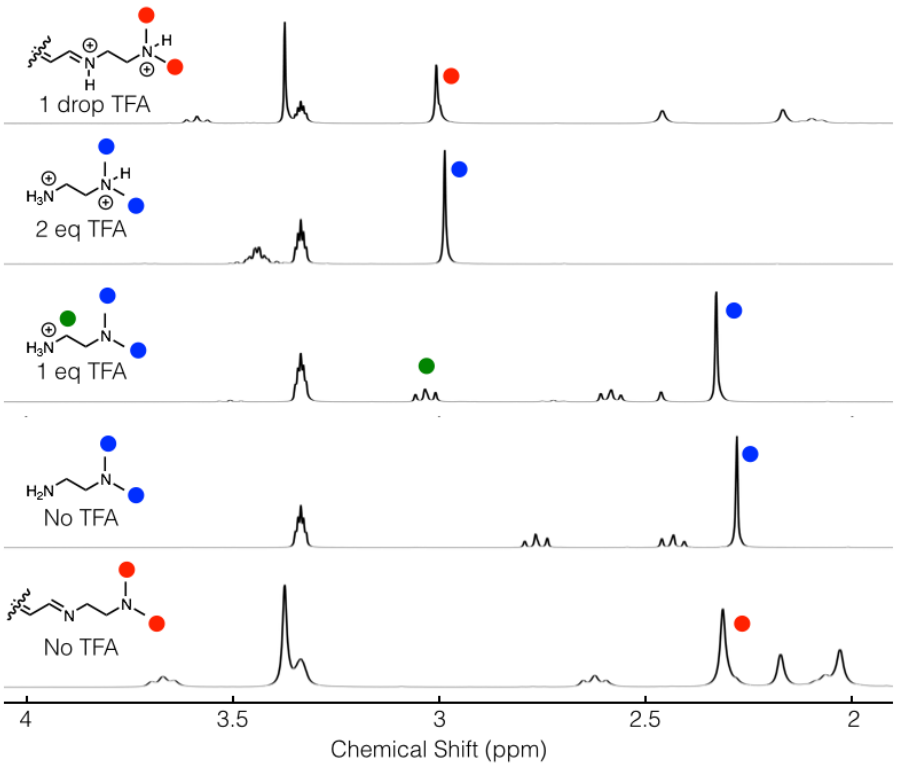

Figure 5.3.3 High field region of the ^{1}H NMR spectra for the free amine and **C2** at increasing acid concentration. Assigned resonances are marked with colour-coded dots.

as would be expected on the basis of its greater accessibility and hence stronger interaction with the solvent.[a] Upon addition of further TFA, the charge on the methyl-bearing nitrogen is clearly visible from NMR.

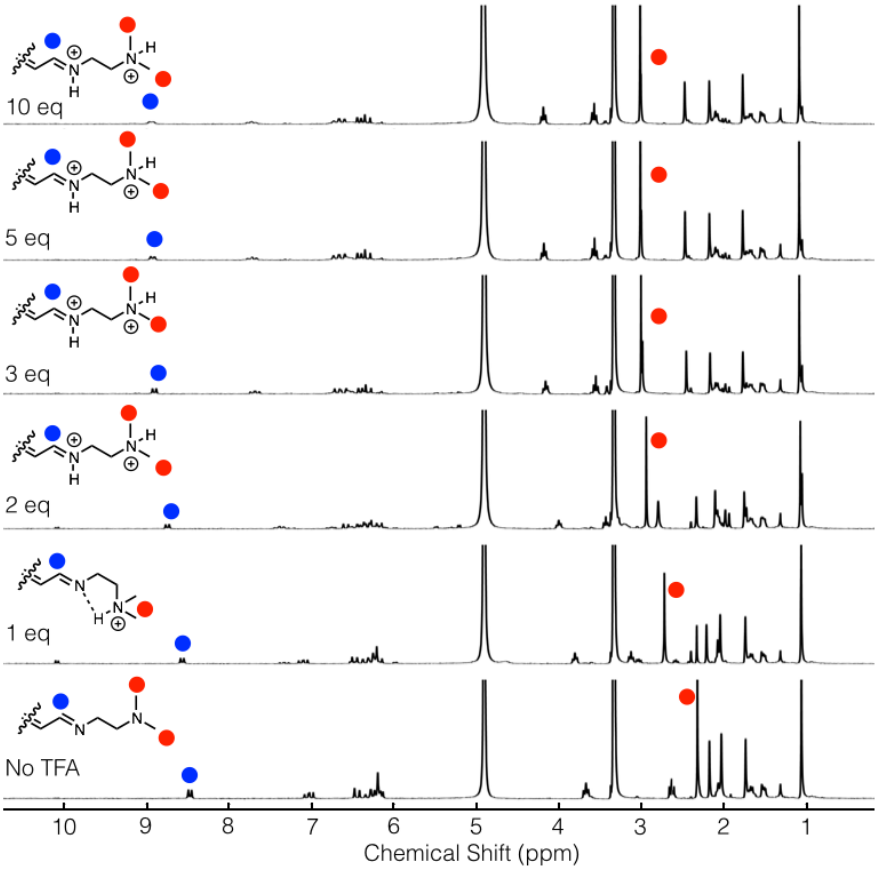

Figure 5.3.4 ^{1}H NMR spectra of **C2** titrated with TFA. Assigned resonances are marked with colour-coded dots.

For **C2**, the protonation order is reversed, as can be seen by the geminal methyl signal (red dots, Figure 5.3.4) shifting to low fields before the H15 one (blue dots) upon addition of 1 eq of TFA. Increasing amounts of acid lead to a complete double protonation, with no further shifts of the resonances after addition of 5 eq of TFA. Closer inspection of the low

[a] A tertiary amine is expected to be more basic than a primary amine in the gas phase due to the presence of more electron donating group on the charge-bearing atom. In solution, this trend is reversed due to the stabilising contribution from solvation, which is greater for the less sterically hindered primary amine. Another way to express this phenomenon is that in the case of the primary amine, more hydrogen bonds can be formed with the solvent (i.e., stronger solvent-charge interactions are possible) as more protons are available. Cfr. Clayden's textbook[228]

field region (7-10 ppm, Figure 5.3.5) of the spectra measured upon addition of 1 and 2 eq of acid reveals the proton to be somewhat shared between the two nitrogens judging by the small shift observed for H15, suggesting the existence of a "chelate" structure.

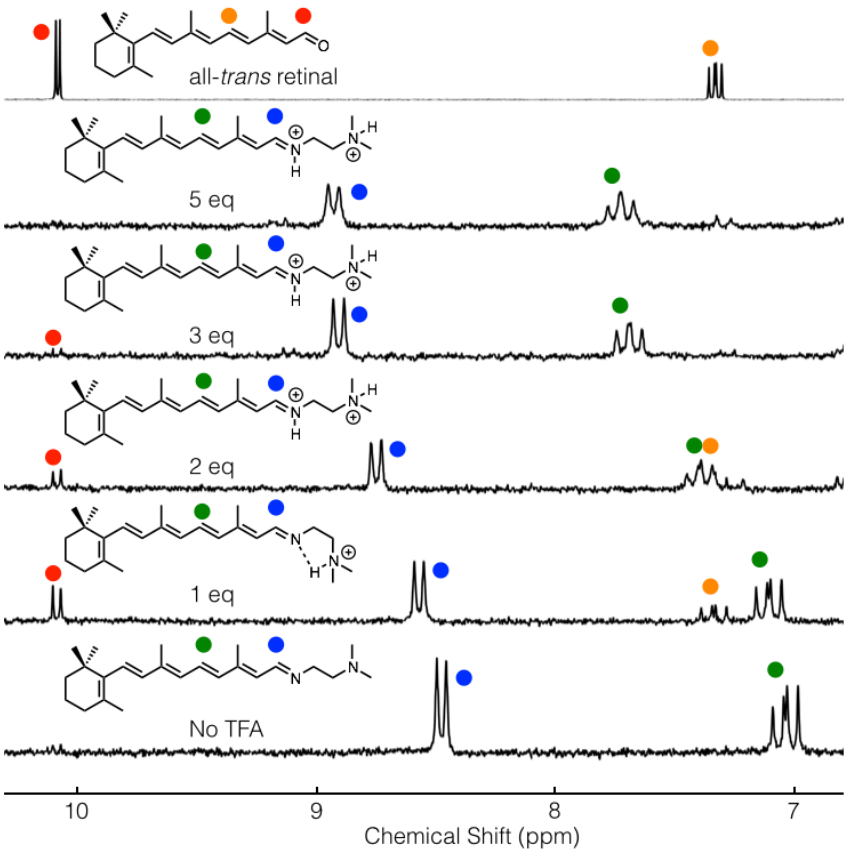

Figure 5.3.5 Expansion of the low field region of the spectra shown in 5.3.4 with the spectrum of all-*trans* retinal added for comparison. Assigned resonances are marked with colour-coded dots.

In the same region a doublet at 10.1 ppm (red dot) can be seen clearly appearing upon addition of 1 eq of TFA together with a doublet of doublets at 7.3 ppm (orange dot). Comparison with the spectrum of all-*trans* retinal helps assigning those resonances to H15 and H11, respectively, indicating that **C2** is hydrolysing upon acid addition. The disappearance of the aldehyde resonances at higher acid concentration has been investigated by measuring the ^{1}H NMR of all-*trans* retinal in presence of TFA, clearly revealing some unidentified degradation products, which do not reconvert back to the starting material following neutralisation. CW

irradiation experiments in deuterated solvent revealed the formation of photoproducts but the existence of hydrolysis equilibria and irreversible degradation of the aldehyde (Figure 5.3.6 and Scheme 5.3.2) rendered it impossible to obtain reliable values for the QY. Neither the use of deuterated methanol dried over alumina nor the use of TFA from a newly opened bottle (less likely to be contaminated by water) improved the compound stability.

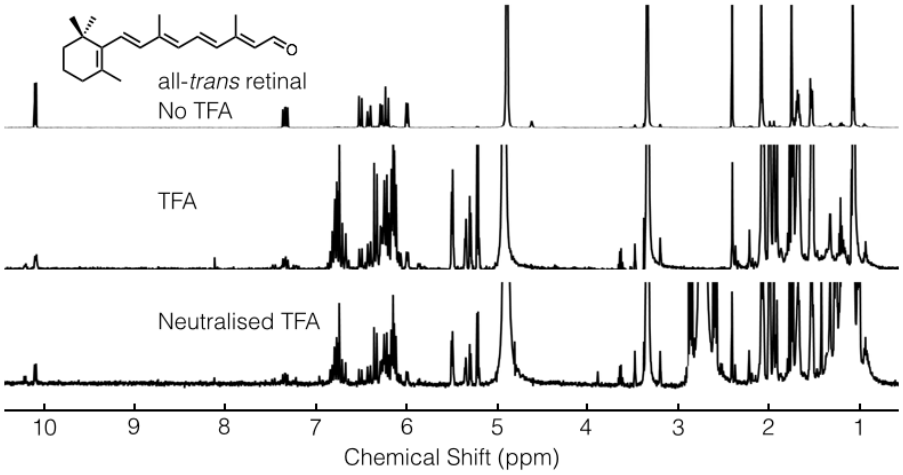

Figure 5.3.6 ^{1}H NMR spectrum of all-*trans* retinal aldehyde in MeOH (top) upon addition of TFA (middle) and neutralisation of the acid (bottom). In the last two spectra new resonances appear which do not change upon neutralisation, indicating irreversible formation of degradation products.

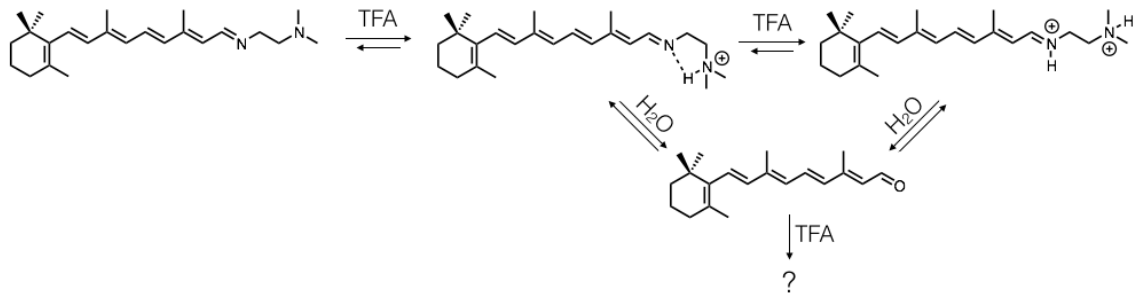

Scheme 5.3.1 Hydrolysis scheme for **C2** including degradation of the all-*trans* retinal aldehyde as evidenced in Figure 5.3.6.

Increasing the length of the alkyl chain between the two positive charges in **C4** resulted in a considerably smaller red shift of the absorption maximum (10 nm, vs. 24 nm observed for **C2**, Figure 5.3.7).

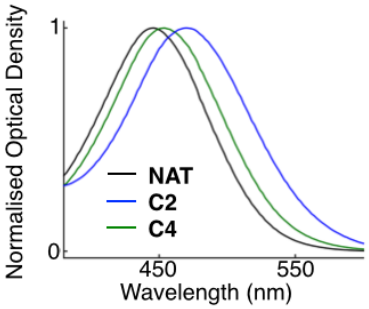

Figure 5.3.7 Comparison of the absorption spectra for **NAT** (black), **C2** (blue) and **C4** (green) in MeOH.

^{1}H NMR spectra at increasing acid concentration have been taken in a similar fashion as described above, and are shown in Figure 5.3.8 (low field) and 5.3.9 (high field). From the comparison with the free amine, clear signatures of double protonation appear while inspection of the low field region reveals no evidence of hydrolysis. Both the geminal methyl groups (green dots in the SB and red dots in the free amine, 2-3 ppm region) and the H15 proton of the Schiff base (blue dot, 8-9 ppm) shift at low field upon increasing amount of acid, similarly to what observed for **C2**.

In the low field region (6-10 ppm, Figure 5.3.9), the lack of any resonance below 10 ppm or of the doublet of doublets at 7.3 ppm supports the absence of hydrolytic processes for **C4**, in contrast to what observed for **C2**.

Irradiation experiments conducted with a CW 532 nm diode laser in deuterated MeOH revealed the formation of two photoproducts (Figures 5.3.10), with a QY of 0.21 and 0.08, respectively.

A comparison of the new resonances appearing in the low field region (between 6 and 7 ppm) of the spectrum with the spectra of the 11-*cis* (red) and 9-*cis* (blue) isomers of **NAT** RPSB is also shown in Figure 5.3.10. This comparison can be made under the assumption that the distant second positive charge does not dramatically affect the chemical shift of the polyenic chain protons. If this hypothesis holds, the similarities of the spectra suggest the main and secondary photoproducts to be 11-*cis* and 9-*cis*, respectively.

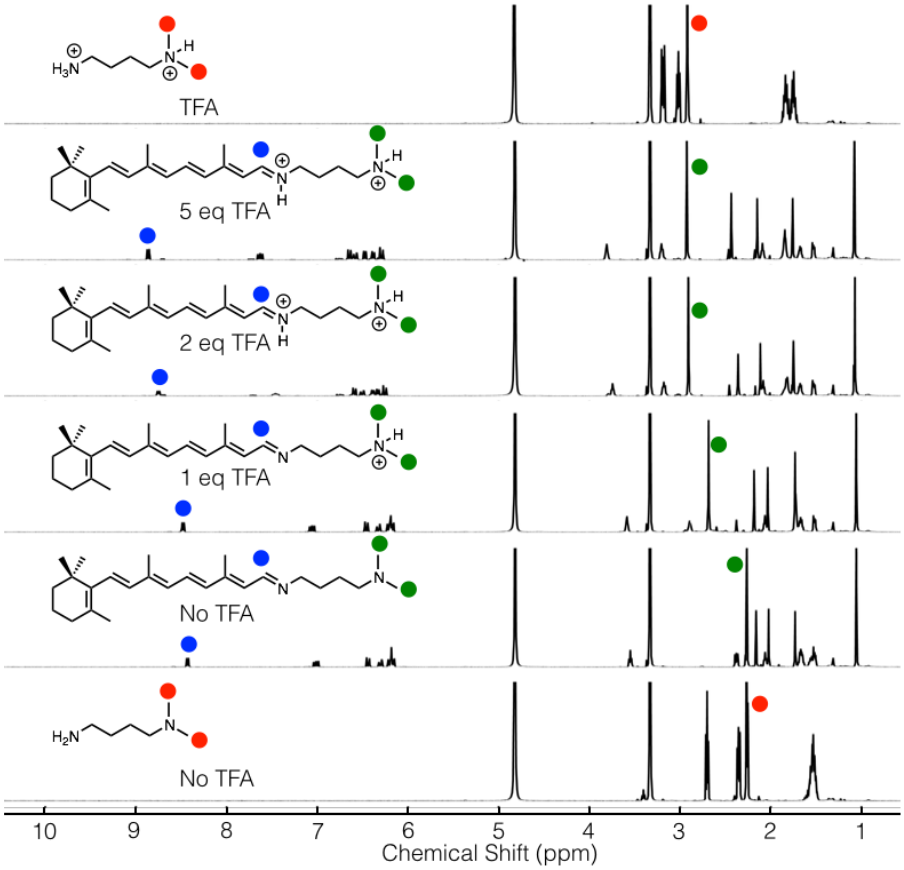

Figure 5.3.8 ^{1}H NMR spectra for the free amine and **C4** at increasing acid concentration. Assigned resonances are marked with colour-coded dots.

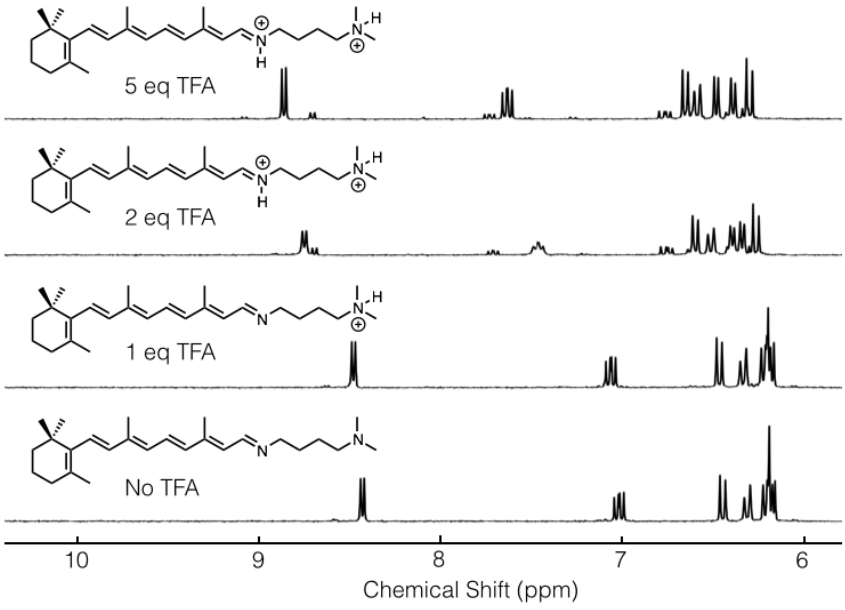

Figure 5.3.9 Expansion of the low field region of the spectra shown in Figure 5.3.8.

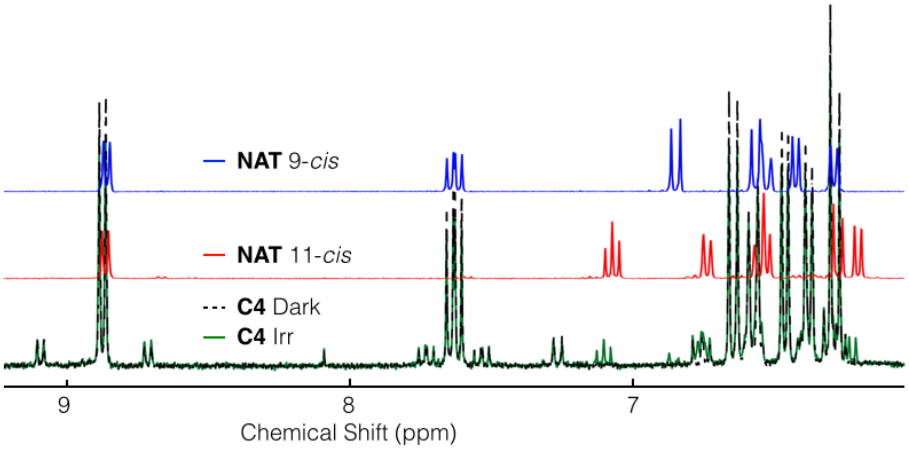

Figure 5.3.10 ^{1}H NMR spectra for **C4** before (black, dashed) and after (green) irradiation. **NAT** spectra of the 11-*cis* (red) and 9-*cis* (blue) isomers are shown for comparison.

5.4 Conclusion

This chapter described the attempt to red shift the absorption of RPSBs in solution by use of different types of amines. A first class of derivatives formed with aromatic amines showed significant bathochromic shift as expected by the extension of conjugation but no photoisomerisation activity was detected. Characterisation of the Franck Condon region via ground state pre-resonant Raman spectroscopy and evaluation of the Merz-Kollman partial atomic charges in the equilibrium position in the S_0 and S_1 did not reveal any significant difference between the nBu model traditionally adopted and the aromatic RPSBs. The excited state of the new derivatives showed marked coherent vibrational activity in the phenyl ring modes and a faster excited state decay for rings bearing electron-donating substituents. These factors together with the known charge transfer character of the CI mediating isomerisation suggested that the observed lack of reactivity might be due to the opening of an alternative decay channel characterised by donation of electronic density towards the polyenic chain from the phenyl ring rather than from the β-ionone end of the molecule. Further testing of this hypothesis was attempted by preparing derivatives with rings bearing strong electron-withdrawing groups, but their synthesis failed, probably due to the lack of reactivity of the

starting amine. Use of different solvents, Lewis acids or strong bases did not improve the yield beyond 50% as judged by ^{1}H NMR. A second class of derivatives was prepared with amines bearing a dimethylamino group at the other end of a linear alkyl chain. A first RPSB prepared with N',N'-dimethylaminoethylamine proved unstable in MeOH upon protonation, undergoing hydrolysis even at low TFA concentration. A second derivative was prepared using a longer linking chain between the two positively charged nitrogen atoms. The latter derivative was stable, but effects on the photochemistry were only marginal.

Chapter 6

Tuneable photochemistry of the GFP chromophore

Overview

This chapter presents the characterisation via time-domain impulsive Raman spectroscopy of the ground and first excited electronic states for the green fluorescent protein chromophore in solution, wild-type GFP (**wtGFP**) and two GFP mutants. Time-domain Raman is first employed to observe the vibrational signatures of the excited state proton transfer in **wtGFP**, providing for the first time Raman spectra of both excited states involved in the proton transfer and fluorescence of the protein. A comparison with the excited state Raman of the chromophore in DMSO solution as well as of two widely used GFP mutants follows. Finally, the wavelength-dispersed detection of the probe pulse is exploited together with the difference in absorption maxima of the protonated and deprotonated states of **wtGFP** to obtain for the first time separate ground state spectra for the protonated and deprotonated forms. Measurements of the excited state time-domain Raman spectra have been performed by Christoph Schnedermann. Measurement of the time-domain ground state Raman spectra have been performed by Alex Soares Duarte, whilst the frequency domain ground state

Raman spectrum has been kindly provided by Tullio Scopigno's research group at the University of Rome. The proteins have been expressed and purified with the assistance of Idlir Liko and Art Laganowski. Chromophore preparation and all data analysis have been performed by the author.

6.1 Photochemistry of the GFP chromophore

The third case study presented in this investigation of tuneable photochemistry in photoactive proteins is the green fluorescent protein (GFP) chromophore. GFP was chosen as it provides an even more drastic example than retinal protonated Schiff bases when comparing the chromophore photochemistry in solution and in the protein environment (Figure 6.1.1a and b).

The absorption spectrum of **wtGFP** (Figure 6.1.1c, top) is dominated by two bands centred at 397 and 474 nm.[230] Mutagenesis combined with spectroscopic[231,232] and crystallographic studies[233] has attributed their origin to a different orientation of some key residues that modify the hydrogen bonding network in the surrounding of the chromophore stabilising different protonation states. The more abundant state for **wtGFP** is commonly called A. It corresponds to the bluest of the two peaks in the absorption spectrum and has been recognised to have the chromophore protonated from the variation with pH of the absorption of model compounds or partially denatured protein.[233–235] It is 6 times more abundant[39] than the deprotonated state, B. The equilibrium between the A and B seems to be regulated by the protonation state and spatial orientation of the Glu222 residue, as the deprotonated state becomes predominant in mutants where steric constraints break the hydrogen bond network linking it to the chromophore[233] or upon photoinduced decarboxylation of the wild-type protein.[236] Irradiation of the A band triggers an ultrafast excited state proton transfer from the chromophore (A*) to Glu222 mediated by the hydrogen bond network[44,233,237] to generate a deprotonated excited state, called I*,[44] that emits at 509 nm with a time constant of

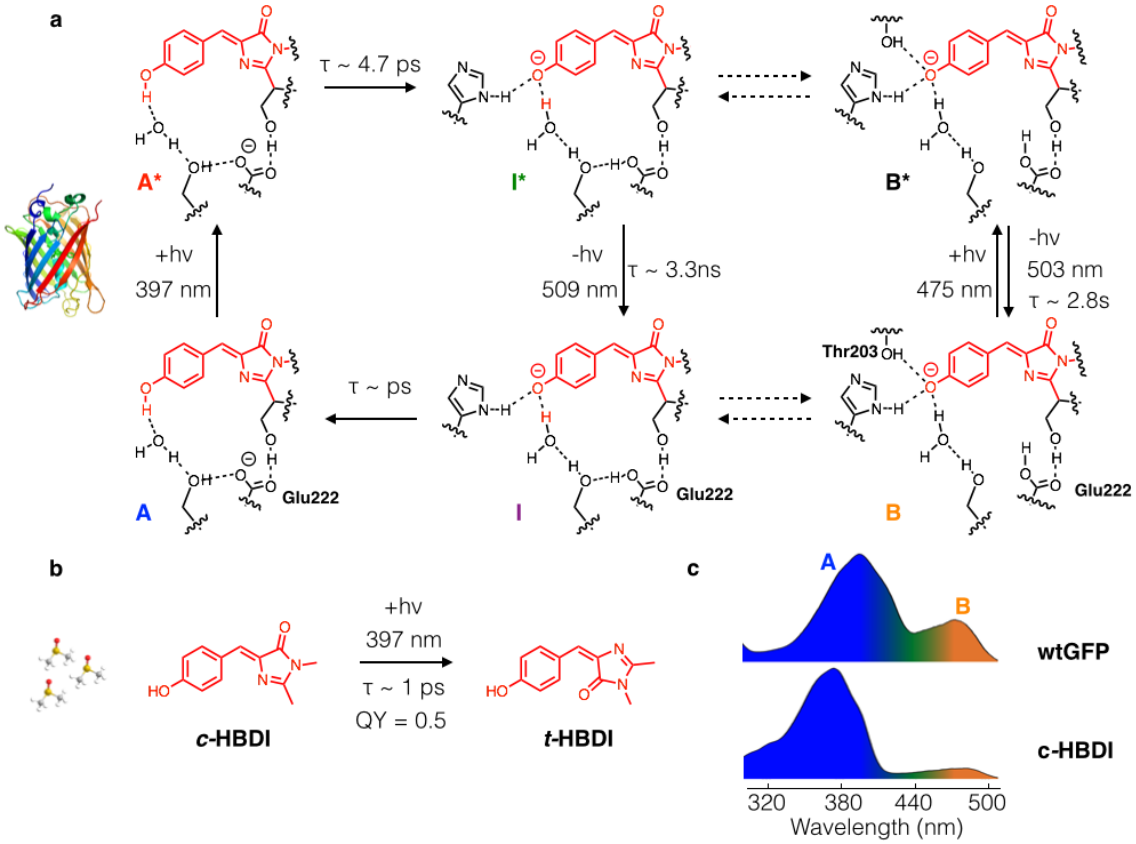

Figure 6.1.1 (a) **wtGFP** and (b) **HBDI** photochemistry. Absorption and emission maxima as well as time constants are indicated close to the arrows representing the respective processes. The dashed arrows in (a) represent possible but very infrequent interconversion between the two species. (c) Absorption spectra of **wtGFP** (top) and **HBDI** in DMSO (bottom). The colours match the protonation state of the phenolic hydroxyl in the corresponding band, blue for the neutral form and orange for the anionic one. GFP structure plotted from 1GFL entry of the RCSB protein data bank.[229]

$\sim$3.3 ns.[237–239] According to the structural model by Brejc et al.,[233] A*, I* and the relative ground states differ only by the position of the protons along the hydrogen bonding network, whilst B differs by the spatial orientation of Thr203 and Glu222. The interconversion between A (through I) and B, and I* and B* is slow and inefficient,[44,237] so that excitation in the A band triggers a photocycle involving only A and I states. Photoexcitation of the B band results in emission at 503 nm from the corresponding excited state B* with a lifetime of 2.8 ns.[239]

To compare the photochemical behaviour in solution, one of the smallest models for the **wtGFP** chromophore is 4-(*p*-hydroxybenzylidene)-1,2-dimethylimidazol-5-one (**HBDI**).[240–244] In neutral and acidic solution, its absorption maximum is at 375 nm, with a shoulder at 480 nm, that becomes predominant in alkaline environment.[235] That the protein environment is critical for the chromophore fluorescence was already known by denaturation studies.[45] Examining the photochemistry of **HBDI**, revealed an excited state lifetime over 3 orders of magnitude shorter, on the order $\sim$1 ps. The rapid deactivation is due to a very efficient *cis-trans* photoisomerisation (quantum yield, QY, $\sim$0.5)[46] around the central double bond, yielding *t*-**HBDI** (Figure 6.1.1b). This photoproduct is unstable in the presence of nucleophiles,[245] rendering the choice of solvent critical when studying the photochemistry. For the present work, DMSO was chosen, as **HBDI** proved to be scarcely soluble at the concentrations required for the spectroscopic work intended in most of the other common non-nucleophilic solvents.

6.1.1 Current understanding of HBDI and wtGFP photochemistry

GFP was first discovered in 1962 as a byproduct during purification of aequorin from *Aequorea Victoria*,[246,247] and eventually recognised in 1974 as the emitter in the jellyfish.[40] Five years later, the structure of its fluorophore was determined, and the complete loss of fluorescence upon denaturation[45] demonstrated the effect of the protein environment on its pho-

tochemical evolution. Since the 1990s, once GFP recombinant expression techniques[42,248] became available and, more importantly, the potential of the protein as a marker for fluorescence imaging[42] was understood, a huge amount of experimental work has been devoted to generate mutants to broaden the spectral range of absorption and emission maxima,[232,249–252] as well as to gain a better understanding of the factors determining the contrasting behaviour in solution and in the correctly folded protein.[48,253–257] The main approach adopted to study the origins of the observed photopysics for **wtGFP** and its chromophore has been to obtain high resolution crystal structures and electronic and vibrational spectroscopic data of the protein, model compounds and carefully engineered mutants, eventually complemented by computational investigations.

Some of the most relevant results were obtained by comparison of the crystal structures for the **wtGFP** and the **S65T** mutant resulting in a model for the GFP photocycle and explaining the dual absorbance and emission discussed above.[233] When adopting the same mutant as a model for the deprotonated state, caution must be taken as the residues surrounding the chromophore are differently oriented than for the **wtGFP** B state, thus leading to some small differences in the absorption and emission maximum[233] (474 vs. 488 nm and 503 vs. 509 nm, for the B state and **S65T**, respectively). These differences have not prevented researchers from using **S65T** or other mutants in vibrational or electronic spectroscopic studies. The first studies of ground state Raman and IR spectra were devoted to mode assignment and characterisation. Raman spectra in solution of ^{13}C or ^{2}H labelled **HBDI**,[244] or solid state IR,[241] sometimes complemented by computational studies[258,259] made it possible to assign the dominant vibrational modes. Comparison of a close analogue of **HBDI** as a chromophore model with **wtGFP** and **S65T** spectra at different pH were used to confirm the protonation state of the phenolic hydroxyl in the protein.[47] Judging by the ground state Raman spectra, and similarly to what was observed in Chapter 5 when comparing the aromatic protonated Schiff base (PSB) derivatives with the *n*-butylamine PSB, the initial evolution out of the

Franck Condon (FC) region seems to be similar in all these environments, with stretching modes in the 1500-1600 cm^{-1} region being predominant. Very little activity is observed below 1000 cm^{-1}, and, in general, not much spectroscopic information is available in that region.

Femtosecond transient absorption spectroscopy coupled with electronic population control has been applied to follow the recovery dynamics of the A state from the intermediate I state,[254] whilst high time resolution pump-probe experiments allowed detection of low frequency (497 cm^{-1}) excited state coherence.[260] More information on the excited state vibrational spectra was obtained by transient IR.[261] A study comparing **HBDI**, **wtGFP**, **S65T** and **T203V/E222Q** (a double point mutant proposed to exist in the ground state in the I configuration)[262] assigned some high-frequency mode (1706 cm^{-1} and 1565 cm^{-1}) to changes in the observed stretching frequencies of Glu222 following the proton transfer reaction.[51] Femtosecond stimulated Raman spectroscopy has also been applied to follow the decay of A*, but no spectra was reported for I*.[255]

In the present chapter, time domain impulsive Raman spectroscopy is used to follow the excited state proton transfer in **wtGFP**, and then to compare the spectra obtained for A* and I* states with the one recorded for the S_1 state of **HBDI** in DMSO, the B* state of **wtGFP** and the excited state of the deprotonated mutants **S65T** and superfolder GFP (**sGFP**).[263] **S65T** is a single point mutant, whilst **sGFP** presents the S65T plus several other mutations, and is chosen to observe the effect of multiple mutations on the Raman spectrum compared to a single-point mutant. Finally, ground state only coherences are probed in the spectral region of the absorption maximum of **wtGFP**, and an attempt is described to disentangle the A and B states contributions to the Raman spectrum. The technique adopted here is complementary to existing transient IR studies, but offers greater sensitivity to the chromophore and its immediate environment rather than to the protein residues.

6.2 Preparation of studied compounds

6.2.1 Synthesis of HBDI

HBDI was prepared following the synthetic scheme suggested by Lee et al.[264] (Scheme 6.2.1).

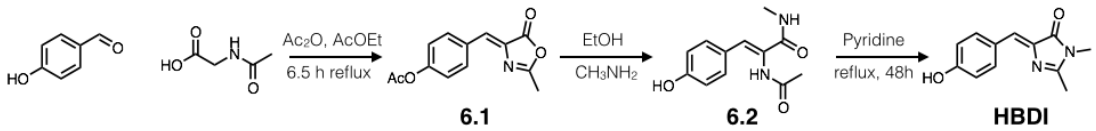

Scheme 6.2.1 Synthesis of **HBDI**

First N-acetylglycine was condensed with *p*-hydroxybenzaldehyde in acetic anhydride in presence of sodium acetate. Possibly due to some slight differences in the work-up procedure, the phenolic hydroxyl of the oxazolone (**6.1**) obtained was acetylated rather than free, as supported by the NMR and mass spectrometry data reported in Appendix D. No adjustment to the synthetic procedure was needed as the excess methylamine used in the subsequent ring opening step removed the undesired acetyl. The linear acrylamide (**6.2**) was then cyclised in refluxing pyridine for 48 hours. Pure **HBDI** was isolated from pyridine following acidified H_2O/EtOAc extraction. Characterisation data for the intermediates and HBDI are provided in Appendix D.

6.2.2 Preparation of wtGFP, S65T and sGFP

Fluorescent proteins **wtGFP**, **S65T** or **sGFP** modified with a 6xHis tag were expressed and purified with the assistance of Idlir Liko and Art Laganowsky following standard protocols.[42,248] The procedure is described in Appendix D. The final sample had an OD of 9-10 at λ=397 nm for **wtGFP**, OD 12 at λ=484 nm for **sGFP** and OD 16 at λ=488 nm for **S65T**.

6.3 Excited state Raman spectra

Time domain impulsive Raman spectra of the excited state were recorded following the two approaches discussed in Chapter 2 and briefly recalled below. For both **HBDI** and the GFPs, excited state population and vibrational coherences were generated by different pulses. Details on the pulses used will be given in the relevant sections. All the fitting and decomposition routines described in the present and the following sections have been performed on intensity spectra (absolute of the Fourier transform), whilst all the plotted spectra are power spectra (squared absolute of the Fourier transform). As the three proteins were measured in aqueous buffers, the solvent contribution to the detected vibrational activity was negligible, and scaled subtraction of the trace in the presence and absence of the Raman pump after subtraction of the electronic dynamics was sufficient to isolate the excited state vibrations, according to Equations 2.2.9-10.

$$\mathrm{ON} = a \cdot \chi_{\mathrm{solv}} + b \cdot \chi_{\mathrm{S_0}} + c \cdot \chi_{\mathrm{S_1}}, \tag{2.2.9}$$

$$\mathrm{OFF} = a' \chi_{\mathrm{solv}} + b' \cdot \chi_{\mathrm{S_0}}. \tag{2.2.10}$$

The oscillating signal obtained in this way was apodised with a Kaiser-Bessel window (β= 4) and Fourier transformed to a final size of 8192 points in the frequency domain. All shown spectra are power spectra obtained by squaring the modulus of the Fourier transformed oscillations and averaging in the 530-645 nm spectral region, corresponding to the stimulated emission (SE) bands isoenergetic with the fluorescence (Figure 6.3.1)

The chromophore was measured in DMSO. The solvent, being a strong Raman scatterer, dominated the retrieved coherences. In order to obtain solvent-free excited state coherences, a fourth dump pulse had to be used to depopulate the excited state. Direct subtraction of

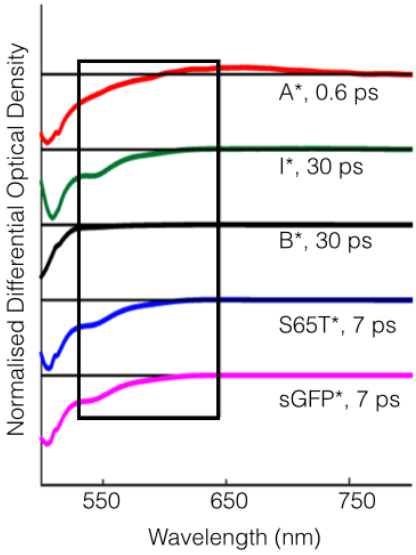

Figure 6.3.1 Normalised transient absorption spectra for all GFPs considered at the indicated delay after excitation. The black rectangle indicates the spectral region used to average the excited state coherences when generating the Raman spectra.

the traces in presence and absence of the dump pulse yielded isolated S_1 VC, according to Equations 2.2.11-12.

$$\mathrm{ON_{ACT}OFF_{DUMP}} = a \cdot \chi_{\mathrm{solv}} + b \cdot \chi_{\mathrm{S_0}} + c \cdot \chi_{\mathrm{S_1}}, \tag{2.2.11}$$

$$\mathrm{ON_{ACT}ON_{DUMP}} = a \cdot \chi_{\mathrm{solv}} + b \cdot \chi_{\mathrm{S_0}} + c(1-\gamma) \cdot \chi_{\mathrm{S_1}}. \tag{2.2.12}$$

The same apodisation, zero-padding and Fourier transform routines used for the proteins were applied. The excited state spectra were obtained by averaging probe dynamics in the 600-850 nm region (Figure 6.3.2), where excited state absorption (ESA) and SE are likely present simultaneously resulting in the observed signal shape.[265]

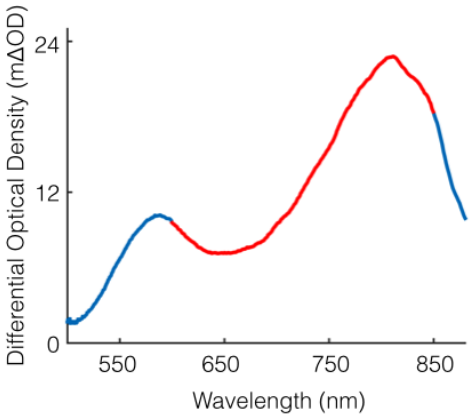

Figure 6.3.2 Transient absorption spectrum at 0.5 ps of **HBDI** in DMSO. The vibrational spectra shown have been obtained by averaging over the spectral region marked in red.

6.3.1 Following wtGFP excited state proton transfer

To follow the structural changes brought about by excited state proton transfer reaction in **wtGFP**, a series of spectra have been measured exciting the protein in the A band and varying the delay (T) between the excitation pulse and the Raman pump. A 250 fs actinic pulse (80 nJ) was centred at 400 nm whilst the 9.4 fs Raman pump (320 nJ) was centred at 800 nm. The probe pulse was scanned from a delay of -150 fs to 3 ps with respect to the Raman pump. The power spectra obtained as a function of the delay time T are shown in Figure 6.3.3 (gray lines), together with the fit retrieved from a global optimisation routine (orange fill).

The lack of Raman activity at negative actinic-Raman pump delays shows the efficacy of the subtraction of the ground state features. In an attempt to obtain "pure" spectra for A* and I* the same global fitting routine presented in Chapter 2 and applied for the analysis of the electronic dynamics of the retinal protonated Schiff bases has been applied to the GFP dataset. A good fit (orange fill) could be obtained by using a single exponential time constant (τ= 4.7 ps) and a long lived offset. As the actinic-Raman pump delay spanned only 15 ps, no significant decay was observed for the I* state and thus a long-lived offset was an adequate description for its contribution. According to the electronic dynamics, the decay of A* has been usually described as "intrinsically" multi-exponential (2 and 11 ps),[254]

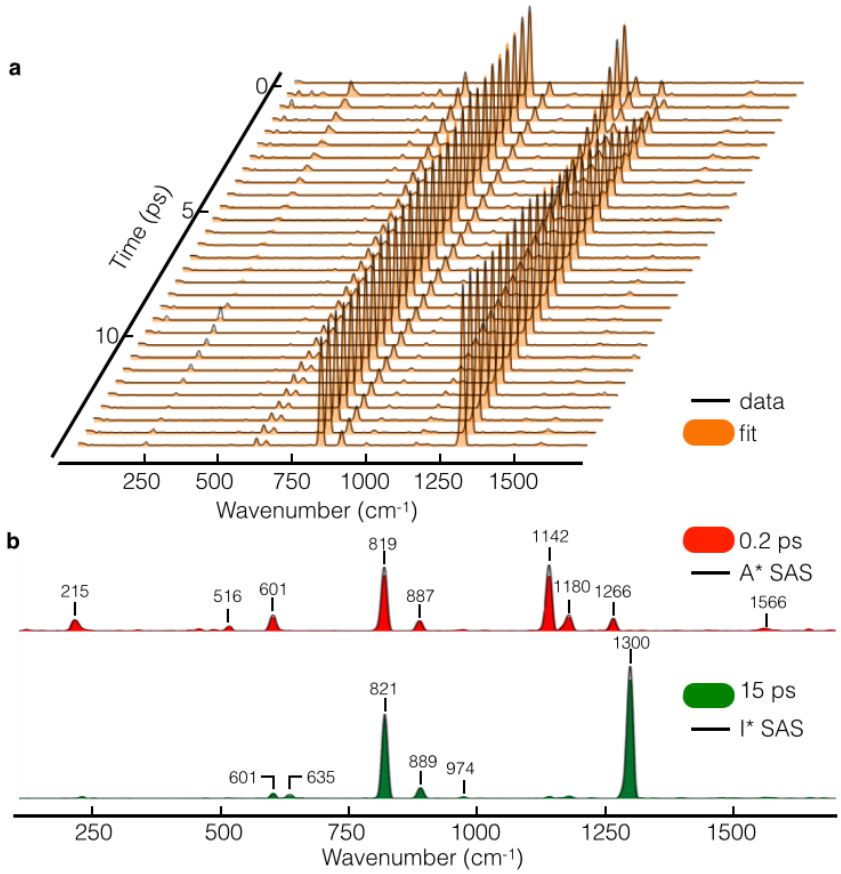

Figure 6.3.3 Evolution of the **wtGFP** excited state Raman spectra during the first 15 ps following excitation (a). Data is given in black, whilst the retrieved fit is plotted as orange fill. (b) Comparison between the species associated spectra (SAS) retrieved for A* (top) and I* (bottom) and the first (0.2 ps, red fill) and last (15 ps, green fill) excited state Raman spectra acquired in the probed time range.

and some researchers advanced the idea of ground state inhomogeneity.[261] The fact that a single time constant is sufficient to fit the presented data may be due to an insufficient signal to noise ratio for the data along the actinic-Raman pump delay T dimension or due to the electronic dynamics being sensitive to spectral shift that do not affect the recorded vibrational spectra. In contrast to the retinal protonated Schiff bases, a kinetic model was applied to the retrieved amplitudes of the exponential term and the offset to obtain the spectra associated species (SAS)[69] for A* and I*. In this case, a linear sequential model was applied, corresponding to the simplest possible scenario where it is assumed that at t_0 only A* is present and decays to I* with the retrieved time constant.[266] The SAS for I* thus corresponds directly to the amplitude retrieved for the long lived offset, whilst the one for A* corresponds to the sum of the decay associated spectrum retrieved for the 4.7 ps time constant and the offset amplitude.[266]

In Figure 6.3.3b the spectra recorded at the first and last positive actinic-Raman pump delay are overlapped (0.2 and 15 ps) with the retrieved SAS for A* and I*. The first spectrum recorded at positive delays T (0.2 ps, red filling) as well as the SAS for A* (plotted in black on top) are dominated by modes below 1300 cm^{-1} with the exception of a small peak at 1566 cm^{-1}. The bands are classified according to their temporal behaviour: there is a first set of bands that is present all the way through the 15 ps observation window, with possibly a small frequency shift but no significant change in intensity, at 819 (821), 887 (889) and 601 cm^{-1}. In the ground state, these have all been identified as ring deformation modes.[241,255,258–260] The values in parenthesis refer to the frequencies for the same peaks in the spectrum at 15 ps actinic-dump delay. Other bands, specifically the 1142, 1180, 1266 and 1566 cm^{-1}, exhibit a steady decrease in intensity, and can be assigned to the disappearing protonated species A*. These have been identified as CH rocking of the phenol ring (1142 cm^{-1}, 1180 cm^{-1}),[244,255,258] C-O stretching of the phenol (1266 cm^{-1})[47,258,261] and C=N or C=C stretch (1566 cm^{-1}) of the imidazolinone ring.[241,244,258] Finally, a third set of bands is seen growing

in, and can be assigned to the deprotonated state I*. The most evident of these is the C-O stretching of the phenolate anion at 1300 cm^{-1}.[47,261]

The resemblance between the experimental and species associated spectra enabled a complementary type of analysis (referred to as *self-fit*) fitting each spectrum S acquired at a time T as a linear combination of a "model spectrum" for A* and I*, according to equations 6.3.1.

$$S(T) = A^{*} \cdot C_A(T) + I^{*} \cdot C_I(T), \tag{6.3.1}$$

$$C_A(T) + C_I(T) = 1. \tag{6.3.2}$$

A least-square minimisation algorithm was employed to find the best series of coefficients $C_I(T)$, with the additional constraint of the total spectrum to be zero for negative values of the actinic-dump delay T. No other constraint was added. As model spectra, the 0.2 ps and 15 ps were used for A* and I*, respectively (and hence the name of the approach). The algorithm was run with several starting guesses for $C_I(T)$ (dashed coloured lines in Figure 6.3.4a) and all converged to the same solution (solid line in Figure 6.3.4a). The agreement between the average of the solutions obtained for $C_A(T)$ and $C_I(T)$ (open circles in Figure 6.3.4b) from the self-fit and the time behaviour retrieved for A* and I* from the global fitting routine (solid lines) suggests that the approximations made in modelling the system are reasonable, even though the imperfect match at later time points does not exclude the possibility of more complicated dynamics. Attempts to fit the excited state Raman spectral map with two time constants and an offset did not yield significant improvement of the fit quality. A 1.7 ps time constant was found with a decay associated spectrum where no peaks were clearly distinguishable, but only dispersive features and noise. The decay associated spectrum for the second 4.9 ps time constant retrieved is identical to the one retrieved for the 4.7 ps time constant discussed above, as is the offset. It should also be considered that in the self-fit routine no assumptions are made on the time behaviour of the coefficients, so that

the retrieved results are not necessarily exponential – on the contrary of the global fit that models all the species decays as exponential processes.

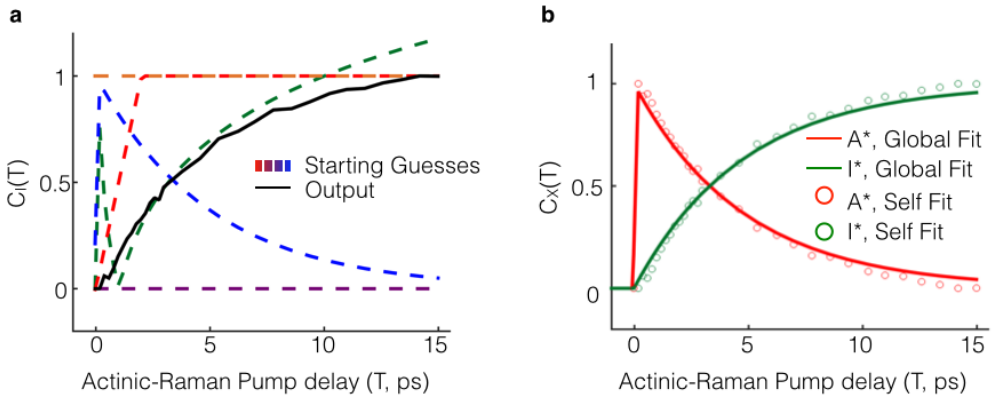

Figure 6.3.4 Comparison of fitting routines outcomes for the **wtGFP** transient Raman data form Figure 6.3.3. (a) Starting guesses (dashed coloured lines) used for the self-fit of $C_I(T)$ and retrieved coefficients (black solid line). (b) Comparison of the coefficients retrieved via the self-fit routine for A* and I* (red and green open circles) with the concentration of the same species (solid lines) as a function of time retrieved from the sequential analysis of the global optimisation results.

6.3.2 Comparison of excited state Raman spectra

Before comparing the S_1 Raman spectrum of **HBDI** in solution, I measured its photoisomerisation QYd relative to the one reported in THF (∼50%),[46] and found it to be equal in the two solvents. Details of the measurements performed can be found in Appendix D.

The power spectra of excited state vibrational activity are shown in Figure 6.3.5. The **wtGFP** spectra shown in Figure 6.3.3 were recorded on a different occasion than the one in Figure 6.3.5, and different effective time resolutions of the experiments might explain the observed differences in intensities for the high frequency band. **HBDI** and **wtGFP** were excited with a pulse centered at 400 nm, whilst the deprotonated mutants **S65T** and **sGFP**, and the B* spectrum of **wtGFP** were obtained by exciting the proteins with a pulse centred at 490 nm. In all cases, the Raman pump was a 9 fs pulse centred at 800 nm (150 nJ). For the **HBDI** experiments, a 200 fs dump pulse centred at 760 nm depleted the S_1 excited state population.

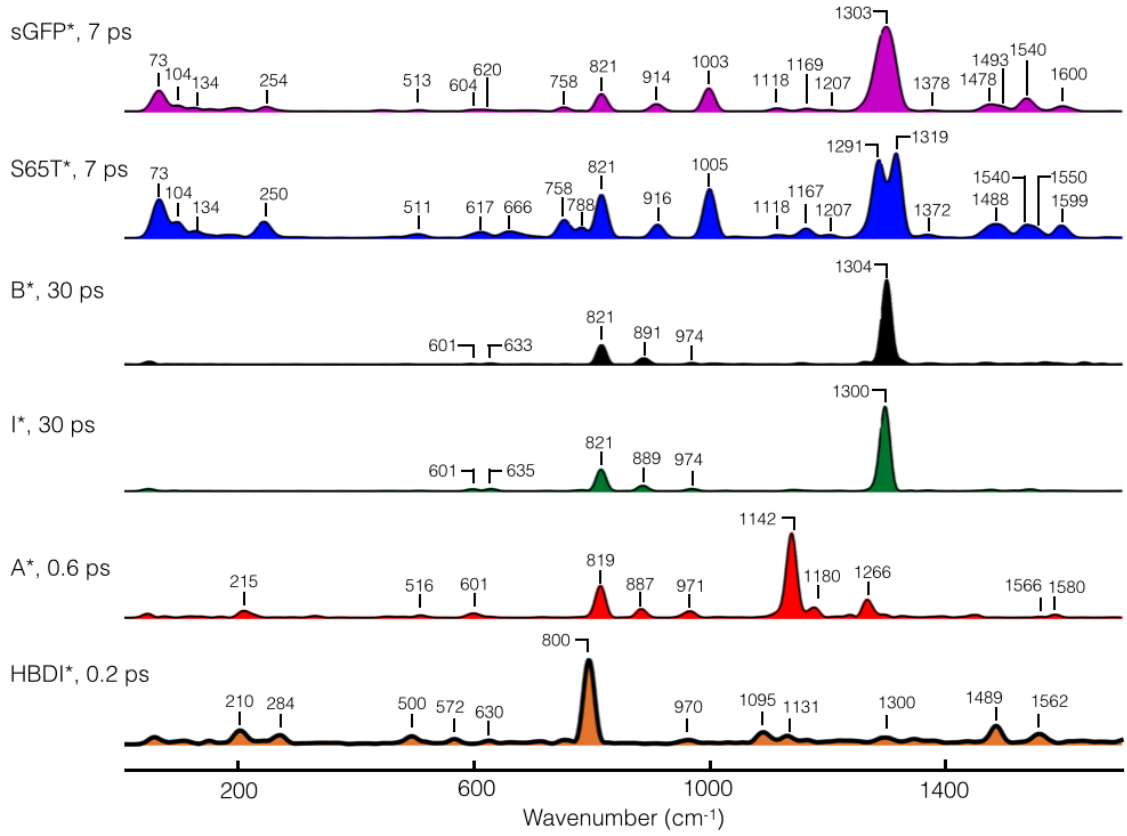

Figure 6.3.5 Excited state Raman spectra for **HBDI** (orange), **wtGFP** A* state (red), **wtGFP** I* state (green), **wtGFP** B* state (black), **S65T** (blue) and **sGFP** (purple). .

The S_1 Raman spectrum of **HBDI** and the A* state of **wtGFP** seem to have only a few peaks in common: the 800 cm^{-1} (819 cm^{-1} in the protein), assigned to ring deformation modes, the 210 cm^{-1}, and some double bond stretching around 1560 cm^{-1}. In the **HBDI** S_1 spectrum the dominant band is the 800 cm^{-1} ring deformation, and only very weak activity is observed from the other modes. The fact that the spectrum has been corrected for effective time resolution as described in Chapter 2[74] and consideration of the entity of the observed difference in band intensity within the spectrum make it unlikely to ascribe the lack of intensity of higher wavenumber bands to time resolution issues. In remarkable contrast, for the protonated chromophore in the protein, the 1142 cm^{-1} CH rock of the phenyl ring dominates, but other peaks as described above still show significant intensity. In the light of the known different outcome of the photochemistry in solution and in the protein, the differences might be explained in terms of the protein inhibition of the photoisomerisation reaction, possibly by steric constraints within the chromophore binding pocket.[255] It would be expected that during the isomerisation process **HBDI** assumes a significantly distorted molecular geometry, possibly resulting in a reduction of the intensity for most of the vibrational modes if compared to the proton transfer process occurring in the protein. The very little vibrational excited state activity observed in solution for the stretching modes that, instead, dominate the ground state spectra,[47] is in line with what would be expected for an ultrafast isomerisation reaction,[267] much alike the RPSB case discussed in the previous chapters.

Another remarkable feature of these spectra is the difference between the deprotonated **wtGFP** spectra (I* and B*) and the deprotonated mutants **S65T*** and **sGFP***. Whilst all are dominated by the C-O stretching appearing around 1300 cm^{-1}, the exact position between all the species is slightly different, and in the case of **S65T** a clear splitting is observed in two bands at 1291 and 1319 cm^{-1}. This might be due to the chromophore existing in a less homogeneous environment than expected. The crystal structure for **S65T** has the

phenolate anion hydrogen bonded with two residues (Hys148 and Thr203) and a water molecule (W318),[233] but this picture is only valid for the ground state. As the excited GFP chromophore in the protein behaves as a strong photoacid, one can envision conformations in the excited state where some of these hydrogen bonds are broken, resulting in the red shifted band at 1290 cm^{-1}. For all the other deprotonated states, a single peak is observed, and all the frequencies fall in a 5 cm^{-1} range, but it should be noted that in the **sGFP** case the peak is significantly broader. This might indicate that the chromophore in **sGFP** exists in a similar hydrogen bonded environment as for **S65T**, or that rapid equilibration between several states interconverts within the time window used for probing the vibrational coherences.

The other difference between the excited state spectra of the wild-type and the mutants is the presence of significant activity at low (<800 cm^{-1}) and high (>1300 cm^{-1}) frequencies, suggesting a tighter environment for the chromophore. The relative intensity in the 800-1000 cm^{-1} range, where ring deformation modes usually appear, is significantly stronger for the mutants, again supporting the idea of a tighter environment in the deprotonated mutants. It cannot be excluded, though, that the different orientation of some bonds in the closeness of the chromophore produces dipolar electrostatic interactions that are partially responsible for some of the differences.[233]

6.4 Isolating the ground state Raman spectra of wtGFP A and B states

This final section describes an attempt to obtain separate Raman spectra for the ground state of the A and B forms of **wtGFP**. Ground state Raman spectra have already been reported for **wtGFP**,[47] but as the protein exists as a mixture of the A and B states[39,230,233] all the frequency domain spectra necessarily present contributions from both states. Time-domain Raman signals detected in a wavelength-dispersed manner as in the present case might

offer a way to disentangle the two contributions, as the intensity of the ground state Raman activity is expected to be related to the absorption maximum of each species.[268] For this reason, ground state VC were excited with 9 fs pulses centred at 520 nm, and probed in the 420-490 nm spectral region, covering the red edge of the A state absorption and most of the B band (Figure 6.4.1). As the system was not excited by the Raman pump, only ground state oscillations are expected - the aqueous buffer contribution being a poor Raman scatterer.

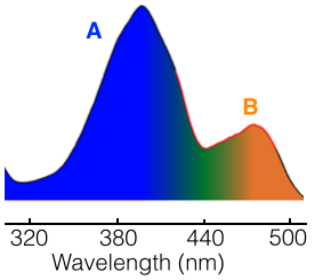

Figure 6.4.1 Ground state absorption spectrum of **wtGFP**. The probed spectral region for retrieving the coherences is marked in red.

An oscillating signal analogous to the ones discussed above was recorded and analysed in a similar fashion. The transient absorption trace was cut at 100 fs after the overlapping of the Raman pump with the probe pulse to avoid contributions to the signal from the coherent artefact arising from mixed order interactions of the Raman pump and probe,[60] and a third degree polynomial was subtracted to remove residual signals possibly due to two photon processes. The isolated coherences were apodised with a Kaiser-Bessel window (β=4) and Fourier transformed to yield 8192 points in the frequency domain. Each wavelength was corrected for the effective time resolution as described in Chapter 2. The resulting Fourier transform map and the spectrum averaged over the whole frequency domain probed are shown in Figure 6.4.2. The averaged spectrum compare sensibly well with the ground state Raman spectrum reported in literature[47] and the one measured by frequency-domain stimulated Raman spectroscopy (black in Figure 6.4.2). Differences in the band intensities

can be explained by the limited spectral range that was probed. For example, the absorption of the A band has its maximum at 397 nm and possibly spans all the way up to 320 nm. In addition, scaling of the spectrum for the effective time resolution is only approximate.

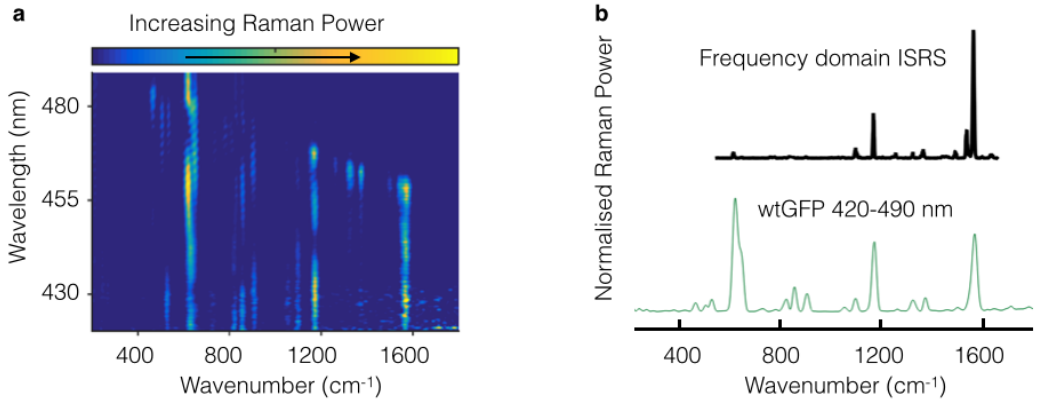

Figure 6.4.2 Wavelength-dispersed Fourier transform map of the ground state coherences induced by the impulsive Raman pump for **wtGFP**. (b). Comparison of ground state **wtGFP** spectra obtained by time-domain (green, averaged between 420 and 490 nm) and frequency domain stimulated Raman spectroscopy (black).

To decompose the Raman map into the individual contributions of the A and B states, it was adopted an approach based on the dependence of the ground state coherent activity described by Pollard et al.[268] The maximum ground state coherent activity upon impulsive excitation with short pulses is expected in the spectral regions where the gradient of the absorption spectrum is greatest. To evaluate these two regions, the absorption spectrum of **wtGFP** was fitted with two three-parameter Gaussians of the type described in Equation 6.4.1.

$$\mathrm{G_X} = F_\mathrm{X} \cdot \frac{2.3546}{\sigma_X \sqrt{2\pi}} e^{-\frac{2.3548^2 \cdot (\lambda - \lambda_{0X})^2}{2\sigma_X^2}}, \tag{6.4.1}$$

where the subscript X refers to species A or B, and the three fitting parameters, F, σ and λ_0 are a scaling factor to take into account the abundance of each species, the full width at half

maximum and the central wavelength of the absorption band, respectively. The results of the fit are shown in Figure 6.4.3.

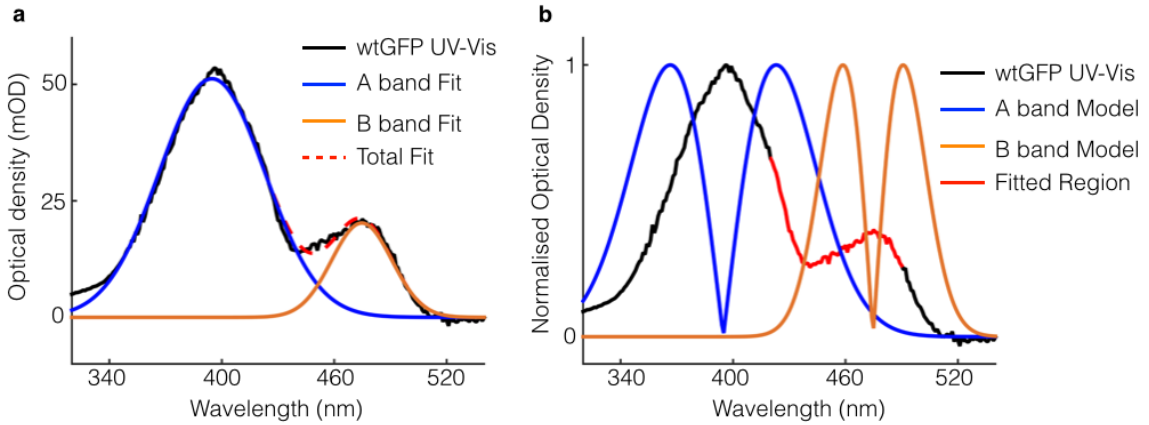

Figure 6.4.3 Fitting of the **wtGFP** absorption spectrum to obtain the amplitude masks to decompose the ground state coherences into A and B contributions. (a) **wtGFP** spectrum (black), fit of the individual A (blue) and B (orange) bands, and total spectrum fitted (red dashed). (b) Amplitude masks used as a model of the activity amplitude for A (blue) and B (orange) state. The **wtGFP** absorption spectrum (black) is plotted in black for completeness. The region where coherent vibrational activity has been probed is highlighted in red.

The derivative with respect to the wavelength was then evaluated for each Gaussian, yielding an "amplitude" mask for the expected coherent activity of each state, according to Equation 6.4.2.

$$\mathrm{A_X}(\lambda) = \frac{d\mathrm{G_X}}{d\lambda} = \frac{2.3546^3}{\sigma_X^3\sqrt{2\pi}} \cdot (\lambda - \lambda_{0X}) e^{-\frac{2.3548^2 \cdot (\lambda - \lambda_{0X})^2}{2\sigma_X^2}}. \tag{6.4.2}$$

The masks generated in this way (Figure 6.4.3b) were normalised and then used to decompose the Fourier transform map, to obtain the associated spectra for A and B. Skipping the normalisation of the masks or including the factor F from Equation 6.4.1 in the derivative given in Equation 6.4.2 results in different amplitudes of the retrieved spectra, but does not change the relative intensity of the bands within the individual spectra. This approach is the analogous in the frequency-wavelength domain of the decomposition in the time-

wavelength domain discussed in previous chapters for the transient absorption data. The Fourier transform map $M(\lambda,\tilde{\omega})$ can be described as the product of the amplitude masks $A(\lambda)$ with the spectra of the individual species $S(\tilde{\omega})$.

$$M(\lambda,\tilde{\omega}) = \sum_X A_X(\lambda) \cdot S_X(\tilde{\omega}). \tag{6.4.3}$$

The Fourier transform maps of the vibrational activity (Figure 6.4.4a) compares well with the decomposition output (Figure 6.4.4b) with most of the residuals being near the absorption maximum of the B state (Figure 6.4.4c). This observation suggests that the coherent activity distribution deviates from the theoretical prediction in proximity of the absorption maximum, where it is inadequately described by a node.

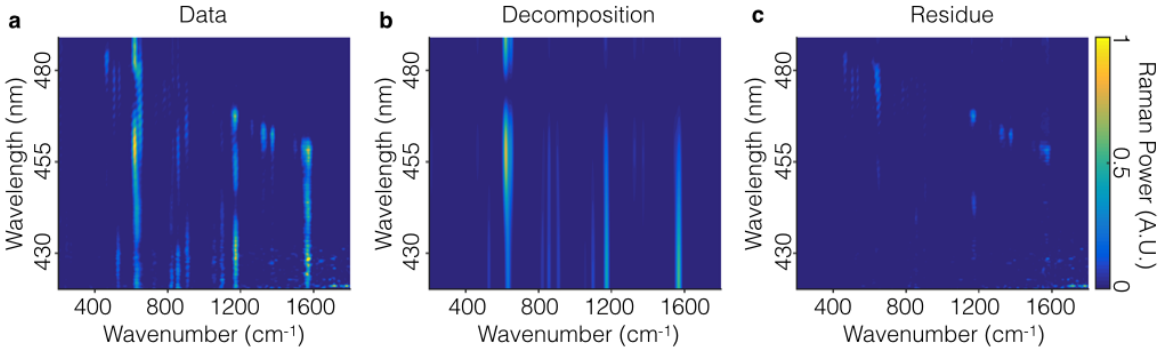

Figure 6.4.4 Outcome of the decomposition algorithm for the Fourier transform coherent activity map. (a) Fourier transform power map of the coherent activity. (b) Reconstructed Fourier transform power map from the decomposition algorithm. (c) Difference between squared experimental (a) and squared reconstructed (b) map. All maps have been plotted with the same colour scale reproduced at the extreme right of the Figure.

The spectra retrieved for the A and B states from this decomposition approach are shown in Figure 6.4.5 (blue and orange, respectively), together with the "traditional" ground state spectrum obtained by averaging over the entire coherence map (black solid line).

Starting from the low wavenumber region, the bands at 465 and 506 cm^{-1} are due to the B state, whilst the 527 cm^{-1} is present only in the A state spectrum. The broad shouldered

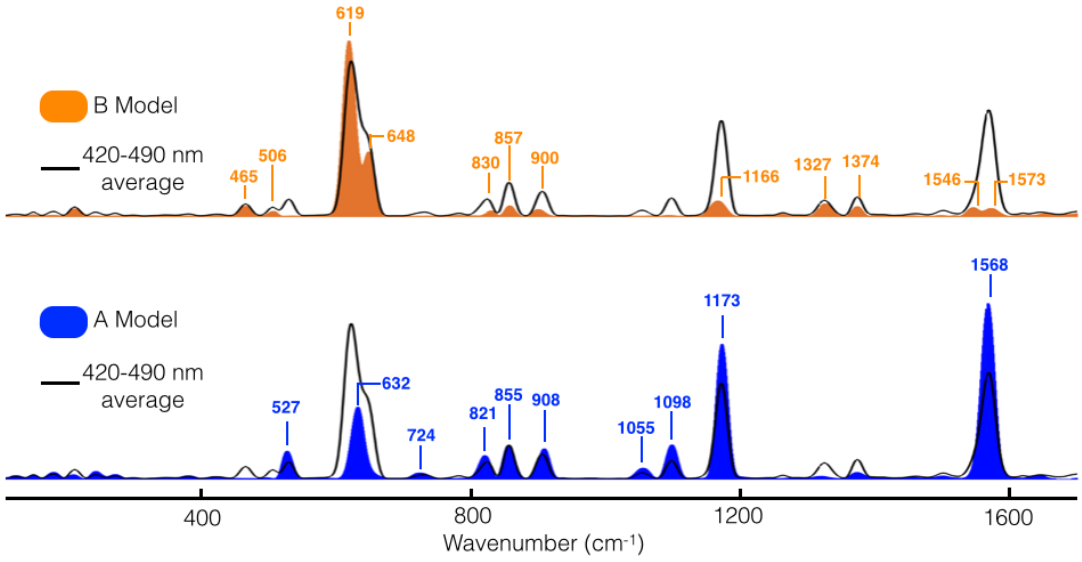

Figure 6.4.5 Deconvolved spectra for the A state (blue, bottom) and B state (orange, top) obtained from the decomposition algorithm. Overlapped is the spectrum obtained by averaging over the entire probed region (black, solid), corresponding to the Raman spectrum usually measured for **wtGFP**.

peak at 620 cm^{-1} is split in two bands in the B state (619 and 648 cm^{-1}), whilst a single peak at the central frequency of 632 cm^{-1} is present in the A state spectrum. Most of the bands between 700 and 1100 cm^{-1} only correspond to the A state spectrum only. In the 830-900 cm^{-1} weak bands are visible in the B spectrum at slightly shifted frequencies than the ones for the A state. The 1173 cm^{-1} band seems to be a clear marker of the A state, with a very weak counterpart at 1166 cm^{-1} in the B state. The two bands at 1327 and 1374 cm^{-1} are unique to the B state, whilst the intense stretching band at 1568 cm^{-1} seems to be present almost exclusively in the A state. To the best of my knowledge, this is the first time that individual Raman spectra are obtained for the two ground states of **wtGFP**. In order to better understand the reported differences, computational studies are needed that are not currently available. All the spectroscopic and computational work in terms of mode assignment for the deprotonated state of GFP has been done on mutants, and, as seen in the previous sections, even a single mutation like in the **S65T** case can significantly alter the surroundings of the chromophore resulting in dramatic spectroscopic differences.

6.5 Conclusion

This chapter presented an impulsive time-domain Raman study of three green fluorescent protein variants (**wtGFP**, **S65T** and "superfolder") and a chromophore model in solution in their excited states. Significant differences were observed between the excited state Raman spectra of the chromophore, the wild-type protein and the two mutants. For the chromophore in solution, the low activity of high frequency modes has been linked to the ultrafast photoisomerisation reaction taking place, that appears to be suppressed by the presence of the protein pocket. Finally, the wavelength-dispersed detection of the probe pulse has been exploited to record the ground state spectrum of **wtGFP** and decompose it for the first time into the individual contributions of the two states.

References

[1] S. E. Braslavsky, *Pure Appl. Chem.*, 2007, **79**, 293–465.

[2] G. Porter, *Science (80-.).*, 1968, **160**, 1299–1307.

[3] M. Eigen, *Nobel Lecture: Immeasurably fast reactions*, 1967, <http://www.nobelprize.org/nobel_prizes/chemistry/laureates/1967/eigen-lecture.html>.

[4] A. H. Zewail, *J. Phys. Chem. A*, 2000, **104**, 5660–5694.

[5] M. F. Kling and M. J. J. Vrakking, *Annu. Rev. Phys. Chem.*, 2008, **59**, 463–492.

[6] R. D. Levine, *Molecular Reaction Dynamics*, Cambridge University Press, Cambridge, UK, 2005, ch. 1, pp. 1–29.

[7] V. Sundstrom, *Annu. Rev. Phys. Chem.*, 2008, **59**, 53–77.

[8] V. Y. Arshavsky, T. D. Lamb and E. N. Pugh, *Annu. Rev. Physiol.*, 2002, **64**, 153–187.

[9] H. Lambers, F. S. Chapin III and T. Pons, *Plant Physiological Ecology*, Springer New York, 2008, pp. 11–99.

[10] S. M. Reppert and D. R. Weaver, *Nature*, 2002, **418**, 935–941.

[11] M. A. Van der Horst and K. J. Hellingwerf, *Acc. Chem. Res.*, 2004, **37**, 13–20.

[12] A. Moglich, X. J. Yang, R. A. Ayers, K. Moffat, S. Merchant, W. R. Briggs and D. Ort, *Annu. Rev. Plant Biol. Vol 61*, 2010, **61**, 21–47.

[13] *Tables for Reference Solar Spectral Irradiances: Direct Normal and Hemispherical on 37 Tilted Surface*, 2008, http://dx.doi.org/10.1520/g0173-03r08/.

[14] O. P. Ernst, D. T. Lodowski, M. Elstner, P. Hegemann, L. S. Brown and H. Kandori, *Chem. Rev.*, 2014, **114**, 126–163.

[15] J. L. Spudich, C. S. Yang, K. H. Jung and E. N. Spudich, *Annu. Rev. Cell Dev. Biol.*, 2000, **16**, 365–392.

[16] H. Kandori, Y. Shichida and T. Yoshizawa, *Biochemistry-Moscow*, 2001, **66**, 1197–1209.

[17] M. Grote, M. Engelhard and P. Hegemann, *Biochim. Biophys. Acta-Bioenergetics*, 2014, **1837**, 533–545.

[18] J. L. Spudich, O. A. Sineshchekov and E. G. Govorunova, *Biochim. Biophys. Acta-Bioenergetics*, 2014, **1837**, 546–552.

[19] K. Inoue, T. Tsukamoto and Y. Sudo, *Biochim. Biophys. Acta - Bioenerg.*, 2014, **1837**, 562–577.

[20] G. Miesenböck, *Annu. Rev. Cell Dev. Biol.*, 2011, **27**, 731–758.

[21] D. Oesterhelt and W. Stoeckenius, *Nature-New Biol.*, 1971, **233**, 149–152.

[22] J. Tittor and D. Oesterhelt, *Febs Lett.*, 1990, **263**, 269–273.

[23] R. A. Mathies, C. H. B. Cruz, W. T. Pollard and C. V. Shank, *Science (80-.).*, 1988, **240**, 777–779.

[24] F. Gai, K. C. Hasson, J. C. McDonald and P. A. Anfinrud, *Science (80-.).*, 1998, **279**, 1886–1891.

[25] K. A. Freedman and R. S. Becker, *J. Am. Chem. Soc.*, 1986, **108**, 1245–1251.

[26] Y. Koyama, K. Kubo, M. Komori, H. Yasuda and Y. Mukai, *Photochem. Photobiol.*, 1991, **54**, 433–443.

[27] G. Zgrablic, M. Ricci, A. M. Novello and F. Parmigiani, *Photochem. Photobiol.*, 2010, **86**, 507–512.

[28] S. L. Logunov, L. Song and M. A. ElSayed, *J. Phys. Chem.*, 1996, **100**, 18586–18591.

[29] P. Hamm, M. Zurek, T. Roschinger, H. Patzelt, D. Oesterhelt and W. Zinth, *Chem. Phys. Lett.*, 1996, **263**, 613–621.

[30] B. Hou, N. Friedman, S. Ruhman, M. Sheves and M. Ottolenghi, *J. Phys. Chem. B*, 2001, **105**, 7042–7048.

[31] G. Zgrablic, K. Voitchovsky, M. Kindermann, S. Haacke and M. Chergui, *Biophys. J.*, 2005, **88**, 2779–2788.

[32] O. Bismuth, N. Friedman, M. Sheves and S. Ruhman, *Chem. Phys.*, 2007, **341**, 267–275.

[33] W. J. Wang, J. H. Geiger and B. Borhan, *Bioessays*, 2014, **36**, 65–74.

[34] J. E. Kim, M. J. Tauber and R. A. Mathies, *Biochemistry*, 2001, **40**, 13774–13778.

[35] R. W. Schoenlein, L. A. Peteanu, R. A. Mathies and C. V. Shank, *Science (80-.).*, 1991, **254**, 412–415.

[36] L. A. Peteanu, R. W. Schoenlein, Q. Wang, R. A. Mathies and C. V. Shank, *Proc. Natl. Acad. Sci. U. S. A.*, 1993, **90**, 11762–11766.

[37] H. Kandori, Y. Katsuta, M. Ito and H. Sasabe, *J. Am. Chem. Soc.*, 1995, **117**, 2669–2670.

[38] A. Wand, I. Gdor, J. Y. Zhu, M. Sheves, S. Ruhman, M. A. Johnson and T. J. Martinez, *Annu. Rev. Phys. Chem. Vol 64*, 2013, **64**, 437–458.

[39] S. J. Remington, *Protein Sci.*, 2011, **20**, 1509–1519.

[40] H. Morise, O. Shimomura, F. H. Johnson and J. Winant, *Biochemistry*, 1974, **13**, 2656–2662.

[41] N. Agmon, *Biophys. J.*, 2005, **88**, 2452–2461.

[42] M. Chalfie, Y. Tu, G. Euskirchen, W. W. Ward and D. C. Prasher, *Science (80-.).*, 1994, **263**, 802–805.

[43] R. M. Wachter, *Acc. Chem. Res.*, 2007, **40**, 120–127.

[44] M. Chattoraj, B. A. King, G. U. Bublitz and S. G. Boxer, *Proc. Natl. Acad. Sci. U. S. A.*, 1996, **93**, 8362–8367.

[45] W. W. Ward, C. W. Cody, R. C. Hart and M. J. Cormier, *Photochem. Photobiol.*, 1980, **31**, 611–615.

[46] J. S. Yang, G. J. Huang, Y. H. Liu and S. M. Peng, *Chem. Commun.*, 2008, 1344–1346.

[47] A. F. Bell, X. He, R. M. Wachter and P. J. Tonge, *Biochemistry*, 2000, **39**, 4423–4431.

[48] W. T. Chuang, C. C. Hsieh, C. H. Lai, C. W. Shih, K. Y. Chen, W. Y. Hung, Y. H. Hsu and P. T. Chou, *J. Org. Chem.*, 2011, **76**, 8189–8202.

[49] M. Liebel and P. Kukura, *J. Phys. Chem. Lett.*, 2013, **4**, 1358–1364.

[50] T. Wende, M. Liebel, C. Schnedermann, R. J. Pethick and P. Kukura, *J. Phys. Chem. A*, 2014, **118**, 9976–9984.

[51] D. Stoner-Ma, A. A. Jaye, P. Matousek, M. Towrie, S. R. Meech and P. J. Tonge, *J. Am. Chem. Soc.*, 2005, **127**, 2864–2865.

[52] T. D. W. Claridge, *High-Resolution NMR Techniques in Organic Chemistry*, Elsevier Science, Oxford, 2nd edn, 2009.

[53] J. K. M. Sanders and B. K. Hunter, *Modern NMR spectroscopy: a guide for chemists*, Oxford University Press, Oxford, 2nd edn, 1993.

[54] B. A. Thrush, *Photochem. Photobiol. Sci.*, 2003, **2**, 453–454.

[55] C. Rullière, T. Amand and X. Marie, *Femtosecond Laser Pulses - Princ. Exp.*, Springer, New York, USA, 2nd edn, 2005, ch. 8, pp. 223–281.

[56] S. Mukamel, *Annu. Rev. Phys. Chem.*, 1990, **41**, 647–681.

[57] S. Mukamel and W. Zhuang, *Proc. Natl. Acad. Sci. U. S. A.*, 2005, **102**, 13717–13718.

[58] S. A. Kovalenko, A. L. Dobryakov, J. Ruthmann and N. P. Ernsting, *Phys. Rev. A*, 1999, **59**, 2369–2384.

[59] A. L. Dobryakov, S. A. Kovalenko and N. P. Ernsting, *J. Chem. Phys.*, 2003, **119**, 988–1002.

[60] A. L. Dobryakov, S. A. Kovalenko and N. P. Ernsting, *J. Chem. Phys.*, 2005, **123**, 044502.

[61] A. L. Dobryakov and N. P. Ernsting, *J. Chem. Phys.*, 2008, **129**, 184504.

[62] W. T. Pollard and R. A. Mathies, *Annu. Rev. Phys. Chem.*, 1992, **43**, 497–523.

[63] K. Blum, *Density Matrix Theory Appl.*, Springer Berlin Heidelberg, 2012, vol. 64, pp. 35–60.

[64] F. Salin, *Femtosecond Laser Pulses - Princ. Exp.*, Springer, New York, 2nd edn, 2005, ch. 6, pp. 175–194.

[65] G. Cerullo and S. De Silvestri, *Rev. Sci. Instrum.*, 2003, **74**, 1–18.

[66] D. J. Kane and R. Trebino, *IEEE J. Quantum Electron.*, 1993, **29**, 571–579.

[67] U. Megerle, I. Pugliesi, C. Schriever, C. F. Sailer and E. Riedle, *Appl. Phys. B-Lasers Opt.*, 2009, **96**, 215–231.

[68] R. I. Shrager and R. W. Hendler, *J. Phys. Chem. B*, 2003, **107**, 1708–1713.

[69] I. H. M. van Stokkum, D. S. Larsen and R. van Grondelle, *Biochim. Biophys. Acta-Bioenergetics*, 2004, **1657**, 82–104.

[70] C. Ruckebusch, M. Sliwa, P. Pernot, A. de Juan and R. Tauler, *J. Photochem. Photobiol. C-Photochemistry Rev.*, 2012, **13**, 1–27.

[71] D. Polli, D. Brida, S. Mukamel, G. Lanzani and G. Cerullo, *Phys. Rev. A*, 2010, **82**, 053809.

[72] I. Szundi, J. W. Lewis and D. S. Kliger, *Biophys. J.*, 1997, **73**, 688–702.

[73] A. E. Johnson and A. B. Myers, *J. Chem. Phys.*, 1996, **104**, 2497–2507.

[74] M. Liebel, C. Schnedermann, G. Bassolino, G. Taylor, A. Watts and P. Kukura, *Phys. Rev. Lett.*, 2014, **112**, 238301.

[75] *Spectral Database for Organic Compounds*, http://sdbs.db.aist.go.jp/sdbs/cgi-bin/cre_index.cgi.

[76] T. Sovdat, G. Bassolino, M. Liebel, C. Schnedermann, S. P. Fletcher and P. Kukura, *J. Am. Chem. Soc.*, 2012, **134**, 8318–8320.

[77] G. Bassolino, T. Sovdat, M. Liebel, C. Schnedermann, B. Odell, T. D. W. Claridge, P. Kukura and S. P. Fetcher, *J. Am. Chem. Soc.*, 2014, **136**, 2650–2658.

[78] H. Kandori and H. Sasabe, *Chem. Phys. Lett.*, 1993, **216**, 126–132.

[79] R. F. Childs and G. S. Shaw, *J. Am. Chem. Soc.*, 1988, **110**, 3013–3017.

[80] E. P. Ippen, C. V. Shank, A. Lewis and M. A. Marcus, *Science (80-.).*, 1978, **200**, 1279–1281.

[81] M. C. Nuss, W. Zinth, W. Kaiser, E. Kolling and D. Oesterhelt, *Chem. Phys. Lett.*, 1985, **117**, 1–7.

[82] J. Dobler, W. Zinth, W. Kaiser and D. Oesterhelt, *Chem. Phys. Lett.*, 1988, **144**, 215–220.

[83] K. C. Hasson, F. Gai and P. A. Anfinrud, *Proc. Natl. Acad. Sci. U. S. A.*, 1996, **93**, 15124–15129.

[84] G. Haran, K. Wynne, A. H. Xie, Q. He, M. Chance and R. M. Hochstrasser, *Chem. Phys. Lett.*, 1996, **261**, 389–395.

[85] S. L. Shapiro, A. J. Campillo, A. Lewis, G. J. Perreault, J. P. Spoonhower, R. K. Clayton and W. Stoeckenius, *Biophys. J.*, 1978, **23**, 383–393.

[86] J. B. Hurley, T. G. Ebrey, B. Honig and M. Ottolenghi, *Nature*, 1977, **270**, 540–542.

[87] S. P. Balashov, E. S. Imasheva, R. Govindjee and T. G. Ebrey, *Photochem. Photobiol.*, 1991, **54**, 955–961.

[88] S. L. Logunov, M. A. El-Sayed, L. Song and J. K. Lanyi, *J. Phys. Chem.*, 1996, **100**, 2391–2398.

[89] S. L. Logunov, M. A. El-Sayed and J. K. Lanyi, *Biophys. J.*, 1996, **70**, 2875–2881.

[90] R. Mathies and L. Stryer, *Proc. Natl. Acad. Sci. U. S. A.*, 1976, **73**, 2169–2173.

[91] M. Garavelli, P. Celani, F. Bernardi, M. A. Robb and M. Olivucci, *J. Am. Chem. Soc.*, 1997, **119**, 6891–6901.

[92] O. Valsson and C. Filippi, *J. Chem. Theory Comput.*, 2010, **6**, 1275–1292.

[93] S. O. Smith, A. B. Myers, R. A. Mathies, J. A. Pardoen, C. Winkel, E. M. M. Van der Berg and J. Lugtenburg, *Biophys. J.*, 1985, **47**, 653–664.

[94] D. W. McCamant, P. Kukura and R. A. Mathies, *J. Phys. Chem. B*, 2005, **109**, 10449–10457.

[95] R. Gonzalez-Luque, M. Garavelli, F. Bernardi, M. Merchan, M. A. Robb and M. Olivucci, *Proc. Natl. Acad. Sci. U. S. A.*, 2000, **97**, 9379–9384.

[96] S. Gozem, F. Melaccio, R. Lindh, A. I. Krylov, A. A. Granovsky, C. Angeli and M. Olivucci, *J. Chem. Theory Comput.*, 2013, **9**, 4495–4506.

[97] T. Mori, K. Nakano and S. Kato, *J. Chem. Phys.*, 2010, **133**, 064107.

[98] A. Wand, B. Loevsky, N. Friedman, M. Sheves and S. Ruhman, *J. Phys. Chem. B*, 2013, **117**, 4670–4679.

[99] J. Zhu, O. Bismuth, I. Gdor, A. Wand, N. Friedman, M. Sheves and S. Ruhman, *Chem. Phys. Lett.*, 2009, **479**, 229–233.

[100] M. Sheves and M. Ottolenghi, *Chem. Biol. Synth. Retin.*, Crc Press, Inc, Boca Raton, 1990, ch. 5, pp. 99–123.

[101] R. K. Crouch, *Chem. Biol. Synth. Retin.*, CRC Press, Boca Raton, 1990, pp. 125–146.

[102] V. Balogh-Nair and K. Nakanishi, *Chem. Biol. Synth. Retin.*, CRC Press, Boca Raton, 1990, pp. 147–176.

[103] M. Ottolenghi and M. Sheves, *J. Membr. Biol.*, 1989, **112**, 193–212.

[104] R. Schiffmiller, R. H. Callender, W. H. Waddell, R. Govindjee, T. G. Ebrey, H. Kakitani, B. Honig and K. Nakanishi, *Photochem. Photobiol.*, 1985, **41**, 563–567.

[105] R. Van der Steen, P. L. Biesheuvel, R. A. Mathies and J. Lugtenburg, *J. Am. Chem. Soc.*, 1986, **108**, 6410–6411.

[106] A. R. de Lera, B. Iglesias, J. Rodriguez, R. Alvarez, S. Lopez, X. Villanueva and E. Padros, *J. Am. Chem. Soc.*, 1995, **117**, 8220–8231.

[107] Y. Yamazaki, J. Sasaki, M. Hatanaka, H. Kandori, A. Maeda, R. Needleman, T. Shinada, K. Yoshihara, L. S. Brown and J. K. Lanyi, *Biochemistry*, 1995, **34**, 577–582.

[108] O. Weidlich, N. Friedman, M. Sheves and F. Siebert, *Biochemistry*, 1995, **34**, 13502–13510.

[109] W. Zinth, J. Dobler, M. A. Franz and W. Kaiser, Second Eur. Conf. Spectrosc. Biol. Mol., Freiburg, West Germany, 1987, pp. 267–274.

[110] T. Brack, W. Gärtner and G. Atkinson, *Chem. Phys. Lett.*, 1992, **190**, 298–304.

[111] H. W. Trissl and W. Gaertner, *Biochemistry*, 1987, **26**, 751–758.

[112] S. V. Danshina, A. L. Drachev, L. A. Drachev, S. V. Eremin, A. D. Kaulen, L. V. Khitrina and B. I. Mitsner, *Arch. Biochem. Biophys.*, 1990, **279**, 225–231.

[113] L. A. Drachev, A. L. Drachev, L. N. Chekulaeva, R. P. Evstigneeva, A. D. Kaulen, L. V. Khitrina, A. A. Khodonov, Z. R. Lazarova and B. I. Mitsner, *Arch. Biochem. Biophys.*, 1989, **270**, 184–197.

[114] K. Fendler, W. Gärtner, D. Oesterhelt and E. Bamberg, *Biochim. Biophys. Acta - Bioenerg.*, 1987, **893**, 60–68.

[115] R. S. H. Liu, F. Crescitelli, M. Denny, H. Matsumoto and A. E. Asato, *Biochemistry*, 1986, **25**, 7026–7030.

[116] D. Koch and W. Gärtner, *Photochem. Photobiol.*, 1997, **65**, 181–186.

[117] M. A. Verhoeven, P. H. M. Bovee-Geurts, H. J. M. de Groot, J. Lugtenburg and W. J. DeGrip, *J. Mol. Biol.*, 2006, **363**, 98–113.

[118] P. H. M. Bovee-Geurts, I. Fernández Fernández, R. S. H. Liu, R. A. Mathies, J. Lugtenburg and W. J. Degrip, *J. Am. Chem. Soc.*, 2009, **131**, 17933–17942.

[119] W. J. De Grip, F. DeLange, P. Bovee-Geurts, P. J. E. Verdegem and J. Lugtenburg, *Pure Appl. Chem.*, 1997, **69**, 2091–2098.

[120] R. Nelson, *Proc. Natl. Acad. Sci.*, 1970, **66**, 531–538.

[121] W. Gartner and S. Ternieden, *J. Photochem. Photobiol. B-Biology*, 1996, **33**, 83–86.

[122] E. Karnaukhova, S. Hu, R. Boonyasai, Q. Tan and K. Nakanishi, *Bioorg. Chem.*, 1999, **27**, 372–382.

[123] W. H. Waddell, D. L. Hopkins, M. Uemura and J. L. West, *J. Am. Chem. Soc.*, 1978, **100**, 1970–1972.

[124] W. Gartner, H. Hopf, W. E. Hull, D. Oesterhelt, D. Scheutzow and P. Towner, *Tetrahedron Lett.*, 1980, **21**, 347–350.

[125] W. H. Waddell and J. L. West, *J. Phys. Chem.*, 1980, **84**, 134–139.

[126] R. S. Becker, *Photochem. Photobiol.*, 1988, **48**, 369–399.

[127] L. U. Colmenares and R. S. Liu, *Tetrahedron*, 1991, **47**, 3711–3718.

[128] K. Tsujimoto, J. Sugiura, N. Takemori and T. Mizukami, *Chem. Lett.*, 1999, 1051–1052.

[129] R. S. Becker and K. Freedman, *J. Am. Chem. Soc.*, 1985, **107**, 1477–1485.

[130] Y. Mukai, T. Imahori and Y. Koyama, *Photochem. Photobiol.*, 1992, **56**, 965–975.

[131] T. Sovdat, *PhD thesis*, Oxford, U.K., 2014.

[132] M. L. Horng, J. A. Gardecki, A. Papazyan and M. Maroncelli, *J. Phys. Chem.*, 1995, **99**, 17311–17337.

[133] G. Zgrablic, S. Haacke and M. Chergui, *J. Phys. Chem. B*, 2009, **113**, 4384–4393.

[134] G. Zgrablic, A. M. Novello and F. Parmigiani, *J. Am. Chem. Soc.*, 2012, **134**, 955–961.

[135] A. Cembran, F. Bernardi, M. Olivucci and M. Garavelli, *Proc. Natl. Acad. Sci. U. S. A.*, 2005, **102**, 6255–6260.

[136] The Mathworks, Inc.: Natick, MA, *No Title*, 2014.

[137] J. R. Taylor, *An Introd. to Error Anal.*, University Science Books, Sausalito (CA), 2nd edn, 1997, ch. Statistica, pp. 93–120.

[138] S. Kovalenko, R. Schanz, V. Farztdinov, H. Hennig and N. Ernsting, *Chem. Phys. Lett.*, 2000, **323**, 312–322.

[139] S. Ruhman, B. X. Hou, N. Friedman, M. Ottolenghi and M. Sheves, *J. Am. Chem. Soc.*, 2002, **124**, 8854–8858.

[140] M. Ruckenbauer, M. Barbatti, T. Mueller and H. Lischka, *J. Phys. Chem. a*, 2013, **117**, 2790–2799.

[141] J. P. Malhado, R. Spezia and J. T. Hynes, *J. Phys. Chem. A*, 2011, **115**, 3720–3735.

[142] J. P. Malhado and J. T. Hynes, *J. Chem. Phys.*, 2012, **137**, 22A543.

[143] M. Ben-Nun, F. Molnar, K. Schulten and T. J. Martinez, *Proc. Natl. Acad. Sci. U. S. A.*, 2002, **99**, 1769–1773.

[144] R. Henderson, J. M. Baldwin, T. A. Ceska, F. Zemlin, E. Beckmann and K. H. Downing, *J. Mol. Biol.*, 1990, **213**, 899–929.

[145] D. Oesterhelt, P. Hegemann and J. Tittor, *EMBO J.*, 1985, **4**, 2351–2356.

[146] A. Losi, A. A. Wegener, M. Engelhard, W. Gärtner and S. E. Braslavsky, *Biophys. J.*, 1999, **77**, 3277–3286.

[147] A. Losi, A. A. Wegener, M. Engelhard, W. Gärtner and S. E. Braslavsky, *Biophys. J.*, 1999, **77**, 3277–3286.

[148] I. Lutz, A. Sieg, A. A. Wegener, M. Engelhard, I. Boche, M. Otsuka, D. Oesterhelt, J. Wachtveitl and W. Zinth, *Proc. Natl. Acad. Sci. U. S. A.*, 2001, **98**, 962–7.

[149] F. Peters, J. Herbst, J. Tittor, D. Oesterhelt and R. Diller, *Chem. Phys.*, 2006, **323**, 109–116.

[150] T. Nakamura, S. Takeuchi, M. Shibata, M. Demura, H. Kandori and T. Tahara, *J. Phys. Chem. B*, 2008, **112**, 12795–12800.

[151] O. Bismuth, P. Komm, N. Friedman, T. Eliash, M. Sheves and S. Ruhman, *J. Phys. Chem. B*, 2010, **114**, 3046–3051.

[152] D. Huppert and P. M. Rentzepis, *J. Phys. Chem.*, 1986, **90**, 2813–2816.

[153] R. S. Becker, K. Freedman, J. A. Hutchinson and L. J. Noe, *J. Am. Chem. Soc.*, 1985, **107**, 3942–3944.

[154] A. G. Doukas, M. R. Junnarkar, R. R. Alfano, R. H. Callender, T. Kakitani and B. Honig, *Proc. Natl. Acad. Sci. United States Am. Sci.*, 1984, **81**, 4790–4794.

[155] G. R. Loppnow and R. A. Mathies, *Biophys. J.*, 1988, **54**, 35–43.

[156] Q. Wang, R. W. Schoenlein, L. A. Peteanu, R. A. Mathies and C. V. Shank, *Science (80-.).*, 1994, **266**, 422–424.

[157] P. Kukura, D. W. McCamant, S. Yoon, D. B. Wandschneider and R. A. Mathies, *Science (80-.).*, 2005, **310**, 1006–1009.

[158] D. W. McCamant, *J. Phys. Chem. B*, 2011, **115**, 9299–9305.

[159] D. Polli, P. Altoe, O. Weingart, K. M. Spillane, C. Manzoni, D. Brida, G. Tomasello, G. Orlandi, P. Kukura, R. A. Mathies, M. Garavelli and G. Cerullo, *Nature*, 2010, **467**, 440–445.

[160] G. G. Kochendoerfer and R. A. Mathies, *J. Phys. Chem.*, 1996, **100**, 14526–14532.

[161] O. Weingart, *Chem. Phys.*, 2008, **349**, 348–355.

[162] I. Schapiro, M. N. Ryazantsev, L. M. Frutos, N. Ferre, R. Lindh and M. Olivucci, *J. Am. Chem. Soc.*, 2011, **133**, 3354–3364.

[163] L. Vukovic, C. F. Burmeister, P. Kral and G. Groenhof, *J. Phys. Chem. Lett.*, 2013, **4**, 1005–1011.

[164] G. G. Kochendoerfer, P. J. Verdegem, I. van der Hoef, J. Lugtenburg and R. A. Mathies, *Biochemistry*, 1996, **35**, 16230–16240.

[165] A. Cembran, F. Bernardi, M. Olivucci and M. Garavelli, *J. Am. Chem. Soc.*, 2004, **126**, 16018–16037.

[166] F. Santoro, A. Lami and M. Olivucci, *Theor. Chem. Acc.*, 2007, **117**, 1061–1072.

[167] P. W. Zhou, J. Y. Liu, K. L. Han and G. Z. He, *J. Comput. Chem.*, 2014, **35**, 109–120.

[168] G. Eyring, B. Curry, R. Mathies, A. Broek and J. Lugtenburg, *J. Am. Chem. Soc.*, 1980, **102**, 5390–5392.

[169] G. Eyring, B. Curry, R. Mathies, R. Fransen, I. Palings and J. Lugtenburg, *Biochemistry*, 1980, **19**, 2410–2418.

[170] G. Eyring, B. Curry, A. Broek, J. Lugtenburg and R. Mathies, *Biochemistry*, 1982, **21**, 384–393.

[171] I. Palings, J. A. Pardoen, E. Van den Berg, C. Winkel, J. Lugtenburg and R. A. Mathies, *Biochemistry*, 1987, **26**, 2544–2556.

[172] I. Palings, E. M. M. Van der Berg, J. Lugtenburg and R. A. Mathies, *Biochemistry*, 1989, **28**, 1498–1507.

[173] S. W. Lin, M. Groesbeek, I. van der Hoef, P. Verdegem, J. Lugtenburg and R. A. Mathies, *J. Phys. Chem. B*, 1998, **102**, 2787–2806.

[174] F. De Lange, P. H. M. Bovee-Geurts, J. VanOostrum, M. D. Portier, P. J. E. Verdegem, J. Lugtenburg and W. J. DeGrip, *Biochemistry*, 1998, **37**, 1411–1420.

[175] W. J. De Grip, F. J. M. Daemen, S. L. Bonting and L. D. W. Donald B. McCormick, *Methods Enzymol.*, Academic Press, 1980, vol. Volume 67, pp. 301–320.

[176] K. M. Spillane, *PhD thesis*, Berkeley, 2011.

[177] M. Yan, L. Rothberg and R. Callender, *J. Phys. Chem. B*, 2001, **105**, 856–859.

[178] M. N. Mozgovaya, O. A. Smitienko, I. V. Shelaev, F. E. Gostev, T. B. Feldman, V. A. Nadtochenko, O. M. Sarkisov and M. A. Ostrovsky, *Dokl Biochem Biophys*, 2010, **435**, 302–306.

[179] S. Linden, H. Giessen and J. Kuhl, *Phys. Status Solidi B-Basic Res.*, 1998, **206**, 119–124.

[180] R. Rowan, A. Warshel, B. D. Sykes and M. Karplus, *Biochemistry*, 1974, **13**, 970–981.

[181] R. H. Callender, A. Doukas, R. Crouch and K. Nakanishi, *Biochemistry*, 1976, **15**, 1621–1629.

[182] K. Palczewski, T. Kumasaka, T. Hori, C. A. Behnke, H. Motoshima, B. A. Fox, I. Le Trong, D. C. Teller, T. Okada, R. E. Stenkamp, M. Yamamoto and M. Miyano, *Science (80-.).*, 2000, **289**, 739–745.

[183] M. Sugihara, V. Buss, P. Entel, M. Elstner and T. Frauenheim, *Biochemistry*, 2002, **41**, 15259–15266.

[184] W. Fuss, *J. Photochem. Photobiol. A - Chem.*, 2015, **297**, 45–57.

[185] M. J. Frisch, G. W. Trucks, H. B. Schlegel, G. E. Scuseria, M. A. Robb, J. R. Cheeseman, G. Scalmani, V. Barone, B. Mennucci, G. A. Petersson, H. Nakatsuji, M. Caricato, X. Li, H. P. Hratchian, A. F. Izmaylov, J. Bloino, G. Zheng, J. L. Sonnenberg, M. Hada, M. Ehara, K. Toyota, R. Fukuda, J. Hasegawa, M. Ishida, T. Nakajima, Y. Honda, O. Kitao, H. Nakai, T. Vreven, J. A. Montgomery Jr., J. E. Peralta, F. Ogliaro, M. Bearpark, J. J. Heyd, E. Brothers, K. N. Kudin, V. N. Staroverov, R. Kobayashi, J. Normand, K. Raghavachari, A. Rendell, J. C. Burant, S. S. Iyengar, J. Tomasi, M. Cossi, N. Rega, N. J. Millam, M. Klene, J. E. Knox, J. B. Cross, V. Bakken, C. Adamo, J. Jaramillo, R. Gomperts, R. E. Stratmann, O. Yazyev, A. J. Austin, R. Cammi, C. Pomelli, J. W. Ochterski, R. L. Martin, K. Morokuma, V. G. Zakrzewski, G. A. Voth, P. Salvador, J. J. Dannenberg, S. Dapprich, A. D. Daniels, O. Farkas, J. B. Foresman, J. V. Ortiz, J. Cioslowski and D. J. Fox, *Gaussian 09, Revision A.02*, 2009.

[186] J. D. Chai and M. Head-Gordon, *Phys. Chem. Chem. Phys.*, 2008, **10**, 6615–6620.

[187] T. H. Dunning, *J. Chem. Phys.*, 1989, **90**, 1007–1023.

[188] H. B. Schlegel, *Wiley Interdiscip. Rev. Comput. Mol. Sci.*, 2011, **1**, 790–809.

[189] A. Wand, R. Rozin, T. Eliash, K. H. Jung, M. Sheves and S. Ruhman, *J. Am. Chem. Soc.*, 2011, **133**, 20922–20932.

[190] P. E. Blatz and J. H. Mohler, *Biochemistry*, 1972, **11**, 3240–3243.

[191] V. Balogh-Nair, J. D. Carriker, B. Honig, V. Kamat, M. G. Motto, K. Nakanishi, R. Sen, M. Sheves, M. A. Tanis and K. Tsujimoto, *Photochem. Photobiol.*, 1981, **33**, 483–488.

[192] H. Kakitani, T. Kakitani, H. Rodman and B. Honig, *Photochem. Photobiol.*, 1985, **41**, 471–479.

[193] C. S. Irving, G. W. Byers and P. A. Leermake, *Biochemistry*, 1970, **9**, 858–864.

[194] M. Arnaboldi, M. G. Motto, K. Tsujimoto, V. Balogh-Nair and K. Nakanishi, *J. Am. Chem. Soc.*, 1979, **101**, 7082–7084.

[195] M. Sheves, B. Kohne and Y. Mazur, *J. Chem. Soc. Commun.*, 1983, 1232–1234.

[196] M. B. Nielsen, *Chem. Soc. Rev.*, 2009, **38**, 913–924.

[197] T. Baasov and M. Sheves, *J. Am. Chem. Soc.*, 1985, **107**, 7524–7533.

[198] P. E. Blatz and J. H. Mohler, *Biochemistry*, 1975, **14**, 2304–2309.

[199] P. E. Blatz, J. H. Mohler and H. V. Navangul, *Biochemistry*, 1972, **11**, 848–855.

[200] L. H. Andersen, I. B. Nielsen, M. B. Kristensen, M. O. A. El Ghazaly, S. Haacke, M. B. Nielsen and M. A. Petersen, *J. Am. Chem. Soc.*, 2005, **127**, 12347–12350.

[201] J. Rajput, D. B. Rahbek, L. H. Andersen, A. Hirshfeld, M. Sheves, P. Altoe, G. Orlandi and M. Garavelli, *Angew. Chemie-International Ed.*, 2010, **49**, 1790–1793.

[202] G. S. Harbison, S. O. Smith, J. A. Pardoen, J. M. L. Courtin, J. Lugtenburg, J. Herzfeld, R. A. Mathies and R. G. Griffin, *Biochemistry*, 1985, **24**, 6955–6962.

[203] L. Mollevanger, A. P. M. Kentgens, J. A. Pardoen, J. M. L. Courtin, W. S. Veeman, J. Lugtenburg and W. J. De Grip, *Eur. J. Biochem.*, 1987, **163**, 9–14.

[204] B. Honig, U. Dinur, K. Nakanishi, V. Balogh-Nair, M. A. Gawinowicz, M. Arnaboldi and M. G. Motto, *J. Am. Chem. Soc.*, 1979, **101**, 7084–7086.

[205] K. Nakanishi, V. Balogh-Nair, M. Arnaboldi, K. Tsujimoto and B. Honig, *J. Am. Chem. Soc.*, 1980, **102**, 7945–7947.

[206] M. G. Motto, M. Sheves, K. Tsujimoto, V. Balogh-Nair and K. Nakanishi, *J. Am. Chem. Soc.*, 1980, **102**, 7947–7949.

[207] F. Melaccio, N. Ferre and M. Olivucci, *Phys. Chem. Chem. Phys.*, 2012, **14**, 12485–12495.

[208] M. Wanko, M. Hoffmann, T. Frauenheim and M. Elstner, *J. Phys. Chem. B*, 2008, **112**, 11462–11467.

[209] O. Valsson, P. Campomanes, I. Tavernelli, U. Rothlisberger and C. Filippi, *J. Chem. Theory Comput.*, 2013, **9**, 2441–2454.

[210] T. P. Sakmar, R. R. Franke and H. G. Khorana, *Proc. Natl. Acad. Sci. U. S. A.*, 1989, **86**, 8309–8313.

[211] E. A. Zhukovsky and D. D. Oprian, *Science (80-.).*, 1989, **246**, 928–930.

[212] J. Nathans, *Biochemistry*, 1990, **29**, 9746–9752.

[213] A. B. Asenjo, J. Rim and D. D. Oprian, *Neuron*, 1994, **12**, 1131–1138.

[214] S. W. Lin, G. G. Kochendoerfer, K. S. Carroll, D. Wang, R. A. Mathies and T. P. Sakmar, *J. Biol. Chem.*, 1998, **273**, 24583–24591.

[215] G. G. Kochendoerfer, S. W. Lin, T. P. Sakmar and R. A. Mathies, *Trends Biochem. Sci.*, 1999, **24**, 300–305.

[216] W. J. Wang, Z. Nossoni, T. Berbasova, C. T. Watson, I. Yapici, K. S. S. Lee, C. Vasileiou, J. H. Geiger and B. Borhan, *Science (80-.).*, 2012, **338**, 1340–1343.

[217] O. Bismuth, N. Friedman, M. Sheves and S. Ruhman, *J. Phys. Chem. B*, 2007, **111**, 2327–2334.

[218] A. R. de Lera, W. Reischl and W. H. Okamura, *J. Am. Chem. Soc.*, 1989, **111**, 4051–4063.

[219] B. Curry, I. Palings, A. D. Broek, J. A. Pardoen, J. Lugtenburg and R. Mathies, *Adv. Infrared Raman Spectrosc.*, John Wiley & Sons, 1985, pp. 115–178.

[220] U. C. Singh and P. A. Kollman, *J. Comput. Chem.*, 1984, **5**, 129–145.

[221] B. H. Besler, K. M. Merz and P. A. Kollman, *J. Comput. Chem.*, 1990, **11**, 431–439.

[222] G. A. Petersson, A. Bennett, T. G. Tensfeldt, M. A. Allaham, W. A. Shirley and J. Mantzaris, *J. Chem. Phys.*, 1988, **89**, 2193–2218.

[223] G. A. Petersson and M. A. Allaham, *J. Chem. Phys.*, 1991, **94**, 6081–6090.

[224] V. Barone and M. Cossi, *J. Phys. Chem. A*, 1998, **102**, 1995–2001.

[225] M. Cossi, N. Rega, G. Scalmani and V. Barone, *J. Comput. Chem.*, 2003, **24**, 669–681.

[226] T. Baasov and M. Sheves, *Biochemistry*, 1986, **25**, 5249–5258.

[227] T. Baasov, N. Friedman and M. Sheves, *Biochemistry*, 1987, **26**, 3210–3217.

[228] J. Clayden, N. Greeves and S. Warren, *Organic Chemistry*, Oxford University Press, Oxford, 1st edn, 2001, ch. 8, pp. 181–208.

[229] F. Yang, L. G. Moss and G. N. Phillips, *Nat. Biotechnol.*, 1996, **14**, 1246–1251.

[230] W. W. Ward, H. J. Prentice, A. F. Roth, C. W. Cody and S. C. Reeves, *Photochem. Photobiol.*, 1982, **35**, 803–808.

[231] T. Ehrig, D. J. Okane and F. G. Prendergast, *Febs Lett.*, 1995, **367**, 163–166.

[232] R. Heim, A. B. Cubitt and R. Y. Tsien, *Nature*, 1995, **373**, 663–664.

[233] K. Brejc, T. K. Sixma, P. A. Kitts, S. R. Kain, R. Y. Tsien, M. Ormo and S. J. Remington, *Proc. Natl. Acad. Sci. U. S. A.*, 1997, **94**, 2306–2311.

[234] O. Shimomura, *Febs Lett.*, 1979, **104**, 220–222.

[235] H. Niwa, S. Inouye, T. Hirano, T. Matsuno, S. Kojima, M. Kubota, M. Ohashi and F. I. Tsuji, *Proc. Natl. Acad. Sci. U. S. A.*, 1996, **93**, 13617–13622.

[236] J. J. van Thor, T. Gensch, K. J. Hellingwerf and L. N. Johnson, *Nat. Struct. Biol.*, 2002, **9**, 37–41.

[237] H. Lossau, A. Kummer, R. Heinecke, F. PollingerDammer, C. Kompa, G. Bieser, T. Jonsson, C. M. Silva, M. M. Yang, D. C. Youvan and M. E. MichelBeyerle, *Chem. Phys.*, 1996, **213**, 1–16.

[238] M. A. Perozzo, K. B. Ward, R. B. Thompson and W. W. Ward, *J. Biol. Chem.*, 1988, **263**, 7713–7716.

[239] G. Striker, V. Subramaniam, C. A. M. Seidel and A. Volkmer, *J. Phys. Chem. B*, 1999, **103**, 8612–8617.

[240] K. L. Litvinenko, N. M. Webber and S. R. Meech, *Chem. Phys. Lett.*, 2001, **346**, 47–53.

[241] A. P. Esposito, P. Schellenberg, W. W. Parson and P. J. Reid, *J. Mol. Struct.*, 2001, **569**, 25–41.

[242] P. Schellenberg, E. Johnson, A. P. Esposito, P. J. Reid and W. W. Parson, *J. Phys. Chem. B*, 2001, **105**, 5316–5322.

[243] D. Mandal, T. Tahara, N. M. Webber and S. R. Meech, *Chem. Phys. Lett.*, 2002, **358**, 495–501.

[244] X. He, A. F. Bell and P. J. Tonge, *J. Phys. Chem. B*, 2002, **106**, 6056–6066.

[245] J. Dong, F. Abulwerdi, A. Baldridge, J. Kowalik, K. M. Solntsev and L. M. Tolbert, *J. Am. Chem. Soc.*, 2008, **130**, 14096–14098.

[246] O. Shimomura, F. H. Johnson and Y. Saiga, *J. Cell. Comp. Physiol.*, 1962, **59**, 223–239.

[247] O. Shimomura, *Angew. Chemie-International Ed.*, 2009, **48**, 5590–5602.

[248] S. Inouye and F. I. Tsuji, *Febs Lett.*, 1994, **341**, 277–280.

[249] B. P. Cormack, R. H. Valdivia and S. Falkow, *Gene*, 1996, **173**, 33–38.

[250] R. Y. Tsien, *Annu. Rev. Biochem.*, 1998, **67**, 509–544.

[251] N. C. Shaner, P. A. Steinbach and R. Y. Tsien, *Nat. Methods*, 2005, **2**, 905–909.

[252] G. J. Kremers, S. G. Gilbert, P. J. Cranfill, M. W. Davidson and D. W. Piston, *J. Cell Sci.*, 2011, **124**, 157–160.

[253] M. B. Nielsen, L. H. Andersen and T. Rocha-Rinza, *Monatshefte Fur Chemie*, 2011, **142**, 709–715.

[254] J. T. M. Kennis, D. S. Larsen, I. H. M. van Stokkum, M. Vengris, J. J. van Thor and R. van Grondelle, *Proc. Natl. Acad. Sci. U. S. A.*, 2004, **101**, 17988–17993.

[255] C. Fang, R. R. Frontiera, R. Tran and R. A. Mathies, *Nature*, 2009, **462**, 200–205.

[256] J. J. van Thor, C. N. Lincoln, B. Kellner, K. N. Bourdakos, L. M. Thompson, M. J. Bearpark, P. M. Champion and J. T. Sage, *Vib. Spectrosc.*, 2012, **62**, 1–6.

[257] M. Zimmer, *Chem. Rev.*, 2002, **102**, 759–781.

[258] V. Tozzini and R. Nifosi, *J. Phys. Chem. B*, 2001, **105**, 5797–5803.

[259] V. Tozzini, A. R. Bizzarri, V. Pellegrini, R. Nifosi, P. Giannozzi, A. Iuliano, S. Cannistraro and F. Beltram, *Chem. Phys.*, 2003, **287**, 33–42.

[260] R. A. G. Cinelli, V. Tozzini, V. Pellegrini, F. Beltram, G. Cerullo, M. Zavelani-Rossi, S. De Silvestri, M. Tyagi and M. Giacca, *Phys. Rev. Lett.*, 2001, **86**, 3439–3442.

[261] J. J. van Thor, G. Zanetti, K. L. Ronayne and M. Towrie, *J. Phys. Chem. B*, 2005, **109**, 16099–16108.

[262] J. Wiehler, G. Jung, C. Seebacher, Z. Zumbusch and B. Steipe, *Chembiochem*, 2003, **4**, 1164–1171.

[263] J. D. Pedelacq, S. Cabantous, T. Tran, T. C. Terwilliger and G. S. Waldo, *Nat. Biotechnol.*, 2006, **24**, 79–88.

[264] C. Y. Lee, Y. C. Chen, H. C. Lin, Y. Jhong, C. W. Chang, C. H. Tsai, C. L. Kao and T. C. Chien, *Tetrahedron*, 2012, **68**, 5898–5907.

[265] K. M. Solntsev, O. Poizat, J. Dong, J. Rehault, Y. B. Lou, C. Burda and L. M. Tolbert, *J. Phys. Chem. B*, 2008, **112**, 2700–2711.

[266] A. Weigel, *PhD thesis*, Berlin, 2011.

[267] A. L. Dobryakov, I. Ioffe, A. A. Granovsky, N. P. Ernsting and S. A. Kovalenko, *J. Chem. Phys.*, 2012, **137**, 244505.

[268] W. T. Pollard, S. L. Dexheimer, Q. Wang, L. A. Peteanu, C. V. Shank and R. A. Mathies, *J. Phys. Chem.*, 1992, **96**, 6147–6158.

Appendix A

Supplementary Data for Chapter 3

1. **General information**
2. **Characterisation data for RPSBs**
3. **Photoproducts identification**
4. **Transient absorption maps, kinetics and spectra**

A.1 General information

Solution NMR spectra were recorded in deuterated solvents at room temperature. Proton (^{1}H), carbon (^{13}C), COSY, HSQC, HMBC, TOCSY and NOESY experiments were performed on Bruker DPX200 (200/50 MHz), Bruker DPX 250 (250/63 MHz), Bruker DPX400 (400/100 MHz), Bruker AV400 (400/100 MHz), Bruker AVIII 400 (400/100 MHz) Bruker AVII500 (500/125 MHz), Bruker DRX500 (500/125 MHz) and Bruker AVIII700 (700 MHz). Chemical shifts (δ) are reported in ppm downfield of tetramethylsilane with residual solvent as the internal standard. Resonances are described as singlet (s), doublet (d), doublet of doublets (dd), triplet (t), quartet (q), quintet (quint), sextet (sxt), doublet of quartets (dq), triplet of doublets (td), triplet of doublets of doublets (tdd) and multiplet (m). Coupling constants (J) are quoted in Hertz (Hz).

Low resolution mass spectra (MS) were recorded using a Walters LCT premier XE. High resolution mass spectra (HRMS) were recorded using a Bruker MicroTOF spectrometer by the internal service at the University of Oxford.

A.2 Characterisation data for RPSBs

all-*trans* retinal *n*-butylamine protonated Schiff base (NAT)

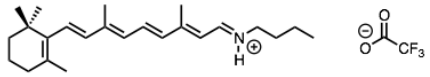

^{1}H NMR (500 MHz, CD_3OD) δ_H/ppm 1.01 (t, J=7.4 Hz, 3 H), 1.06 (s, 6 H), 1.44 (sxt, J=7.5 Hz, 2 H), 1.49 - 1.53 (m, 2 H), 1.63 - 1.68 (m, 2 H), 1.74 (s, 3 H), 1.70 - 1.77 (m, 2 H), 2.07 (br. t, J=6.1, 2 H), 2.12 (s, 3 H), 2.40 (s, 3 H), 3.73 (t, J=7.2 Hz, 2 H), 6.26 (d, J=16.0 Hz, 1 H), 6.35 (d, J=11.7 Hz, 1 H), 6.41 (d, J=11.0 Hz, 1 H), 6.54 (d, J=15.8 Hz, 1 H), 6.62 (d, J=14.9 Hz, 1 H), 7.58 (dd, J=14.7, 11.6 Hz, 1 H), 8.84 (d, J=11.5 Hz, 1 H).

^{13}C NMR (125 MHz, CD_3OD) δ_C/ppm 13.3, 14.0, 14.3, 20.4, 20.8, 22.1, 29.6, 32.4, 34.3, 35.4, 40.9, 52.9, 117.9 (q, J=290.4 Hz), 120.3, 131.1, 132.4, 133.1, 134.9, 138.6, 139.1,140.0, 147.0, 162.2 (q, J=36.3 Hz), 166.9, 167.4.

HRMS (ESI_+) m/z calcd for $C_{24}H_{38}N$ $[M]_+$: 340.2999, found: 340.2992.

all-*trans*-8-methyl retinal *n*-butylamine protonated Schiff base (8-Me)

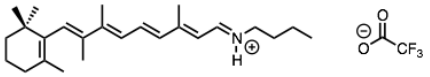

^{1}H NMR (500 MHz, CD_3OD) δ_H/ppm 0.92 (br. s, 3 H), 1.00 (t, J=7.3 Hz, 3 H), 1.07 (br. s., 3 H), 1.40 - 1.47 (m, 2 H), 1.47 (d, J=0.7 Hz, 3 H), 1.53 (br. s, 2 H), 1.65 - 1.71 (m, 2 H), 1.70 - 1.77 (m, 2 H), 1.78 (d, J=0.6 Hz, 3 H), 2.02 (br. s, 2 H), 2.18 (s, 3 H), 2.41 (s, 3 H), 3.73 (t, J=7.2 Hz, 2 H), 6.43 (d, J=11.2 Hz, 1 H), 6.48 (br. s., 1 H), 6.56 (d, J=11.3 Hz, 1 H), 6.66 (d, J=14.9 Hz, 1 H), 7.61 (dd, J=14.8, 11.4 Hz, 1 H), 8.85 (d, J=11.1 Hz, 1 H).

^{13}C NMR (125 MHz, CD_3OD) δ_C/ppm 14.0, 14.4, 15.1, 15.8, 20.5, 20.8, 21.6, 29.07 (br. s.), 32.4, 33.0, 36.2, 40.5, 52.9, 120.3, 117.0 (q, J=287.1 Hz), 127.0, 130.3, 132.2, 135.1, 137.7, 139.8, 140.7, 148.9, 160.6 (q, J=39.1 Hz), 167.1, 167.6.

HRMS (ESI^+) m/z calcd for $C_{25}H_{40}N$ $[M]^+$: 354.3155 found: 354.3144.

all-*trans*-9-demethyl retinal *n*-butylamine protonated Schiff base (9-dm)

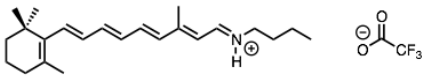

^{1}H NMR (500 MHz, CD_3OD) δ_H/ppm 1.00 (t, J=7.3 Hz, 3 H), 1.07 (s, 6 H), 1.40 - 1.47 (m, 2 H), 1.48 - 1.53 (m, 2 H), 1.60 - 1.68 (m, 2 H), 1.76 - 1.78 (m, 2 H), 1.76 (s, 3 H), 2.08 (t, J=6.1 Hz, 2 H), 2.36 (s, 3 H), 3.73 (t, J=7.2 Hz, 2 H), 6.31 (dd, J=15.5, 10.9 Hz, 1 H), 6.40 (d, J=11.2 Hz, 1 H), 6.48 (dd, J=14.7, 11.2 Hz, 1 H), 6.54 (d, J=15.7 Hz, 1 H), 6.58 (d, J=15.1 Hz, 1 H), 6.82 (dd, J=14.5, 10.9 Hz, 1 H), 7.27 (dd, J=15.0, 11.1 Hz, 1 H), 8.84 (d, J=11.0 Hz, 1 H).

^{13}C NMR (125 MHz, CD_3OD) δ_C/ppm 14.0, 14.3, 20.3, 20.8, 22.1, 29.5, 32.4, 34.6, 35.3, 41.1, 52.9, 117.2 (q, J=287.5 Hz), 120.3, 131.8, 134.1, 134.2, 134.5, 138.8, 138.9, 144.4, 144.6, 161.0 (q, J=38.4 Hz), 166.8, 167.5.

HRMS (ESI^+) m/z calcd for $C_{23}H_{36}N$ $[M]^+$: 326.2842, found: 326.2833

all-*trans*-9,13-demethyl retinal *n*-butylamine protonated Schiff base (9,13-dm)

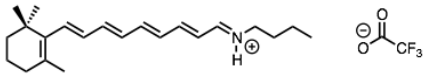

^{1}H NMR (700 MHz, CD_3OD) δ_H/ppm 1.00 (t, J=7.4 Hz, 3 H), 1.07 (s, 6 H), 1.43 – 1.48 (m, 2 H), 1.50 - 1.52 (m, 2 H), 1.62 - 1.67 (m, 2 H), 1.70 - 1.75 (m, 2 H), 1.77 (s, 3 H), 2.09 (t, J=6.2 Hz, 2 H), 3.70 (t, J=7.2 Hz, 2 H), 6.33 (dd, J=15.6, 11.0 Hz, 1 H), 6.49 (dd, J=14.7, 11.4 Hz, 1 H), 6.53 (dd, J=14.5, 10.6 Hz, 1 H), 6.57 (d, J=15.6 Hz, 1 H), 6.64 (dd, J=14.4, 11.6 Hz, 1 H), 6.82 (dd, J=14.6, 11.0 Hz, 1 H), 7.12 (dd, J=14.4, 11.4 Hz, 1 H), 7.59 (dd, J=14.4, 11.6 Hz, 1 H), 8.43 (d, J=10.6 Hz, 1 H).

^{13}C NMR (176 MHz, CD_3OD) δ_C/ppm 13.9, 20.3, 20.8, 22.2, 29.5, 32.2, 34.6, 35.3, 41.2, 52.9, 118.1 (q, J=291.2 Hz), 120.8, 130.6, 131.5, 134.3, 134.7, 138.9, 139.7, 145.6, 151.4, 160.8, 162.5 (q, J=35.6 Hz), 171.6.

HRMS (ESI^+) m/z calcd for $C_{22}H_{34}N$ $[M]^+$: 312.2686, found: 312.2680.

all-*trans*-10-methyl retinal *n*-butylamine protonated Schiff base (10-Me)

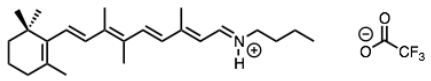

^{1}H NMR (500 MHz, CD_3OD) δ_H/ppm 1.00 (t, J=7.4 Hz, 3 H), 1.06 (s, 6 H), 1.44 (sxt, J=7.5 Hz, 2 H), 1.49 - 1.53 (m, 2 H), 1.61 - 1.69 (m, 2 H), 1.69 - 1.75 (m, 2 H), 1.76 (s, 3 H), 2.02 (s, 3 H), 2.07 (br. t, J=6.1 Hz, 3 H), 2.16 (s, 3 H), 2.41 (s, 3 H), 3.73 (t, J=7.2 Hz, 2 H), 6.49 (d, J=11.1 Hz, 1 H), 6.59 (d, J=15.9 Hz, 1 H), 6.69 (d, J=15.4 Hz, 1 H), 6.77 (d, J=15.9 Hz, 1 H), 7.79 (d, J=15.3 Hz, 1 H), 8.84 (d, J=10.6 Hz, 1 H).

^{13}C NMR (125 MHz, CD_3OD) δ_C/ppm 14.0, 14.0, 14.4, 14.6, 20.4, 20.8, 22.2, 29.6, 32.5, 34.3, 35.4, 40.9, 52.9, 116.2 (q, J=284.5 Hz), 120.4, 131.0, 131.5, 132.4, 134.1, 134.1, 139.7, 142.6, 143.1, 159.2 (q, J=42.2 Hz), 167.4, 167.6.

HRMS (ESI$^+$) m/z calcd for $C_{25}H_{40}N$ $[M]^+$: 354.3155, found: 354.3153.

all-*trans*-10-*iso*-propyl retinal *n*-butylamine protonated Schiff base (10-iPr)

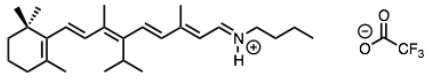

^{1}H NMR (500 MHz, CD_3OD) δ_H/ppm 1.01 (t, J=7.4 Hz, 3 H), 1.05 (s, 6 H), 1.20 (d, J=7.2 Hz, 6 H), 1.42 - 1.48 (m, 2 H), 1.50 - 1.53 (m, 2 H), 1.64 - 1.70 (m, 2 H), 1.74 (s, 3 H), 1.71 - 1.78 (m, 2 H), 2.07 (t, J=6.2 Hz, 2 H), 2.10 (s, 3 H), 2.41 (s, 3 H), 3.29 (spt, J=7.1 Hz, 1 H), 3.75 (t, J=7.2 Hz, 2 H), 6.47 (d, J=11.2 Hz, 1 H), 6.50 (d, J=15.8 Hz, 1 H), 6.68 (d, J=15.1 Hz, 1 H), 6.71 (d, J=15.1 Hz, 1 H), 7.45 (d, J=15.9 Hz, 1 H,), 8.89 (d, J=11.1 Hz, 1 H).

^{13}C NMR (125 MHz, CD_3OD) δ_C/ppm 14.0, 14.2, 16.5, 20.4, 20.8, 22.2, 22.5, 29.6, 30.1, 32.4, 34.1, 35.4, 40.9, 53.0, 117.0 (q, J=287.5 Hz), 120.5, 131.5, 133.1, 133.7, 133.7, 138.9, 139.8, 141.9, 142.2, 160.6 (q, J=38.9 Hz, 167.0, 167.8.

HRMS (ESI$^+$) m/z calcd for $C_{27}H_{44}N$ $[M]^+$: 382.3468, found: 382.3473.

all-*trans*-10-fluoro retinal *n*-butylamine protonated Schiff base (10-F)

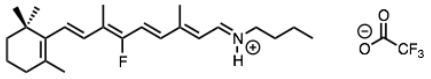

^{1}H NMR (500 MHz, CD_3OD) δ_H/ppm 1.00 (t, J=7.4 Hz, 3 H), 1.07 (s, 6 H), 1.41 - 1.49 (m, 2 H), 1.49 - 1.55 (m, 2 H), 1.62 - 1.83 (m, 2 H), 1.75 (s, 3 H), 1.63 - 1.69 (m, 2 H), 2.07 (d, J=2.2 Hz, 3 H), 2.08 (br. t, J=5.5, 2 H), 2.41 (s, 3 H), 3.76 (t, J=7.2 Hz, 1 H), 6.53 (d, J=11.0 Hz, 1 H), 6.55 (d, J=16.2 Hz, 1 H), 6.72 (d, J=16.2 Hz, 1 H), 6.82 (d, J=15.2 Hz, 1 H), 7.34 (dd, J=27.0, 15.1 Hz, 1 H), 8.91 (d, J=11.0 Hz, 1 H).

^{1}3C NMR (125 MHz, CD_3OD) δ_C/ppm 12.1 (d, J=3.8 Hz), 14.0, 14.2, 20.3, 20.8, 22.1, 29.6, 32.3, 34.4, 35.4, 41.0, 53.2, 117.6 (q, J=289.0 Hz), 122.1, 125.6 (d, J=11.9 Hz), 128.5 (d, J=11.2 Hz), 129.2 (d, J=21.7 Hz), 130.8 (d, J=6.0 Hz), 133.2, 134.3 (d, J=4.8 Hz), 139.3, 154.3 (d, J=245.6 Hz), 161.6 (q, J=37.0 Hz), 165.3, 167.9.

HRMS (ESI$^+$) m/z calcd for $C_{24}H_{37}FN$ $[M]^+$: 358.2905, found: 358.2906.

all-*trans*-10-chloro retinal *n*-butylamine protonated Schiff base (10-Cl)

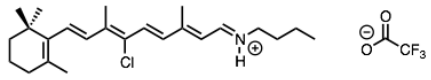

^{1}H NMR (500 MHz, CD_3OD) δ_H/ppm 1.01 (t, J=7.4 Hz, 3 H), 1.09 (s, 6 H), 1.45 (m, 2 H), 1.51 - 1.56 (m, 2 H), 1.64 - 1.70 (m, 2 H), 1.72 - 1.78 (m, 2 H), 1.79 (s, 3 H), 2.11 (t, J=6.3 Hz, 2 H), 2.26 (s, 3 H), 2.43 (s, 3 H), 3.77 (t, J=7.3 Hz, 2 H), 6.56 (d, J=11.0 Hz, 1 H), 6.75 (d, J=16.0 Hz, 1 H), 7.02 (d, J=14.7 Hz, 1 H), 7.05 (d, J=16.2 Hz, 1 H), 7.68 (d, J=14.6 Hz, 1 H), 8.93 (d, J=11.0 Hz, 1 H).

^{13}C NMR (125 MHz, CD_3OD) δ_C/ppm 14.0, 14.6, 15.3, 20.3, 20.8, 22.2, 29.6, 32.3, 34.5, 35.4, 41.1, 53.2, 122.1, 128.9, 133.1, 134.0, 134.4, 135.9, 136.6, 139.3, 141.7, 165.7, 167.9.

HRMS (EI/FI$^+$) m/z calcd for $C_{24}H_{36}ClN$ $[M]^+$: 373.2536, 375.2517 found: 373.2552, 375.2696.

all-*trans*-10-bromo retinal *n*-butylamine protonated Schiff base (10-Br)

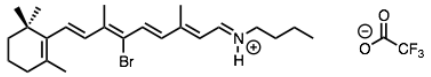

^{1}H NMR (500 MHz, CD_3OD) δ_H/ppm 1.01 (t, J=7.4 Hz, 3 H), 1.10 (s, 6 H), 1.41 - 1.49 (m, 2 H), 1.50 - 1.56 (m, 2 H), 1.65 - 1.70 (m, 2 H), 1.72 - 1.79 (m, 2 H), 1.80 (s, 3 H), 2.11 (t, J=6.3 Hz, 2 H), 2.29 (s, 3 H), 2.44 (s, 3 H), 3.77 (t, J=7.2 Hz, 2 H), 6.54 (d, J=11.1 Hz, 1 H), 6.78 (d, J=16.2 Hz, 1 H), 7.03 (d, J=14.1 Hz, 1 H), 7.06 (d, J=16.0 Hz, 1 H), 7.64 (d, J=14.4 Hz, 1 H), 8.93 (d, J=11.0 Hz, 1 H).

HRMS (ESI$^+$) m/z calcd for $C_{24}H_{37}BrN$ $[M]^+$: 418.2104, 420.2085 in 1:1 ratio, found: 418.2093, 420.2076 in 1:1 ratio.

all-*trans*-10-(trimethylsilyl)methyl retinal *n*-butylamine protonated Schiff base (10-Si)

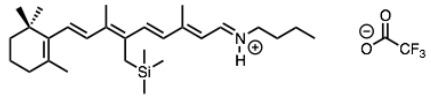

^{1}H NMR (500 MHz, CD_3OD) δ_H/ppm 0.00 (s, 9 H), 1.01 (t, J=7.4 Hz, 3 H), 1.06 (s, 6 H), 1.45 m, 2 H), 1.50 - 1.55 (m, 2 H), 1.64 - 1.70 (m, 2 H), 1.70 - 1.79 (m, 2 H), 1.76 (s, 3 H), 2.06 - 2.11 (m, 2 H), 2.19 (s, 3 H), 2.42 (s, 3 H), 3.73 (t, J=7.2 Hz, 2 H), 6.48 (d, J=11.1 Hz, 1 H), 6.57 (d, J=16.1 Hz, 1 H), 6.63 (d, J=15.6 Hz, 1 H), 6.67 (d, J=16.0 Hz, 1 H), 7.80 (d, J=15.4 Hz, 1 H), 8.86 (d, J=11.1 Hz, 1 H).

^{13}C NMR (125 MHz, CD_3OD) δ_C/ppm –0.1, 14.2, 14.6, 14.8, 19.0, 20.6, 21.0, 22.7, 29.9, 32.6, 34.4, 35.7, 41.1, 53.1, 117.4 (q, J=288.9 Hz), 120.4, 132.0, 132.2, 133.8, 135.0, 135.0, 140.0, 140.8, 142.3, 161.6 (q, J=37.1 Hz), 167.4, 167.5.

HRMS (ESI$^+$) m/z calcd for $C_{28}H_{48}NSi$ $[M]^+$: 426.3551, found: 426.3537.

all-*trans*-10,14-dimethyl retinal *n*-butylamine protonated Schiff base (10,14-Me)

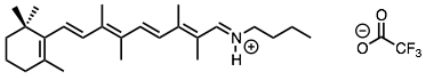

^{1}H NMR (500 MHz, CD_3OD) δ_H/ppm 1.01 (t, J=7.4 Hz, 3 H), 1.07 (s, 6 H), 1.44 (m, 2 H), 1.49 - 1.55 (m, 2 H), 1.63 - 1.72 (m, 2 H), 1.77 (s, 3 H), 1.73 - 1.81 (m, 2 H), 2.07 (s, 3 H), 2.09 (t, J=6.2 Hz, 2 H), 2.12 (s, 3 H), 2.19 (s, 3 H, CH39), 2.47 (s, 3 H, CH313), 3.78 (t, J=7.4 Hz, 2 H), 6.61 (d, J=16.0 Hz, 1 H), 6.79 (d, J=16.0 Hz, 1 H), 7.05 (d, J=15.2 Hz, 1 H), 7.88 (d, J=15.2 Hz, 1 H), 8.94 (s, 1 H).

^{13}C NMR (125 MHz, CD_3OD) δ_C/ppm 12.1, 14.0, 14.1, 14.7, 15.3, 20.4, 20.9, 22.3, 29.6, 32.9, 34.3, 35.4, 40.9 , 53.4, 117.0 (q, J=286.0 Hz), 125.0, 126.9, 132.1, 132.5, 134.1, 134.2, 139.7, 143.1, 143.2, 160.5 (q, J=40.0 Hz), 163.4, 167.9.

HRMS (ESI$^+$) m/z calcd for $C_{26}H_{42}N$ $[M]^+$: 368.3312, found: 368.3303.

all-*trans*-13-demethyl retinal *n*-butylamine protonated Schiff base (13-dm)

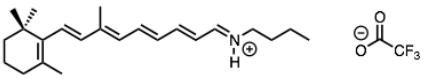

^{1}H NMR (500 MHz, CD_3OD) δ_H/ppm 1.00 (t, J=7.3 Hz, 3 H), 1.06 (s, 6 H), 1.39 - 1.48 (m, 2 H), 1.49 - 1.53 (m, 2 H), 1.62 - 1.68 (m, 2 H), 1.69 - 1.76 (m, 2 H), 1.74 (s, 3 H), 2.07 (t, J=5.7 Hz, 2 H), 2.11 (s, 3 H), 3.70 (t, J=7.1 Hz, 2 H), 6.28 (d, J=16.0 Hz, 1 H), 6.36 (d, J=12.1 Hz, 1 H), 6.53 (dd, J=14.4, 10.6 Hz, 1 H), 6.58 (d, J=16.1 Hz, 1 H), 6.67 (dd, J=14.2, 11.7 Hz, 1 H), 7.51 (dd, J=14.2, 12.0 Hz, 1 H), 7.66 (dd, J=14.4, 11.6 Hz, 1 H), 8.43 (d, J=10.6 Hz, 1 H).

^{13}C NMR (125 MHz, CD_3OD) δ_C/ppm 13.4, 14.1, 20.5, 20.9, 22.3, 29.7, 32.4, 34.5, 35.6, 41.1, 53.1, 117.4 (q, J=287.8 Hz), 120.9, 131.0, 131.4, 133.1, 134.2, 138.6, 139.3, 147.3, 148.6, 161.0 (q, J=38.9 Hz), 161.2, 171.7.

HRMS (ESI$^+$) m/z calcd for $C_{23}H_{36}N$ $[M]^+$: 326.2842, found: 326.2851.

all-*trans*-14-methyl retinal *n*-butylamine protonated Schiff base (14-Me)

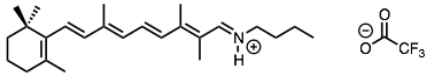

^{1}H NMR (500 MHz, CD_3OD) δ_H/ppm 1.00 (t, J=7.4 Hz, 3 H), 1.06 (s, 6 H), 1.38 - 1.48 (m, 2 H), 1.49 - 1.54 (m, 2 H), 1.59 - 1.69 (m, 2 H), 1.69 - 1.77 (m, 2 H), 1.74 (s, 3 H), 2.08 (t, J=5.8 Hz, 2 H), 2.09 (s, 3 H), 2.13 (s, 3 H), 2.43 (s, 3 H), 3.77 (t, J=7.4 Hz, 2 H), 6.28 (d, J=16.0 Hz, 1 H), 6.45 (d, J=11.6 Hz, 1 H), 6.55 (d, J=16.2 Hz, 1 H), 7.04 (d, J=14.7 Hz, 1 H), 7.64 (dd, J=14.7, 11.7 Hz, 1 H), 8.91 (s, 1 H).

^{13}C NMR (125 MHz, CD_3OD) δ_C/ppm 12.2, 13.5, 14.2, 20.5, 21.0, 21.0, 29.7, 30.9, 33.0, 34.5, 35.6, 41.1, 53.6, 117.1 (q, J=287.1 Hz), 125.2, 131.2, 132.0, 132.7, 133.4, 138.9, 139.3, 140.9, 147.3, 160.6 (q, J=40.4 Hz), 163.0, 168.0.

HRMS (ESI$^+$) m/z calcd for $C_{25}H_{40}N$ $[M]^+$: 354.3155, found: 354.3143.

all-*trans*-15-methyl retinal *n*-butylamine protonated Schiff base (15-Me)

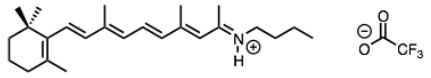

^{1}H NMR (700 MHz, CD_3OD) δ_H/ppm 0.97 - 1.03 (m, 6 H), 1.05 (s, 6 H), 1.05 (s, 6 H), 1.46 (m, 4 H), 1.50 (m, 4 H), 1.65 (m, 4 H), 1.72 (br. s., 3 H), 1.73 (br. s., 3 H), 1.75 (m, J=7.1 Hz, 4 H), 2.06 (m, 4 H), 2.08 (s, 3 H), 2.10 (s, 3 H), 2.35 (s, 3 H), 2.41 (s, 3 H), 3.66 (t, J=7.3 Hz, 2 H), 3.70 (t, J=7.3 Hz, 2 H), 6.21 (d, J=16.4 Hz, 1 H), 6.24 (d, J=16.6 Hz, 1 H), 6.29 (d, J=11.4 Hz, 1 H), 6.33 (d, J=11.8 Hz, 1 H), 6.40 (s, 1 H), 6.45 (d, J=15.9 Hz, 1 H), 6.49 (d, J=15.3 Hz, 1 H), 6.51 (d, J=14.4 Hz, 1 H), 6.53 (s, 1 H), 6.69 (d, J=14.8 Hz, 1 H), 7.38 (dd, J=14.6, 11.8 Hz, 1 H), 7.48 (dd, J=14.6, 11.8 Hz, 1 H).

^{13}C NMR (176 MHz, CD_3OD) δ_C/ppm 13.2, 13.2, 14.0, 16.2, 16.8, 20.4, 20.4, 21.1, 21.2, 22.1, 22.1, 29.5, 31.3, 31.3, 34.2, 34.2, 35.4, 35.4, 40.9, 40.9, 47.8, 48.0, 117.0 (q, J=287.4 Hz), 119.5, 124.1, 130.9, 131.0, 131.8, 131.8, 132.1, 132.4, 136.2, 136.9, 136.9, 138.1, 138.7, 138.8, 139.1, 139.1, 144.5, 145.7, 158.7, 160.6 (q, J=38.8 Hz), 163.6, 179.1, 181.6.

HRMS (ESI$^+$) m/z calcd for $C_{25}H_{40}N$ $[M]^+$: 354.3155, found: 354.3139.

A.3 Photoproducts identification

When the photoproduct has been identified by comparison of the ^{1}H NMR spectra, the irradiated mixture is plotted on the bottom in red with overlapped the non-irradiated control sample in black. The spectra plotted on top are labeled to identify the isomer they belong to, and are plotted in blue or green only for easiness of comparison.

In all the Figures of this section plotting 1D selective experiments, the irradiated proton is labeled in red, and the colour of the spectrum identify it as NOESY (black) or TOCSY (red). The spectrum plotted at the bottom in black is always the irradiated mixture on which the experiments plotted on top were performed. Colored parts within the photoproducts structures shown indicate scalar coupling between the protons.

all-*trans* retinal *n*-butylamine protonated Schiff base (NAT)

The identified photoproducts were 11-*cis* and 9-*cis*, with a quantum yield of 0.16 and 0.05, respectively. Apart from being the reported photoproducts,[25,26] they were identified by comparison of the ^{1}H NMR spectra of the two isomers.

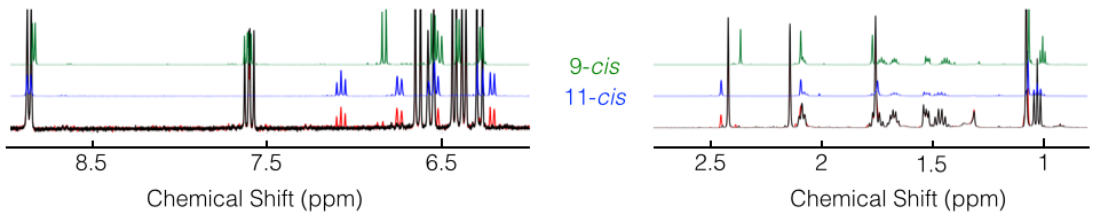

Figure A.1 Photoproduct identification for all-*trans* **NAT** with the ^{1}H NMR spectrum of pure 11-*cis* and 9-*cis* **NAT**

all-*trans*-8-methyl retinal *n*-butylamine protonated Schiff base (8-Me)

The identified photoproducts were 11-*cis* and 7-*cis*, with a quantum yield of 0.08 and 0.05, respectively.

11-*cis*-8-Me This photoproduct has been assigned in the following way: the doublet of doublets at 7.12 ppm can be recognized as H11 by its appearance, as is the only proton of the polyenic chain to show scalar coupling with two other nuclei. When selectively irradiated, it gives dipolar coupling with a doublet at 6.25 ppm and a Me at 2.14 ppm. The Me is identified as Me9 by its dipolar coupling with H7, appearing as a singlet at 6.50 ppm. The proton at

6.25 ppm is recognized as H12 for its dipolar coupling with other two protons, H11 and H14 at 6.52 ppm, as H10 could show dipolar coupling with one proton (H11 or H12) at most . This assignment would already be enough to confirm the *cis* configuration of the C11=C12 bond. The doublet at 6.93 ppm is recognized as H10 for its dipolar coupling with two Me groups, at 2.49 and 1.81 ppm. The former is assigned as Me13 from its dipolar coupling with H15, recognisable for its extremely low field shift at 8.90 ppm. The Me at 1.81 ppm is thus assigned as Me8 by exclusion.

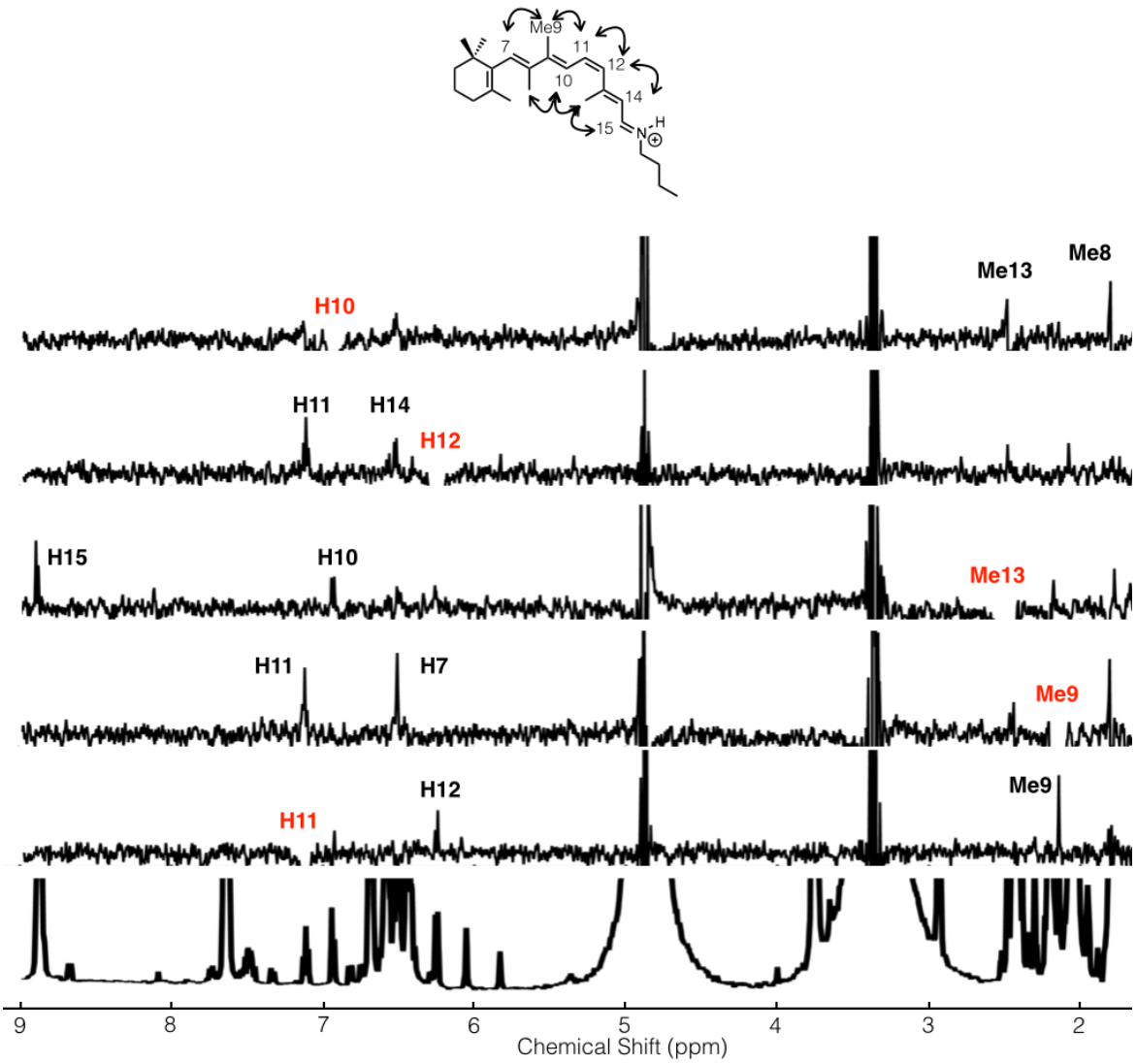

Figure A.2 NOESY experiments (t_{mix} = 500 ms) for identification of 11-*cis*-**8-Me**

7-*cis*-8-Me This photoproduct has been assigned in the following way: The singlet at 2.43 ppm is recognised as Me13 due to its dipolar coupling with a doublet at 8.88 ppm, identifiable by its chemical shift with H15, and with a doublet of doublets at 7.51 ppm, identifiable by its scalar coupling with H11. The assignment of H11 is further confirmed by its dipolar coupling with a Me at 2.07 ppm, possibly Me9. Irradiation of a singlet at 2.04 ppm adjacent to Me9 reveals dipolar coupling with a singlet at 6.06 ppm, H7, and a doublet at 6.42 ppm, possibly H10. The assignment of Me8 and Me9 is further confirmed by their scalar coupling, probed with via 1D selective TOCSY with short mixing time (t_{mix} 100 ms): irradiation of the singlet at 2.04 ppm shows scalar coupling only with the H7 at 6.06 ppm, identifying it as Me8. The other Me at 2.07 ppm shows scalar coupling with a doublet at 6.42 ppm, confirming its assignment as Me9.

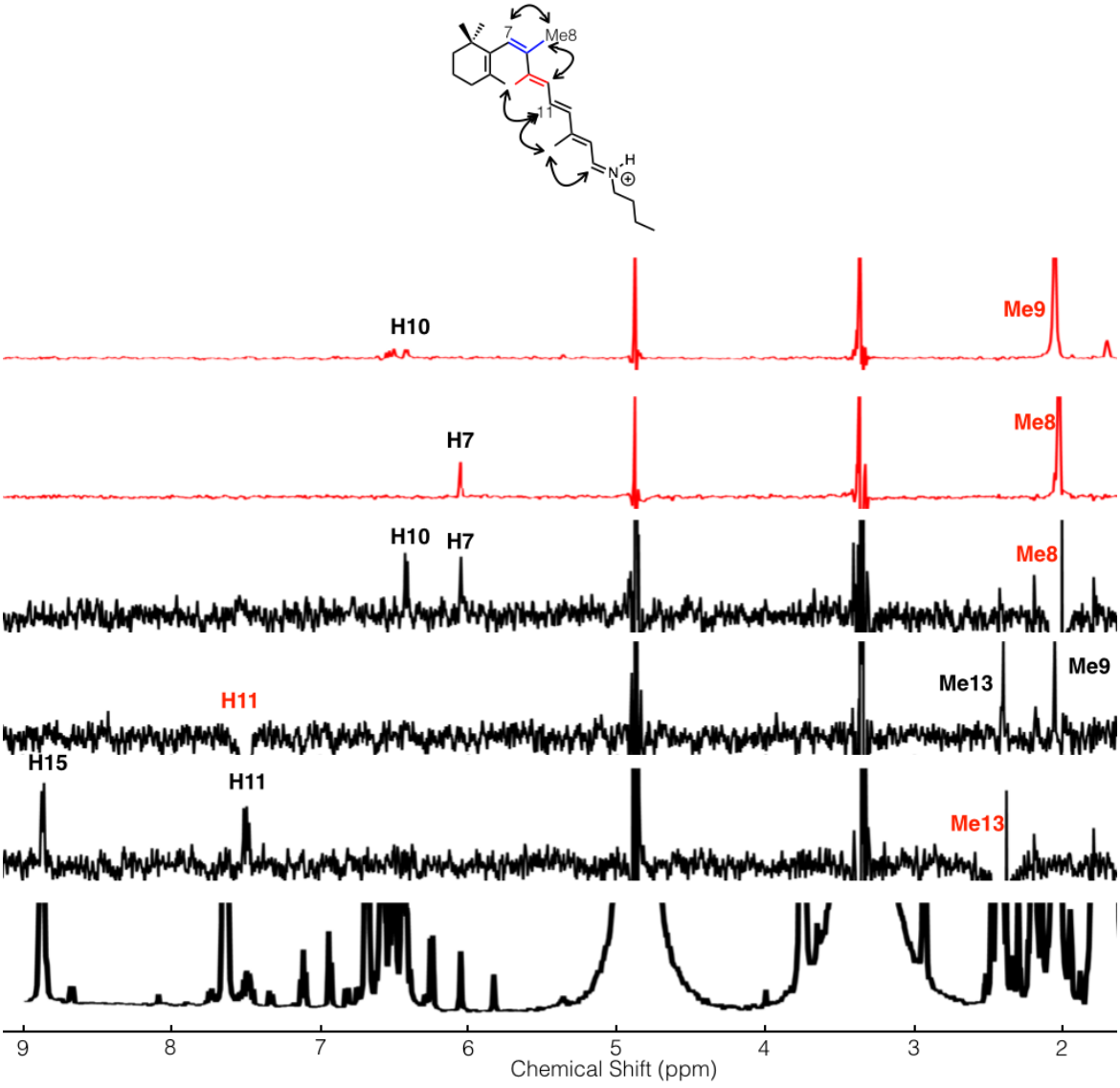

Figure A.3 NOESY (t_{mix} = 500 ms) and TOCSY (t_{mix} = 100 ms) experiments for identification of 7-*cis*-**8-Me**

all-*trans*-9-demethyl retinal *n*-butylamine protonated Schiff base (9-dm)

The identified photoproduct was 11-*cis* with a QY of 0.25.

11-*cis*-9-dm This photoproduct was assigned in the following way: First a 1D TOCSY spectrum (t_{mix} = 100 ms) was done irradiating the multiplet at 6.94 ppm, and is plotted as external projection on the COSY spectrum in Figure A.4. Between the TOCSY and the COSY it is possible to identify to possible sequences for the resonances of the protons from H7 to H12, shown in the Figure by coloured circle and numbers, red if H7 is at 6.15 ppm or black if H7 is at 6.56 ppm. Irradiation of the resonance at 6.14 ppm, showing dipolar coupling to two protons at 6.70 and 6.51 ppm, identifies it as H12, as it couples with a polyenic proton,, H14, not belonging to the H7-H12 spin system. Therefore, the black order is the correct one (H7 at 6.56 ppm), as marked in Figure A1.4. Identity of H12 is further confirmed by a weak correlation with a singlet at 2.49 ppm, whose dipolar coupling with a proton at 8.88 ppm, H15, identifies it as Me13. Furthermore, the dipolar correlations between H12 and H11 (6.70 ppm) and Me13 and H10 (6.94 ppm) prove the 11-*cis* configuration of the C11=C12 double bond. Finally, the dipolar couplings of H9 at 6.76 ppm with H11 (6.70 ppm) and H7 (6.56 ppm) reveals the *trans* configuration of the C7=C8 and C9=C10 double bonds. The simultaneous dipolar coupling of H12 with Me13 and H14 suggests the presence in solution of two conformations.

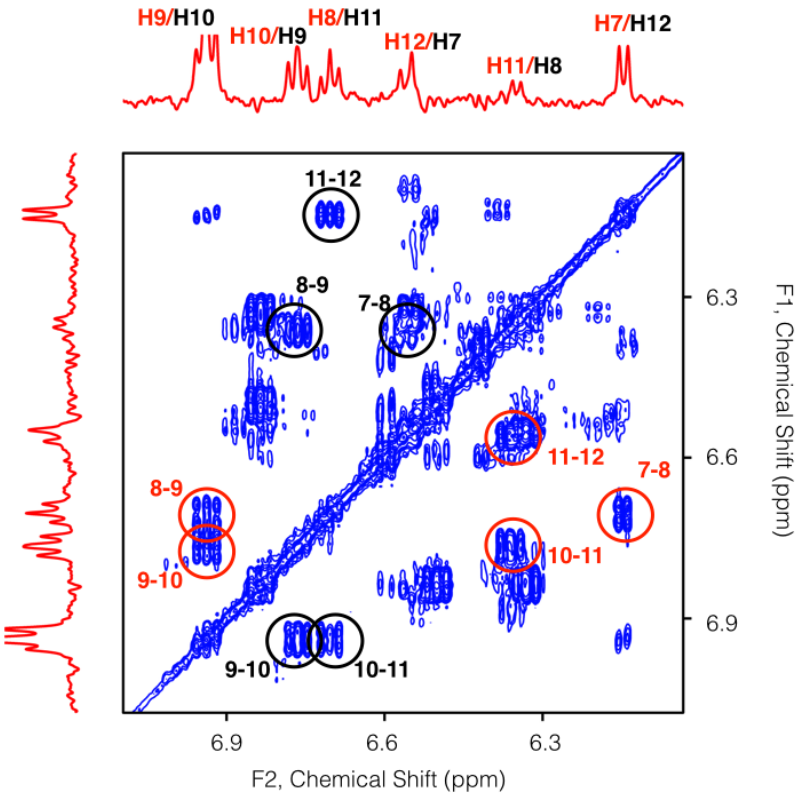

Figure A.4 COSY spectrum of the irradiated mixture of all-*trans*-**9-dm** with TOCSY (t_{mix} =100 ms) experiment as external projections. The red and black circles and numbers identify the two possible orders for the resonances from H7 to H12.

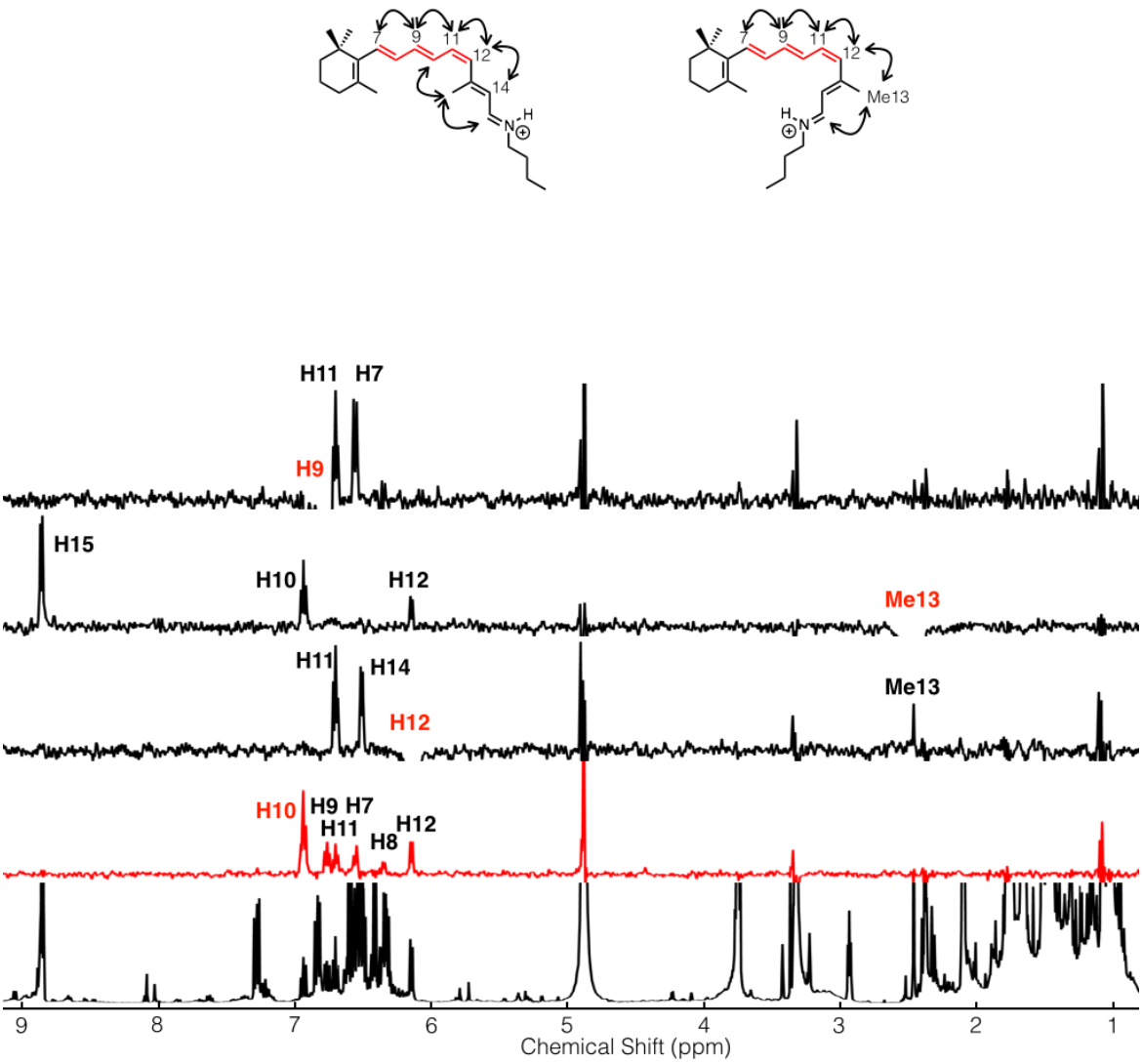

Figure A.5 NOESY (t_{mix} = 800 ms) and TOCSY (t_{mix} = 100 ms) experiments for identification of 11-*cis*-**9-dm**.

all-*trans*-9,13-demethyl retinal *n*-butylamine protonated Schiff base (9,13-dm)

The photoproducts were identified as 11-*cis* and 9-*cis*, with a quantum yield of 0.22 and 0.09, respectively.

11-*cis*-9,13-dm This photoproduct was identified in the following way: The TOCSY (t_{mix}= 150 ms) spectrum obtained by irradiation of the multiplet at 8.17 ppm revealed all the polyenic chain protons. The COSY spectrum in Figure A.6 allowed to identify each one of them following the scalar coupling starting from the H15, the most deshielded doublet

at 8.48 ppm. The relevant cross peaks are marked with black circles and the numbers of the protons generating them. The dipolar couplings observed for H13 (8.16 ppm) with H15 and H10 (7.01 ppm), and for H11 (6.88 ppm) with H12 (6.37 ppm) and H9 (6.80 ppm) are sufficient to prove the *cis* configuration of the C11=C12 double bond.

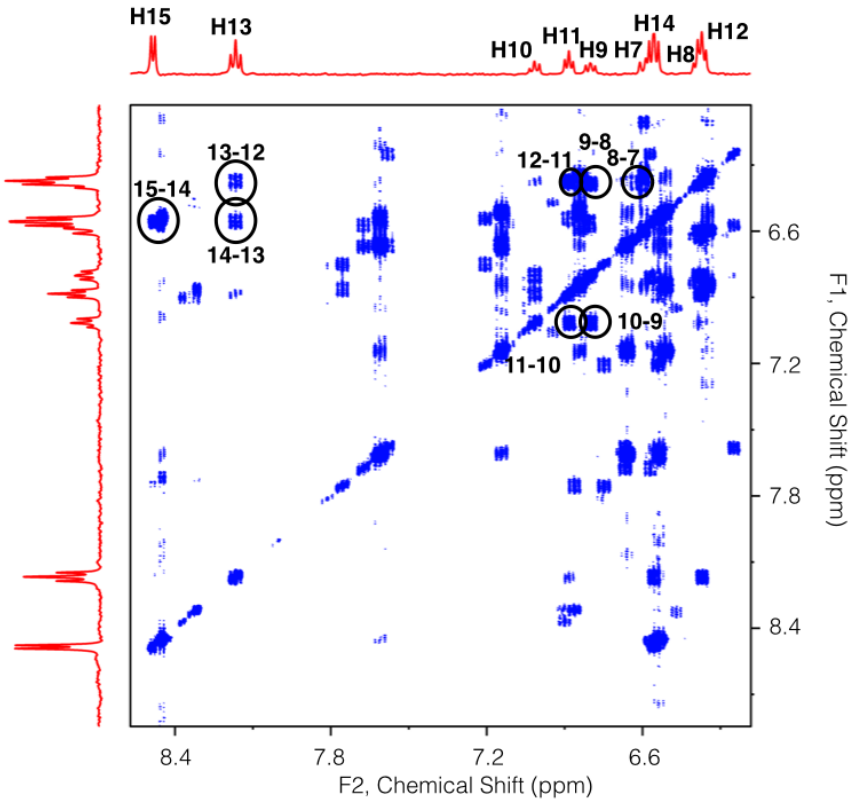

Figure A.6 COSY spectrum of the irradiated mixture of all-*trans*-**9,13-dm** with TOCSY (t_{mix} =150 ms) experiment as external projections. The black circles identify the cross peaks of the protons indicated by the respective numbers that allow to reconstruct the H15 to H7 sequence.

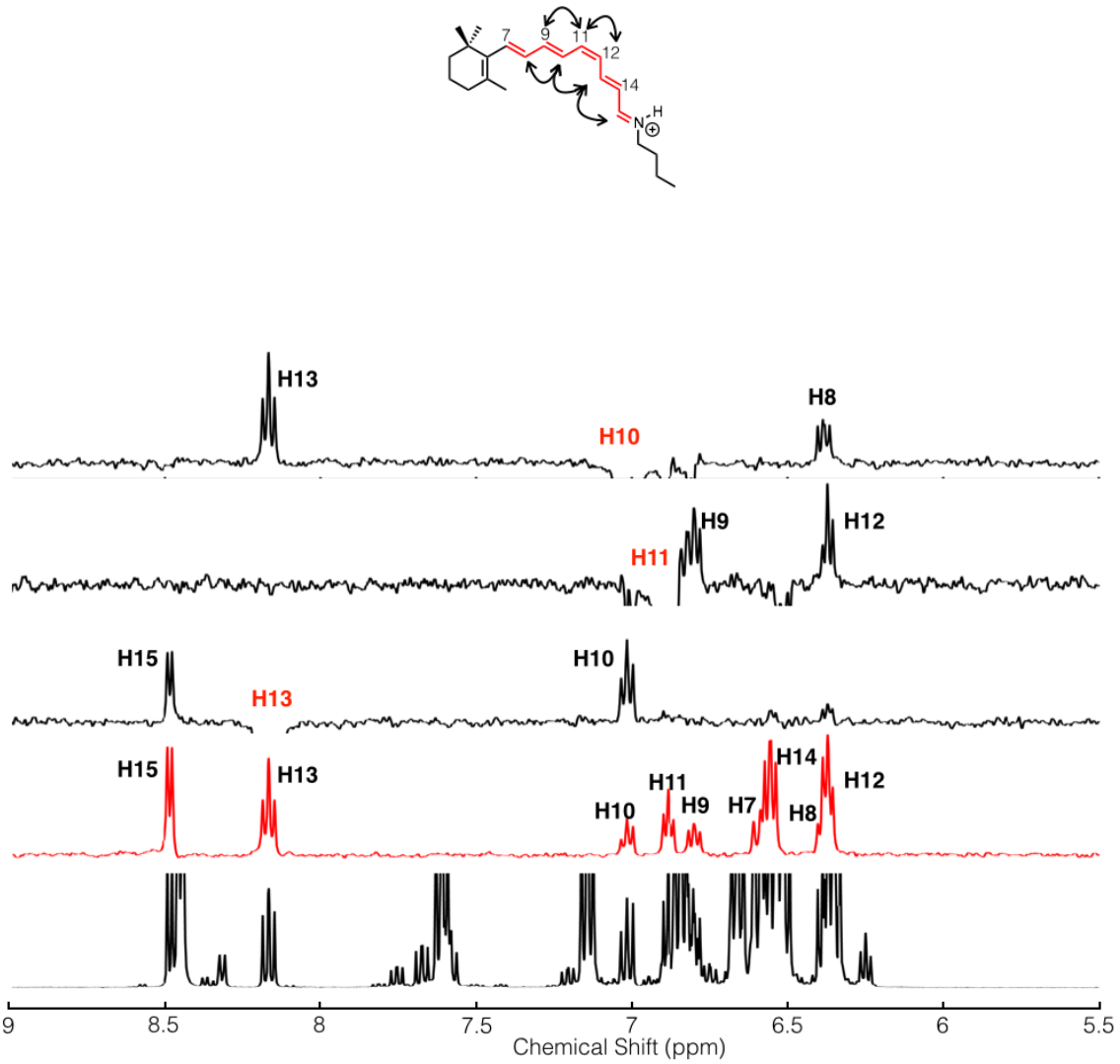

Figure A.7 NOESY (t_{mix} = 800 ms) and TOCSY (t_{mix} = 150 ms) experiments for identification of 11-*cis*-**9,13-dm**.

9-*cis*-9,13-dm This photoproduct was identified in the following way: The TOCSY (t_{mix}= 150 ms) spectrum obtained by irradiation of the multiplet at 6.25 ppm revealed all the polyenic chain protons. The COSY spectrum in Figure A.8 allowed to identify each one of them following the scalar coupling starting from the H15, the most deshielded doublet at 8.45 ppm. The relevant cross peaks are marked with black circles and the numbers of the protons generating them. The dipolar couplings observed for H13(7.67 ppm) with H15 and H11 (7.58 ppm), and for H10 (6.25 ppm) with H9 (6.56 ppm) and H12 (6.66 ppm) are sufficient to prove the *cis* configuration of the C9=C10 double bond. The second TOCSY measured irradiating H10 with a shorter mixing time (t_{mix} = 20 ms) was recorded to reveal the expected doublet of doublets shape with similar coupling constants for H9.

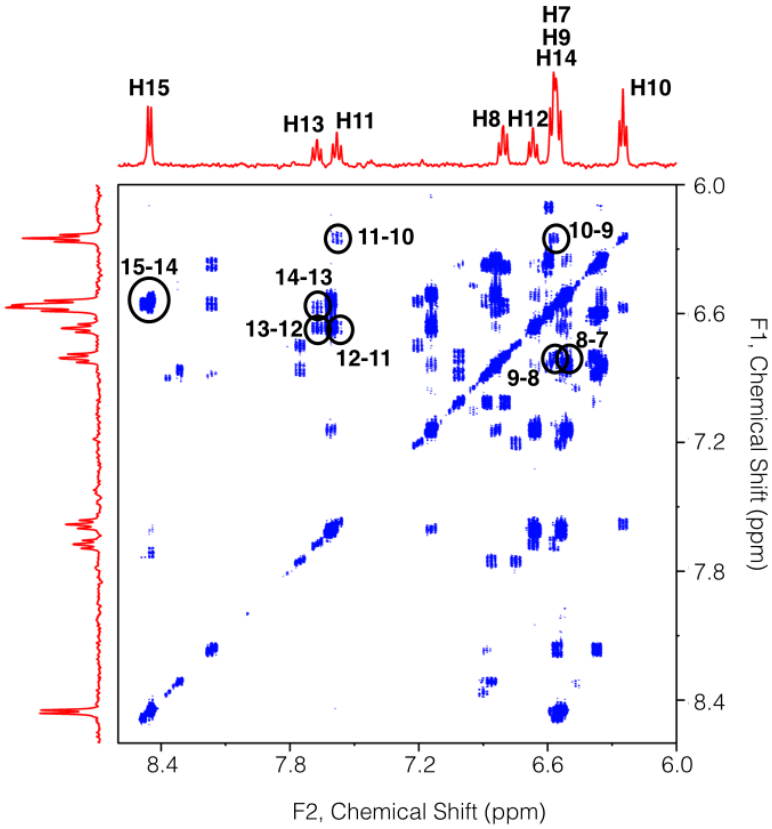

Figure A.8 COSY spectrum of the irradiated mixture of all-*trans*-**9,13-dm** with TOCSY (t_{mix} =150 ms) experiment as external projections. The black circles identify the cross peaks of the protons indicated by the respective numbers that allow to reconstruct the H15 to H7 sequence.

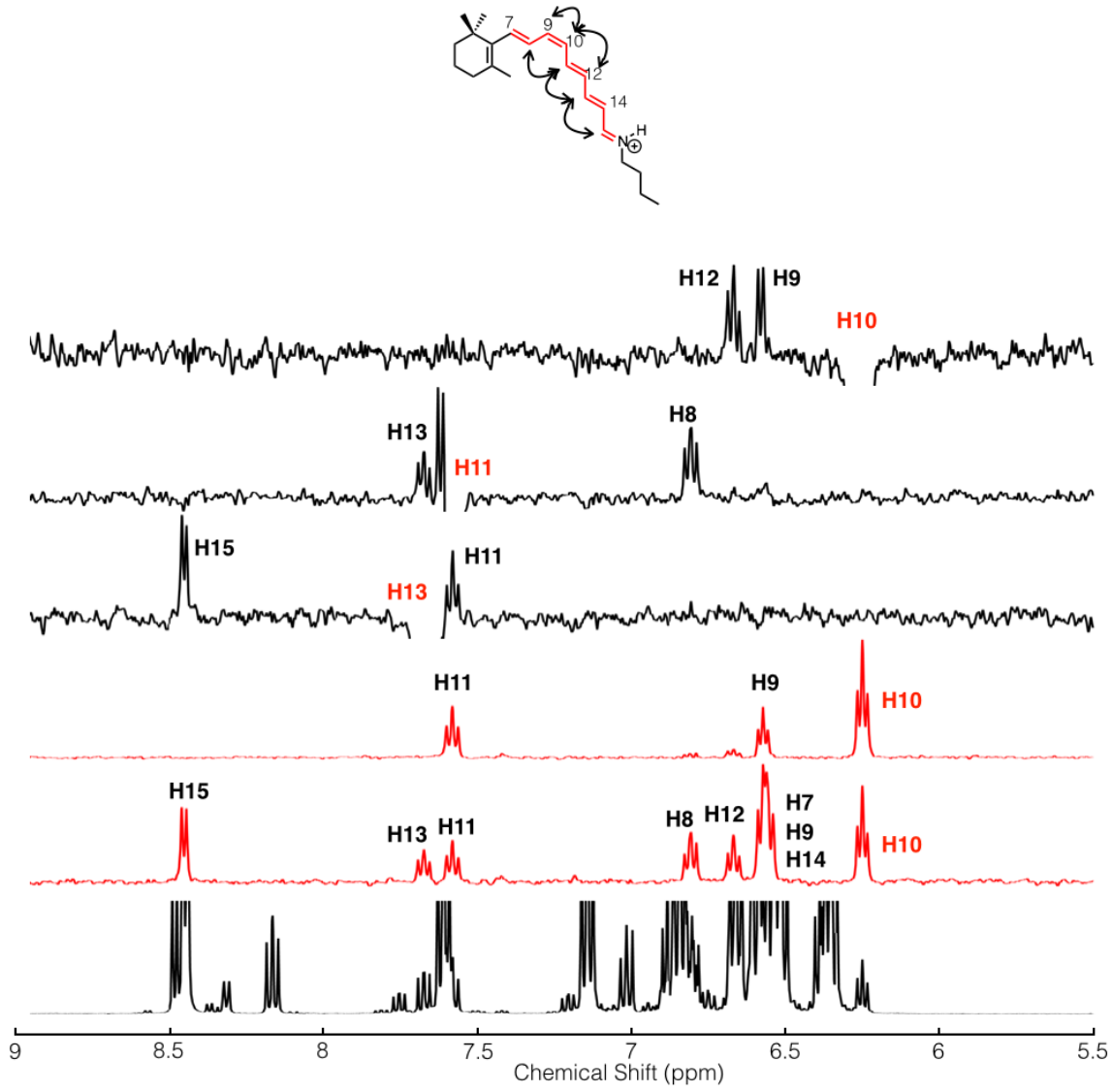

Figure A.9 NOESY (t_{mix} = 800 ms) and TOCSY (t_{mix} = 150 and 20 ms) experiments for identification of 9-*cis*-**9,13-dm**.

all-*trans*-10-methyl retinal *n*-butylamine protonated Schiff base (10-Me)

The photoproduct was identified as 11-*cis*, with a QY of 0.09.

11-*cis*10-Me The photoproduct was identified by comparison of the ^{1}H NMR spectrum of the irradiated mixture and the pure compound. Characterisation data for 11-*cis*-**10-Me** are given in Appendix B, as the photochemistry of the compound has been presented in Chapter 4.

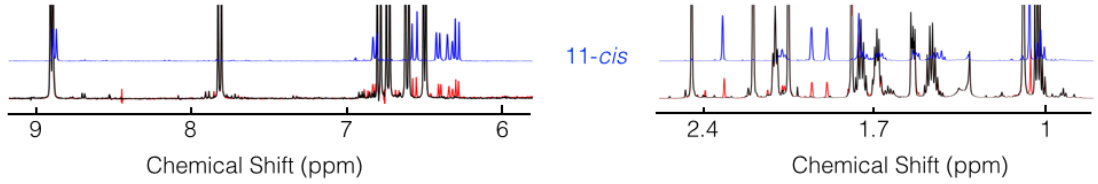

Figure A.10 Photoproduct identification for all-*trans*-**10-Me** with the ^{1}H NMR spectrum of pure 11-*cis*-**10-Me**.

all-*trans*-10-*iso*-propyl retinal *n*-butylamine protonated Schiff base (10-iPr)

The main photoproduct was identified as 11-*cis*, with a QY of 0.07. Its characterisation data are given in Appendix B as the photochemistry of the compound has been studied in Chapter 4. The secondary photoproduct, with a QY of 0.05, could not be identified, but comparison of the irradiated mixture with the ^{1}H NMR of the pure 9-*cis* isomer likely excludes it being 9-*cis*.

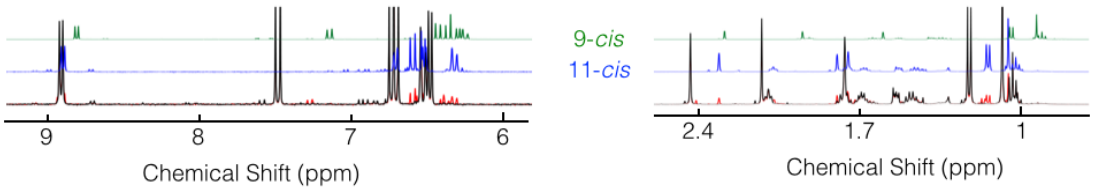

Figure A.11 Photoproduct identification for all-*trans*-**10-iPr** with the ^{1}H NMR spectrum of pure 11-*cis*-**10-iPr** and 9-*cis*-**10-iPr**.

9-*cis*-10-iPr Characterisation data for 9-*cis*-**10-iPr** are reported below

^{1}H NMR (500 MHz, CD_3OD) δ_H/ppm 0.90 (t, J=7.4 Hz, 3 H), 0.93 (s, 6 H), 1.04 (d, J=7.0 Hz, 6 H), 1.34 (m, 2 H), 1.37 - 1.42 (m, 2 H), 1.49 - 1.56 (m, 2 H), 1.59 (d, J=0.6 Hz, 3 H), 1.61 - 1.68 (m, 2 H), 1.92 (t, J=6.1 Hz, 2 H), 1.94 (t, J=0.6 Hz, 3 H), 2.28 (s, 3 H), 3.07

(spt, J=7.0 Hz, 1 H), 3.65 (t, J=7.3 Hz, 2 H), 6.24 (d, J=15.8 Hz, 1 H), 6.29 (d, J=11.0 Hz, 1 H), 6.36 (d, J=16.0 Hz, 1 H), 6.42 (d, J=15.8 Hz, 1 H), 7.14 (d, J=15.8 Hz, 1 H), 8.81 (d, J=11.0 Hz, 1 H).

^{13}C NMR (125 MHz, CD_3OD) δ_C/ppm 14.0, 14.3, 15.8, 20.4, 20.8, 21.9, 22.5, 29.6, 31.7, 32.3, 34.0, 35.4, 40.8, 53.1, 117.4 (q, J=278.3 Hz), 120.7, 130.5, 130.9, 135.5, 136.8, 137.0, 139.7, 141.7, 142.8, 161.2 (q, J=37.7 Hz), 166.1, 168.1.

HRMS (ESI^+) m/z calcd for $C_{27}H44N$ $[M]^+$: 382.3468, found: 382.3477.

The 9-*cis* configuration of the C9=C10 double bond is supported by the dipolar coupling of the methyl groups of the *iso*-propyl group at 1.03 ppm with Me9 (1.94 ppm) and H11 (7.14 ppm) in the 2D NOESY spectrum in Figure A1.12 (t_{mix} = 800 ms). The dipolar couplings of Me13 (2.29 ppm) with H15 (8.81) and H11 indicates the *trans* configuration of C13=C14 and C11=C12 double bonds, as do the dipolar couplings of H7 (6.24 ppm) with Me9 for the C7=C8 double bond. H7 is further identified by its dipolar coupling with the Me1 (0.93 ppm).

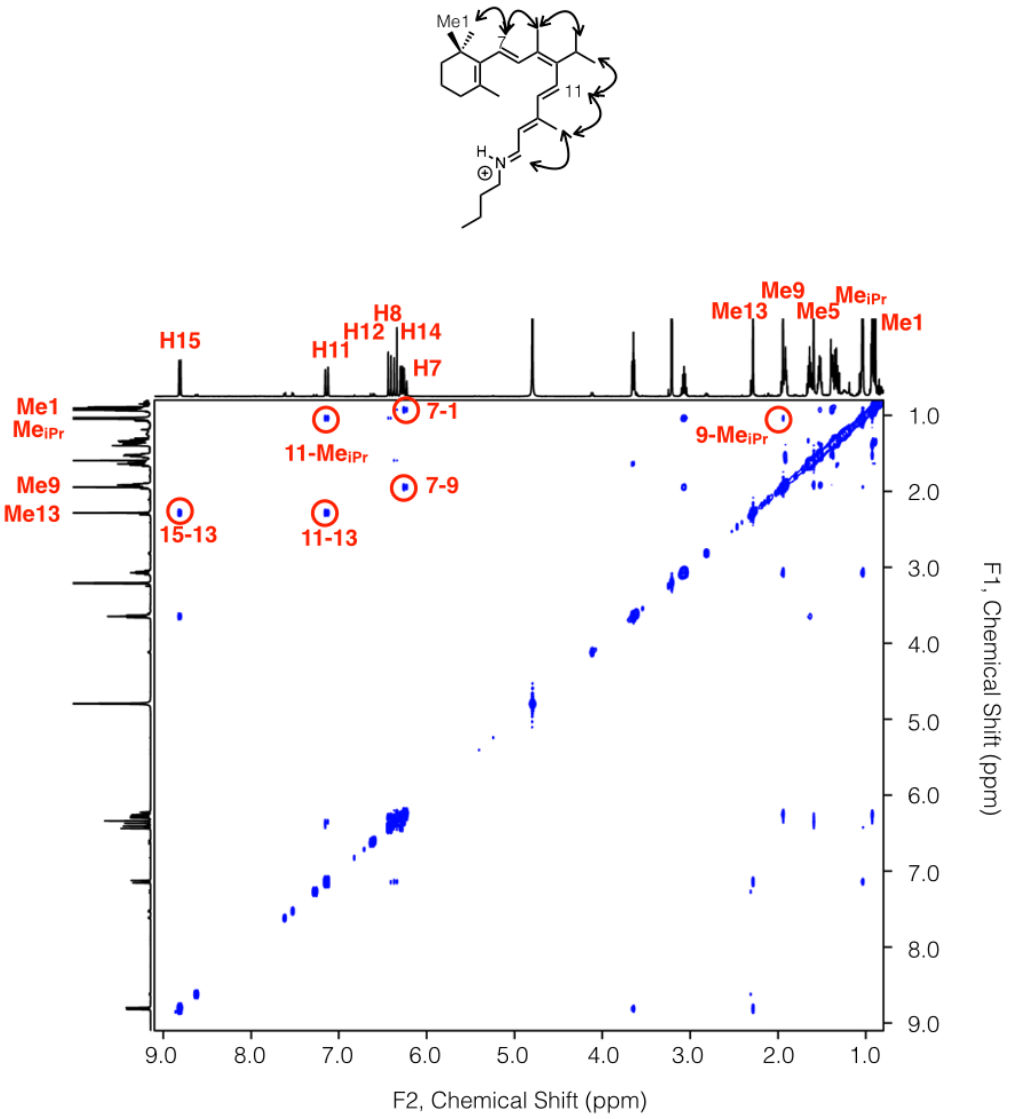

Figure A.12 NOESY (t_{mix}=800 ms) experiment for identification of 9-*cis*-**10-iPr**. Relevant cross-peaks are circled in red and labelled with the corresponding proton numbers.

all-*trans*-10,14-methyl retinal *n*-butylamine protonated Schiff base (10,14-Me)

The photoproducts were identified as 11-*cis* and 9-*cis*, with a QY of 0.08 and 0.01, respectively.

11-*cis*-10,14-Me This photoproduct was identified through dipolar couplings observed in a 2D NOESY experiment (t_{mix} = 1 s). The relevant cross peaks are circled in the figure, and the number refers to the protons generating them. H7 at 6.33 ppm is identified through its dipolar coupling with Me1 at 1.05 ppm, assignable due to their higher intensity (being two germinal methyl groups, their peaks integrates for 6 protons) and characteristic low chemical shift. H7 shows dipolar coupling with a Me at 1.85 ppm, identifying the latter as Me9 and the C7=C8 double bond configuration as *trans*. The dipolar coupling Me9 with what is likely a doublet at 6.81 ppm, identify the latter as H11. The proton at 6.55 ppm can be identified as H8 by exclusion and because of its 16 Hz scalar coupling constant in common with H7(Figure A.13). This leaves the proton at 6.41 ppm as H12, that shows a correlation with Me 14 at 1.95 ppm. The methyl at 2.33 ppm that show dipolar coupling with H15 (buried under the starting material) is Me13. The dipolar coupling of H11 with H12 (Figure A.14) clearly reveal the *cis* configuration of the C11=C12 double bond.

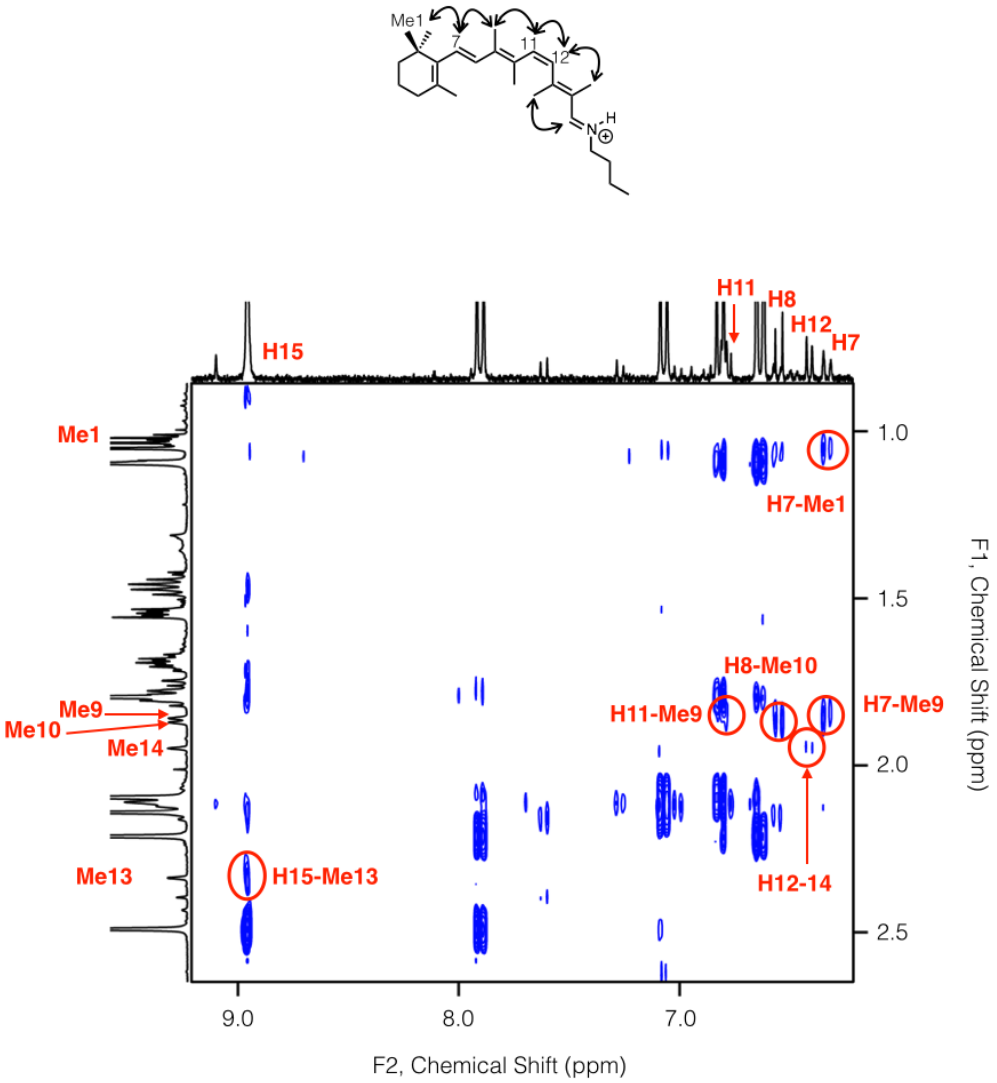

Figure A.13 NOESY (t_{mix}=800 ms) experiment for identification of 11-*cis*-**10,14-Me**.Correlations between signals in the high field (F_1, 0.8-2.7 ppm) and low field region (F_2, 6.2-9.2 ppm). Relevant cross-peaks are circled in red and labelled with the corresponding proton numbers.

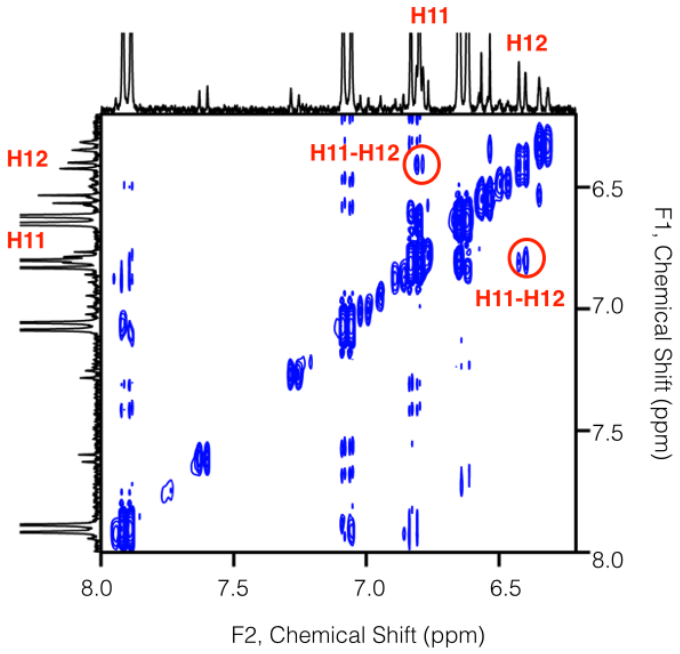

Figure A.14 NOESY (t_{mix}=800 ms) experiment for identification of 11-*cis*-**10,14-Me**.Correlations between signals in the low field region (F_1, F_2 6.2-8.0 ppm). Relevant cross-peaks are circled in red and labelled with the corresponding proton numbers.

9-*cis*-10,14-Me The photoproduct was identified by comparison of the ^{1}H NMR spectrum of the irradiated mixture and the pure compound. Characterisation data for 9-*cis*-**10,14-Me** are reported below Figure A.15.

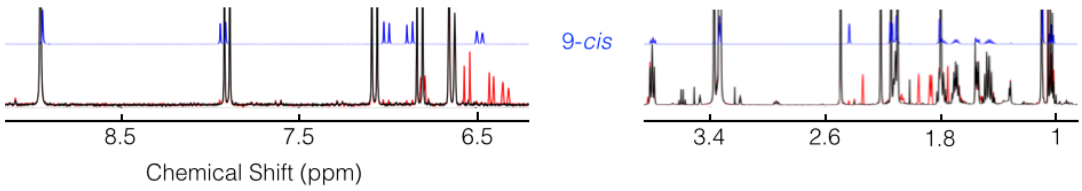

Figure A.15 Photoproduct identification for all-*trans-10,14-Me* with the ^{1}H NMR spectrum of pure 9-*cis*-**10,14-Me**.

Characterisation data for 9-*cis*-**10,14-Me** are given below.

^{1}H NMR (500 MHz, CD_3OD) δ_H/ppm 1.01 (t, J=7.4 Hz, 3 H), 1.07 (s, 6 H), 1.38 - 1.48 (m, 2 H), 1.50 - 1.54 (m, 2 H), 1.64 - 1.70 (m, 2 H), 1.77 - 1.79 (m, 2 H), 1.78 (s, 3 H), 2.08 (t, J=6.3 Hz, 2 H), 2.08 (s, 3 H), 2.11 (s, 3 H), 2.12 (s, 3 H), 2.41 (s, 3 H), 3.77 (t, J=7.4 Hz, 2 H), 6.46 (d, J=15.9 Hz, 1 H), 6.85 (d, J=15.8 Hz, 1 H), 6.98 (d, J=15.2 Hz, 1 H), 7.90 (d, J=15.3 Hz, 1 H), 8.92 (s, 1 H).

^{13}C NMR (126 MHz, CD_3OD) δ_C/ppm 12.1, 14.0, 15.4, 15.5, 17.3, 20.4, 20.9, 22.3, 29.6, 32.8, 34.2, 35.4, 40.8, 53.4, 116.8 (q, J=286.3 Hz), 125.1, 126.3, 131.9, 132.3, 132.4, 133.2, 139.6, 141.5, 144.3, 160.2 (q, J=39.6 Hz), 163.3, 168.0.

HRMS (ESI^+) m/z calcd for $C_{26}H_{42}N$ $[M]^+$: 368.3312, found: 368.3312.

The 9-*cis* configuration is confirmed by the 2D NOESY (tmix = 800 ms) shown in figure A.15. It can be assigned judging from the dipolar couplings circled in red. Specifically, the coupling between H15 (8.92 ppm) and Me13 (2.41 ppm) and between H11 (7.90 ppm) and Me13 reveals the *trans* configuration of the C11=C12 and C13=C14 double bonds. The dipolar coupling of H11 with H8 (6.85 ppm) and H12 (6.98 ppm) with Me14 (2.09 ppm) confirm the *cis* configuration of the C9=C10 double bond. The dipolar coupling observed for H7 (6.46 ppm) with Me9 (2.11 ppm) and Me1 (1.07 ppm) confirms the *trans* configuration of the C7=C8 double bond.

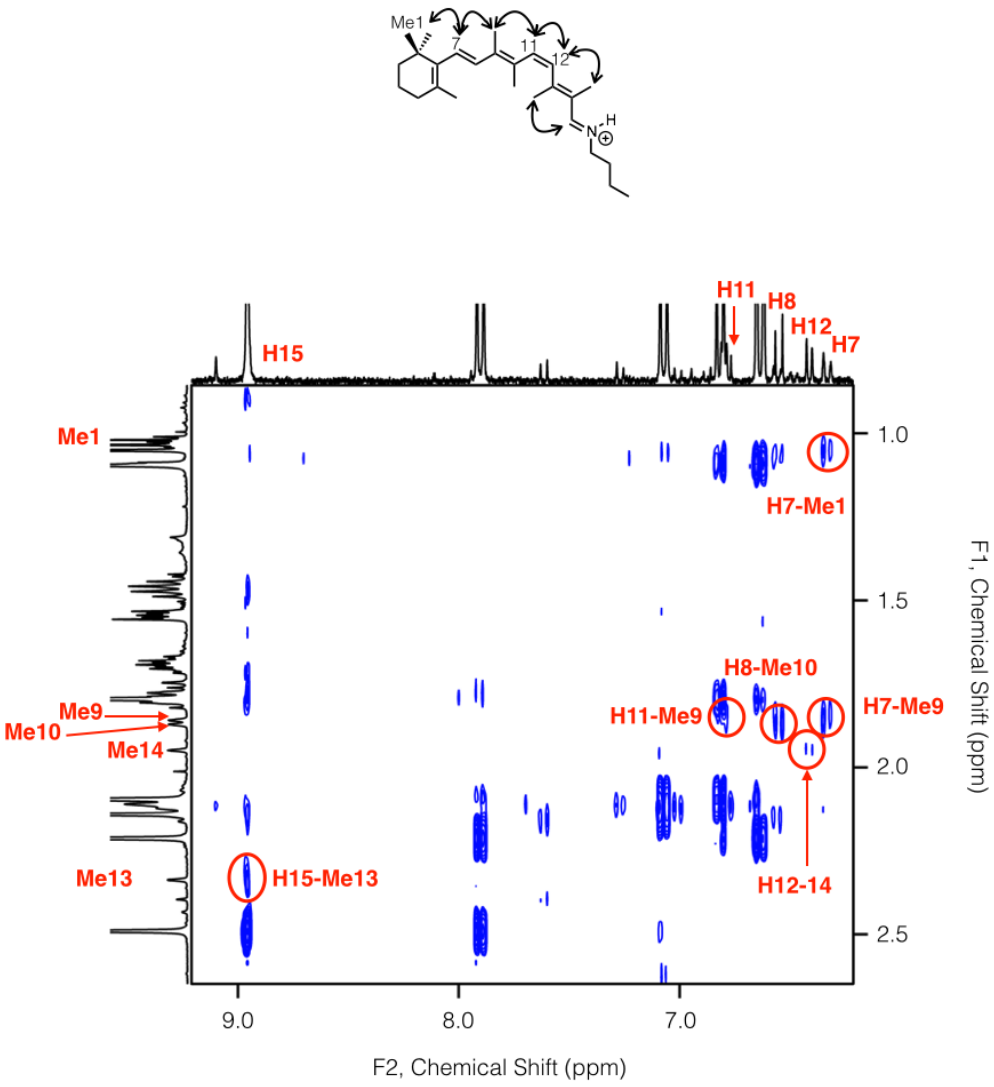

Figure A.16 NOESY (t_{mix}=800 ms) experiment for identification of 9-*cis*-**10,14-Me**. Relevant cross-peaks are circled in red and labelled with the corresponding proton numbers.

all-*trans*-13-demethyl retinal *n*-butylamine protonated Schiff base (13-dm)

The identified photoproducts were 11-*cis* and 9-*cis*, with a QY of 0.33 and 0.19, respectively.

11-*cis*-13-dm This photoproduct was identified in the following way: The TOCSY (t_mix= 80 ms) spectrum obtained by irradiation of the multiplet at 8.23 ppm revealed the polyenic chain protons from H15 to H10. The COSY spectrum in Figure A.17 allowed identification of each one of them following the scalar coupling starting from the H15, the most deshielded doublet at 8.48 ppm. The relevant cross peaks are marked with black circles and the numbers of the protons generating them. The dipolar couplings (Figure A.18) observed for H13 (8.23 ppm) with H15 and H10 (6.88 ppm), and for H10 with H13 and H8 (6.35 ppm) are sufficient to prove the *cis* configuration of the C10=C11 double bond.

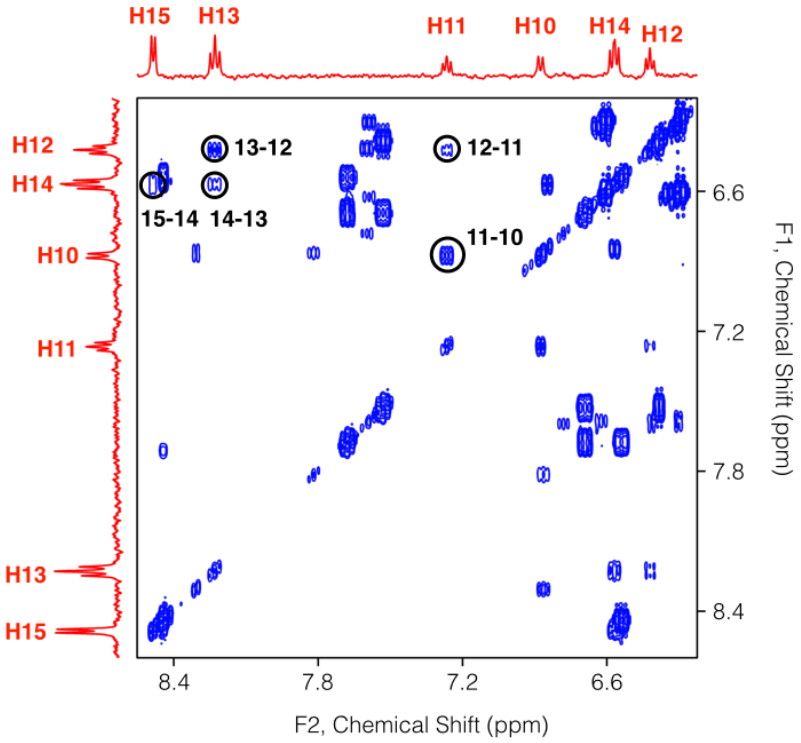

Figure A.17 COSY spectrum of the irradiated mixture of all-*trans*-**13-dm** with TOCSY (t_{mix} =80 ms) experiment as external projections. The black circles identify the cross peaks of the protons indicated by the respective numbers that allow to reconstruct the H15 to H10 sequence.

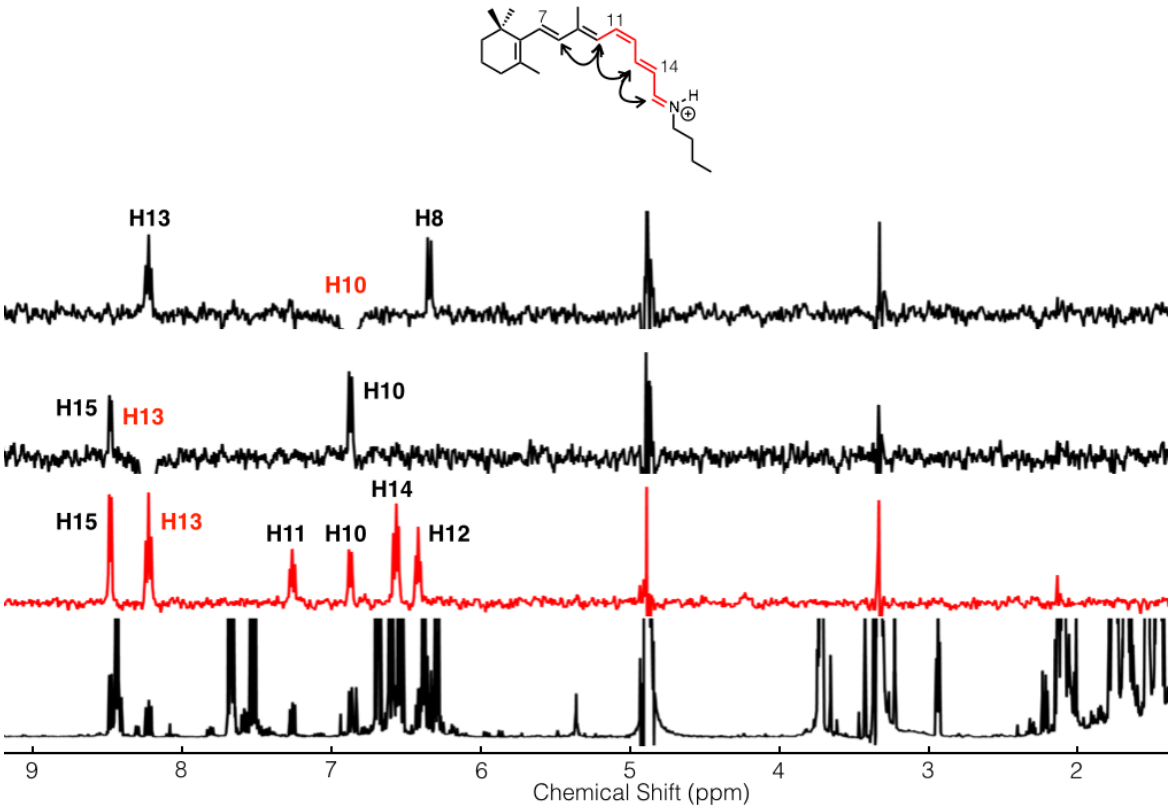

Figure A.18 NOESY (t_{mix} = 500 ms) and TOCSY (t_{mix} = 80 ms) experiments for identification of 11-*cis*-**13-dm**.

9-*cis*-13-dm This photoproduct was identified in the following way: The TOCSY (t_{mix} = 80 ms) spectrum obtained by irradiation of H15 at 8.42 ppm revealed the polyenic chain protons from H15 to H10. The COSY spectrum in Figure A.19 allowed assignment of each one of them following the scalar coupling starting from the H15, the most deshielded doublet. The relevant cross-peaks are marked with red circles and the numbers of the protons generating them. The dipolar couplings (Figure A.20) observed for H13 (7.67 ppm) with H15 and H11 (7.59 ppm), and for H11 with H13 and H8 (6.85 ppm) are sufficient to prove the *cis* configuration of the C9=C10 double bond. Other protons could not be irradiated as buried under more intense resonances from the starting material.

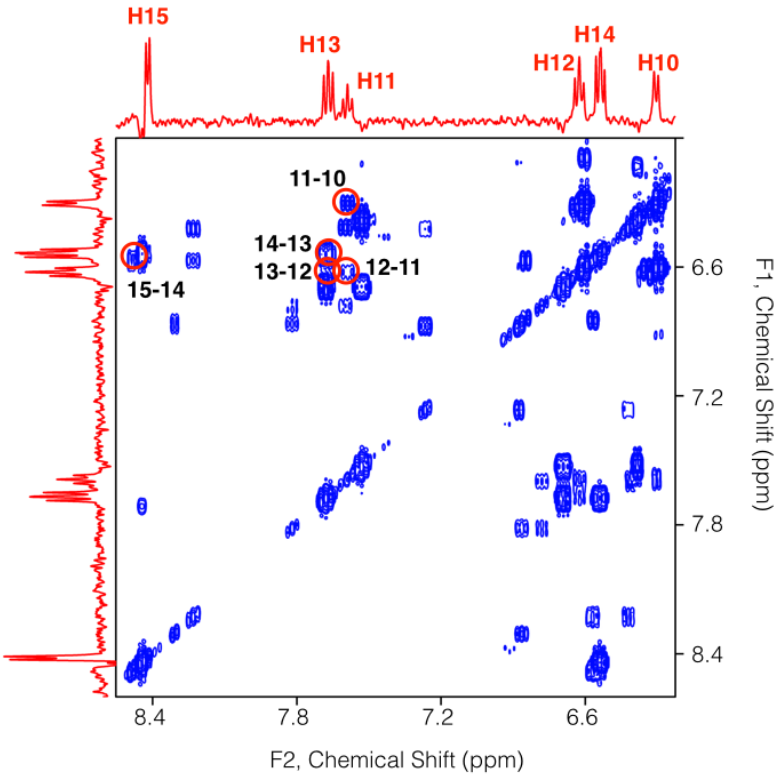

Figure A.19 COSY spectrum of the irradiated mixture of all-*trans*-**13-dm** with TOCSY (t_{mix} =80 ms, irradiation at 8.42 ppm) experiment as external projections. The black circles identify the cross peaks of the protons indicated by the respective numbers that allow to reconstruct the H15 to H10 sequence.

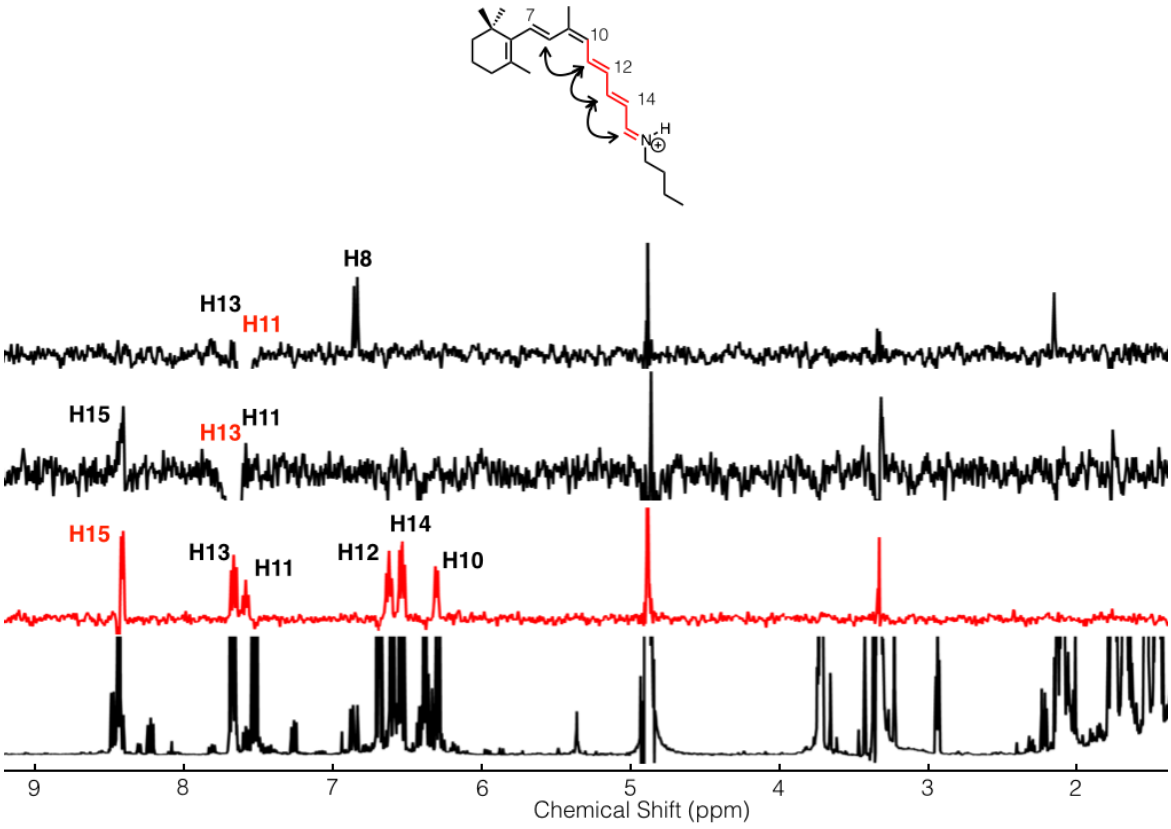

Figure A.20 NOESY (t_{mix} = 500 ms) and TOCSY (t_{mix} = 80 ms) experiments for identification of 9-*cis*-**13-dm**.

all-*trans*-14-methyl retinal *n*-butylamine protonated Schiff base (14-Me)

Photoproducts identification has been already discussed in Chapter 2, section 2.1.4, and is here repeated.

The identified photoproducts were 11-*cis* and 13-*cis*, with a QY of 0.11 and 0.03, respectively.

11-*cis*-14-Me This photoproduct was identified in the following way: The doublet of doublets at 6.95 ppm is identified as H11. It shows dipolar coupling with Me9 at 2.06 ppm and H12 at ppm 6.33 ppm, supporting the *cis* configuration for the C11=C12 double bond. Assignment of Me9 is confirmed by its dipolar coupling with H11 and H7 at 6.46 ppm. The latter assignment is made on the basis that H15 is expected to be a singlet at a much lower chemical shift. Irradiation of Me13 at 2.44 ppm reveals its dipolar coupling with H15 at 8.96 ppm and H10 at 7.07 ppm.

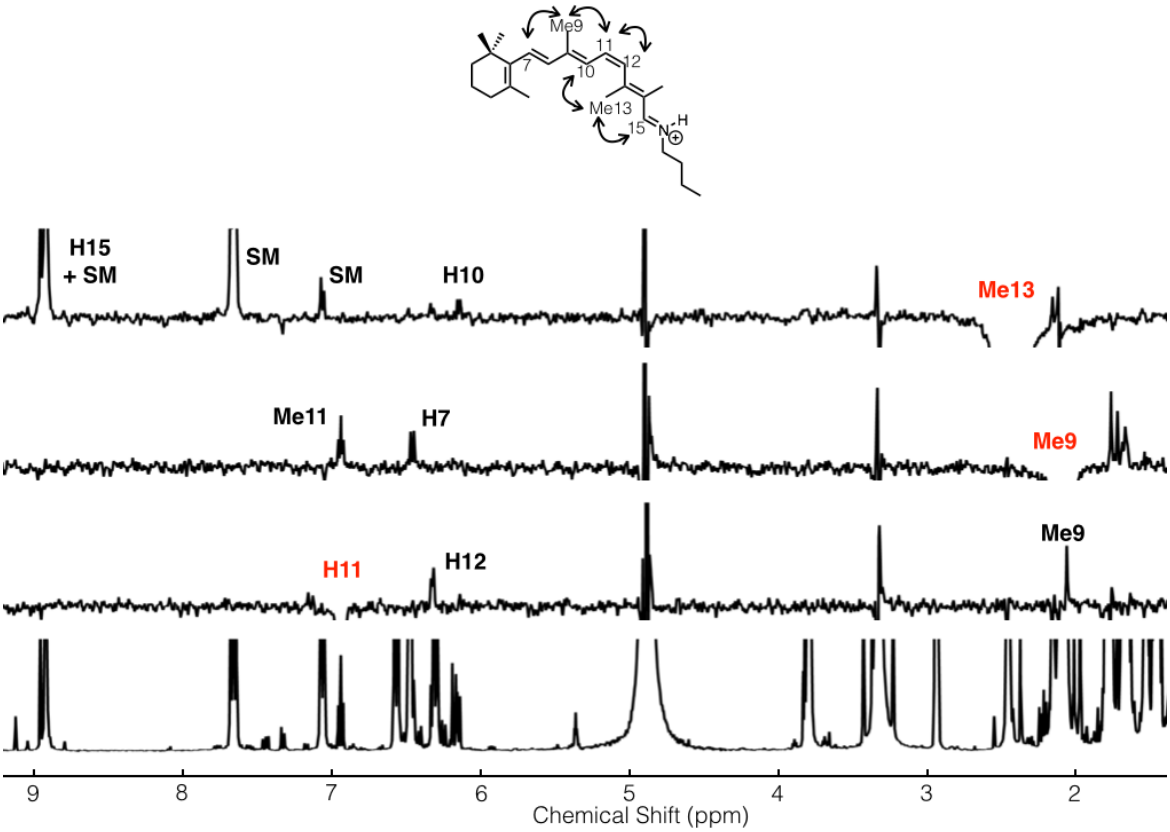

Figure A.21 NOESY (t_{mix} = 600 ms) experiments for identification of 11-*cis*-**14-Me**.

13-*cis*-14-Me The photoproduct was identified by comparison of the ^{1}H NMR spectrum of the irradiated mixture and the pure compound.

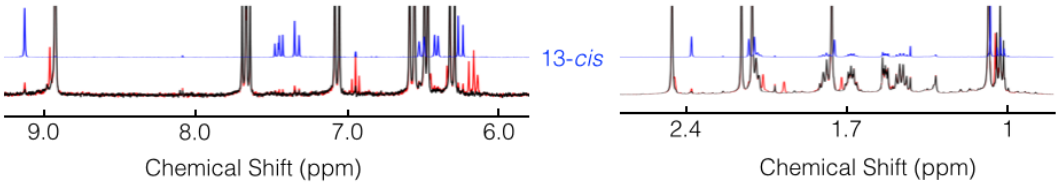

Figure A.22 Photoproducts identification for all-*trans*-**14-Me** by comparison of the ^{1}H NMR spectrum of the irradiated mixture with pure 13-*cis*-**14-Me**.

Characterisation data for 13-*cis*-**14-Me** are given below.

^{1}H NMR (500 MHz, CD_3OD) δ_H/ppm 1.00 (t, J=7.4 Hz, 3 H), 1.05 (s, 6 H), 1.39 - 1.46 (m, 2 H), 1.47 - 1.53 (m, 2 H), 1.59 - 1.68 (m, 2 H), 1.75 (s, 3 H), 1.69 - 1.81 (m, 2 H), 2.07 (s, 3 H), 2.04 - 2.09 (m, 2 H), 2.09 (s, 3 H), 2.34 (s, 3 H), 3.77 (t, J=7.4 Hz, 2 H), 6.23 (d, J=16.1 Hz, 1 H), 6.38 (d, J=11.3 Hz, 1 H), 6.48 (d, J=16.2 Hz, 1 H), 7.30 (d, J=14.6 Hz, 1 H), 7.42 (dd, J=14.5, 11.4 Hz, 1 H), 9.11 (s, 1 H)

^{13}C NMR (125 MHz, CD_3OD) δ_C/ppm 13.3, 13.4, 14.0, 18.3, 20.4, 20.9, 22.1, 29.5, 32.8, 34.2, 35.4, 40.9, 53.4, 116.7 (q, J=285.7 Hz), 125.3, 128.4, 131.3, 132.0, 132.3, 138.6, 138.7, 139.1, 145.5, 160.1 (q, J=40.1 Hz), 165.6, 166.6.

HRMS (ESI$^+$) m/z calcd for C_25H_40N $[M]^+$: 354.3155, found: 354.3143.

The 13-*cis* configuration of the C13=C14 double bond is confirmed by the dipolar coupling of H15 (9.11 ppm) with H12 (7.30 ppm) and Me13 (2.34 ppm) with Me14 (2.07 ppm). The *trans* configuration of the other double bonds is confirmed by following dipolar couplings: H11 (7.42 ppm) with Me13 and Me9 (2.09 ppm), and H7 (6.48 ppm) with H9. H7 is identified by its dipolar coupling with Me1(1.05 ppm).

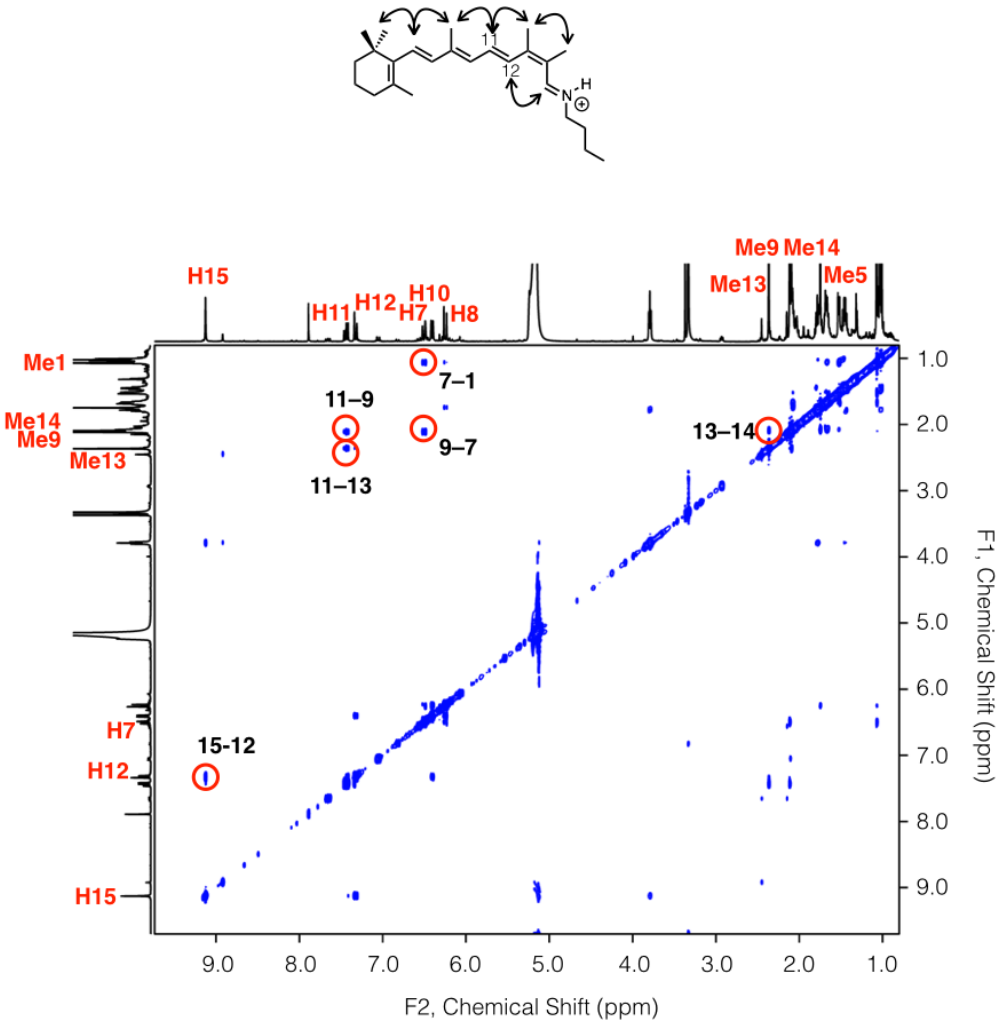

Figure A.23 NOESY (t_{mix} = 800 ms) experiments for identification of 13-*cis*-**14-Me**. Relevant cross-peaks are circled in red and labelled with the numbers of the relative protons.

all-*trans*-15-methyl retinal *n*-butylamine protonated Schiff base (15-Me)

The photoproducts were possibly identified as 11-*cis* and 13-*cis*, with QY of 0.09 and 0.03, respectively. A third photoproduct with QY 0.03 was formed but could not be identified.

11-*cis*-15-Me The evidence supporting the proposed identification is the following: the doublet of doublets at 6.94 ppm, H11, shows dipolar coupling with only one methyl group, Me9 at 2.08 ppm, (Figure A.24) and with a proton at 6.23 ppm, H12, (Figure A.25) with which is also scalarly coupled (Figure A.26). The cross-peaks discussed for this photoproduct are marked in orange in Figures A.24-26.

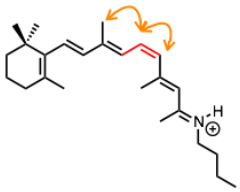

13-*cis*-15-Me The evidence supporting the proposed identification is the following: the doublet of doublets at 7.44 ppm shows dipolar coupling with two methyls group at 2.11 ppm and 2.38 ppm (Figure A.24). These can be identified either as Me9 or Me13. Both of them show dipolar coupling with two different protons, at 6.24 ppm and 6.33 ppm (Figure A.24), respectively. Considering the molecular structure, they can only be H7 and H14 (not necessarily in this order). The dipolar coupling of Me13 and H14 reveals the *cis* configuration of the C13=C14 double bond. The cross-peaks discussed for this photoproduct are marked in red in Figures A.24-26.

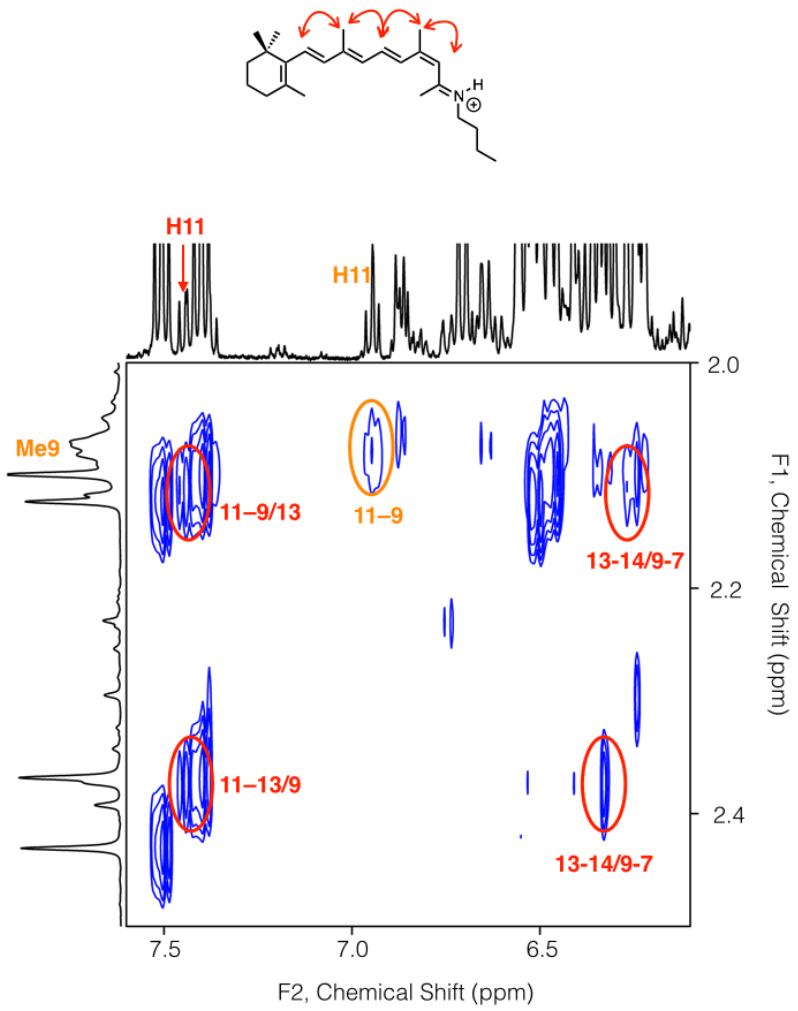

Figure A.24 NOESY (t_{mix} = 600 ms) experiments for identification of all-*trans*-**15-Me** photoroducts. Relevant cross-peaks for 11-*cis*-**15-Me** and 13-*cis*-**15-Me** are circled and labelled in red and orange, respectively.

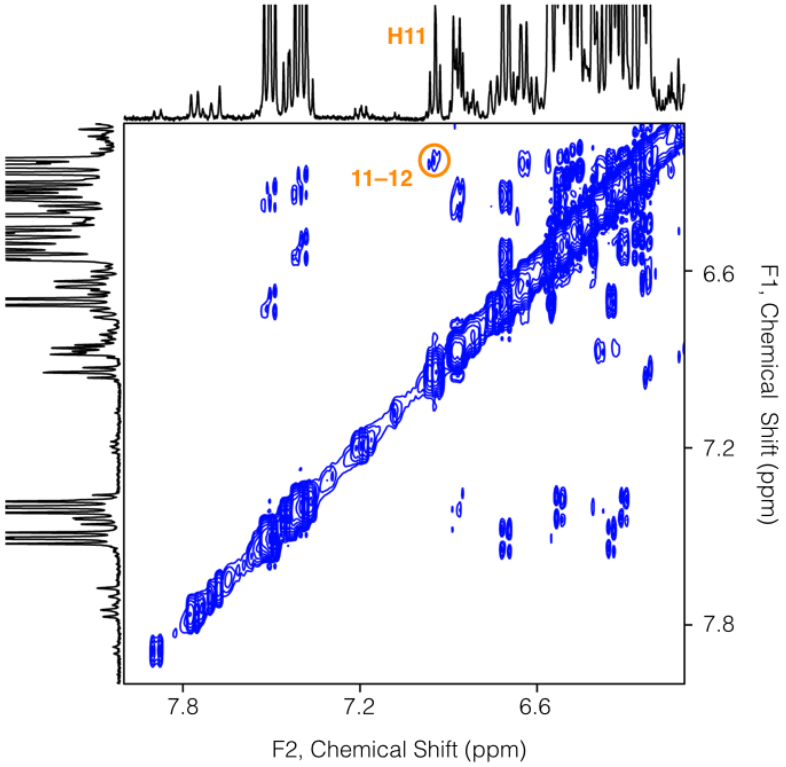

Figure A.25 NOESY (t_{mix} = 600 ms) experiments for identification of all-*trans*-**15-Me** photoroducts. Relevant cross-peaks for 11-*cis*-**15-Me** are circled and labelled in orange.

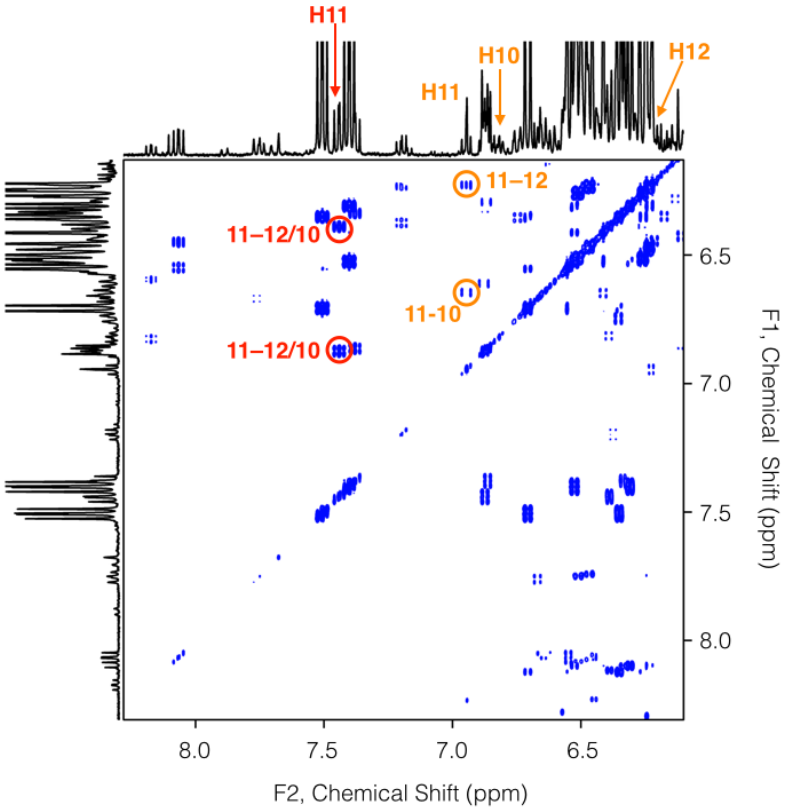

Figure A.26 COSY experiment for identification of all-*trans*-**15-Me** photoproducts. Relevant cross-peaks for 11-*cis* and 13-*cis* isomers are circled and labelled in orange and red, respectively.

A.4 Transient absorption maps, kinetics and spectra

All the Figures in this section are structured in the following way: (a) Transient absorption data map, with plotted on top the excited state lifetimes retrieved with the two methods described in Chapter 3 (red for DADS-weighted average and black for 1/e signal decay). (b) Kinetics at selected wavelength plotted in colours with the corresponding fit on top as a black dashed line. (c) Transient spectra at selected time delays plotted in colours with the corresponding fit on top as a black dashed line. All data have been acquired exciting the system with 20-30 fs pulses centred at 500 nm (20 nJ) and probing with 2 nJ of broadband white light. Solvent is methanol in all cases.

all-*trans* retinal *n*-butylamine protonated Schiff base (NAT)

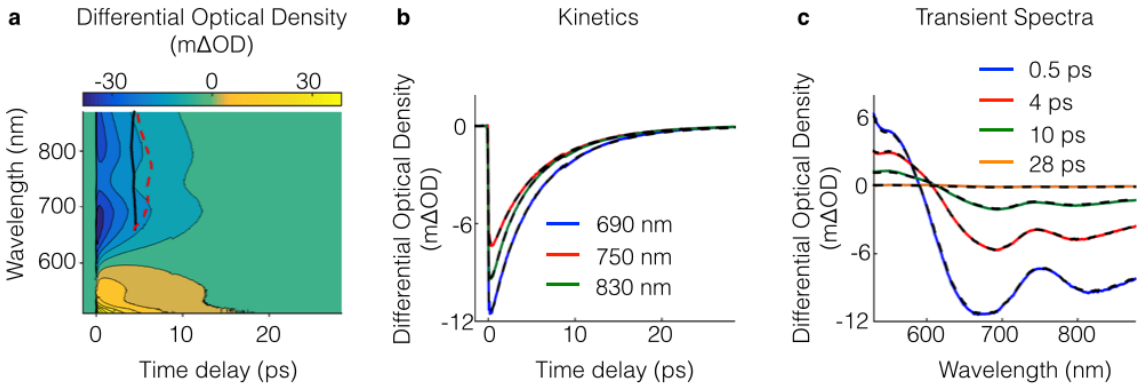

Figure A.27 all-*trans*-**NAT** transient absorption data

all-*trans*-8-methyl retinal *n*-butylamine protonated Schiff base (8-Me)

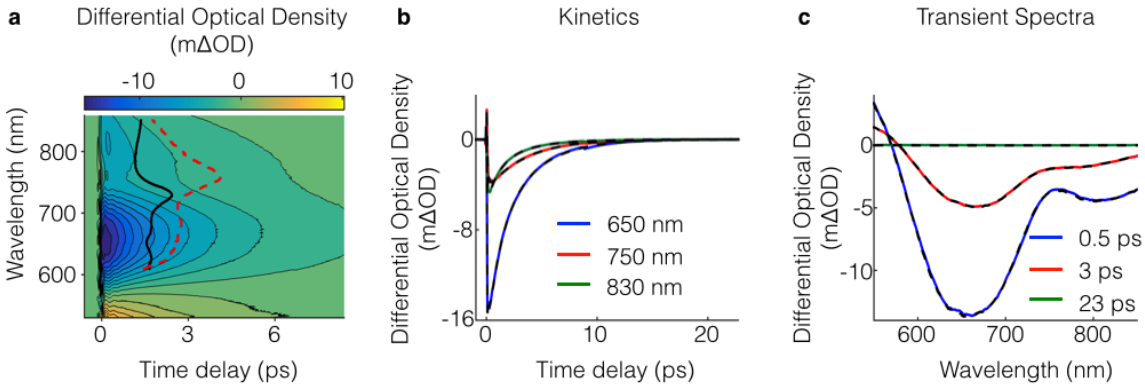

Figure A.28 all-*trans*-**8-Me** transient absorption data

all-*trans*-9-demethyl retinal *n*-butylamine protonated Schiff base (9-dm)

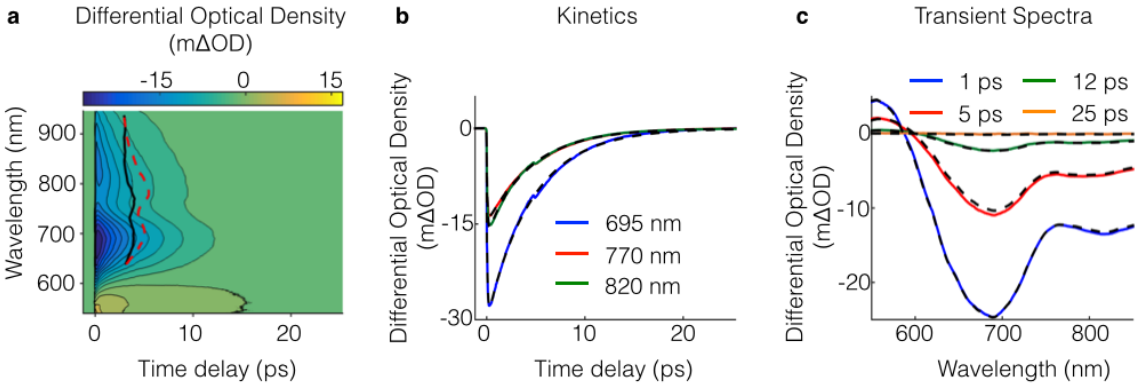

Figure A.29 all-*trans*-**9-dm** transient absorption data

all-*trans*-9,13-demethyl retinal *n*-butylamine protonated Schiff base (9,13-dm)

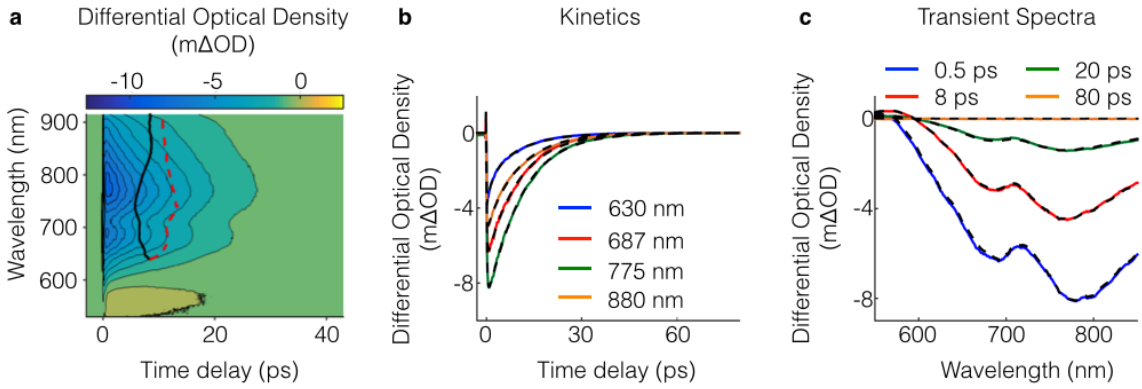

Figure A.30 all-*trans*-**9,13-dm** transient absorption data

all-*trans*-10-methyl retinal *n*-butylamine protonated Schiff base (10-Me)

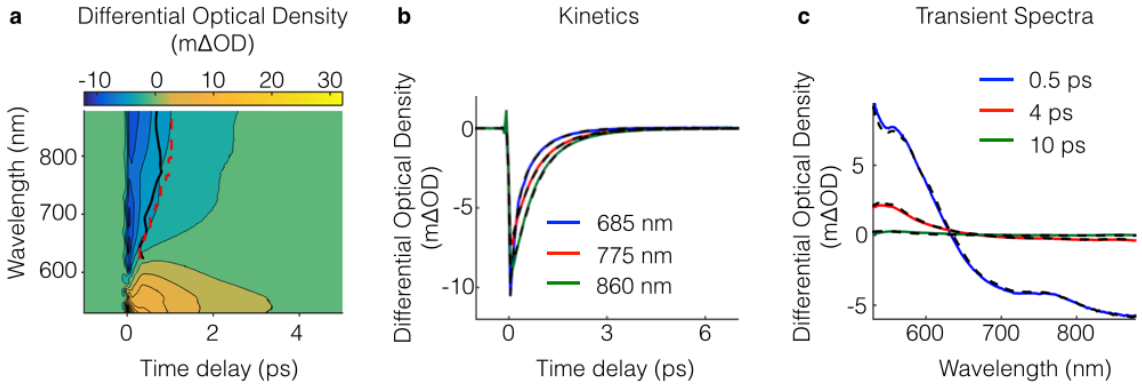

Figure A.31 all-*trans*-**10-Me** transient absorption data

all-*trans*-10,14-methyl retinal *n*-butylamine protonated Schiff base (10,14-Me)

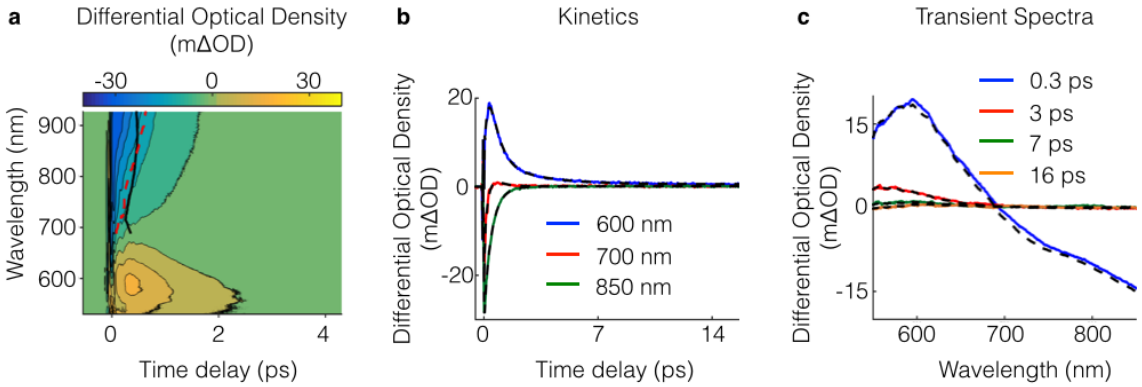

Figure A.32 all-*trans*-**10,14-Me** transient absorption data

all-*trans*-13-demethyl retinal *n*-butylamine protonated Schiff base (13-dm)

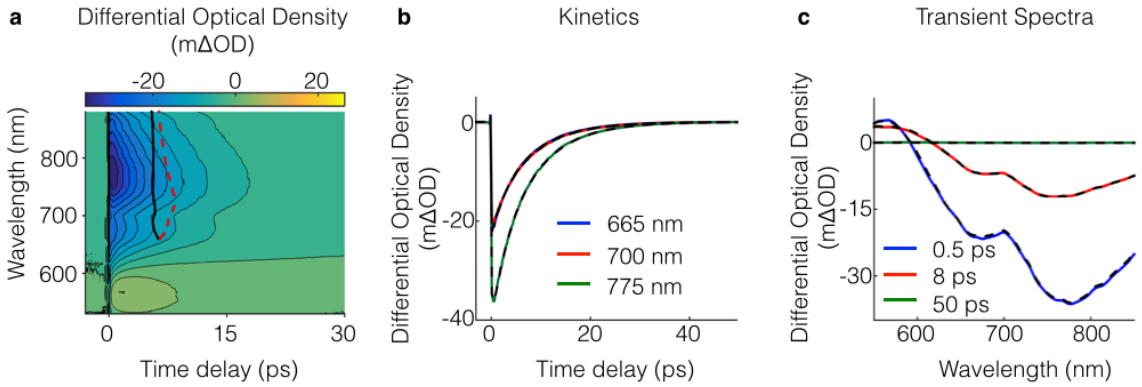

Figure A.33 all-*trans*-**13-dm** transient absorption data

all-*trans*-14-methyl retinal *n*-butylamine protonated Schiff base (14-Me)

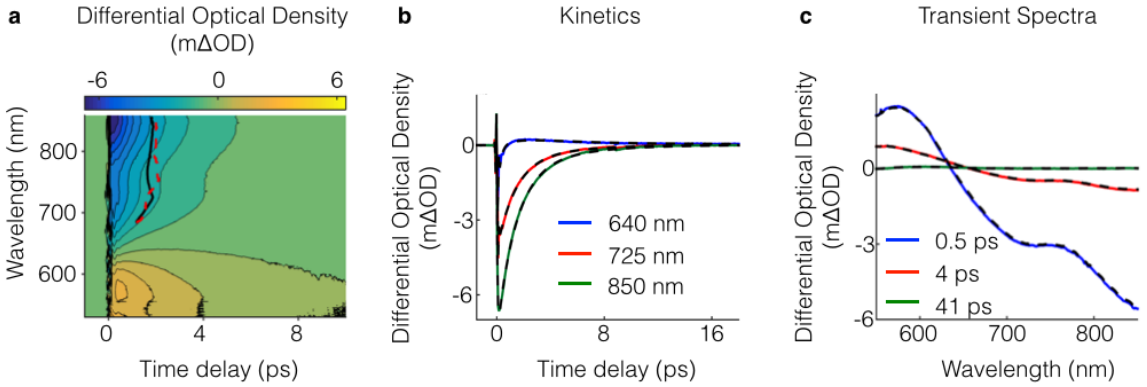

Figure A.34 all-*trans*-**14-Me** transient absorption data

all-*trans*-15-methyl retinal *n*-butylamine protonated Schiff base (15-Me)

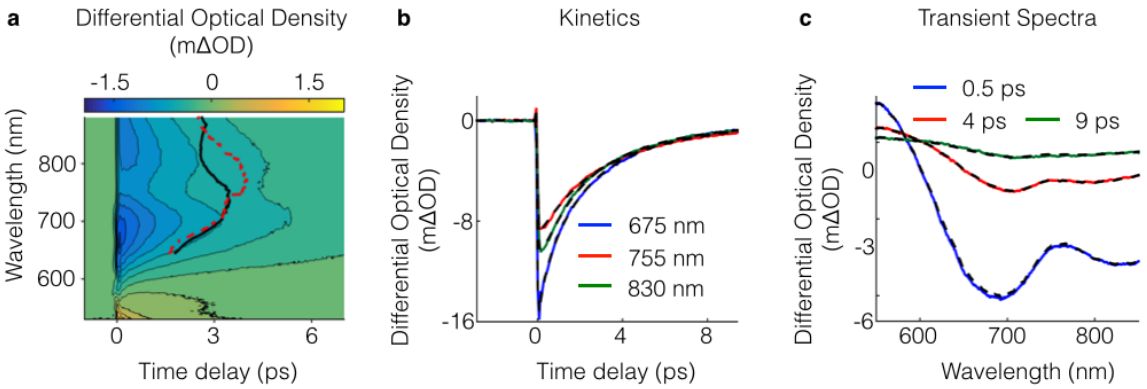

Figure A.35 all-*trans*-**15-Me** transient absorption data

all-*trans*-10-*iso*-propyl retinal *n*-butylamine protonated Schiff base (10-iPr)

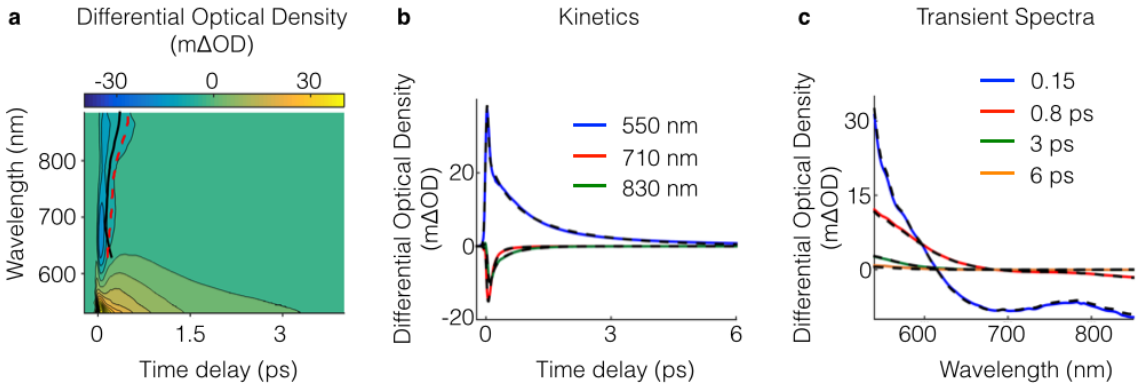

Figure A.36 all-*trans*-**10-iPr** transient absorption data

all-*trans*-10-fluoro retinal *n*-butylamine protonated Schiff base (10-F)

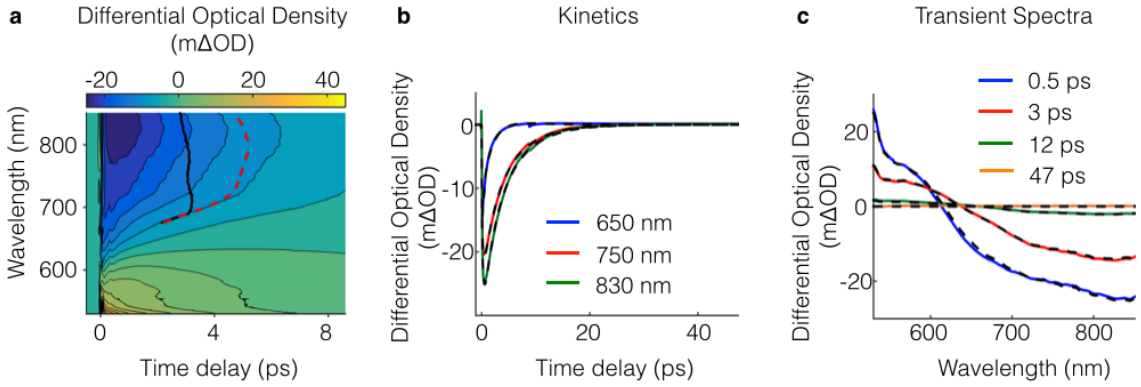

Figure A.37 all-*trans*-**10-F** transient absorption data

all-*trans*-10-chloro retinal *n*-butylamine protonated Schiff base (10-Cl)

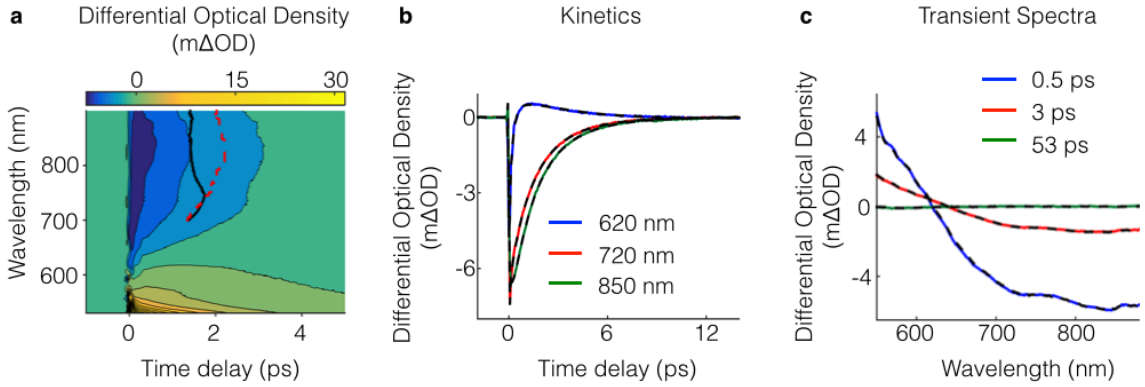

Figure A.38 all-*trans*-**10-Cl** transient absorption data

all-*trans*-10-bromo retinal *n*-butylamine protonated Schiff base (10-Br)

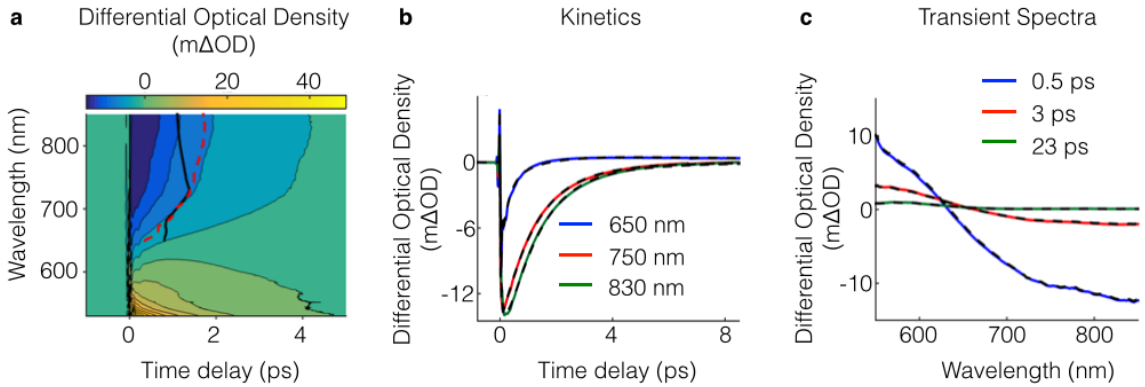

Figure A.39 all-*trans*-**10-Br** transient absorption data

all-*trans*-10-(trimethylsilyl)methyl retinal *n*-butylamine protonated Schiff base (10-Si)

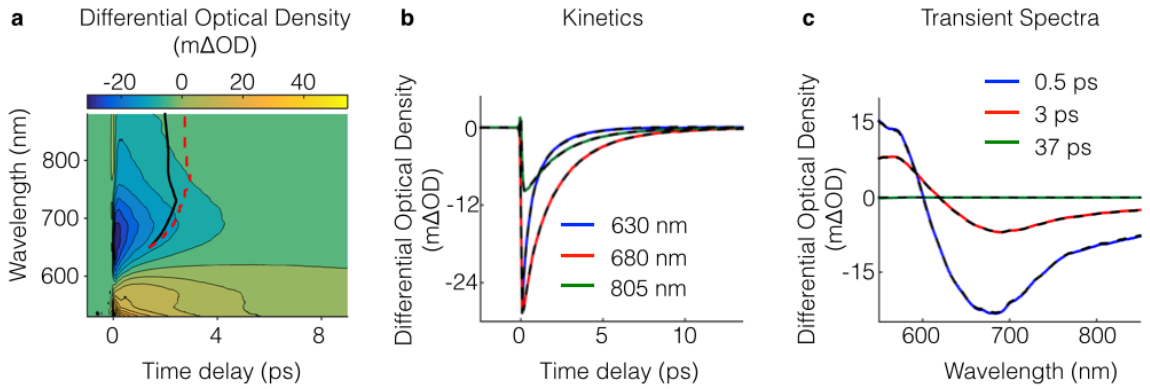

Figure A.40 all-*trans*-**10-Si** transient absorption data

Appendix B

Supplementary data for Chapter 4

1. **Bovine rod rhodopsin extraction protocol**
2. **Characterisation data for RPSBs**
3. **Photoproduct identification**
4. **Transient absorption maps, kinetics and spectra**

B.1 Bovine rod rhodopsin extraction protocol[175,176]

Dark-adapted bovine retinas were purchased from W.L. Lawson Company[a] and stored at -80 °C until use. All sample preparation and handling were performed under dim red light illumination. For each preparation, one hundred bovine retinas were thawed, resuspended in buffer A (35% wt sucrose in MOPS buffer[b] and vortexed for 4 min. Rod outer segment (ROS) were separated from cell debris by centrifuging the suspension at 6000 rpm, and isolated as supernatant. Further purification of ROSs was achieved by diluting the supernatant with MOPS buffer and centrifuging at increasing speed from 18000 to 20000 rpm. After each centrifuge step during this stage, ROSs were collected as a pellet at the bottom of the tube and resuspended before addition of fresh buffer. After this stage, ROSs were loaded onto sucrose gradient, generated with a gradient mixer with buffer A and B (22% wt sucrose in MOPS) and centrifuged in a spinning bucket rotor at 25000 rpm for 2.5 hours. The ROS band was collected after discarding the overlying bands, diluted 1:1 (v/v) with MOPS buffer

[a] W. L. Lowson Company, 15307 Fowler Ave, Omaha, NE, 68116, USA

[b] 1 L of Milli-Q®water, 4.20g MOPS, 0.17 g $CaCl_2$, 0.10 g EDTA, 0.77 g DTT, adjusted to pH 7.4 with KOH and HCl solutions.

and spun down in a centrifuge at 18000 rpm. Cells were lysed after resuspension in ice cold Milli-Q®water and spun down centrifuging twice at 18000 rpm for 45 minutes. Ammonyx®-LO was added up to a third of the final volume and gently stirred overnight. Rhodopsin samples were purified from cell lipids and bleached retinal by affinity chromatography on an hydroxyapatite column. The column was equilibrated with an imidazole buffer C,[c] and upon completion of sample loading, washed with buffer D[d] (30 mM phosphate) . The sample was then eluted from the column with buffer E[e] (150 mM phosphate) , and concentrated by centrifuge filters up to a final OD/cm of $\sim$10. Hydroxylamine was added to a final concentration of 2 mM.

B.2 Characterisation data for RPSBs

11-*cis*-10-*iso*-propyl-retinal n-butyl amine protonated Schiff base (11-*cis*-10-iPr)

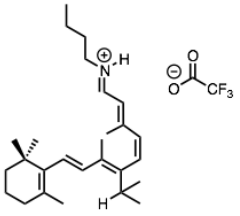

^{1}H NMR (500 MHz, CD_3OD) δ_H/ppm 0.90 (t, J=7.3 Hz, 3 H), 0.93 (s, 6 H), 1.02 (d, J=7.0 Hz, 6 H), 1.29 - 1.37 (m, 2 H), 1.38 - 1.43 (m, 2 H), 1.52 - 1.59 (m, 2 H), 1.60 - 1.65 (m, 2 H), 1.63 (s, 3 H), 1.68 (s, 3 H), 1.95 (t, J=6.2 Hz, 2 H), 2.19 (s, 3 H), 3.25 (spt, J=6.9 Hz, 1 H), 3.64 (t, J=7.2 Hz, 2 H), 6.19 (d, J=16.0 Hz, 1 H), 6.39 (d, J=10.6 Hz, 1 H), 6.40 (d, J=12.5 Hz, 1 H), 6.47 (d, J=16.0 Hz, 1 H), 6.58 (d, J=12.3 Hz, 1 H), 8.78 (d, J=11.0 Hz, 1 H).

^{13}C NMR (125 MHz, CD_3OD) δ_C/ppm 14.0, 17.0, 17.2, 20.4, 20.8, 22.2, 22.4, 29.6, 30.9, 32.2, 34.0, 35.3, 40.8, 53.3, 116.9 (q, J=287.1 Hz), 122.0, 130.6, 131.1, 131.6, 132.3, 134.5, 139.6, 141.5, 142.2, 160.4 (q, J=39.6 Hz), 168.5, 168.8.

HRMS (ESI^+) m/z calcd for $C_{27}H_{43}N$ $[M]^+$: 382.3468, found: 382.3473.

The 11-*cis* configuration of the C11=C12 double bond is supported by the dipolar coupling of H11 at 6.58 ppm with H12 (6.49 ppm) and 2D NOESY spectrum in Figure B.1 (t_{mix} = 800 ms). The dipolar couplings of Me13 (2.19 ppm) with H15 (8.78 ppm) indicates the *trans* configuration of C13=C14, as do the dipolar couplings of H7 (6.19 ppm) with Me9

[c] 1 L of Milli-Q®water, 0.7 g imidazole, 30 mL Ammonyx®-LO, adjusted to pH 7 with HCl or NaOH
[d] 500 mL Milli-Q®water, 1.07 g Na_2HPO_4, 0.9 g NaH_2PO_4, 16.5 mL Ammonyx®-LO, pH 6.86
[e] 500 mL Milli-Q®water, 5.35 g Na_2HPO_4, 4.5 g NaH_2PO_4, 16.5 mL Ammonyx®-LO, pH 6.86

(1.68 ppm) and H8 (6.47 ppm) with Me5 (1.63 ppm) for the C7=C8 double bond. H7 is further identified by its dipolar coupling with the Me1 (0.93 ppm). The dipolar coupling of H8 with the CH proton of the *iso*-propyl group indicates a *trans* configuration for the C9=C10 double bond.

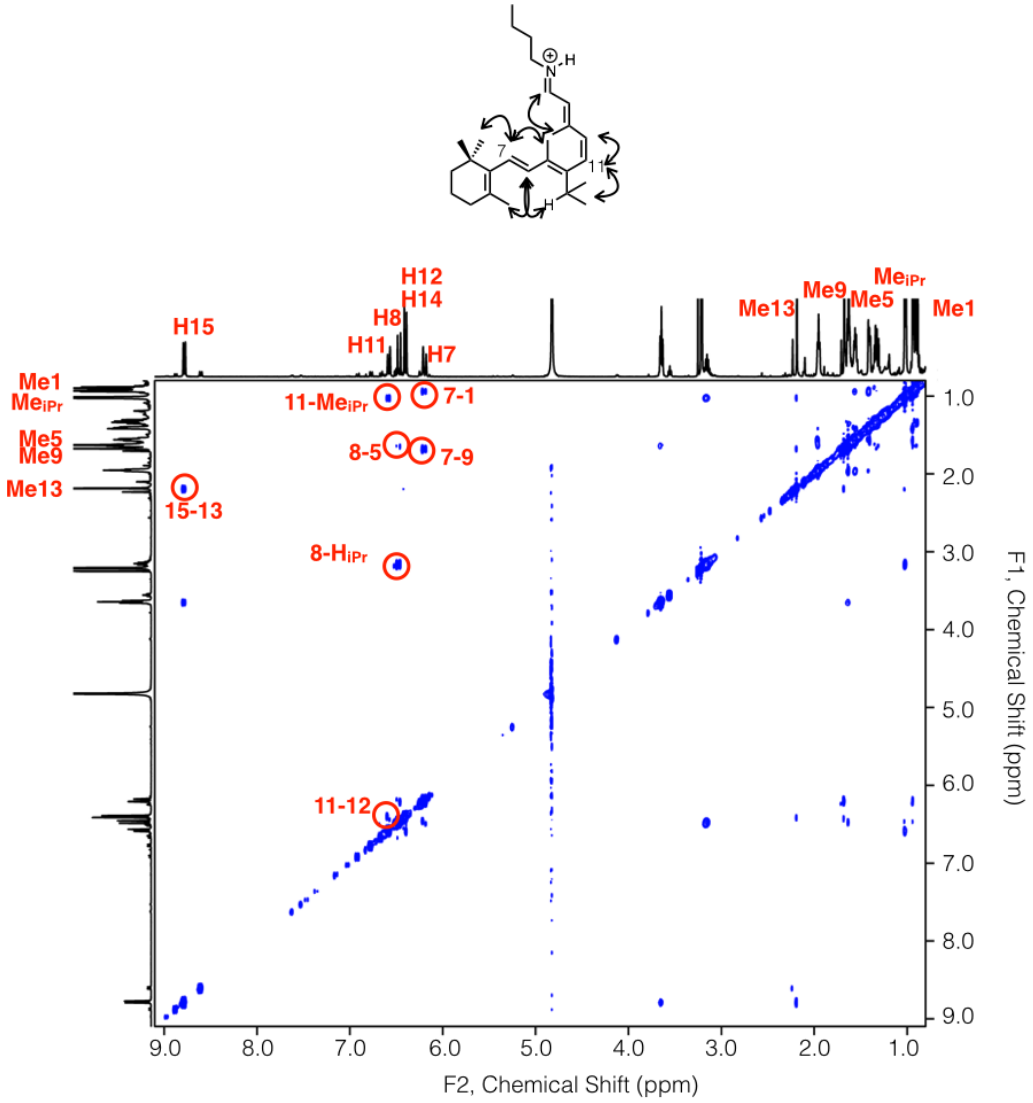

Figure B.1 NOESY (t_{mix}=800 ms) experiment for identification of 11-*cis*-**10-iPr**. Relevant cross-peaks are circled in red and labelled with the corresponding proton numbers.

11-*cis*-10-methyl n-butyl amine protonated Schiff base (11-*cis*-10-Me)

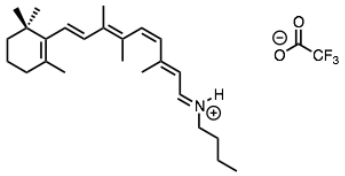

^{1}H NMR (500 MHz, CD_3OD) δ_H/ppm 1.01 (t, J=7.4 Hz, 3 H), 1.06 (s, 6 H), 1.40 - 1.48 (m, 2 H), 1.50 - 1.55 (m, 2 H), 1.63 - 1.71 (m, 2 H), 1.75 - 1.77 (m, 2 H), 1.76 (s, 3 H), 1.89 (s, 3 H), 1.95 (s, 3 H), 2.07 (t, J=6.2 Hz, 2 H), 2.32 (s, 3 H), 3.76 (t, J=7.3 Hz, 2 H), 6.29 (d, J=12.1 Hz, 1 H), 6.33 (d, J=15.9 Hz, 1 H), 6.43 (d, J=11.0 Hz, 1 H), 6.56 (d, J=16.1 Hz, 1 H), 6.81 (d, J=12.1 Hz, 1 H), 8.89 (d, J=11.0 Hz, 1 H).

^{13}C NMR (125 MHz, CD_3OD) δ_C/ppm 13.8, 15.9, 17.8, 18.3, 20.3, 20.7, 22.1, 29.4, 32.0, 34.0, 35.2, 40.7, 53.1, 116.8 (q, J=286.8 Hz), 121.5, 130.7, 130.7, 130.9, 131.7, 130.7, 132.7, 135.0, 139.3, 144.4, 160.3 (q, J=39.3 Hz), 168.4, 168.5.

HRMS (ESI^+) m/z calcd for $C_{25}H_{40}N$ $[M]^+$: 354.3155, found: 354.3150.

The dipolar coupling of Me10 (1.95 ppm) with Me13 (2.32 ppm) and H12 (6.29 ppm) with H11 (6.81 ppm) support a *cis* configuration for the C11=C12 double bond. Me13 is further identified by its dipolar coupling with H15 (8.89 ppm), whilst H11 by its dipolar coupling with Me9 (1.89 ppm). Similarly to what discussed for the native backbone in Chapter 4, this photoproduct is likely to exists in more than one conformation, as supported by the simultaneous coupling of H12 with Me13 and H14 (6.43 ppm). The presence of several spurious signals may be attributed to imperfect selective irradiation and thermal isomerisation of the compound.

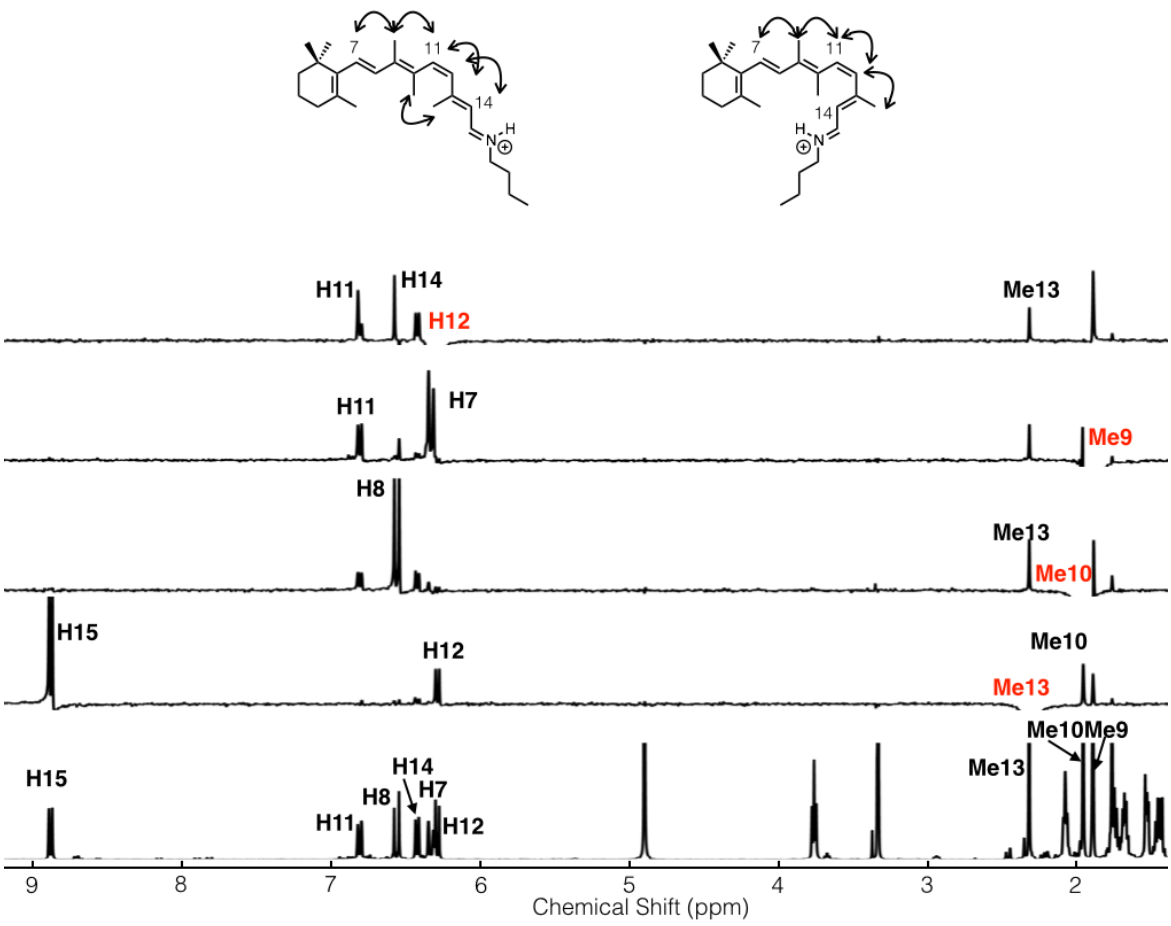

Figure B.2 NOESY (t_{mix}=800 ms) experiment for identification of 11-*cis*-**10-Me**.

B.3 Photoproduct identification

In all cases the all-*trans* photoproduct has been identified by comparison of the ^{1}H NMR spectra of the irradiated mixture with the corresponding pure all-*trans* isomer. The irradiated mixture is plotted on the bottom in red with overlapped the non-irradiated control sample in black. The spectra plotted on top in blue is the ^{1}H NMR of the relevant all-*trans* isomer. Characterisation data for the all-*trans* isomers are given in Appendix A.

11-*cis* retinal *n*-butylamine protonated Schiff base (11-*cis* NAT

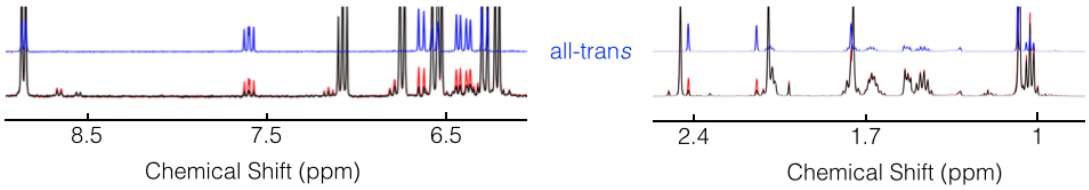

Figure B.3 Photoproduct identification for 11-*cis* **NAT**

11-*cis*-10-methyl retinal *n*-butylamine protonated Schiff base (11-*cis*-10-Me)

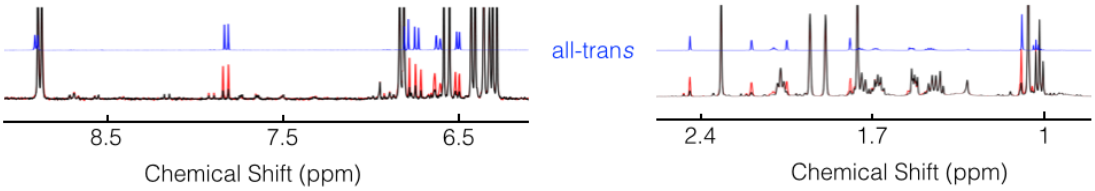

Figure B.4 Photoproduct identification for 11-*cis*-**10-Me**

11-*cis*-10-*iso*-propyl retinal *n*-butylamine protonated Schiff base (11-*cis*-10-iPr)

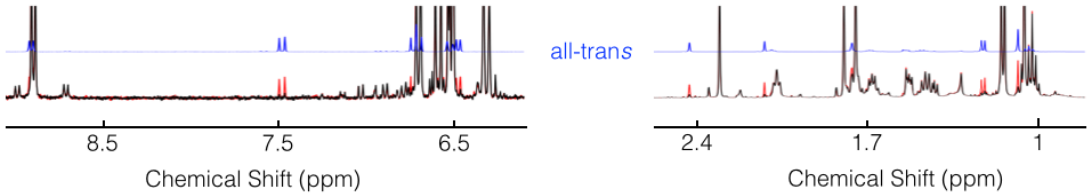

Figure B.5 Photoproduct identification for 11-*cis*-**10-iPr**

B.4 Transient absorption maps, kinetics and spectra

All the Figures in this section are structured in the following way: (a) Transient absorption data map, with plotted on top the excited state lifetimes retrieved with the two methods described in Chapter 3 (red for DADS-weighted average and black for 1/e signal decay). (b) Kinetics at selected wavelength plotted in colour with the corresponding fit on top as a black dashed line. (c) Transient spectra at selected time delays plotted in colours with the corresponding fit on top as a black dashed line. All data have been acquired exciting the system with 20-30 fs pulses centred at 500 nm (20 nJ) and probing with 2 nJ of broadband white light. Solvent is methanol in all cases.

11-*cis* retinal *n*-butylamine protonated Schiff base (11-*cis* NAT)

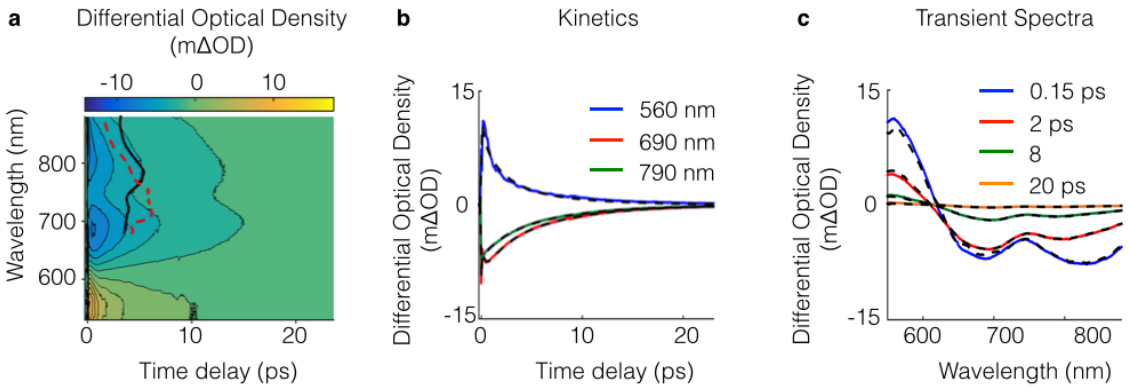

Figure B.6 11-*cis* **NAT** transient absorption data

11-*cis*-10-methyl retinal *n*-butylamine protonated Schiff base (11-*cis*-10-Me)

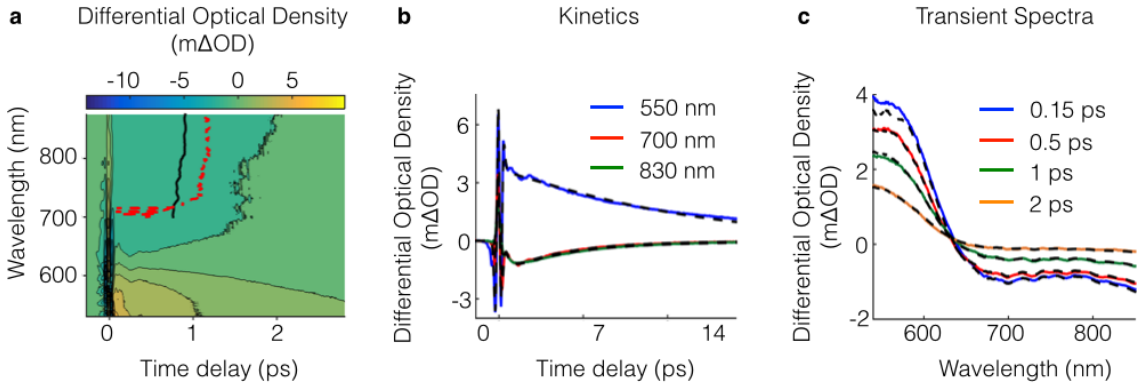

Figure B.7 11-*cis*-**10-Me** transient absorption data

11-*cis*-10-*iso*-propyl retinal *n*-butylamine protonated Schiff base (11-*cis*-10-iPr)

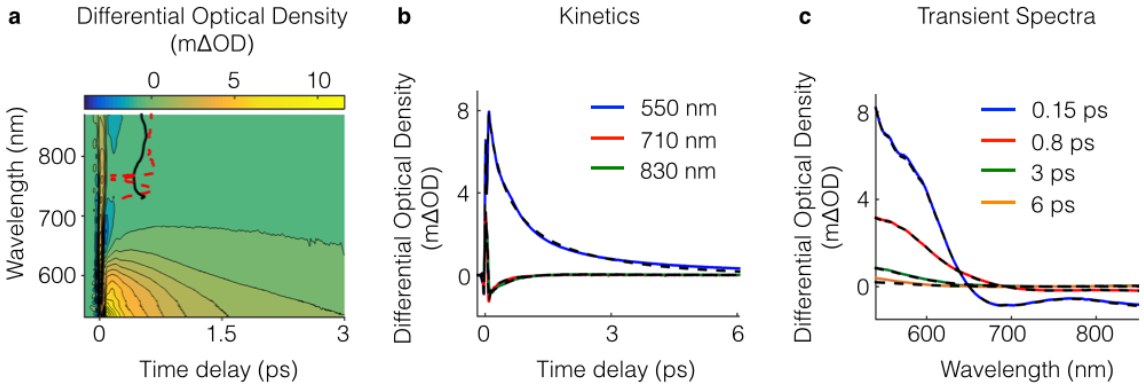

Figure B.8 11-*cis*-**10-iPr** transient absorption data

Appendix C

Supplementary data for Chapter 5

1. **Characterisation data for RPSBs**

C.1 Characterisation data for RPSBs

all-*trans* retinal aniline Schiff base (ANIsb)

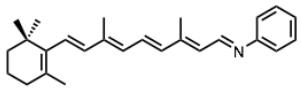

^{1}H NMR (500 MHz, CD_3OD) δ_H/ ppm 1.07 (s, 6H), 1.52 (m, 2H), 1.67 (m, 2H), 1.74 (s, br, 3H), 2.05 (s, br, 3H), 2.07 (t, J= 6.3 Hz, 2H), 2.27 (s, br, 3H), 6.20 (d, J=16.1 Hz, 1H), 6.26 (d, J=11.4 Hz, 1H), 6.34 (d, J=16.1 Hz, 1H), 6.40 (d, J= 9.9Hz, 1H), 6.54 (d, J=15.0 Hz, 1H), 7.12 (dd, J=15.0, 11.5 Hz, 1H), 7.24-7.26 (m, 3H) , 7.40 (t, J= 7.9 Hz, 2H), 8.69 (d, J= 9.9 Hz, 1H)

^{13}C NMR (125 MHz, CD_3OD) δ_C/ ppm 12.9, 13.3, 20.3, 22.0, 29.4, 34.0, 35.3, 40.8, 122.1, 127.5, 129.5, 129.7, 130.4, 130.8, 131.3, 131.3, 136.8, 139.1, 139.1, 140.5, 150.8, 152.6, 160.6

HRMS (ESI^+) m/z calculated for $C_{26}H_{34}N$ $[M+H]^+$:320.2686, measured: 320.2688.

all-*trans* retinal aniline protonated Schiff base (ANI)

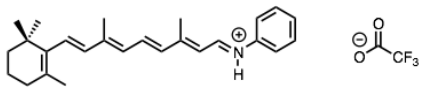

^{1}H NMR (500 MHz, CD_3OD) δ_H/ ppm 1.09 (s, 6H), 1.54 (m, 2H), 1.68 (m, 2H), 2.11 (t, br, J=6.2Hz), 2.19 (s, 3H), 2.57 (s, 3H), 6.35 (d, J=16.2 Hz, 1H), 6.47 (d, J=11.8 Hz, 1H), 6.65 (d, J=16.2 Hz, 1H), 6.72 (d, J=11.3 Hz, 1H), 6.78 (d, J=14.8 Hz, 1H), 7.52 (m, 1H), 7.60 (m, 2H), 7.69 (m, 2H), 7.77 (dd, J= 11.8 Hz, 14.8 Hz, 1H), 9.24 (d, J=11.3 Hz, 1H).

^{13}C NMR (125 MHz, CD_3OD) δ_C/ ppm 13.3, 14.6, 20.2, 22.0, 29.4, 34.3, 35.3, 40.8, 121.0, 130.9, 131.3, 131.4, 133.1, 134.2, 135.4, 138.4, 138.7, 139.0, 142.0, 149.1, 159.7, 170.2.

HRMS (ESI$^+$) m/z calculated for $C_{26}H_{34}N$ $[M]^+$:320.2686, measured: 320.2688.

all-*trans* retinal *p*-methoxyaniline Schiff base (PMAsb)

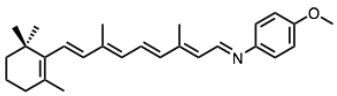

^{1}H NMR (500 MHz, CD_3CN) δ_H/ ppm 1.06 (s, 6H), 1.51 (m, 2H), 1.65 (m, 2H), 1.74 (s, 3H), 2.04 (s, 3H), 2.06 (br, t, J=6.33 Hz, 2H), 2.23 (d, J= 0.9 Hz, 3H), 3.82 (s, 3H), 6.20 (d, J= 15.7Hz, 1H), 6.26 (br, d, J=11.6 Hz, 1H), 6.33 (br, d, J= 16.9 Hz, 1H), 6.36 (br, d, 9.7 Hz, 1H), 6.52 (d, J=15.2 Hz, 1H), 6.95 (m, J= 10.1 Hz, 3.5 Hz, 2H), 7.03 (dd, J=15.0Hz, 11.3 Hz 1H). 7.21 (m, J= 10.1 Hz, 3.5 Hz, 2H), 8.64 (d, J=9.6 Hz, 1H).

^{13}C NMR (125 MHz, CD_3CN) δ_C/ ppm 12.0, 12.4, 19.0, 21.0, 28.3, 32.7, 34.0, 39.4, 55.1, 114.2, 122.3, 127.9, 128.7, 129.7, 130.3, 130.3, 136.1, 137.4, 137.7, 138.6, 145.0, 146.4, 156.2, 158.2

HRMS (ESI$^+$) m/z calculated for $C_{27}H_{36}NO$ $[M+H]^+$:390.2791, measured: 390.2776.

all-*trans* retinal *p*-methoxyaniline protonated Schiff base (PMA)

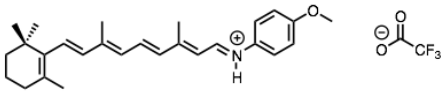

^{1}H NMR (500 MHz, CD_3CN) δ_H/ ppm 1.09 (s, 6H), 1.52 (m, 2H), 1.66 (m, 2H), 1.78 (s, 3H), 2.10 (br, tr, J= 6.4 Hz, 2H), 2.17 (s, 3H), 2.47 (s, 3H), 3.88 (s, 3H), 6.35 (d, J=16.1 Hz, 1H), 6.44 (br, d, J= 12 Hz, 1H), 6.64-6.65 (m, 2H), 6.73 (d, J=14.9 Hz, 1H), 7.11 (ddd, J= 9.1 Hz, 3.7 Hz, 2H), 7.57 (m, J= 9.1 Hz, 3.7 Hz, 2H), 7.67 (dd, J=11.8 Hz, 14.7 Hz, 1H), 8.77 (d, J=11.2 Hz, 1H).

^{13}C NMR (125 MHz, CD_3CN) δ_C/ ppm 12.5, 13.8, 18.8, 21.1, 28.3, 32.9, 34.0, 39.4, 55.6, 115.4, 119.8, 121.6, 130.1, 130.1, 132.2, 132.8, 134.0, 136.7, 137.6, 140.3, 147.6, 156.2, 160.9, 167.2

HRMS (ESI^+) m/z calculated for $C_{27}H_{36}NO$ $[M]^+$:390.2791, measured: 390.2776.

HRMS (ESI^+) m/z calculated for $C_{27}H_{32}D_4NO$ $[M]^+$:394.3042, measured: 394.3024.

all-*trans* retinal *p*-phenilenediamine Schiff base (PAAsb)

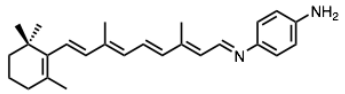

^{1}H NMR (500 MHz, CD_3CN) δ_H/ppm 1.04 (s, 6H), 1.49 (m, 2H), 1.65 (m, 2H), 1.72 (s, 3H), 2.01 (s, 3H), 2.04 (t, br, J=6.2 Hz, 3H), 2.21 (s, 3H), 6.16 (d, J=16.1 Hz, 1H), 6.21 (d, J=11.5 Hz, 1H), 6.29 (d, 16.5 Hz, 1H), 6.34 (d, J= 9.9 Hz), 6.49 (d, J=15.0 Hz, 1H), 6.72 (d, 8.6 Hz, 2H), 7.01 (dd, J= 15.0 Hz, 11.5 Hz, 1H), 7.10 (d, J=8.6 Hz, 2H), 8.65 (d, J=9.9 Hz, 1H).

^{13}C NMR (125 MHz, CD_3CN) δ_C/ppm 13.0, 13.3, 20.4, 22.1, 29.5, 34.1, 35.4, 40.9, 116.8, 123.5, 129.2, 130.2, 130.3, 130.8, 131.6, 137.3, 139.2, 139.8, 142.7, 148.4, 148.7, 155.6

HRMS (ESI^+) m/z calculated for $C_{26}H_{35}N_2$ $[M+H]^+$:375.2795, measured: 375.2790

all-*trans* retinal *p*-phenilenediamine protonated Schiff base (PAA)

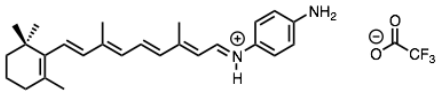

^{1}H NMR (500 MHz, CD_3CN) δ_H/ppm 1.08 (s, 6H), 1.52 (m, 2H), 1.66 (m, 2H), 1.76 (s, 3H), 2.09 (t, J= 6.2, 2H), 2.12 (s, 3H), 2.37 (s, 3H), 6.29 (d, J=16.2 Hz, 1H), 6.38 (d, J=11.1

Hz, 1H), 6.54 (d, J=16.2 Hz, 1H), 6.57 (d, J=14.7 Hz, 1H), 6.74 (d, J= 8.1 Hz, 2H), 6.92(m, 1H), 7.45 (m, 1H), 7.46 (m, 2H), 8.62 (d, J=11.5 Hz, 1H).

^{13}C NMR (125 MHz, CD_3CN) δ_C/ppm 12.3, 13.4, 18.9, 21.1, 28.3, 32.9, 34.0, 39.4, 114.7, 120.8, 121.6, 127.3, 130.2, 131.4, 131.6, 134.3, 136.9, 137.6, 145.2, 150.3, 152.3, 161.8.

HRMS (ESI$^+$) m/z calculated for $C_{26}H_{35}N_2$ $[M]^+$:375.2795, measured: 375.2801.

all-*trans* retinal N,N-dimethylethylenediamine Schiff base (C2sb)

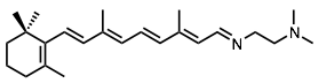

^{1}H NMR (500 MHz, CD_3OD) δ_H/ppm 0.93 (s, 6H), 1.39 (m, 2H), 1.54 (m, 2H), 1.61 (s, 3H), 1.90 (s, 3H), 1.94 (t, J= 6.6 Hz, 2H), 2.05 (s, 3H), 2.19 (s, 6H), 2.50 (t, J= 7 Hz, 2H), 3.54 (t, J=7 Hz, 2H), 6.06 (m, 3H), 6.18 (d, J= 16Hz, 1H), 6.32 (d, J=15 Hz, 1H), 6.90 (dd, J= 15, 11.5 Hz, 1H), 8.34 (d, J= 10Hz, 1H).

^{13}C NMR (125 MHz, CD_3OD) δ_C/ppm 11.5, 11.7, 18.9, 20.6, 28.0, 32.6, 33.9, 39.4, 44.3, 57.9, 59.3, 127.4, 127.7, 127.9, 128.9, 129.2, 129.9, 135.4, 137.7, 138.3, 146.9, 162.2.

HRMS (ESI$^+$) m/z calculated for $C_{24}H_{39}N_2$ $[M+H]^+$:355.3108, measured: 355.3094.

all-*trans* retinal retinal N,N-dimethyl-1,4-butanediamine Schiff base (C4sb)

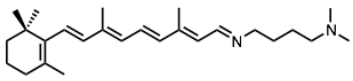

^{1}H NMR (500 MHz, CD_3OD) δ_H/ppm 0.93 (s, 6H), 1.38-1.45 (m, 4H), 1.50-1.58 (m, 4H), 1.61 (s, 3H), 1.90 (s, 3H), 1.94 (m, 2H), 2.04 (s, 3H), 2.13 (s, 6H), 2.25 (m, 2H), 3.42, (m, 2H), 6.02-6.10 (m, 3H), 6.18 (d, J= 16 Hz, 1H), 6.32 (d, J= 15 Hz, 1H), 6.89 (dd, J= 15.3, 11.3 Hz, 1H), 8.31 (d, J= 9.6 Hz, 1H).

^{13}C NMR (125 MHz, CD_3OD) δ_C/ppm 11.4, 11.6, 18.9, 20.6, 24.5, 28.0, 28.4, 32.6, 33.8, 39.4, 43.9, 59.0, 60.2, 127.3, 127.7, 127.9, 128.8, 129.2, 129.9, 135.4, 137.7, 138.2, 146.5, 161.3.

HRMS (ESI$^+$) m/z calculated for $C_{26}H_{43}N_2$ $[M+H]^+$:383.34317, measured: 383.34225.

all-*trans* retinal retinal N,N-dimethyl-1,4-butanediamine protonated Schiff base (C4)

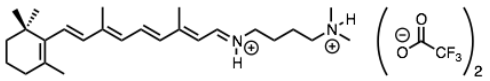

^{1}H NMR (500 MHz, CD_3OD) δ_H/ppm 0.95 (s, 6H), 1.40 (m, 2H), 1.56 (m, 2H), 1.64 (s, 3H), 1.72 (m, 4H), 1.97 (m, 2H), 2.03 (s, 3H), 2.31 (s, 3H), 2.80, (s, 6H), 3.08 (m, 2H), 3.70 (m, 2H), 6.16 (d, J= 16 Hz, 1H), 6.26 (d, J= 11.2 Hz, 1H), 6.37 (d, J= 11 Hz, 1H), 6.45 (d, J= 16 Hz, 1H), 6.52 (d, 15 Hz, 1H), 7.49 (dd, J= 11.2, 15 Hz, 1H), 8.75 (d, J= 11 Hz, 1H).

^{13}C NMR (125 MHz, CD_3OD) δ_C/ppm 11.7, 12.9, 18.8, 20.58, 21.3, 25.7, 28.0, 32.7, 33.9, 39.4, 42.0, 50.6, 56.7, 115.7 (q, J= 288 Hz), 118.8, 129.6, 131.0, 131.8, 133.3, 137.0, 137.6, 138.8, 145.9, 159.6 (q, J= 38 Hz), 166.0, 166.3.

HRMS (ESI^+) m/z calculated for $C_{26}H_{43}N_2$ $[M]^+$:383.34317, measured: 383.34225.

Appendix D

Supplementary data for Chapter 6

1. **GFPs expression and purification protocols**
2. **Preparation and characterisation data of HBDI**
3. **HBDI quantum yield measurements**

D.1 GFPs expression and purification protocols[42,248]

Plasmids containing **wtGFP**, **S65T** or **sGFP** modified with a 6xHis tag were transformed in *E. coli* BL21(DE3) cell line. Briefly, 0.5 μL of plasmid were added in 25 μL of competent BL21(DE3) cells and incubated on ice for 25 min, heat shocked for 45 sec at 42 °C and incubated further for 2 min on ice, followed by the addition of 150 μL of pre-warmed SOC media at 37 °C SOC and incubated at 37 °C with shaking for one hour. In a LB-media Petri dish supplemented with 100 μg/mL ampicillin (for **sGFP**) or kanamycin (**wtGFP** and **S65T**), 50 μL of the cell culture were plated and incubated overnight at 37 °C. A few colonies were selected and allowed to inoculate 100 μL of LB-media in the presence of 100 μg/mL of the appropriate antibiotic and allowed to grow overnight. The overnight cell culture was used to inoculate 8 L (8x1 L in 2 L flasks) of TB media with 100 μg/ml antibiotic. Cells were grown at 37 °C to an OD_{600} of 0.6-0.8 upon which 0.5 mM IPTG was added. **sGFP** was allowed to express for an additional 3 hours at the same temperature, whilst **wtGFP** and **S65T** were expressed overnight at 20 °C. Cells were harvested through centrifugation at 10,000xg for 10 min and the pellets were re-suspended in cell lysis buffer[a] supplemented with a protease inhibitor tablet (Roche). Cells were lysed by microfluidizer and the cell debris were removed

[a] 300mM NaCl, 50mM Tris, pH 7.4

by centrifugation at 20,000xg for 20 min. In the supernatant, imidazole was added to a final concentration of 20mM and the first purification step was achieved by immobilised metal ion affinity chromatography (IMAC) using a 20 mL IMAC column equilibrated in buffer A[b]. After four column volumes washes with buffer A the sample was eluded with buffer B[c]. The sample was concentrate to a final volume of 10mL and loaded in a size exclusion chromatography (SEC) column 26/60 Superdex 75 previously equilibrated in SEC buffer[d]. The fractions were selected based on their fluorescence and pooled and concentrated to the desired OD (OD 9-10 at λ 398 nm for **wtGFP**, OD 12 at λ 484 nm for **sGFP** and OD 16 at λ 474 for **S65T**).

D.2 Preparation and characterisation data of HBDI

4-(*p*-Acetoxy)benzylidene-2-methyl-5-oxazolone (6.1)

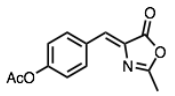

N-acetylglycine (1 g), *p*-hydroxybenzaldehyde (1.2 g, 1.2 eq) and sodium acetate (480 mg, 0.7 eq) were mixed in a flame dried flask. Acetic anhydride (8.5 mL) was added and the system brought to reflux for 6.5 h. After that time, ice was poured in the reaction mixture and the system was allowed to cool down and then stored overnight in the fridge. The solid residue was dissolved and extracted in $CHCl_3/H_2O$. The organic phase was washed with brine, dried over $MgSO_4$ and evaporated under vacuum. The product was further purified by flash chromatography (Petroleum ether 40-60/Ethyl acetate 8/2 v/v). Clean Product collected: 1.04 g (yield 43%).

^{1}H NMR (500 MHz, $CDCl_3$), δ_H/ppm 2.22 (sb, 3H), 2.29 (sb, 3H), 6.99 (sb, 1H), 7.08 (m, J= 8.7 Hz, 2H), 8.00 (m, J= 8.7 Hz, 2H).

^{13}C NMR (125 MHz, $CDCl_3$), δ_C/ppm 15.6, 21.1, 122.15, 130.1, 130.8, 132.5, 133.5, 152.6, 166.3, 167.7, 168.9.

HRMS (ESI^+) m/z calcd for $C_{13}H_{11}NNaO_4$ $[M+Na]^+$: 268.0580, found: 268.0587.

[b]300 mM NaCl, 20 mM Tris and 20 mM imidazole, pH 7.4
[c]300 mM NaCl, 20 mM Tris and 500 mM imidazole pH 7.4
[d]150 mM NaCl and 20 mM Tris pH 7.4

9-Methyl-2-acetamido-3-(4-hydroxyphenyl)acrylamide (6.2)

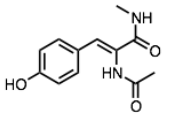

4-(*p*-Acetoxy)benzylidene-2-methyl-5-oxazolone (**6.1**) (600 mg) was dissolved in EtOH (15 mL) and aqueous methylamine (40%, 4.5 mL) were added under magnetic stirring. The reaction was stirred for two hours until completion (as monitored by TLC, Petroleum ether/Ethyl acetate 8/2 v/v) and the solvent evaporated. The product retrieved was used in the final cyclization step without any further purification step.

^{1}H NMR (500 MHz, d_6-DMSO), δ_H/ppm 2.01 (s, 3H), , 2.67 (d, J= 4.5 Hz, 3H), 6.75 (m, J= 8.7 Hz, 2 H), 7.04 (s, 1H), 7.36 (m, J= 8.7 Hz, 2H), 7.76 (q, J= 4.5 Hz, 1H), 9.23 (s, 1H).

^{13}C NMR (125 MHz, d_6-DMSO), δ_C/ppm 23.4, 26.7, 115.9, 125.4, 127.3, 129.1, 131.6, 158.6, 166.1, 169.9.

HRMS (ESI$^+$) m/z calcd for $C_{12}H_{14}N_2NaO_3$ $[M+Na]^+$: 268.0580, found: 268.0587.

4-(4-Hydroxybenzylidene)-1,2-dimethylimidazol-5-one (HBDI)

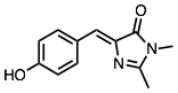

9-Methyl-2-acetamido-3-(4-hydroxyphenyl)acrylamide (**6.2**) retrieved from the previous step after evaporation was dissolved in pyridine (∼10 mL) and kept under refluxing conditions for 48 hours. The solution was allowed to cool down, ethyl acetate was added and an extraction with HCl was repeatedly performed. The aqueous phase reunited were neutralised with sodium bicarbonate (as checked by litmus paper) and extracted with ethyl acetate. The organic phase was dried over $MgSO_4$ and evaporated under reduced pressure. The product was retrieved clean (as evaluated by ^{1}H NMR), without need of further purification. (Yield 50%)

^{1}H NMR (500 MHz, d_6-DMSO), δ_H/ppm 2.33 (s, 3H), 3.09 (s, 3H), 6.83 (m, J= 8.7 Hz, 2H), 6.89 (s, 1H), 8.08 (m, J= 8.7 Hz, 2H), 10.1 (s br, 1H).

^{13}C NMR (125 MHz, d_6-DMSO), δ_C/ppm 15.7, 26.6, 116.2, 125.8, 125.9, 134.5, 136.7, 160.0, 162.7, 170.3.

HRMS (ESI$^+$) m/z calcd for $C_{12}H_{13}N_2O_2$ $[M+H]^+$: 217.09715, found: 217.09686.

D.3 Quantum yield measurements for HBDI

The photoisomerisation quantum yield of **HBDI** in d_6-DMSO has been measured relatively to the one in d_8-THF, as a literature value of 0.5 was available only for the latter solvent.[46] Concentrated samples (1mg/mL, OD ∼7) were irradiated with a 375 nm low power LED (nominal power ∼0.4 mW) in a pyrex test tube for 16 minutes each. The average photoisomerisation rate (in molecules s^{-1}) was evaluated in the two solvents. The number of photoisomerised molecules was evaluated via Equation 2.1.5

$$\text{Molec}_{photo} = [Sample] \cdot V_{irr} \cdot F_{photo} \cdot N_A, \tag{2.1.5}$$

The ratio between the two values is equal to the ratio of the QYs, provided that the incident power stays constant during the different measurements.

$$\frac{k_{DMSO}}{K_{THF}} = \frac{\phi_{DMSO} P_{inc}}{\phi_{THF} P_{inc}}, \tag{D.3.1}$$

where k is the photoisomerisation rate, ϕ the quantum yield and P_{inc} the absorbed power that can be considered equal to the incident power due to the high optical density of the samples.

The concentration of each sample [Sample] was evaluated individually with the method described in Chapter 2, via equation (2.1.6), using benzene as internal standard.

$$[\text{Sample}] = [Standard] \cdot \frac{Area_{sample}}{Area_{standard}} \cdot \frac{N_{standard}}{N_{sample}}. \tag{2.1.6}$$

The fraction of photoisomerised molecules F_{photo} was evaluated by integration of the starting material and photoproduct resonances as described in Chapter 2.

The average phoisomerisation rates in DMSO and THF were 2.36×10^{14} and 2.32×10^{14} molecules $s^{-}1$, respectively, suggesting an identical quantum yield in the two solvents within the experimental error of the measurements.

In Figure D.1 are shown the irradiated (coloured) and control (black) spectra of **HBDI** in d_6-DMSO (red) and d_8-THF (blue). Starred resonances are photoproduct peaks, whilst the resonance at 7.3 ppm is benzene in the non-irradiated sample.

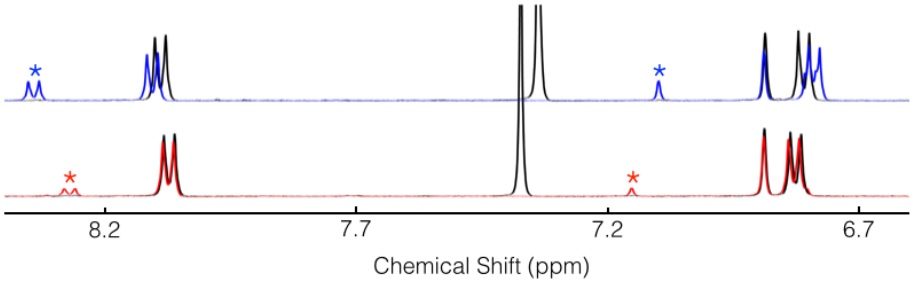

Figure D.1 Irradiation of **HBDI** in DMSO (red) and THF (blue), with the non-irradiated spectra plotted in black underneath. The starred resonances are the appearing photoproduct peaks.

To check that no spontaneous back-isomerisation of the photoproduct occurred (as reported in presence of nucleophiles),[245] the spectra of the irradiated mixtures were measured again after standing in the dark for 70 (THF, blue) and 41 (DMSO, red) minutes, and no changes were observed (Figure D.2).

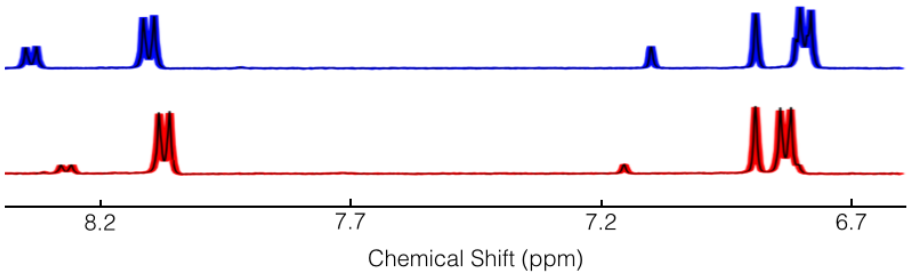

Figure D.2 Stability control for the irradiated mixtures in DMSO (red) and THF (blue). The spectrum measured after 41 and 70 minutes is plotted in black

Acknowledgements

At the end of a four years journey, there are several people that should be acknowledged, people without whose guidance and help this work would have been much poorer than it ended up being.

I would like to thank Philipp, for giving me in the first place the possibility to join his group and for all the help received in carrying out the project assigned, the more when things were not clear or working.

The current and former members in the Kukura research group, for generating a scientifically stimulating environment. I would like to thank particularly:

Matz Liebel, Cristoph Schnedermann, Alex Duarte and Jong Min Lim for the help with the laser;

Jaime Ortega Arroyo, for helping me defeat the LaTeX monster;

Alexander Weigel, for a lot of helpful and stimulating discussions, and his generosity in providing insightful suggestions;

Katelyn Spillane, for patiently initiating me to the dimly light world of purification of photosensitive proteins;

Joanna Andrecka and Gabrielle de Wit, for helping me looking at things from different prospectives.

I would also like to thank the research collaborators who in different ways helped with carrying out the work here presented, Dr. Tim Claridge, Dr. Barbara Odell, Dr. Stephen Fletcher, Tina Sovdat and Idlir Liko.

I would finally like to thank my family without whose support I would not have managed to go through these four years, for having always made me feel they believed in me and having been present in my life anytime I needed, most often than not without need for me to ask.

To my parents, whose ability to face the difficulties encountered has been a constant source of strength and inspiration;

To Serena. Seeing you thriving in the work you love is a constant source of joy;

To my aunts and uncles, whose presence in my life has given to the concept of family a broader and warmer dimension;

To my grandmother, whose cheerful and caring presence I still have the luck to enjoy, and to the grandparents who are now gone, whose loving memories bring bittersweet smiles, mixture of affection and loss;

To Alessio, Barbara, and Olga, brother and sisters in mind and spirit if not in blood. Scattered through the world as we might be, I'll make sure the fishing vessels will always reach you;

And to Chih-Suei, for making every day special and rendering it a treasure to cherish and preserve. Looking forward to a lifetime more.

This work, small thing as it is, is dedicated to you all.